Search for compressed supersymmetry at the LHC in final states with one hadronic tau and one energetic jet

By

Manuel Alejandro Segura Delgado

Dissertation Submitted to the Faculty of the Physics of the University of Los Andes in Fulfillment of the Requirements for the Degree of:
Doctor en Ciencias, Física

Supervised by:
Andrés Flórez Ph. D.
University Los Andes, Colombia

Co-Supervised by:
Alfredo Gurrola Ph. D.
Vanderbilt University, USA

Universidad de los Andes

Bogotá, Colombia.
2019

Acceptance note

Jury signs

Jury signs

Advisor signs

Co-advisor signs

Bogotá, 2019

To Jesus Christ owner of everything...

To my son and his mom for existing in my life...

Santiago Segura Bernal
Monica Bernal

Acknowledgments

Along the way, many people have contributed to my scientific education by imparting small but important knowledge or challenging my perspective just enough to help me see the solution to a problem. I would like to take a moment to express my gratitude to some of them.

- To my advisor, Dr. Andrés Florez for his full attention given to my work, his patience, he helped me to handle the stress and all challenges during this time.
- To my co-advisor, Dr. Alfredo Gurrola and to his Ph.D student Ms. Savanna Starko for all the support and guidance throughout the experimental analysis.
- To my family and friends, Monica Bernal, Carlos Gonzalez and Luis Bravo for helping me focus on what is truly important.
- To the **CERN** laboratory, for that unforgettable year and all of those experiences, I lived there.
- To High Energy Physics group of the **University Los Andes** and the **BSM3G** group, for all experiences, new knowledge and the opportunity to participate in the current challenges of this area of Physics.
- To Physics department of the **University Los Andes** and **COLCIENCIAS**, for the financial support received that made possible this work.

Abstract

We present an experimental search of supersymmetry (SUSY) in compressed mass spectra scenarios with scalar taus ($\tilde{\tau}$'s), using data from proton-proton (pp) collisions in the Large Hadron Collider, LHC, at CERN laboratory, at $\sqrt{s} = 13$ TeV, collected by the CMS experiment in 2016 and 2017. Compressed mass spectra scenarios, where the mass difference between the lightest neutralino ($\tilde{\chi}_1^0$) and the $\tilde{\tau}$ is small, have been proposed in several models in order to incorporate coannihilation as a mechanism to obtain a relic dark matter density consistent with that predicted by astronomy. The compressed mass region in SUSY is challenging to probe experimentally. We focus on a final state containing exactly one tau lepton, with low transverse momentum (p_{T}), that has decayed hadronically (τ_h), at least one initial state radiation jet (ISR) with high p_{T}, and a large imbalance of missing transverse momentum (p_{T}^{miss}). An integrated luminosity of 77.2 fb^{-1} of pp data was used for this analysis. The data was found to be in agreement with respect to the expected background. Therefore, upper limits on the production cross-section as function of $\tilde{\chi}_1^{\pm}$ ($\tilde{\chi}_2^0$) mass were set, excluding masses up to 290 GeV for a mass splitting of $\Delta m(\tilde{\chi}_1^0, \tilde{\tau}) = 50$ GeV. The limits set on this search, constitute the most stringent limits today for all $\tilde{\tau}$ related searches.

Resumen

Presentamos una búsqueda experimental de supersimetría (SUSY) en escenarios de espectros comprimidos de masa con taus escalares ($\tilde{\tau}$'s), usando datos de colisiones protón-protón (pp) en el gran colisionador de hadrones, LHC, del laboratorio CERN, a $\sqrt{s} = 13$ TeV, colectados por el experimento CMS en 2016 y 2017. Los escenarios de espectros comprimidos de masa, donde la diferencia de masa entre el neutralino más ligero ($\tilde{\chi}_1^0$) y el $\tilde{\tau}$ es pequeña, han sido propuesto por varios modelos con el fin de incorporar coaniquilación como mecanismo para obtener una densidad de reliquia de materia oscura consistente con el valor estimado usando mediciones astronómicas. Es un reto probar la región comprimida de masas en SUSY experimentalmente. Nos enfocamos en estados finales que contienen exactamente un leptón tau, con bajo momento transversal (p_{T}), que decae hadronicamente (τ_h), al menos un jet de radiación de estado inicial (ISR) con alto p_{T} y un gran imbalance de momento transverso faltante (p_{T}^{miss}). Una luminosidad integrada de 77.2 fb^{-1} de datos pp fue usada para este análisis. Los datos concuerdan con los eventos esperados del modelo estándar. Por lo tanto, se establecen límites superiores en la sección eficaz de producción como función de la masa del $\tilde{\chi}_1^{\pm}$ ($\tilde{\chi}_2^0$), excluyendo masas hasta 290 GeV para una diferencia de masas de $\Delta m(\tilde{\chi}_1^0, \tilde{\tau}) = 50$ GeV. Los resultados obtenidos de este análisis, constituyen hoy los limites más rigurosos para todas las búsquedas relacionadas con $\tilde{\tau}$'s hasta el momento.

Table of content

List of figures

List of tables

CHAPTER 1

Introduction

Section 1.1

Brief overview of the Standard Model

The composition of matter has been one of the hardest and most interesting questions throughout human thought. Leucippus and Democritus proposed that matter is made of small particles, which they called atoms, over 2400 years ago. Today, we know that the matter that composes planets, stars, and human beings, has the exact same basic components and characteristics. This knowledge is the result of great effort during the last century to understand the hidden world behind of the atoms. Particle physics started with the discovery of the *electron* (e^-) in 1897 by J.J. Thomson, who by studying the behavior of cathodic rays with magnetic fields, inferred that those rays consisted of charged and massive particles [1].

The charge of the electron suggested a positive charged environment to get the neutral charge of the atom. The frequency of the radiation within of the simplest atom was consistent with the experimental yield, $2.47 \times 10^{15}\ Hz$. Nevertheless, the scattering experiments performed by Rutherford in 1911 showed the positive charge (the *proton*) had to be in the center of the atom. Classical theories could not explain the stability of the electron rotating around the nuclei, considering the expected energy lost due to radiation, neither provided an estimation of the size of the atom. Niels Bohr in 1914 suggested a new idea about the motion within the atom by quantizing the angular momentum of the electron. Bohr's model predicted correctly the spectrum of the hydrogen atom and it was the first attempt to understand its dynamics using a non-relativistic semi-classical approach [2].

In 1905, Einstein had introduced a theory to explain the invariance of the speed of light and its consequences, known as the theory of relativity. The first equation that combined the quantum effects and the relativistic regime was Dirac's equation $(i\gamma^\mu \partial_\mu - m) = 0$, which describes the dynamics of electrons. In addition, it seemed to predict particles with exactly the same mass of the electron but with opposite charge. Moreover, the negative energy values would be contradictory with the stability of matter. This theoretical aspect was interpreted by Feynman as a new type of matter called anti-matter. In 1932, Carl Anderson, an American physicist, discovered the first antiparticle called the *positron* (e^+).

The theory that describes the interactions between the electron and positron is known as Quantum Electrodynamics (QED), in which the *photon* (γ) is the mediator of such interaction. This theory was developed by Feynman and Schwinger in 1940. Nevertheless, the dynamics of the nucleus remained a puzzle. By trying to understand the behavior of the nucleus, in 1935, Hideki Yukawa, a Japanese physicist, proposed a new particle called the *meson*. Later, Carl Anderson, an American physicist, who led cosmic rays experiments discovered this new particle.

In 1930, Wolfgang Pauli, an Austrian physicist proposed a new particle, which is massless and electrically neutral. This particle is known today as the neutrino, and its physical properties solved two physics problems at that moment: The β decay and an angular anomaly in the pion decay. In the β^- decay, the neutron is converted to a proton plus an electron, the expected spectrum of the energy of the electron is determined by its kinematics. Nevertheless, the experimental result showed that the spectrum of the kinetic energy of the electron is continuous, which was the evidence of the existence of the neutrino. On the other hand, the pion decay requires an additional particle to suppressed the angular anomaly, which is further evidence of the existence of the neutrino. In 1956, Clyde Cowan and Frederick Reines, American physicists, studied inverse β decay ($\bar{\nu} + p^+ \to n + e^+$) using nuclear reactors. The result of this research was the discovery of the neutrino.

In 1947, George Rochester, British physicist discovered a new neutral particle known as the *kaon* (K), which decays into two pions ($K^0 \to \pi^+ + \pi^-$) and charged kaons that can decay into three pions ($K^+ \to \pi^+ + \pi^- + \pi^+$). The later discovery of several new particles throughout 1950s and 1960s, known as the *Particles Zoo* age, led to theoretical physicists to think in a more fundamental structure of the known particles. In 1964, Murray Gell-Mann and George Zweig, American physicists, proposed that the non-fundamental particles discovered in colliders such as: K's and π's could have an internal structure. The model that describes the structure of these particles is known as the quark-model. A quark (q) is a fundamental particle with spin 1/2, fractional electric charge, and a new quantum property known as *color* charge. Different combinations of quarks can generate the spectrum of observed non-fundamental particles such as the pion ($q\bar{q}$). The discovery of the color charge allows the existence of bound states with three quarks, which is predicted by the quark-model such as the proton and the Ω^- (qqq) [1].

In 1970, deep inelastic scattering experiments carried out at the SLAC laboratory, allowed to classify the known particles into generations [3]. These generations were defined by three type of quarks: *up* (u), *down* (d), and *strange* (s). In 1974, the discovery of the $J/\psi(c\bar{c})$ particle was explained for a new type of quark: *charm* (c). In the subsequent years, a third generation of quarks was discovered. In 1977, the particle $\Upsilon(b\bar{b})$ was observed, which was explained by the quark *bottom* (b). In 1995, the *top* (t) quark was discovered in $p\bar{p}$ collisions at the Tevatron collider, in Fermilab [4]. In 1975, Martin Perl, an American Physicist, discovered the *tau* (τ) lepton in the SLAC laboratory.

The particles associated with interactions in the SM, which are called bosons: the gluon related to the strong interaction, the Z and W related to the electroweak interaction, and the Higgs boson associated with the mechanism to generate the mass in the SM, were discovered in the subsequent years. In 1970, the gluon was discovered by the DESY collaboration [5]. In 1983, the Z and W were discovered at CERN laboratory [6]. Finally, the Higgs boson was discovered at CERN laboratory in 2012 [7].

1.1.1 Description of the Standard Model

The historical context of particle physics, that is led by the development of theoretical ideas and the experimental evidence, can be summarized in a global benchmark known as the Standard Model (SM). This model has been built upon both theoretical predictions and experimental observations. In the SM, the matter is formed by fundamental particles known as *fermions*, which are half-integer-spin objects that satisfy Pauli's exclusion principle. The SM includes three of the four fundamental known interactions: electromagnetic, weak and strong. These interactions are mediated by particles classified to as *gauge bosons*, which are integer-spin objects that satisfy the Bose-Einstein statistics principle.

In the SM, fermions are divided into two different categories: leptons (e, μ, τ) and quarks (u, d, c, s, b, t). Among leptons, we find the electron (e), the muon (μ) and the tau (τ). These three different types of leptons are characterized by having the same electric charge, all equal to the fundamental charge of the electron, but each with a different mass. Each of these leptons has an associated particle known as the neutrino, which does not carry an electric charge (ν_e, ν_μ, ν_τ). Neutrinos are exotic particles whose properties are still under study.

Quarks are particles which carry two different types of charge: electric and color charge. All quarks have an electric charge that is a fraction of the electron charge, $|\frac{1}{3}|$ or $|\frac{2}{3}|$ of $|e|$, depending on the quark. Just as the electric charge is an intrinsic property of some particles, similarly, color charge is a quantum property that has been observed only in quarks so far. In the SM, leptons and quarks are divided into three different generations (families) organized according

Table 1.1: Basic properties of quarks and leptons in the SM; rgb means red-green-blue color interactions.

Particle	Symbol	Spin	Charge (e^-)	Color charge	Mass [MeV/c^2]
	First Generation				
up	u	1/2	$+\frac{2}{3}$	rgb	$2.3^{+0.7}_{-0.5}$
down	d	1/2	$-\frac{1}{3}$	rgb	$4.8^{+0.5}_{-0.3}$
electron	e^-	1/2	-1	0	0.511
electron neutrino	ν_e	1/2	0	0	$< 10^{-5}$
	Second Generation				
charm	c	1/2	$+\frac{2}{3}$	rgb	1275 ± 2.5
strange	s	1/2	$-\frac{1}{3}$	rgb	95 ± 5
muon	μ^-	1/2	-1	0	105.7
muon neutrino	ν_μ	1/2	0	0	$< 10^{-5}$
	Third Generation				
top	t	1/2	$+\frac{2}{3}$	rgb	173211 ± 510
botton	b	1/2	$-\frac{1}{3}$	rgb	4660 ± 30
tau	τ^-	1/2	-1	0	1777
tau neutrino	ν_τ	1/2	0	0	$< 10^{-5}$

to their mass. The first family is the lightest and the third family the heaviest. As mentioned above, in the SM the interactions among particles are mediated by gauge bosons. The photon, γ, is the mediator of the electromagnetic interaction, the $W^{\pm}$ and Z^0 are the mediators for charged and neutral weak processes respectively, and the gluon, g, is the mediator of the strong interaction. Furthermore, in the SM, particles acquire mass through their interaction with the so-called Higgs field, which is mediated by the Higgs boson. The basic characteristics of the fundamental SM particles [8] are summarized in Tables [1.1] and [1.2].

Table 1.2: Basic properties of bosons in the SM.

Particle	Symbol	Spin	Charge (e^-)	Color charge	Mass [GeV/c^2]
gluon	g	1	0	8 colors	0
photon	γ	1	0	0	0
Z	Z^0	1	0	0	80.385 ± 0.015
W	$W^{\pm}$	1	± 1	0	91.187 ± 0.002
Higgs	H^0	0	0	0	125.3 ± 0.4

Mesons and baryons are generally referred to as *hadrons*, which are particles composed by quarks. For example, protons are baryons composed of two up quarks and a down quark, while neutrons are formed by two down quarks and one up quark. Similarly, pions ($\pi^{\pm}, \pi^0$) are mesons that can have a positive, negative or neutral electric charge. Pions are composed of a $u\bar{d}$ pair

(π^+), $d\bar{u}$ (π^-), and $u\bar{u}$ or $d\bar{d}$ in the case of the π^0. Another important set of mesons are the kaons: K^+ ($u\bar{s}$), K^- ($s\bar{u}$) and K^0 ($d\bar{s}/s\bar{d}$). Kaons have an important role in our understanding of the charge (C) and parity (P) violation [9, 10]. Some basic properties of protons, neutrons, pions and kaons, are summarized in Table [1.3].

Table 1.3**:** Basic properties of the some composed particles in the SM.

Particle	Symbol	Spin number	Charge (e)	Mass [MeV/c^2]
Proton	p^+	1/2	1	938.272013(23)
Neutron	n^0	1/2	0	939.565560(81)
Pion	$\pi^\pm$	1	±1	139.57018(35)
Kaon	$K^\pm$	0	±1	493.667 ± 0.013

1.1.2 Symmetry in the Standard Model

The concept of *symmetry* is commonly used in physics in order to explain various laws of nature that rely upon the invariance of conserved quantities, such as energy, electric charge or momentum. The basic premise is that fundamental laws of nature must remain invariant under coordinate transformations, rotations or changes from one inertial frame to another. In particle physics, particles are described in terms of fields. A field can be understood as a mathematical representation of a physical quantity that has a defined value in each point in time and space. Therefore, each particle will have a unique associated field with specific transformation properties. There are four symmetries considered in the SM [11, 12]:

- *Local:* transformations that depend on every point of the space-time.
- *Global:* transformations that do not depend on the specific point of the space-time.
- *Space-time:* transformations of the space-time coordinates that describe the fields.
- *Internal:* transformations of the fields.

Mathematically, these symmetries can be represented through *groups*. Groups are a set of mathematical elements that satisfy certain algebraic rules [13]. One of the simplest symmetry group is the unitary group, $U(1)$, which represents rotational symmetry of a circle. For example, let us define a field ϕ that undergoes a phase transformation of the form $\phi \to \phi' = e^{i\theta}\phi$, where θ is constant, which belongs to the $U(1)$ group. Under this simple transformation, the value of the physical observables of the ϕ field remains unchanged. Similarly, the $SU(2)$, referred to as a special unitary group of order two, represents rotations in two dimensions. In the SM, the electromagnetic interaction is represented by the group $U(1)$, while, the weak interaction is represented by the $SU(2)$ group, and the strong interaction is represented by the $SU(3)$ group. It is important to mention that the order of the group is related to the order of the matrix representing the group. For example, the $SU(2)$ group is represented by a 2×2 matrix and the $SU(3)$ by a 3×3 matrix. Furthermore, a $S(n)$ group has $n^2 - 1$ number of carriers of the interaction; three in the case of the weak interaction (W^+, W^-, Z^0) and eight in the case of the strong interaction (gluons) [1].

In general, the $n \times n$ matrices associated with the $SU(n)$ groups do not commute. These groups are called *non-abelian groups*. Hence, the SM is a non-abelian theory in which there are three interactions protected by the symmetry of the global group generated by the product among them:

$$SU(3)_C \otimes SU(2)_L \otimes U(1)_Y, \tag{1.1}$$

where the subscript C represents the color charge, the subscript L entitles a distinction between particles with left and right chirality in electroweak interactions, and Y is the hyper-charge, which associates the electric charge and the isospin number, $Y = 2(Q - I)$ [8]. In particle physics, chirality denotes the relation between the direction of the spin of the particle and its momentum vector. States with right-handed chirality represent a projection of the spin vector of the particle along the same direction as its momentum vector and left-handed states correspond to anti-parallel directions. In the SM, neutrinos resulting from the electroweak process have only been measured with left-handed chirality, implying a violation of parity symmetry. In order to incorporate this experimental fact, which could change if right-handed neutrinos are observed, the left-handed and right-handed states are described differently in the SM, using doublets for left-handed states and singlets for right-handed states. Similarly, quarks are organized as *up*-type and *down*-type quarks. Therefore, in the SM, particles are associated in the following way:

$$Q_{jL} = \begin{pmatrix} U_j \\ D_j \end{pmatrix}_L, \quad L_{jL} = \begin{pmatrix} \nu_j \\ l_j \end{pmatrix}_L, \quad U_{jR}, \quad D_{jR}, \quad l_{jR}, \tag{1.2}$$

where $U_j = (u, c, t)$, $D_j = (d, s, b)$, $l_j = (e, \mu, \tau)$ and $\nu_j = (\nu_e, \nu_\mu, \nu_\tau)$. Hence, the chirality is a relevant quantity in the description of fields. Chiral states are defined through the following projection operator [14]:

$$P_{L^-}^{R^+} = \frac{1}{2}(1 \pm \gamma_5) \tag{1.3}$$

1.1.3 Feynman diagrams

Feynman diagrams are pictorial representations of interactions among particles or their radiative decays. In fact, the diagrams contain deep physical meaning, as each part is directly related to a mathematical expression that characterizes an interaction or decay. As an example, Figure [1.1] presents the Feynman diagram for an electroweak process in which a top quark decays into a b quark through the emission of a W^+ boson, which subsequently decays into a μ^+ and a ν_μ. In this diagram, the solid straight lines represent initial or final state particles, while the curved line represents the gauge boson mediating the process. The points at which the straight and curved lines converge, are referred to as vertices, and imply that the associated particles are interacting; indeed, they are coupled [1, 11].

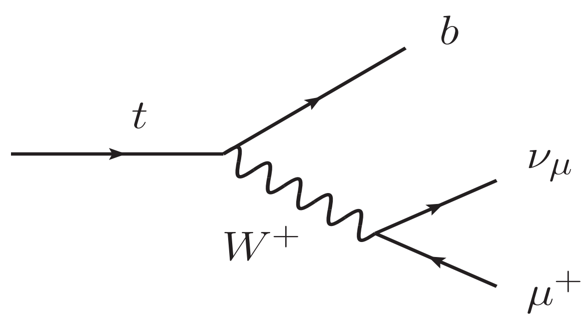

Figure 1.1: The top (t) decay is mediated by charged currents of the weak interaction (W^+), $t \to b + \mu + \nu_\mu$. This Feynman diagram describes the decay at tree level approximation.

1.1.4 The Higgs mechanism

As mentioned before, particles acquire mass through the Higgs mechanism in the SM [15]. The Higgs mechanism postulates the existence of a field that permeates space-time through which particles move and acquire mass. In addition, the mass of a particle depends on the level of interaction with the Higgs field. In 2012, the CMS and ATLAS collaborations reported the detection of a new boson with compatible characteristics of the hypothetical Higgs field [16, 17]. This elusive boson is referred to as the Higgs boson. The ground state of the Higgs field is not symmetric, which explains why the photon is massless but, the $W^\pm$ and Z^0 have large masses of 80.385 GeV and 91.876 GeV, respectively.

The Lagrangian of the Higgs field has two terms, the first is the kinetic term and the other two represent the self-interaction potential, as shown in Equation (1.4):

$$\mathcal{L}_H = (\mathcal{D}_\mu \phi)^\dagger (\mathcal{D}^\mu \phi) - \mu^2(\phi^\dagger \phi) - \lambda(\phi^\dagger \phi)^2, \tag{1.4}$$

where the Higgs field ϕ is a complex potential defined in terms of two scalars fields in a doublet and the covariant derivative is given by:

$$\phi(x) = \frac{1}{\sqrt{2}} \begin{pmatrix} \varphi_1(x) \\ \varphi_2(x) \end{pmatrix} \qquad \mathcal{D}_\mu = I\partial_\mu - igT_i W^i_\mu \tag{1.5}$$

The $T_i = \tau_i/2$ are the Pauli's matrices of the Lie algebra $SU(2)$ described by Equation (1.6). As a reminder, the Lie algebra defines the possible operations among the elements inside the electroweak group and their derivatives. The computation rules of this algebra allow us to construct a gauge-invariant Lagrangian, which requires a re-definition of the standard derivative operator.

$$\left[\frac{\tau_i}{2}, \frac{\tau_j}{2}\right] = i\epsilon^{ijk}\frac{\tau_k}{2} \tag{1.6}$$

W^a_μ is similar to the free electromagnetic field tensor ($F_{\mu\nu}$), but it has a more general meaning. This term represents a *gauge triple*, explicitly, the super-script $i = 1, 2, 3$ is associated with the electroweak force carriers ($W^\pm, Z$). The free parameters λ and μ^2 in the Higgs potential are chosen so that ϕ has an expectation value different from zero [18]. This is an important condition in order to have a spontaneous symmetry breaking, necessary to accommodate weak force carriers with mass:

$$|\langle 0|\phi|0\rangle|^2 = \frac{\nu^2}{2}, \qquad \text{with} \qquad \nu^2 = -\frac{\mu^2}{\lambda} \tag{1.7}$$

In other words, we minimize the Lagrangian in order to find the ground state:

$$\phi^\dagger\phi = -\frac{\mu^2}{\lambda} \tag{1.8}$$

Using the components of the Higgs doublet from Equation (1.5), we calculate $\phi^+\phi$ as follows:

$$\phi^\dagger\phi = \varphi_1^2 + \varphi_2^2 \tag{1.9}$$

To illustrate the shape of the potential we use the abelian Higgs field [11], which has two components, one scalar and other imaginary. Figure [1.2] shows the Higgs potential with $\mu^2 > 0$ and $\lambda > 0$. Nevertheless, with these choices for μ and λ it is not possible to obtain a massless γ, massive $W^{\pm}$ and Z^0 particles, as measured experimentally.

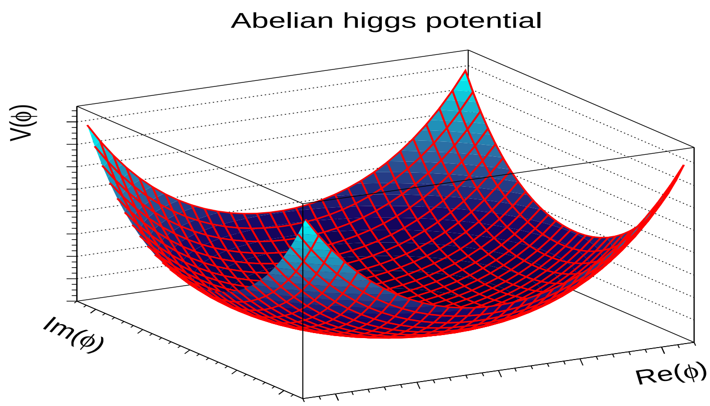

Figure 1.2**:** The abelian Higgs potential described by: $\mu^2 > 0$ and $\lambda > 0$.

The case where $\mu^2 < 0$ is shown in Figure [1.3], where the potential has two stable minimum values $(\pm\nu^2)$. Using Equation (1.9) we get.

$$\varphi_2 = \nu, \varphi_1 = 0 \rightarrow \phi = \frac{1}{\sqrt{2}} \begin{pmatrix} 0 \\ \nu \end{pmatrix} \tag{1.10}$$

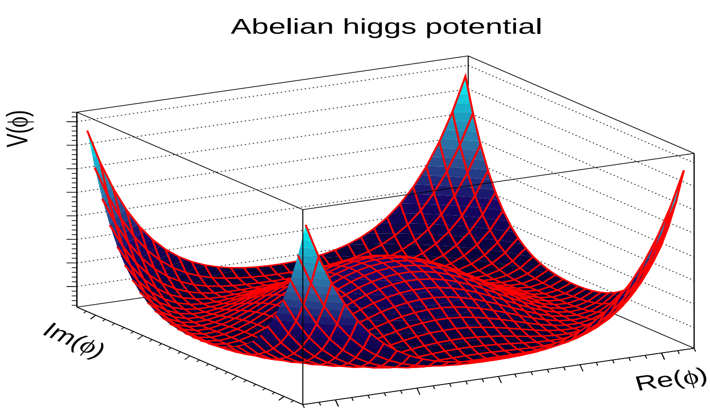

Figure 1.3**:** The abelian Higgs potential described by: $\mu^2 < 0$ and $\lambda > 0$.

A specific direction implies breaking of the original symmetry of the field. Nevertheless, if we use the covariant derivative to preserve the invariance under $SU(2)_L \otimes U(1)_Y$, it is possible to introduce three massive gauge bosons and a massless boson (Goldstone boson) [18], that is the W^+, W^-, Z^0, and γ. We will describe how the Higgs mechanism operates using the covariant derivative definition, to guarantee that the SM Lagrangian is invariant under transformations in the symmetry group. Applying this derivative, some extra terms naturally appear in the Lagrangian, the mass of the W boson can be calculated following the Equation (1.11):

$$\phi^\dagger(-igT_iW^i_\mu)^\dagger(-igT_iW^i_\mu)\phi \tag{1.11}$$

Note that,

$$\begin{aligned}
W_\mu &= T_iW^i_\mu = \frac{1}{2}\begin{pmatrix} 0 & 1 \\ 1 & 0 \end{pmatrix} W^1_\mu + \frac{1}{2}\begin{pmatrix} 0 & -i \\ i & 0 \end{pmatrix} W^2_\mu + \frac{1}{2}\begin{pmatrix} 1 & 0 \\ 0 & -1 \end{pmatrix} W^3_\mu \\
&= \frac{1}{2}\begin{pmatrix} W^3_\mu & \sqrt{2}\frac{W^1_\mu - iW^2_\mu}{\sqrt{2}} \\ \sqrt{2}\frac{W^1_\mu + iW^2_\mu}{\sqrt{2}} & -W^3_\mu \end{pmatrix} \\
&= \begin{pmatrix} \frac{1}{2}W^3_\mu & \frac{1}{\sqrt{2}}W^-_\mu \\ \frac{1}{\sqrt{2}}W^+_\mu & -\frac{1}{2}W^3_\mu \end{pmatrix}
\end{aligned} \tag{1.12}$$

where we have defined.

$$W^+_\mu = \frac{W^1_\mu + iW^2_\mu}{\sqrt{2}} \qquad W^-_\mu = (W^+_\mu)^* = \frac{W^1_\mu - iW^2_\mu}{\sqrt{2}} \tag{1.13}$$

By expanding Equation (1.11) we get:

$$\begin{aligned}
&= \frac{g^2}{2}\begin{pmatrix} 0 & \nu \end{pmatrix}\begin{pmatrix} \frac{1}{2}(W^3_\mu)^* & \frac{1}{\sqrt{2}}(W^+_\mu)^* \\ \frac{1}{\sqrt{2}}(W^-_\mu)^* & -\frac{1}{2}(W^3_\mu)^* \end{pmatrix}\begin{pmatrix} \frac{1}{2}W^3_\mu & \frac{1}{\sqrt{2}}W^-_\mu \\ \frac{1}{\sqrt{2}}W^+_\mu & -\frac{1}{2}W^3_\mu \end{pmatrix}\begin{pmatrix} 0 \\ \nu \end{pmatrix} \\
&= \frac{g^2\nu^2}{2}\begin{pmatrix} \frac{1}{\sqrt{2}}W^+_\mu & -\frac{1}{2}W^3_\mu \end{pmatrix}\begin{pmatrix} \frac{1}{\sqrt{2}}W^-_\mu \\ -\frac{1}{2}W^3_\mu \end{pmatrix} \\
&= \frac{g^2\nu^2}{2}W^+_\mu W^-_\mu + \frac{g^2\nu^2}{8}(W^3_\mu)^2 \\
&= m^2_w W^+_\mu W^-_\mu + \frac{g^2\nu^2}{8}(W^3_\mu)^2
\end{aligned} \tag{1.14}$$

where the term $m_w = \frac{g\nu}{2}$ represents the mass of the W particle and the second term is related to the contribution to the potential of the third component of the W. The Higgs mechanism was quite interesting among the scientific community because of it accurately predicted the masses of the $W^\pm$ and Z^0 bosons before they were experimentally measured in 1983 [1,6].

Figure [1.4] (left) shows the confidence level of the SM Higgs hypothesis as a function of the reconstructed Higgs mass in the $H \to \gamma\gamma$ final state, performed by the CMS experiment using 10.4 fb^{-1} of data from pp collisions in 2012 [16]. The observed values are described by the solid black lines. The dashed line shows the expected background-only hypothesis. In the right side of the Figure [1.4] the excess in the observed events around 125 GeV is presented.

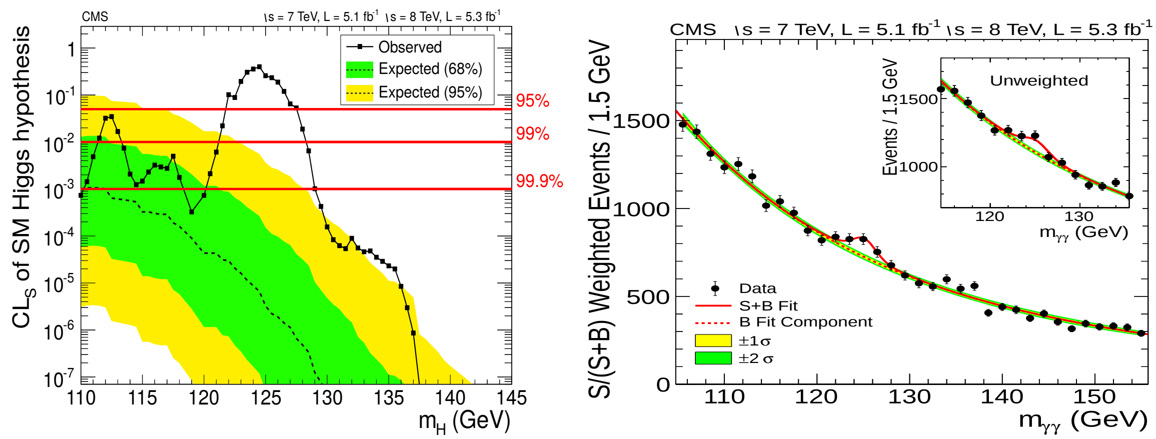

Figure 1.4**:** The confidence level of the SM Higg hypothesis (σ/σ_{SM}) as a function of the Higgs mass (left). The invariant mass distribution of the di-photon ($\gamma\gamma$) system (right).

Section 1.2

Problems of the Standard Model

Although the SM has been very successful, there are several open questions that it can not explain. For example, the observation of neutrino oscillations implies that they have mass, while the SM predicts these particles are massless. [19]. John Bahcall, an American physicist, calculated the nuclear reactions within the solar nucleus and their relation with neutrinos. Detecting neutrinos is quite difficult, however, the experiments performed by Ray Davis showed that only 34%, of the total expected rate, of neutrinos from the sun, are detected on earth [20]; it was referred to as *the problem of the solar neutrinos*. Afterwards, the *Kamiokande* [21] experiment observed that only 60% of atmospheric neutrinos reached the detector, which was known as *the problem of the atmospheric neutrinos* [18, 19].

Because neutrinos have mass, then a neutrino of a given family (flavor) can spread and turn into a neutrino of another family. This phenomenon is called neutrino oscillation, which explains the inconsistency with the experimental results. In fact, the deficiency in the observation of solar neutrinos produced in the sun is due to the transformation of electron-neutrinos (ν_e)

into muon-neutrinos (ν_μ) and tau-neutrinos (ν_τ), which are not detected by the experiments designed to measure ν_e events.

The concept of neutrino mixing belongs to gauge theories with massive particles. The simplest form of this theory is expressed as a unitary transformation that relates the flavor and mass eigenbasis:

$$\begin{aligned} |\nu_\alpha\rangle &= \sum_i U^*_{\alpha i} |\nu_i\rangle \\ |\nu_i\rangle &= \sum_\alpha U_{\alpha i} |\nu_\alpha\rangle , \end{aligned} \tag{1.15}$$

where $U_{\alpha i}$ represents the *Pontecorvo-Maki-Nakagawa-Sakata* matrix, which is not the identity to obtain mixing between the flavor states [22]:

$$U = \begin{pmatrix} c_{12}c_{13} & s_{12}c_{13} & s_{13}e^{-i\delta} \\ -s_{12}c_{23} - c_{12}s_{23}s_{13}e^{i\delta} & c_{12}c_{23} - s_{12}s_{23}s_{13}e^{i\delta} & s_{23}c_{13} \\ s_{12}s_{23} - c_{12}c_{23}s_{13}e^{i\delta} & -c_{12}s_{23} - s_{12}c_{23}s_{13}e^{i\delta} & c_{23}c_{13} \end{pmatrix} \tag{1.16}$$

The propagation of the mass eigenstates can be described as plane waves,

$$|\nu_i(t)\rangle = e^{-i(E_i t - \vec{p}_i.\vec{r})} |\nu_i(0)\rangle \tag{1.17}$$

In the ultra relativistic limit $|\vec{p_i}| = p_i >> m_i$ we approximate the energy, using natural units as:

$$E_i = \sqrt{p_i^2 + m_i^2} \approx p_i + \frac{m_i^2}{2p_i} \approx E + \frac{m_i^2}{2E} \tag{1.18}$$

Including $L \approx t$ the wave functions become:

$$|\nu_i(L)\rangle = e^{-im_i^2 L/2E} |\nu_i(0)\rangle , \tag{1.19}$$

where L represents the distance that the neutrino travels to oscillate and transform back to its original flavor again. This distance (time) is referred to as the time of phases. Finally, the probability that a neutrino of flavor α turns into a flavor β is given by:

$$\begin{aligned}\mathcal{P}_{\alpha\to\beta} &= |\langle 0|\nu_\beta|\nu_\alpha(t)\rangle|^2 = \left|\sum_i U^*_{\alpha i}U_{\beta i}e^{-im_i^2 L/2E}\right|^2 \\ &= \delta_{\alpha\beta} - 4\sum_{i>j}\mathfrak{Re}(U^*_{\alpha i}U_{\beta i}U_{\alpha j}U^*_{\beta j})sin^2\big(\frac{\Delta m^2_{ij}L}{4E}\big) \\ &- 2\sum_{i>j}\mathfrak{Im}(U^*_{\alpha i}U_{\beta i}U_{\alpha j}U^*_{\beta j})sin\big(\frac{\Delta m^2_{ij}L}{2E}\big) \end{aligned} \tag{1.20}$$

where $\Delta m^2_{ij} = m_i^2 - m_j^2$ contributes to the oscillation process [23].

Another known issue with the SM is the so-called *hierarchy* problem. The quantum corrections of the mass of the Higgs boson to the *bare theoretical mass* is needed to match the experimental value ($m_H = 125\ GeV$) [16]. In fact, the coupling of the Higgs field with a fermion gives a Yukawa term $\mathcal{L}_{yukawa} = -\lambda_f\overline{\psi}H\psi$, where ψ represents a Dirac field and a H symbolizes the Higgs field. In SM, the mass of a fermion is proportional to the Yukawa coupling and therefore to the Higgs field. This correction is given by [24]:

$$\Delta m_H^2 = -\frac{|\lambda_f^2|}{8\pi^2}[\Lambda^2_{UV} + ...], \tag{1.21}$$

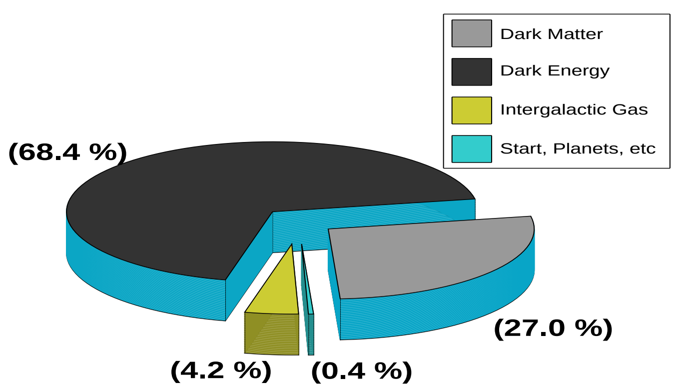

Figure 1.5**:** The composition of the universe is mostly Dark Matter and Dark Energy, the barionic matter is less than 5%.

where Λ_{UV} represents the SM energy scale. If we extend the scale to grand unified energy the mass of the Higgs boson become a divergent value. Nevertheless in SUSY scenarios, by matching each quark and lepton of the SM with a constant coupling given by $\lambda_s = |\lambda_f|^2$ [24], the factor Λ_{UV} as well as the divergence of the Higgs mass vanish.

In addition, the SM does not provide an explanation for dark matter (DM) and dark energy (DE). Although neither DM nor DE have been experimentally measured, indirect cosmological observations suggest their existence [25]. For example, the disagreement between the expected and measured rotational velocity of galaxies, or cosmological phenomena such as the bullet cluster observations [26], point the scientific community towards postulating a new type of matter which is dense, stable, electrically neutral and that only interacts gravitationally referred to as DM. Similarly, the accelerated expansion of the universe leads us to think there is a sort for negative pressure responsible for this behavior, DE [27]. Extensions of the SM such as supersymmetry (SUSY), provide an explanation for DM and naturally provide a particle candidate to DM, commonly referred to as the Lightest Supersymmetric Particle (LSP). Both DM and DE are currently being broadly explored experimentally and theoretically. Figure [1.5] shows a pie chart that illustrates the current belief of the energy composition of our universe [28].

The organization of this work is described as follows. Chapter 2 shows the theoretical aspects of the SUSY as an extension of the SM. The CMS detector is described in Chapter 3, the reconstruction of particles is presented in Chapter 4 and the state of art (Latest electroweak SUSY searches) is mentioned in Chapter 5. The phenomenological study is explained in Chapter 6, and the experimental analysis is presented in Chapter 7. Finally, we present the conclusions of this dissertation in Chapter 8.

CHAPTER 2

Physics beyond the Standard Model

New phenomena, interactions and fields beyond the SM are suggested ideas by theoretical arguments as well as experimental evidence. There are many extensions of the SM, such as models based on SUSY, string theories [29] or extra dimensions [30]. Nevertheless, the correct theory must resolve the issues of the SM mentioned in the previous chapter. This document presents a search for physics beyond SM using the data collected by the CMS detector in 2016 and 2017 ($L = 77.2\ fb^{-1}$), and a minimum SUSY model as a benchmark scenario. We will start introducing some general concepts which are important to understand the main result presented in this document.

Section 2.1

Supersymmetry

2.1.1 General aspects

In Quantum Mechanics, constructing bosonic states from fermionic states is feasible; for example, when two electrons interact in a closed quantum system by being coupled through their spin states. By adding the individual angular momentum states, two fermions of spin $\frac{1}{2}$ lead to a total angular momentum of spin 1 (i.e., for $m = 0$) [31].

$$\frac{1}{2} \otimes \frac{1}{2} \longrightarrow |1, 0\rangle = \frac{1}{\sqrt{2}} \left[\left| \frac{1}{2}, -\frac{1}{2} \right\rangle + \left| \frac{1}{2}, \frac{1}{2} \right\rangle \right] \tag{2.1}$$

However, there is an apparent asymmetry in Quantum Mechanics due to it is not possible to construct a fermionic state from bosonic states. Understanding why the matter is composed of fermionic fields, whereas interactions among particles are mediated exclusively by bosonic fields is an interesting question.

SUSY is a hypothetical symmetry of space-time that restores the relationship between bosons and fermions. Essentially, the SM is modified by including new bosonic fields associated with matter, and fermionic fields associated with interactions to the spectrum of particles.

Within this theory, the symmetry is related to the Poincaré group as well as the gauge symmetry of the SM [12]. Internal symmetries correspond to transformations only acting on the fields, such as electric and colour invariance. These do not transform the spacetime points. Furthermore, the Poincaré group is Lorentz transformation plus spacetime translations. For this group, the transformations can be written as:

$$\begin{aligned}\delta x^{\mu} &= \epsilon^{\mu} + \delta W^{\mu\nu} x^{\nu} \\ \delta\psi_a(x) &= \frac{1}{2}\delta W^{\mu\nu}(I_{\mu\nu})_{ab}\psi_b(x),\end{aligned} \tag{2.2}$$

where ϵ^{μ} is an infinitesimal constant four-vector of the space-time translation, $W^{\mu\nu}$ is an infinitesimal constant tensor that protects the gauge invariance of the x^{μ}, and $I_{\mu\nu}$ corresponds to the infinitesimal Lorentz group generators. The Poincaré group leads to the following ten invariant quantities [32]:

$$E, \qquad \vec{p}(p_x, p_y, p_z), \qquad \vec{l}(l_x, l_y, l_z), \qquad \vec{s}(s_x, s_y, s_z) \tag{2.3}$$

According to the spin-statistical theorem bosons and fermions obey different statistical rules. Overall, bosons follow rules of commutation and fermions follow rules of anti-commutation. A more general algebra named Lie Super Algebra describes the whole set. By taking a and b as two different sets of variables, where the elements in a commute following the Lie algebra G_a, and the elements in b anti-commute following the Lie algebra G_b, the Super Algebra is defined by the *direct sum* between them [33]:

$$G_a \oplus G_b \tag{2.4}$$

This new algebra fully satisfies:

$$\begin{aligned}[a, b] &= -(-1)^{\alpha\beta}[b, a] \\ \big[a, [b, c]\big] &= \big[[a, b], c\big] + (-1)^{\alpha\beta}\big[b, [a, c]\big]\end{aligned} \tag{2.5}$$

The α y β values can be zero (0) for commutative algebras and one (1) for anti-commutative algebras. Essentially, to construct fermionic states from bosonic states and vice-versa we have an operator ($\hat{Q}$) that satisfies the algebra mentioned above.

$$\hat{Q}|f> \propto |b>, \qquad \hat{Q}|b> \propto |f> \tag{2.6}$$

The commutators describe the algebra and the four-momentum (P_{μ}) [32, 34].

$$\left\{\hat{Q}_\alpha, \hat{Q}_\beta\right\} = 0, \qquad \left[\hat{Q}_\alpha, P_\mu\right] = 0, \qquad \left\{\hat{Q}_\alpha, \overline{\hat{Q}_\beta}\right\} = 2\sigma^\mu_{\alpha\beta} P_\mu \tag{2.7}$$

where $\sigma^\mu_{\alpha\beta}$ are the Pauli's matrices. Note that, $P_\mu P^\mu \hat{Q}|b>= m_f^2|f>$ and through the algebra described by Equation (2.7) we get [34]:

$$P_\mu P^\mu \hat{Q}|b>= \hat{Q}P_\mu P^\mu|b>= Qm_b^2|b>= m_b^2|f>, \tag{2.8}$$

Fermions and bosons should have the same mass. Therefore, SUSY would be a broken symmetry as a result of the non-observation of these particles.

2.1.2 Minimal supersymmetric standard model

The Minimal Supersymmetric Standard Model (MSSM) is a SUSY model that describes the minimum number of particles that should be included in the SM to keep the phenomenological consistency with the known experimental yields. Howard Georgi and Savas Dimopoulus proposed this model in 1981 [34, 35]. The named super-partners (of the SM particles) are a new set of particles illustrated in Figure [2.1].

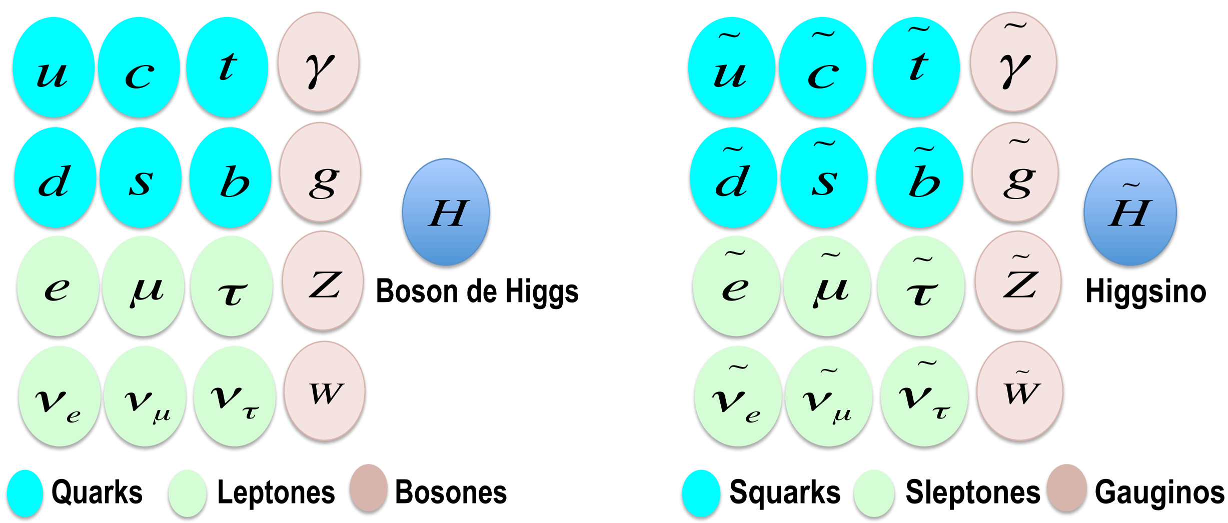

Figure 2.1: Set of known particles in the SM (left) and the hypothetical particle spectrum in MSSM (right).

The super-partners are named as follows: for fermions, the letter *s* is added in front of the name to rename them. The super-partner associated with the t is referred to as the **stop**, as well as the counterpart of the e^-, which is called **selectron**. For bosons, the name of the super-partner particle is identified by adding the termination *ino* to the last part of the name.

The $\tilde{\gamma}$ and $\tilde{g}$ correspond with **photino** and **gluiono**, respectively.

Furthermore, another Higgs doublet is required by MSSM to generate mass for both *up-type* and *down-type* quarks [36]. As a result, five Higgs bosons, three neutral (h^0, H^0, A^0), and two electrically charged ($H^{\pm}$) are obtained. This produces the Higgs boson super-partners called the *higgsinos*: $\tilde{H}_u^0$, $\tilde{H}_u^+$, $\tilde{H}_d^0$ and $\tilde{H}_d^-$. The masses of the higgsinos are free parameters within the theory and thereby, they do not have a specific range or boundary to constrain them. Since the Higgs causes the breaking of the electroweak symmetry, the mixing matrix generates four neutral *gauginos*: two higgsinos, the *wino* $\tilde{W}^3$ and the *bino* $\tilde{B}$. The $\tilde{W}^3$ is the super-partner of the W^3 gauge boson and the $\tilde{B}$ is the super-partner of the B gauge boson [24, 35].

Another interesting feature of MSSM is related to the spectrum of the particles. The observable states such as the *chargino* ($\tilde{\chi}_i^{\pm}$ with $i = 1, 2$) and the *neutralino* ($\tilde{\chi}_j^0$ with $j = 0, 1, 2, 3$) are produced by the mixing of gauginos and Higgsinos. The mixing matrix associated with the charginos is [37]:

$$M_C = \begin{pmatrix} M_2 & \sqrt{2}m_W \sin\beta \\ \sqrt{2}m_W \cos\beta & \mu \end{pmatrix} \tag{2.9}$$

In this matrix, M_2 is the gaugino mass parameter, μ is the Higgsino mass and β is related to a ratio of the expectation value of the Higgs field for up-type and down-type quarks. In addition, by normalizing this matrix using U and V unitary matrices, we can obtain the eigen-mass states.

$$U^* M_C V^\dagger = diag(m_{\tilde{\chi}_1^{\pm}}, m_{\tilde{\chi}_2^{\pm}}), \qquad m_{\tilde{\chi}_1^{\pm}} < m_{\tilde{\chi}_2^{\pm}} \tag{2.10}$$

$$m_{\tilde{\chi}_1^{\pm}, \tilde{\chi}_2^{\pm}} = \frac{1}{2}\Big[M_2^2 + \mu^2 + 2m_W^2 \mp \sqrt{(M_2^2 - \mu^2)^2 + 4m_W^4 cos^2(2\beta) + 4m_W^2(M_2^2 + \mu^2 + 2M_2\mu sin(2\beta))}\Big]$$

Theses mass states are called *Dirac fermions* (a particle that is not its own anti-particle) [38]. On the other hand, the mixing matrix in terms of the higgsinos ($\tilde{H}_1^0$, $\tilde{H}_2^0$) and gauge bosons ($\tilde{B}, \tilde{W}^3$) associated to the neutralinos is [37, 39]:

$$M_N = \begin{pmatrix} M_1 & 0 & -m_Z \cos\beta \sin\theta_W & m_Z \sin\beta \sin\theta_W \\ 0 & M_2 & m_Z \cos\beta \cos\theta_W & -m_Z \sin\beta \cos\theta_W \\ -m_Z \cos\beta \sin\theta_W & m_Z \cos\beta \cos\theta_W & 0 & -\mu \\ m_Z \sin\beta \sin\theta_W & -m_Z \sin\beta \cos\theta_W & \mu & 0 \end{pmatrix} \tag{2.11}$$

In the previous formula, the gaugino masses are represented by M_1, M_2, the Higgsino mass is μ, $\tan\beta = v_2/v_1$ which is related to vacuum expectation values of the two neutral Higgs, and θ_W is the conventional electroweak mixing angle. To diagonalize the neutralinos mixing matrix a unitary matrix N is needed [37, 40]. Therefore, the eigen-mass states are:

$$N^* M_N N^\dagger = diag(m_{\tilde{\chi}_1^0}, m_{\tilde{\chi}_2^0}, m_{\tilde{\chi}_3^0}, m_{\tilde{\chi}_4^0}), \qquad (m_{\tilde{\chi}_1^0} < m_{\tilde{\chi}_2^0} < m_{\tilde{\chi}_3^0} < m_{\tilde{\chi}_4^0}). \tag{2.12}$$

These mass states are called *Majorana fermions* (meaning the particle is its own anti-particle). The explicit values of the mass eigen-states for the neutralinos can be found in [38].

2.1.3 Lagrangian of the MSSM

We approach the main ideas behind of the supersymmetric Lagrangian density of the MSSM since this research is supported by this theoretical framework [41]. On one side, in conventional particle Physics the fields are based upon the ordinary Minkowski space (x_μ), instead, in SUSY the fields are defined on a new *Superspace* ($x_\mu, \theta_\alpha, \bar{\theta}_\alpha$).

$$\begin{array}{ccc} Space & \rightarrow & Superspace \\ x_\mu & & x_\mu, \theta_\alpha, \bar{\theta}_\alpha \end{array} \tag{2.13}$$

In this formula, θ^α and $\bar{\theta}_\alpha$ are *spinors* (i.e, Grassman variables [42]) of two constant complex components. These variables satisfy the following anti-commutation rules:

$$\begin{aligned} \{\theta_\alpha, \theta_\beta\} &= 0, \\ \{\bar{\theta}_{\dot{\alpha}}, \bar{\theta}_{\dot{\beta}}\} &= 0, \\ \theta_\alpha^2 &= 0, \\ \bar{\theta}_{\dot{\alpha}}^2 &= 0, \qquad \alpha, \beta, \dot{\alpha}, \dot{\beta} = 1, 2. \end{aligned} \tag{2.14}$$

By expanding any analytic function in θ, we get:

$$f(\theta) = \sum_{k=0}^{\infty} f_k \theta^k = f_0 + f_1\theta + \underbrace{f_2\theta_2^2}_{0} + ... = f_0 + f_1\theta \tag{2.15}$$

The most general function is linear. There are other interesting properties if we define

$$\int d\theta \frac{df}{d\theta} := 0 \Longrightarrow \int d\theta = 0, \tag{2.16}$$

$$\int d\theta\theta := 1 \Longrightarrow \delta(\theta) = \theta \tag{2.17}$$

Therefore, the integral over $f(\theta)$ is identical to its derivative.

$$\int d\theta f(\theta) = \int d\theta(f_0 + f_1\theta) = f_1 = \frac{df(\theta)}{d\theta} \tag{2.18}$$

Using the properties of the Grassman algebra, we can construct the most general scalar super-field [42].

$$\begin{aligned} S(x_\mu, \theta, \bar{\theta}_{\dot{\alpha}}) &= \phi(x) + \theta\psi(x) + \bar{\theta}\bar{\chi}(x) + \theta\theta M(x) + \bar{\theta}\bar{\theta}N(x) \\ &+ (\theta\sigma^\mu\bar{\theta})V_\mu(x) + (\theta\theta)\bar{\theta}\bar{\lambda}(x) + (\bar{\theta}\bar{\theta})\theta\rho(x) + (\theta\theta)(\bar{\theta}\bar{\theta})D(x) \end{aligned} \tag{2.19}$$

Since the symmetries of the MSSM are inherited from the SM given by Equation (1.1), the super-fields will have transformation properties associated with such symmetries and other properties of the MSSM model itself. Therefore, the MSSM particle content commonly found is given by [42]:

- Five left-handed *chiral* super-fields (spinors), Φ_ℓ, Φ_e, Φ_q, Φ_u, Φ_d, of each generation.
- Three *gauge* super-fields. V^a, V, V_s^α for gauge bosons.
- Two left-handed chiral super-fields Φ_{H_1}, Φ_{H_2} for the Higgs field.

The chiral super-fields are either $SU(2)_L$ *doublets* ($\Phi_{\ell,q}$) described by Equation (2.20) or *singlets* ($\Phi_{e,u,d}$) described by Equation (2.21).

$$\begin{aligned} \Phi_q &\rightarrow \begin{pmatrix} u_L \\ d_L \end{pmatrix}, \begin{pmatrix} A(u_L) \\ A(d_L) \end{pmatrix}, \begin{pmatrix} F(u_L) \\ F(d_L) \end{pmatrix} \\ \Phi_\ell &\rightarrow \begin{pmatrix} \nu_L \\ e_L \end{pmatrix}, \begin{pmatrix} A(\nu_L) \\ A(e_L) \end{pmatrix}, \begin{pmatrix} F(\nu_L) \\ F(e_L) \end{pmatrix} \end{aligned} \tag{2.20}$$

$$\begin{aligned} \Phi_e &\rightarrow e_R, A(e_R), F(e_R) \\ \Phi_u &\rightarrow u_R, A(u_R), F(u_R) \\ \Phi_d &\rightarrow d_R, A(d_R), F(d_R) \end{aligned} \tag{2.21}$$

The asymmetry of the electroweak interactions leads to the following property of the covariant derivative [42]:

$$\bar{\mathcal{D}}_L = -(\frac{\partial}{\partial\bar{\theta}} + i\theta\sigma^{\mu}\partial_{\mu})\Phi = 0, \tag{2.22}$$

On the other hand, the gauge super-field V^a is a *triplet* given by Equation (2.23), V is a *singlet* and V_s^{α} is a $SU(3)_c$ *octet* in Equation (2.24).

$$V^a \rightarrow \begin{pmatrix} W_{\mu}^a \\ \lambda^a \\ D^a \end{pmatrix}, \tag{2.23}$$

$$V \rightarrow B_{\mu}, \qquad V_s^{\alpha} \rightarrow (g_{\mu}^{\alpha}, \tilde{g}^{\alpha}, D^{\alpha}). \tag{2.24}$$

The doublets associated with the Higgs sector are defined in Equation (2.25).

$$\Phi_{H1} \rightarrow \begin{pmatrix} H_1^0 \\ H_1^- \end{pmatrix}, \qquad \Phi_{H2} \rightarrow \begin{pmatrix} H_2^+ \\ H_2^0 \end{pmatrix}. \tag{2.25}$$

After checking the concept of the super-field, we can introduce the Lagrangian of the MSSM. This Lagrangian must contain terms corresponding to kinetic field terms, gauge field terms, interaction terms (Yukawa), and Higgs terms associated with the breaking mechanism. The gauge field and Yukawa Lagrangians are given by [41]:

$$\begin{aligned} \mathcal{L}_{Gauge} &= \sum \frac{1}{4}\Big(\int d^2\theta Tr(W^{\alpha}W_{\alpha})\int d^2\bar{\theta}Tr(\bar{W}^{\alpha}\bar{W}_{\alpha})\Big) \\ &+ \sum_{Matter}\int d^2\theta \int d^2\bar{\theta}\Phi_i^{\dagger}e^{g_3\hat{V}_3+g_2\hat{V}_2+g_1\hat{V}_1}\Phi_i \end{aligned} \tag{2.26}$$

$$\mathcal{L}_{Yukawa} = \int d^2\theta(W_R + W_{NR}) + h.c. \tag{2.27}$$

W_{α} has the analog meaning to the electromagnetic stress tensor ($F_{\mu\nu}$).

$$W_{\alpha} = -\frac{1}{4}\overline{D}^2 e^V D_{\alpha} e^{-V} \tag{2.28}$$

2.1.4 R-parity

In SUSY, some models require the conservation of a quantity to preserve the initial leptonic (L) and baryonic (B) numbers involved in supersymmetric decays. This quantity is referred to as *R-parity* [35, 41]:

$$P_R = (-1)^{3(B-L)+2S} \tag{2.29}$$

For instance, quarks have $B = \frac{1}{3}$ and $L = 0$, and leptons have $B = 0$ and $L = 1$. Therefore, SM particles have $P_R = 1$ and SUSY particles have $P_R = -1$. In scenarios where R-parity is a conserved quantity, we get the following features:

- There are not composed states between SM and SUSY particles.
- SUSY particles are produced in pairs and as a consequence, the LSP must be **stable**. In the MSSM, the LSP can be either neutralino ($\tilde{\chi}_1^0$) or the gravitino ($\tilde{g}$) [41] depending on the parametrization. These hypothetical particles could explain DM.
- The super-partners must decay into an odd number of $\tilde{\chi}_1^0$, which would explain the large amount of DM we observe in the universe.

Section 2.2
Some theoretical motivations

SUSY is a feasible proposal to explain the issues of SM. Two of the most interesting features of this model is that it is a Grand Unified Theory (GUT) and that it provides a solution to the hierarchy problem. The GUT establishes that at some energy scale, the three interaction couplings achieve the same value. Nevertheless, in SM the coupling constant of the strong and weak interactions decreases, while the electromagnetic force increases with the energy, so there is not a unique point anywhere. In contrast to the SM, the MSSM provides a unification scheme to an energy scale of 1.5×10^{16} GeV, as shown in Figure [2.2] taken from [43].

Moreover, SUSY gives a solution to the Hierarchy problem. The quadratic divergences that appear across the radiative loop corrections are systematically cancelled out by the super-partners associated with each particle. Roughly speaking, the loops coming from bosons are cancelled out by the (-1) fermion contribution due to the Fermi-Dirac statistics. The corrections of the Higgs mass due to boson contribution is given by [31]:

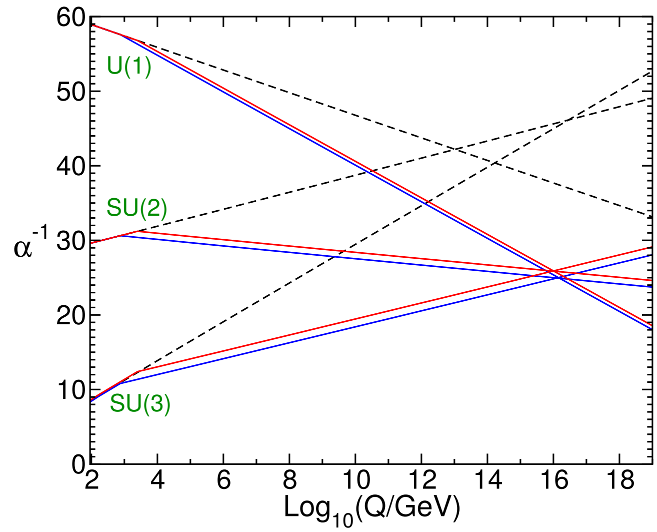

Figure 2.2**:** Evolution of the coupling constants as a function of the energy. Note that, the MSSM naturally provides a GUT scheme.

$$\lambda \int^{\Lambda} d^4k \frac{1}{k^4 - m^4}, \tag{2.30}$$

Since the SM is a renormalizable theory, the value of the mass depends on the energy scale constrained by Λ. Nevertheless, this value is indeterminate when $\Lambda \rightarrow \infty$. Instead, SUSY generates a further correction throughout the fermion loop [43].

$$- g^2 \int^{\Lambda} d^4k \frac{1}{kk} \phi^\dagger \phi \approx -g^2 \Lambda^2 \phi^\dagger \phi, \tag{2.31}$$

By combining these results we get:

$$(\lambda - g^2)\Lambda^2 \phi^\dagger \phi \tag{2.32}$$

If for each boson there is a fermion partner, such that, $\lambda = g^2$, there is not more divergences for the mass correction.

CHAPTER 3

Experimental setup

As was mentioned before, the main focus of this thesis is to perform an experimental search for SUSY, in a compressed mass spectra scenarios with τ's, motivated by a phenomenological study previously performed. This chapter describes some of the main aspects of the LHC and the CMS detector.

Section 3.1

The Large Hadron Collider (LHC)

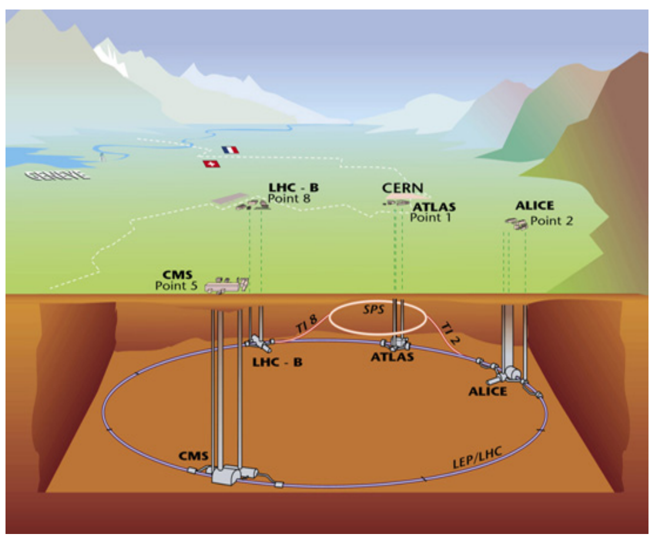

Figure 3.1: Sketch of the LHC underground tunnel. The main experiments are: CMS, ATLAS, ALICE and LHCb.

The Large Hadron Collider is a particle accelerator built at the European Center for Nuclear Research (CERN), located on the border between France and Switzerland. Figure [3.1] shows a sketch of the LHC, including the four main experiments [44]: CMS (Compact Muon Solenoid), ATLAS (A Toroidal LHC Apparatus), ALICE (A Large Ion Collider Experiment) and LHCb (Large Hadron Collider beauty) †. The accelerator collides bunches of protons for ten months and heavy ions, led-led collisions, for one month per year. The proton collisions have aimed to

†All pictures of the CMS experiment respect the CERN policy copyrights: https://copyright.web.cern.ch/

further test physics beyond SM (BSM). Meanwhile, the heavy ions experiments are aimed to study the dynamics of quarks and gluons at high energies. The LHC is inside an underground tunnel from 100 m up to 150 m deep, and it has a perimeter of around 27 km. Moreover, this machine has 1232 superconducting dipole magnets to guide the beam through the ring and quadrupole magnets to focus the bunches. Using liquid helium, the magnets are cooled down to temperatures of 2.0 K to maintain the superconducting state [45].

The protons are accelerated by a set of linear and circular accelerators, where their speed is increased progressively. The protons are clustered in bunches, spaced in gaps of 25 ns. Initially, in a linear accelerator called LINAC2, the bunches are driven until they reach an energy of 50 MeV. Then, the acceleration process continues in the Proton Synchrotron Booster (PSB), where the particles reach an energy of 1.4 GeV. After passing by the PSB, the bunches are injected to the Proton Synchrotron (PS) accelerator, where the energy is increased up to 25 GeV. The bunches are then passed to the Super Proton Synchrotron (SPS) where their energy increased up to 450 GeV. Finally, the bunches are transferred to the LHC where they reach their maximum energy of 6.5 TeV per beam before they collide [46]. Figure [3.2] illustrates the acceleration chain at the LHC [44].

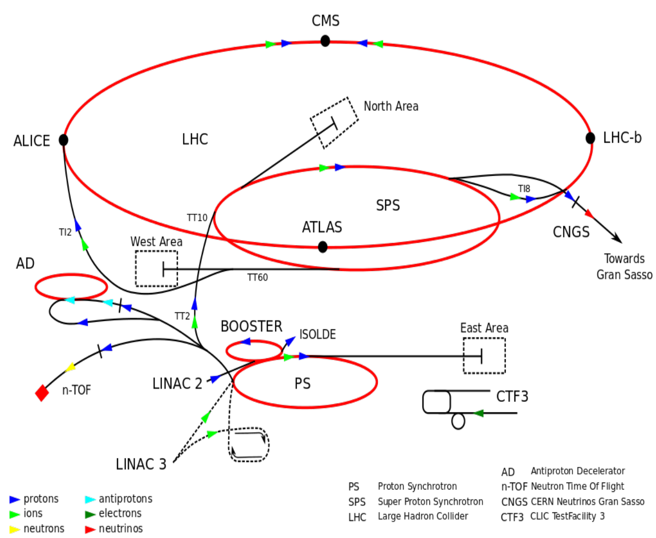

Figure 3.2: Sketch of the acceleration chain in the LHC.

So far, the experiment has had two main running periods: Run-I and Run-II. Those periods are divided from 2010 up to 2012, and from 2015 up to 2018. The properties associated with the accelerator, such as: luminosity, bunch crossing, bunch energy, pile-up and so on, have been changing during the years. Table [3.1] shows some features of the performance of the LHC throughout Run-I and Run-II [47].

Table 3.1: Some parameters associated with the accelerator performance.

	Run-I			Run-II	
	2010	2011	2012	2015	2018
Beam Energy [TeV]	3.5	3.5	4	6.5	6.5
Proton per Bunch [$\times 10^{11}$]	1.0	1.3	1.5	1.1	1.1
Bunches per Beam	368	1380	1380	2244	2200
Bunch time spacing [ns]	150	50	50	25	25
Pile-up in CMS			21	14	27
Maximum peak of Luminosity [$\times 10^{34}$ cm^{-2}s^{-1}]	0.021	0.35	0.77	0.51	1.4
Integrate Luminosity [fb^{-1}]	0.048	5.5	22.8	4.2	40.82

The integrated luminosity is an important quantifier associated with the amount of information recorded during the collision. Figure [3.3] describes the behavior of luminosity per year in the CMS experiment [48]. This huge amount of information (15 petabytes per year) generated for this collider is stored using a robust grid computing scheme.

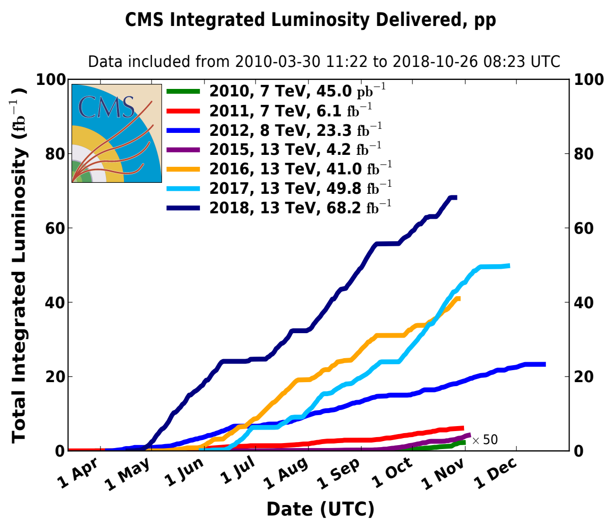

Figure 3.3: Integrated luminosity during stable beams for *pp* collisions at CMS experiment.

As mentioned before, one of the aims of this experiment was the discovery of the Higgs boson (finding reported on July 4 2012). Other searches are focused on physics BSM as: SUSY and other different models. However, there is not any evidence of new physics yet.

Section 3.2

The Compact Muon Solenoid (CMS) detector

The CMS detector is one of the two largest detectors at the LHC, with a total weight of 12500 tons, a length of 21.6 m and a diameter of 14.6 m. This detector consists of several sub-detectors. The first set of detectors are used to detect vertices from particles that decay promptly, near the beam pipe after the collision (Silicon Pixels), and to reconstruct the curvature of particles with electric charge (Silicon Strips). The two different sets of detectors are referred to as the tracking system. This system is followed by two calorimeters used to measure the energy of particles with electromagnetic and hadronic interactions, respectively. A superconducting solenoid encloses the tracking system and the electromagnetic and hadronic calorimeters. Outside the solenoid, three different gas-based detectors are used to detect muons. The muon detectors are alternated with three segments of a steel yoke, used for the return of the magnetic field. A diagram of the CMS detector is presented in Figure [3.4] taken from [49].

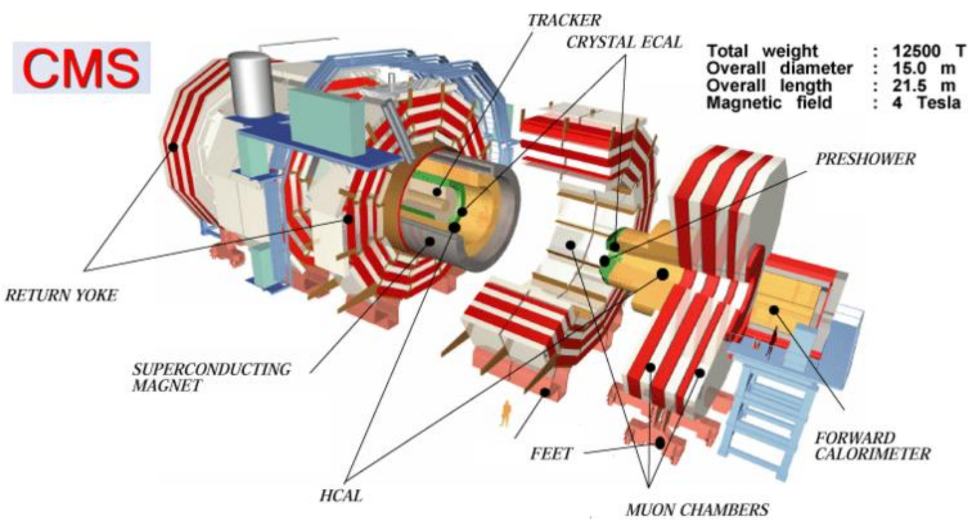

Figure 3.4: CMS detector diagram. The detector is composed of several sub-detectors used to measure the position, momentum, and energy of some of the particles resulting from the collisions.

Particles traversing the detector, resulting from the pp collision, can leave a different kind of signature depending on their characteristics. Particles that have an electric charge, such as electrons, muons and charged hadrons, leave a signature in the tracker system and bend in the presence of the magnetic field. By measuring the radius of curvature and the direction of the velocity of the particle concerning the magnetic field, the momentum of the particle can be estimated using the Lorentz Equation (3.1):

$$\frac{d\vec{p}}{dt} = \frac{e}{c}\vec{v} \times \vec{B}, \qquad \frac{dE}{dt} = 0 \tag{3.1}$$

In Equation (3.1), e is the electric charge, c is the velocity of light, $\vec{v}$ is the velocity of the particle, and $\vec{B}$ is the magnetic field [50].

Particles such as electrons and photons can deposit a large fraction of their energy in the electromagnetic calorimeter. Electrons and photons mainly interact with the electromagnetic calorimeter and generate cascades of particles known as showers. On the other hand, charged pions have dominantly strong (color) interactions and deposit most of their energy in the hadronic calorimeter. Because muons are two hundred times heavier than electrons, they do not bend as much for the same velocity as electrons in the magnetic field. For this reason, the momentum of muons cannot be measured very precisely in the tracker system. Additionally, the small change in the direction of the muon acceleration implies very low bremsstrahlung radiation, which results in a small energy deposition in the electromagnetic calorimeter. Therefore, three different types of detectors have been built at CMS to measure kinematic information for muons more accurately.

3.2.1 The CMS coordinate system

CMS uses a right-handed coordinate system. The Z-axis points in the anticlockwise direction of the beam, the X-axis points to the center of the LHC ring, and the Y-axis points towards the LHC plane. A *spherical coordinate* system is used to describe the position of the reconstructed particles in the detector. The azimuthal and polar angles are measured as follows: the polar angle θ is measured with respect to the Z-axis and the azimuthal angle ϕ is measured with respect the $X - Y$ plane.

The CMS experiment does not directly use θ to measure the polar coordinate. Instead, a coordinate called *pseudorapidity* (η) is used. To get the expression of the pseudorapidity, we start with the definition of the *rapidity* [51]:

$$y = \frac{1}{2} ln \left(\frac{E + p_z c}{E - p_z c} \right) \tag{3.2}$$

This quantity has a convenient definition: in high relativist regime in a collision event the p_z would be small, and the rapidity would be close to 0. Particles moving parallel to the beam axis have a $y \to \infty$. Therefore, high energetic events, which come from collisions, will be in the central part of the detector, otherwise, events will be in the Endcaps. Given all mentioned conditions, the pseudorapidity can be calculated from Equation (3.2).

$$y = \frac{1}{2} ln \left(\frac{(p^2c^2 + m^2c^4)^{1/2} + p_z c}{(p^2c^2 + m^2c^4)^{1/2} - p_z c} \right) \tag{3.3}$$

In the high relativistic limit, $pc >> mc^2$, the term pc can be taken out of the square root, the binomial expansion can be used to approximate the rapidity to:

$$
\begin{aligned}
y &= \frac{1}{2}ln\left(\frac{pc(1+\frac{m^2c^4}{p^2c^2})^{1/2}+p_zc}{pc(1+\frac{m^2c^4}{p^2c^2})^{1/2}-p_zc}\right) \\
&\backsimeq \frac{1}{2}ln\left(\frac{1+\frac{p_z}{p}+\frac{m^2c^4}{2pc^2}+\ldots}{1-\frac{p_z}{p}+\frac{m^2c^4}{2pc^2}+\ldots}\right)
\end{aligned}
\tag{3.4}
$$

We have $p_z/p = \cos\theta$, where θ is the mentioned polar angle. Hence:

$$
1+\frac{p_z}{p} = 1+\cos\theta = 1+\left(\cos^2\frac{\theta}{2}-\sin^2\frac{\theta}{2}\right) = 2\cos^2\frac{\theta}{2},
\tag{3.5}
$$

Likewise,

$$
1-\frac{p_z}{p} = 1-\cos\theta = 1-\left(\cos^2\frac{\theta}{2}-\sin^2\frac{\theta}{2}\right) = 2\sin^2\frac{\theta}{2},
\tag{3.6}
$$

Replacing the expressions above in Equation (3.4), we get:

$$
y \backsimeq -ln\left(\tan\frac{\theta}{2}\right).
\tag{3.7}
$$

The definition of pseudorapidity (η) is given by Equation (3.7). Note that, $y \approx \eta$ in the high relativist limit. This variable gives a more uniform distribution of particles across the polar coordinate than the θ angle alone. Another important characteristic of η is that its change $\Delta\eta_{ij}$ is invariant under Lorentz transformations along the beam axis, while $\Delta\theta$ is not [51]. A Lorentz boost parallel to the Z-axis is given by:

$$
\begin{aligned}
y' &= \frac{1}{2}ln\left(\frac{\gamma E/c-\beta\gamma p_z+\gamma p_z-\beta\gamma E/c}{\gamma E/c-\beta\gamma p_z-\gamma p_z+\beta\gamma E/c}\right) \\
&= \frac{1}{2}ln\left(\frac{E/c+p_z}{E/c-p_z}\frac{\gamma-\beta\gamma}{\gamma+\beta\gamma}\right) \\
&= \frac{1}{2}ln\left(\frac{E+cp_z}{E-cp_z}\right)+ln\sqrt{\frac{1-\beta}{1+\beta}} \\
&= y+ln\sqrt{\frac{1-\beta}{1+\beta}}
\end{aligned}
\tag{3.8}
$$

Consequently, for two particles that come from a collision with y_1 and y_2 measured in a specific reference frame, their differences transform as:

$$
\begin{aligned}
y_1^{'} - y_2^{'} &= y_1 + \sqrt{\frac{1-\beta}{1+\beta}} - (y_2 + \sqrt{\frac{1-\beta}{1+\beta}}) = y_1 - y_2 \\
\Delta y_{12}^{'} &= \Delta y_{12}, \longrightarrow \Delta \eta_{12}^{'} = \Delta \eta_{12}
\end{aligned} \tag{3.9}
$$

3.2.2 The superconducting solenoid

The main component of the CMS detector is the superconducting solenoid. This magnet produces a magnetic field ($\vec{B}$) of 3.8 T, which is around one hundred thousand times bigger than the earth's magnetic field (25 to 65 μT). This solenoid is made of niobium-titanium refrigerated by liquid Helium down to 2 K. It has 2168 turns, a length of 12.9 m and an inner bore of 5.9 m [52]. To perform precise measurement of the momentum of charged particles with high velocities a strong magnetic field is important. The most relevant features of the CMS magnet are shown in Table [3.2].

Table 3.2: Nominal values of the superconducting solenoid.

Features	Value
Magnetic Field	3.8 T
Inner bore	5.9 m
Length	12.9
N. of turns	2168
Current	19.5 kA
Stored energy	2.7 GJ

One of the most important challenges was the measurement of the magnetic field. For that purpose, a cylinder of 3.448 m diameter and 7 m length has been used. The components of $\vec{B}$ are done with this pneumatic-mechanical field mapper designed at Fermilab [52]. This machine has a precision of 5×10^{-4} at 4.5 T. The measurements of the magnetic field outside of the solenoid have been quite difficult to perform. The maximum precision achieved is 10^{-3} at 1.4 T by using 91 non-movable and 7 movable sensors [53]. Figure [3.5] taken from [53] shows the view of the CMS solenoid (left) and the intensity mapping (right) reported by the CMS collaboration in 2010. Note that, the intensity of the magnetic field is quite uniform in the Barrel region, but it is complex in the Endcaps. For that reason, the reconstruction efficiency of muons in the Endcaps region is worse than in the central part of the detector. There have been great efforts through MVA-tools to improve this issue for run-III, which starts in 2021.

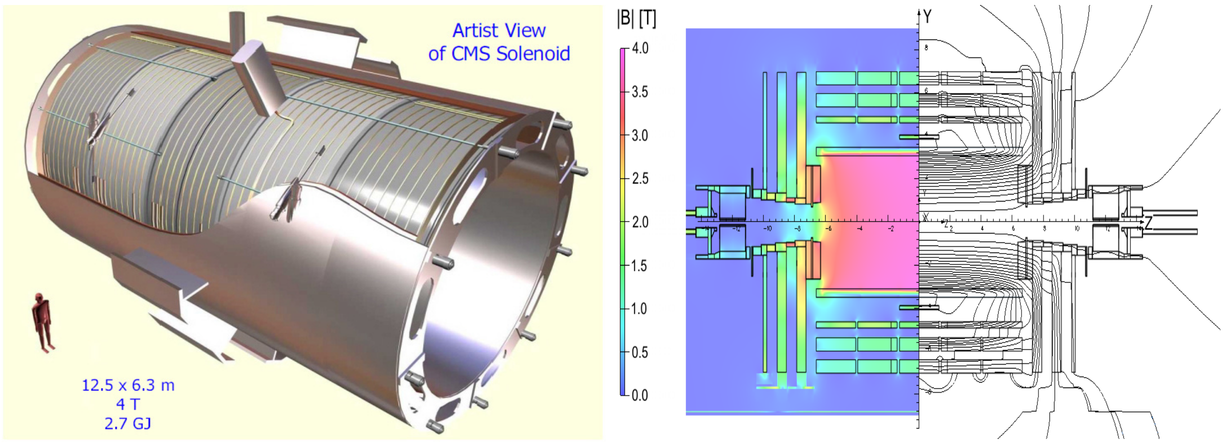

Figure 3.5: View of the CMS solenoid (left), the magnetic field mapping $|\vec{B}|$ of the superconducting solenoid at the CMS detector (right).

3.2.3 The tracker system

The tracker is a system used to provide a precise measurement of the position and electric charge of charged particles resulting after the collisions. The correct reconstruction of b-quarks from heavy decay, such as the top quark decay, is of special physical interest for the scientific community at the LHC. Since heavy particles generally decay near the beam pipe, the tracking system should be close to the interaction point. The tracking system is composed of the pixel detector and the silicon strips.

3.2.4 The pixel detector

The pixel detector is the closest detector to the LHC beam pipe. It has around 66 million pixels, which are rectangular and their area is $100 \times 150\ \mu m^2$. This detector was designed to provide two or more hits per each track of one charged particle. In addition, the pixel allows measuring a secondary vertex generated by long-lived particles, such as b or c quarks or τ leptons. The geometry of the pixel detector is basically some concentric Barrel layers located at 4.4, 7.3 and 10.2 cm from the center of the interaction point, and two Endcap disks on each side. The three Barrel layers have a length of 53 cm, and the Endcap disks are located at $|Z| = 34.5\ cm$ and $46.5\ cm$. The pixel detector covers a pseudorapitidy region up to $|\eta| < 2.5$. The layers of this detector are composed of modular units of segmented sensor plates, each of them connected to a readout chip (ROC) using a micro-soldering technique known as bump bond [54]. Figure [3.6] shows a sketch of the pixel sensors [49].

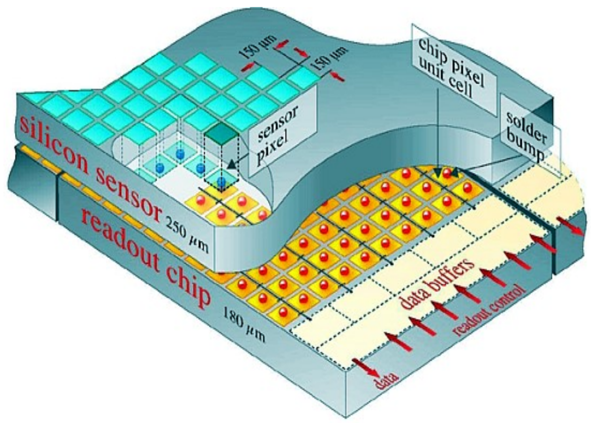

Figure 3.6: Description of the pixel sensors, the sensors are connected to the readout chip using bump bonds in the pixel sensor.

3.2.5 The silicon strips tracker

The silicon strips detector has 15400 modules, which are arranged in the Barrel and Endcap regions of the CMS detector. The Barrel is divided into two sections: the Tracker Inner Barrer (TIB) and the Tracker Outer Barrel (TOB). The TIB used silicon sensors of 320 μm thickness and strip pitches of different widths, the dimensions can vary from 80 to 120 μm. The TIB is organized in four cylindrical layers, whose pseudorapidity coverage is up to $|\eta| < 1.4$. Figure [3.7] presents a real picture of the TIB [49, 54].

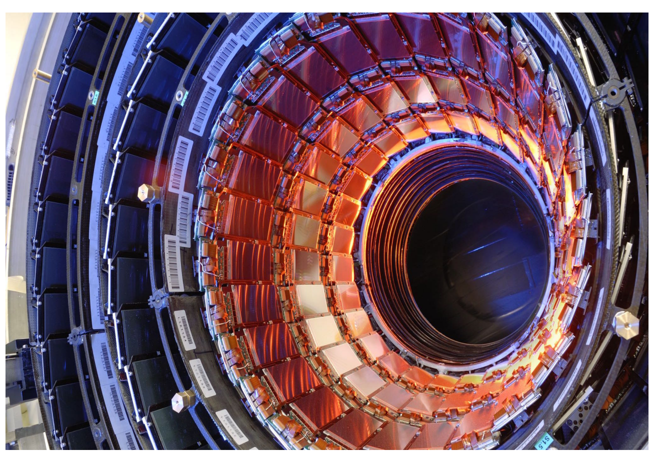

Figure 3.7: The Tracker Inner Barrel (TIB) of the CMS detector.

The TOB is composed of four identical disks, which have six cylindrical concentric layers. The TOB has a set of silicon sensors of 500 μm thickness and strip pitches that vary from 80 to 120 μm. The Endcap region of the detector has a total of twelve disks on each side. The disks are divided into nine disks called Tracker End Caps (TEC) and three smaller disks called Tracker Inner Disks (TID). These TID fill the gap between the TIB and the TEC. Moreover, silicon sensors of 320 μm thickness are used for the TID and three innermost disks of the TEC, the remaining disks of the TEC have sensors of 500 μm. The TID and TEC cover a pseudorapidity region of $1.2 < \eta < 2.1$ and $1.0 < \eta < 2.5$ respectively [54]. The tracker resolution depends on the type of particle that is detected. For example, light charged particles with momentum above 1 GeV have an efficiency of 94% for $|\eta| < 0.9$ and 85% for $0.9 < \eta < 2.5$. In addition, the spatial resolution of the primary vertex reconstruction is around 12 μm [55].

3.2.6 The electromagnetic calorimeter

The Electromagnetic Calorimeter (ECAL) is composed of 74524 lead tungsten crystals ($PbWO_4$). The detector is divided into two sectors, Barrel ECAL (EB) and Endcaps ECAL (EE) [45]. The crystals are shaped like a quadrangular prism with an area of 22×22 mm^2 and length of 230 mm each. When charged particles pass through the ECAL crystals, they interact with the material generating an electromagnetic shower. This shower is developed by high energy photons, which create electron-positron pairs that generate more photons. The $PbWO_4$ crystals are connected to photo-detectors that collect the scintillation light that comes from the photon cascade, amplify it and convert it into an electrical signal. In order to measure the position of the shower and its energy, the final electric signal is then sent to the readout system. Figure [3.8] shows a picture of the electromagnetic calorimeter taken from [49].

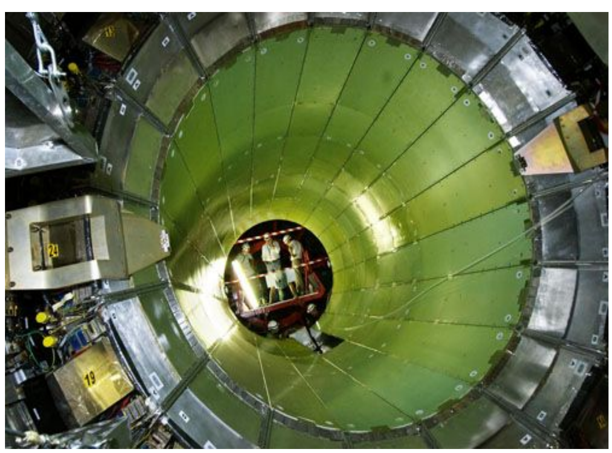

Figure 3.8: Picture of the electromagnetic calorimeter of the CMS detector.

The Barrel system has been structured into four modules. The first module is composed of 500 crystals and the three remaining have 400 crystals. Each module covers half of the total Barrel length, and 36 modules cover the whole EB section. The EB has an inner radius of 1.29 m and covers a interval of $0 < |\eta| < 1.479$. The Endcap system is composed of two half-disks, consisting of a set of units. Each unit is assembled with 5×5 crystals called super crystals. The crystals that make up the units have the same dimensions: $24.7 \times 24.7 \times 220\ mm^3$. They are located at 314 cm from the interaction point, which have a pseudorapidity coverage of $1.479 < \eta < 3.0$ [54]. The resolution of the ECAL is obtained by fitting the reconstructed energy, the number of secondary particles (S), the electronic noise (N), and calibration factors (C) [56].

$$\left(\frac{\sigma(E)}{E}\right)^2 = \left(\frac{S}{\sqrt{E}}\right)^2 + \left(\frac{N}{\sqrt{E}}\right)^2 + C^2 \tag{3.10}$$

3.2.7 The hadron calorimeter

The Hadronic Calorimeter (HCAL) has been designed to measure the energies and directions of particles that have strong interaction, such as pions, kaons, neutrons, among others. In addition, particles that have no strong interaction, such as photons, electrons and muons are detected with the help of the HCAL detector. Therefore, the HCAL detector complements the ECAL and muon detectors. For instance, by using the information from the ECAL and the HCAL detectors, different energy thresholds can be implemented in each detector to identify the type of particle. The HCAL is made of alternating layers of non-magnetic brass, such as: copper, zinc and stainless steel. The hadronic particles generate showers of particles in the HCAL, which are detected with plastic scintillators in between the metal layers and this light from the scintillators is sent to the readout system using optical fibers.

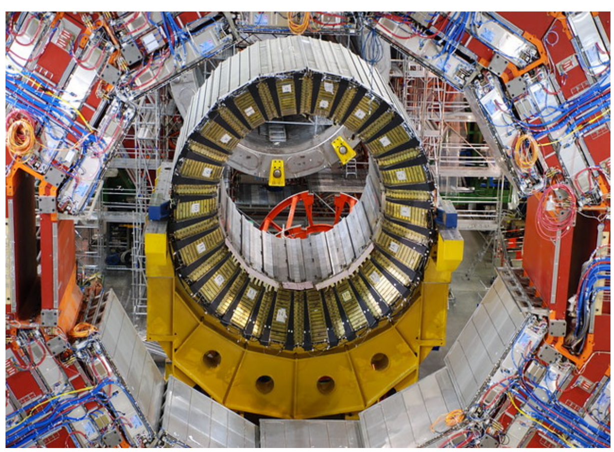

Figure 3.9**:** Real picture of the Hadronic calorimeter of the CMS detector.

Figure [3.9] shows a real picture of the HCAL taken from [49]. The HCAL has three main sections: central, outer, and forward. The central part has two segments, the Hadron Barrel (HB) and the Hadron Endcap (HE). The HB is composed of two half barrels, each half barrel contains a total of 16 towers, covering a pseudorapidity of $0 < \eta < 1.4$. The HB gives a total of 1152 channels per a half-barrel with a ϕ segmentation of 5^o. On the other hand, the HE consists of a set of 14 towers covering a pseudorapidity of $1.3 < \eta < 3.0$ with the segmentation of 5^o around the 5 outermost towers (whose η is smaller), and segmentation of 10^o for the inner towers [54].

The Hadron Outer (HO) calorimeter is placed outside the magnetic solenoid but inside the barrel of the muon system. The HO covers a pseudorapidity region of $-1.26 < \eta < 1.26$. The HO is essentially a layer of scintillators used to measure the energy of hadron showers that go beyond the calorimeters and the solenoid [54]. Finally, the Hadron Forward (HF) calorimeter is located at 11.2 m from the beam pile. It covers a pseudorapidity region of $3 < \eta < 5$. The HF contains steel/quartz fibers running parallel to the beamline. The HF is composed of 13 towers in η, with a segmentation of 10^o around ϕ, except for the highest η, where $\Delta\phi = 20^o$. This distribution gives a total of 900 towers for the entire HF detector. The expression of the resolution of the HCAL looks like the resolution of the ECAL, which is described by Equation (3.10). The resolution of the HCAL depends on the granularity of the detector and the type of particle as well. For pions, the resolution is given by [57]:

$$\left(\frac{\sigma(E)}{E}\right)^2 = \left(\frac{138\%}{\sqrt{E}}\right)^2 + \left(13\%\right)^2 \tag{3.11}$$

3.2.8 The muon system

The muon system at CMS is composed of three different types of technologies: Drift Tubes (DT), Chatode Strip Chambers (CSC) and Resistive Plate Chambers (RPC). As mentioned before, the muon system is interlaid between the layers of the iron return yoke. The muon system was designed to provide good identification and fast trigger response. The barrel region of the muon system is composed of five wheels. The wheels are divided into 12 identical sectors, organized in four layers (MB1, MB2, MB3 and MB4) per wheel [54]. The resolution of the muon system has been studied from the Run-I, for muons with p_T greater than 1 GeV, the resolution achieved 95% within the whole pseudorapidity coverage of this sub-detector, moreover, the charged hadron fake rate as a muon is maintained below 1% [58].

3.2.9 The drift tubes chambers

The DT units consist of a cell filled with an ionizing gas. Figure [3.10] shows a sketch of the basic components of a DT unit taken from [54]. When charged particles pass through the DT cells, it ionizes the gas leaving a trail of electrons and ions that produce a signal collected by the anode. The DT detector covers the barrel region ($|\eta| < 1.2$) where the multiplicity of muons is relatively low.

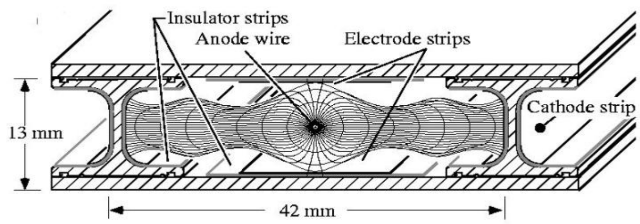

Figure 3.10: Sketch of the basic unit cell of a DT chamber at CMS. A voltage of +3600 V is applied to the anode wire, 1800 V for the electrode strip at the top and bottom of the cell and −1200 V for the cathode strips on the sides.

3.2.10 The cathode strip chambers

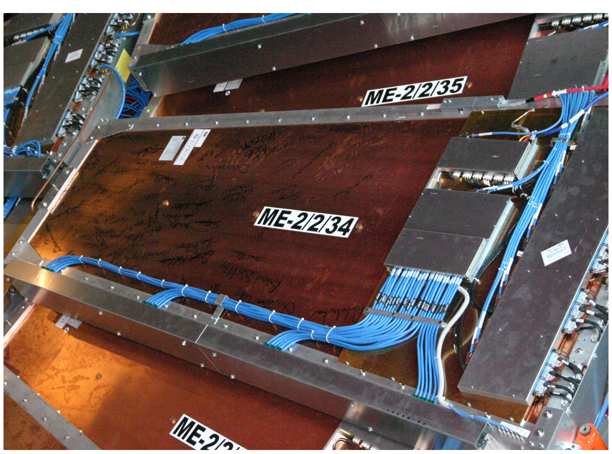

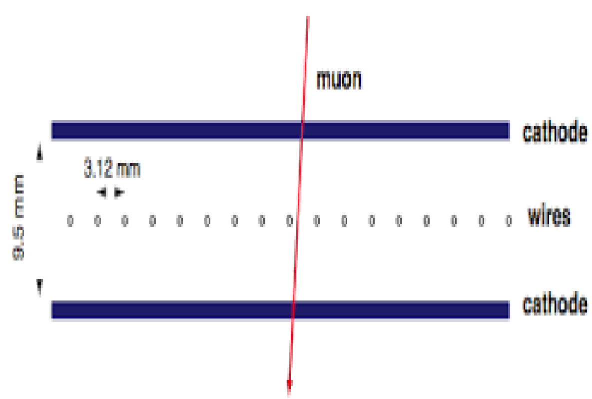

Figure 3.11: Real picture of CSC unity (left), sketch of a single gas unit of a CSC chamber (right).

The CSC's are only located in the endcaps of the CMS detector. The system has a total of 468 units, equally distributed in the two endcaps. Each CSC module has a trapezoidal shape and is symmetrically distributed in concentric rings around the beam line (Z coordinate). The chambers consist of six detecting layers filled with gas. Figure [3.11] shows a real picture and a sketch of a basic CSC unit taken from [49, 54]. When charged particles go through the chambers, the corresponding ionization of the gas generates an avalanche of electrons which produce a charge on the anode wire and a subsequent image charge on the group of cathode strips. The CSC chambers are used in the two endcaps ($|\eta| < 2.4$) of the detector, where the muon rate and the magnetic field are high [54]. This detector produces a fast signal, which is very useful for triggering purposes.

3.2.11 The resistive plate chambers

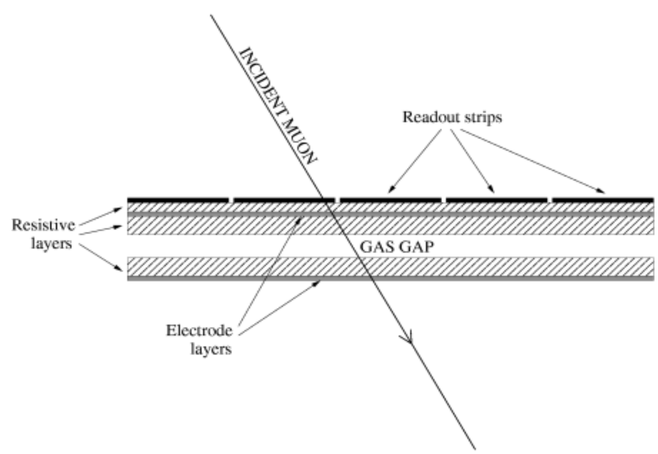

Figure 3.12: Sketch of a simple RPC chamber.

The RPC's are detector units consisting of two parallel plates with a high polarization voltage. These are filled with ionizing gas. Figure [3.12] shows a sketch of a basic unit of an RPC detector taken from [54]. The RPC chambers are located in both detector regions: barrel and endcaps. The RPC chambers provide good spatial and timing resolution. Additionally, this detector is used for triggering purposes and complements the measurements performed by the DT and the CSC modules. For the barrel section, a total of six layers of RPCs are installed. There are two layers of RPCs at stations MB1 and MB2 and just one layer for the MB3 and MB4 sectors. On each endcap, there are four layers of RPC, one per each CSC. The RPC's cover a region of $|\eta| < 1.6$.

Section 3.3

The trigger system

CMS has to handle a large amount of information every bunch crossing. The event rate that comes from collisions is 40 MHz for Run-II. The event size in storage is around 1 MB, consequently, by operating at 40 MHz at nominal luminosity, 40 TB per second of data is generated. Therefore, CMS has developed a trigger system to select interesting events. The main task of this system is to reduce the rate of information from 40 MHz to 100 Hz, based upon physics criteria, and collect the desired information via the Data Acquisition System (DAQ, section 3.4). The Trigger System has two filtering stages: the Level 1 Trigger (L1-Trigger) and the High Level Trigger (HLT).

3.3.1 L1-Trigger (L1T)

The L1T executes the selection events based on hardware criteria, by reading out the electronics of each detector. The L1T uses information from ECAL, HCAL and muon detectors to make a fast decision regarding the event [59]. Therefore, the L1-Trigger searches information from Calorimeters (ECAL and HCAL) and Muon (CSC, DT, RPC) systems. This information has several pre-processing steps to evaluate the Global Trigger decision (GT) where the event is accepted or not.

3.3.2 High level trigger (HLT)

The HLT is a step of processing of the events based on software [60].The complex reconstruction algorithms operate with the whole information in each read-out channel of the detector and generate a specific dataset for each physics object(electron, muon tau, p_{T}^{miss}, etc). Finally, the information is stored in a computer farm at CERN referred to as the Tier-0 and then transferred to other computers farms located in other places in the world known as Tiers-1. The HLT has different types of algorithms such as clustering algorithms to establish the energy deposit by the electron in the ECAL, and island algorithms to avoid overlapping between clusters. Reconstruction techniques to find the exact position of the clustering and the full tracking of the electrons and photons are used [60]. In summary, HLT generates physics objects based on algorithms[†] and it decreases the event rate down to 100 Hz of the information provided by the L1T.

[†]The particle reconstruction will be further explained in Chapter 4

Section 3.4

The data acquisition system

The Data Acquisition System (DAQ) is related to the whole set of functions needed to store the information that comes from collisions. The non-discarded events by the L1T are saved within a time of 32 μs and the DAQ can write the information with a speed of 100 Gb/s. During the L1T processing, the DAQ must keep storing data. There are specific electronic devices for this purpose [61]. The Front End Systems (FES) is buffering devices to store the information continuously. Once the information is processed there, data is pushed into the Front End Driver Devices (FED). Finally, the DAC combines the information from different FEDs of each sub-detector by using a Front-end Read-out Link (FRL). The last step is through optic fiber where the information is transferred and processed by the HLT. Figure [3.13] shows the performance of the FED system as a function of the transferring bytes taken from [61]. Note that, the working point is around 200 Mb/s.

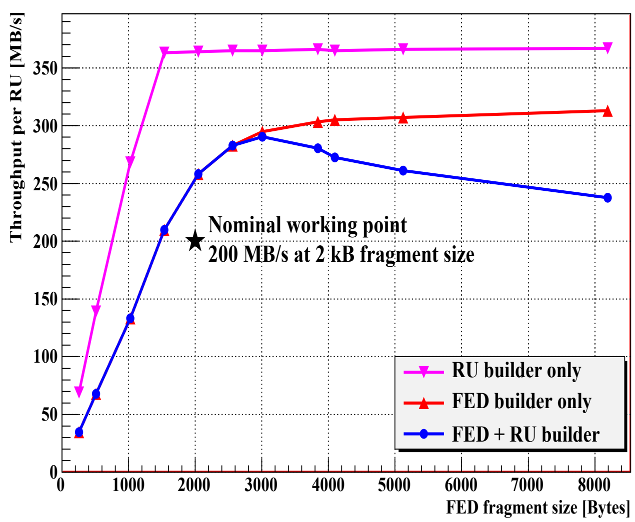

Figure 3.13**:** Performance of the FED as a function of transferring bytes (fragment of the information).

The information stored by the DAQ includes all the relevant physics information of a specific event. A first format launch by the HLT is the RAW format, which is a complete set of the features about the event. Nevertheless, this format does not contain explicitly physics quantities such as the kinematic variables or the identification of particles among others. In order to obtain the relevant physics information, an additional reconstruction step is needed. CMS utilizes the Particle Flow Algorithm (PFA) to reconstruct outcoming particles from collisions, as discussed in Chapter 4. This new more readable format is called RECO format, but it is still not small enough to be used for data analysis. The final format for physical analysis is called mini-AOD format, which has a smaller size than the RECO format but, it has a piece of complete information from the collisions for analysing. Recently, the size of the format has been reduced even more to a new format called nano-AOD[†].

Section 3.5

Service work and other contributions at CMS

The service work inside of the CMS collaboration can be summarized as follows:

- I was in charge of the data certification through Data Quality Monitor (DQM) for the RPC system detectors for 1 year.
- There were two contributions of software to the CMSSW off-line repository for the L1 trigger in the RPC detectors. These contributions can be located in the following links:
  - CPPF emulator: https://github.com/cms-sw/cmssw/tree/master/L1Trigger/L1TMuonCPPF
  - Primitive Trigger Producer: https://github.com/cms-sw/cmssw/tree/master/L1Trigger/RPCTriggerPrimitives
- The CPPF emulator is referred to as a module to create integers coordinates based on the global geometry of hits in the RPC chambers. These coordinates are input for another system in the endcap region known as EMTF, which are given by:

$$\begin{aligned} \theta_{int} &= (\theta_{global} - 8.5) \times 32./36.5 \\ \phi_{int} &= (\phi_{local} + 22.) \times 15. \end{aligned} \tag{3.12}$$

  θ_{global} and ϕ_{local} is available information in current RPC collections, which are already included in the CMSSW repository.
- RPC Primitive Trigger Digis are referred to a module to create an additional collection based on a map between the RPC chambers and the real optic fibers in each chamber. This information was not included in before versions of CMSSW, which is already implemented for all geometry of RPC detectors.

[†]For this thesis, the analysis for 2016 and 2017 data samples are based upon mini-AOD and nano-AOD respectively as discussed in Chapter 7

CHAPTER 4

Particle reconstruction and identification

Section 4.1

The Particle flow algorithm

The Particle Flow Algorithm (PFA) is a set of instructions based on hardware and software. The main aim of the PFA is the identification and reconstruction of the stable particles after the collisions. By combining the information of each sub-detector, CMS can perform the reconstruction processes. Particles such as electrons, photons, muons, and neutral and charged hadrons can be reconstructed with the PFA. There is another type of objects such as jets or the Missing Transverse Energy (p_{T}^{miss}), named High-Level Objects which are reconstructed as well.

Electrons are reconstructed by adding information from the tracker and the deposited energy in the ECAL [62]. The energy loss is mainly due to bremsstrahlung, thus the first electron leads to $e^{\pm}$ cascades plus photons. This process continues with the energy of the electrons produced by the cascades achieves the critical energy, where the ionization process is balanced by the bremsstrahlung. The critical energy is approximately given by $E_c \approx 600/Z$ GeV [51]. On the other hand, photons are reconstructed following the same behavior. The reconstruction of photons has high accuracy due to the performance of the ECAL detector. Charged and neutral hadrons are reconstructed by using their deposited energy in the HCAL detector, with pseudorapidity coverage of ± 3. The HCAL detector can separate these particles with transverse momentum above 100 GeV/c spatially. Moreover, the resolution is around 10% at 100 GeV [51]. As we mentioned, the global information about the reconstruction and identification is taken from each sub-detector, and it is processed through three routines: tracking, clustering, and link algorithms, which belong to the PFA framework.

4.1.1 Tracking

Although the combined ECAL-HCAL resolution is quite good, the main aim is basically to discern as many particles or jets as possible. The tracker is included in the reconstruction process to reach this goal. Since the tracker has a much better spatial resolution than the calorimeters, on the order of μm, this detector can provide the primary and secondary vertex of the decay products and their directions. Essentially, the tracking algorithm processes the measurements of the tracker to keep fake rates as small as possible.

The steps to reconstruct tracks go as follows: tracks are reconstructed using very tight criteria, then, another less strong criteria are applied which must not exceed the fake rate. In the next step, the ambiguous tracks are deleted, this is then repeated by reducing the maximum value of criteria. This iterative method increases the efficiency of the tracking hits, which reduces fake hits. The rough efficiency is around 99.5% for isolated muons and 90% for charged hadrons [62]. With this technique, charged particles with three hits and momentum around 150 MeV/c are reconstructed, and their fake rates are as small as the method allows. Figure [4.1] taken from [62] describes the tracking iteration for a hadronic jet.

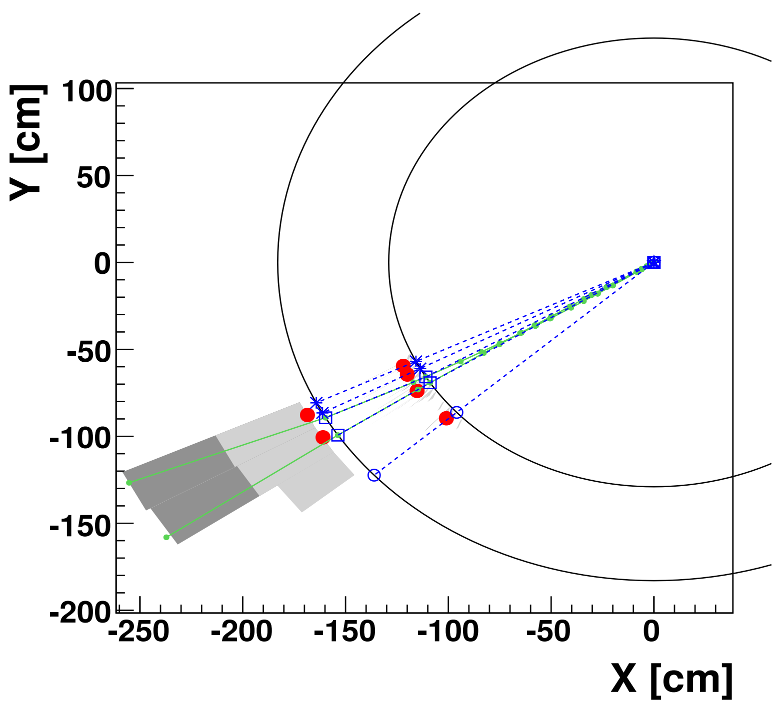

Figure 4.1: The tracking algorithm increases the efficiency of the hit tracking. This information helps the ECAL and HCAL in the reconstruction process.

4.1.2 Clustering

The clustering algorithm has three aims. The first one is the measurement of the energy and direction of the particles, the next step is to separate the neutral particles such as photons from the charged hadrons, and the last is to identify the electrons and their associated bremsstrahlung. In addition, the clustering is performed in each sub-detector by adding the information of the deposited energy in a set of cells. This algorithm calculates the cell with the largest energy deposition, which is referred to as the *seed-cell*. The seed-cell is activated by adding at least one cell with energy above a certain threshold. In fact, this threshold determines the resolution of each calorimeter. For the ECAL detector, the threshold is 80 MeV in the barrel region and 300 MeV for the endcaps, and for the HCAL detector, the threshold is roughly 800 MeV [62]. Finally, the iterative process in each sub-detector gives the best cluster and position to the PFA algorithm.

4.1.3 The Link algorithm

The PFA algorithm in each sub-detector must be combined to reconstruct a global object such as a jet, electron or muon. The linking algorithm connects the separate information in each sub-detector to generate the global reconstructed object. The linking algorithm avoids to count duplicate physics objects as well as to qualify the distance between them [62]. This distance depends on the granularity in the sub-detector, which is measured in the $\eta - \phi$ plane. In CMS, the granularity of the ECAL detector is better than of the granularity of the HCAL detector. This granularity allows the link algorithm to build two or three blocks of information, depending on each detector. In addition, if this cluster has an associated track in the tracking algorithm, there will be enough information to isolate this physics object using the PFA. Another feature of the link algorithm is that the criteria to get global objects is based on the minimum value returned by the χ^2 estimator, which determines the optimal link distance between objects.

Section 4.2

Jet reconstruction

In experimental particle physics, a collection of particles that comes from the hadronization (or fragmentation) processes initiated by quarks or gluons are called jets. Such hadronization processes are due to the nature of the strong interaction, which does not allow free-quark states, maintaining the color confinement [51]. The strong potential has a confining term that increases in magnitude with the distance of separation between quarks anti-quark pair, allowing, at a certain point, the creation from the vacuum of an additional quark anti-quark pair. this process is subsequently repeated, resulting in a large variety of light and heavy hadrons after hard scattering events. The decay products are clustered following specific software algorithmic routines. Some neutral and charged hadrons, such as kaons, pions, and neutrons are reconstructed by the CMS detector.

The PFA algorithm reconstructs all particles as a single object, tagged as a jet, through the information in each sub-detector. In general, reconstruction algorithms for jets focus mainly on clustering tracks, which is described as follows:

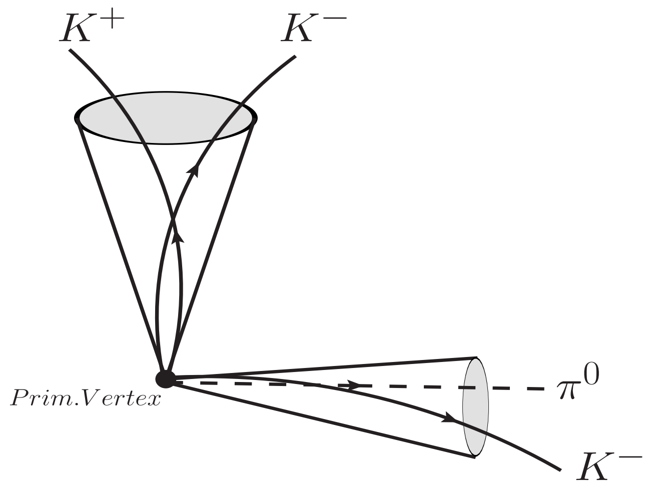

Figure 4.2**:** The spatial notion of jets can be sketched as a mathematical cone, which is defined by the $\eta - \phi$ coordinates. By minimizing the distance in the $\eta - \phi$ space, algorithms can reconstruct a single object (jet) based on the clustering tasks in each sub-detector.

- **Sequential algorithms:** In CMS, the coordinate space is defined by the coordinates (η, ϕ). By minimizing the distance in the variable ΔR defined as $\Delta R = \sqrt{(\Delta\eta)^2 + (\Delta\phi)^2}$, reconstruction algorithms generate global physics objects (jets) using individual clusters in each sub-detector. Iteratively, the code flow searches all particles contained within a distance ΔR measured from the beam axis, which is the primary vertex of the collision. ΔR defines a mathematical cone in space. Figure [4.2] sketches the geometry of the clusterization using the geometric distance ΔR. The algorithm is completed when there are no more particles outside of the cone. In addition, the clusterization also depends upon the transverse momentum of the particles involved. The geometric distance between two particles is defined as:

$$\begin{aligned} d_{ij} &= min(k_{ti}^{2p}, k_{tj}^{2p})\frac{((y_i - y_j)^2 + (\phi_i - \phi_j)^2)}{R} \\ d_{iB} &= k_{ti}^{2p} \end{aligned} \tag{4.1}$$

  In Equation (4.1), k_T is referred to the transverse momentum carried by a given particle, and R is the minimum value of the distance among particles that constitute the jet.

In references, depending on the specific value of the exponent p, you can find different versions of the sequential algorithms. For $p = 1$ the algorithm is called *kt algorithm* [63], for $p = -1$ the algorithm is called *anti-kt algorithm* [64] and for $p = 0$ the algorithm is called *Cambridge-Aachen* [65]. The algorithm that is most commonly used by the CMS and ATLAS collaborations is the *anti-kt algorithm*, which constructs the cone using the particle with highest p_{T} as a seed, after that, the algorithm includes other particles with lower p_{T} [66]. Finally, some corrections are taken into account to build the final jet, such as efficiencies, the acceptance of the detector, pileup, electronic noise, and overlap removal. For example, the pileup dominates corrections for low p_{T} regimen up to 50% at CMS [67].

4.2.1 B-jet reconstruction

After the hard scattering processes, all kind of hadronization processes is produced. These final states generate different signatures in each layer of the detector. In general, the distinction between jets that come from the hadronization of u, d, s and b-quarks is quite difficult. Jets composed of b-quarks have different time-decay and are characterized by secondary vertices, which have a typical length on the order of mm. This secondary vertex can be measured using the tracker sub-detector [68].

The CMS experiment has several algorithms to identify this type of jets. These algorithms are based on the information of isolated leptons, tracks and vertices to achieve the maximum isolation power of b-jets. One of the algorithms is known as Combined Secondary Vertex (`CSV`), which has is a multi-variable algorithm characterized by different isolation working points. These working points are referred to as isolation criteria to obtain more certainty about the identity of the jet. Commonly, these isolation criteria are denoted as: Very Loose, Loose, Medium, Tight, and Very Tight. For instance, the Medium working point has a misidentification rate associated with light-jets (u,d,s) of 1% for a $p_{\mathrm{T}} \geq 80\ GeV/c$ [68]. In CMS, b-jets are clustered using the *anti-kt* algorithm with $R = 0.5$ by default. On the other hand, the reconstruction of b-jets has shown a good performance, by including Multi-Variable Analysis (MVA) tools, which use as input the secondary vertex, among others. According to the efficiency of the algorithm and the misidentification rates, the most used working points are described as follows [69].

- `CSVL`: Loose working point, which has an efficiency of 83% and a misidentification rate of 10%.
- `CSVM`: Medium working point, which has an efficiency of 69% and a misidentification rate of 1%.

- `CSVT`: Tight working point, which has an efficiency of 49% and a misidentification rate of 0.1%.

The `CSV` algorithm was the predecessor of the `CSVv2` algorithm, which was implemented in the Run-II period. This `CSVv2` is based upon neural networks and has an enhancement in the efficiency of around 10%. Figure [4.3] taken from [69] shows the behavior of the efficiency as a functions of fake rates. Table [4.1] summaries the features of the different working points for the `CSVv2` algorithm.

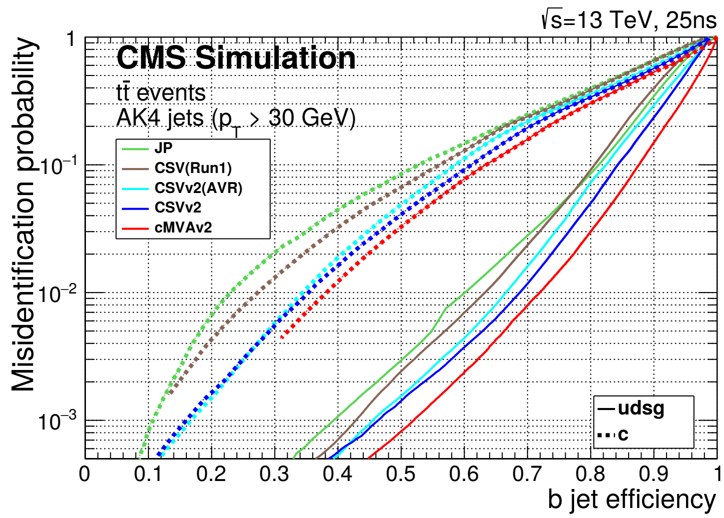

Figure 4.3: b-tagging efficiency as a function of the misidentification rate. The behavior depends on the regimen of the momentum (p_{T}) and the pseudorapidity (η) coverage. Simulated $t\bar{t}$ events from pp collision at $\sqrt{s} = 13$ TeV have been used.

Table 4.1: Working points of the b-tagging algorithm as a function of the discriminators of the neural networks.

WP	Discriminator	b-tagging efficiency	fake-rate
Loose	0.5426	83%	10%
Medium	0.8484	69%	1%
Tight	0.9535	49%	0.1%

Section 4.3

Introduction to tau (τ) physics

The tau (τ) lepton is a lepton identical to the electron or the muon but with a significantly larger mass. Taus can decay either to leptons ($\tau \to \nu_\tau \ell \nu_\ell$), with $\ell = e, \mu$, or to light hadrons

($\tau \to q\bar{q}$). Figure [4.4] shows the Feynman diagram illustrating the possible decays of the τ. Hadronic decays of the τ lepton are expressed as τ_h. The τ_h decays are characterized by one, three, or five charge hadrons with neutral particles in the final state, which depends basically on the fragmentation processes of the initial quarks.

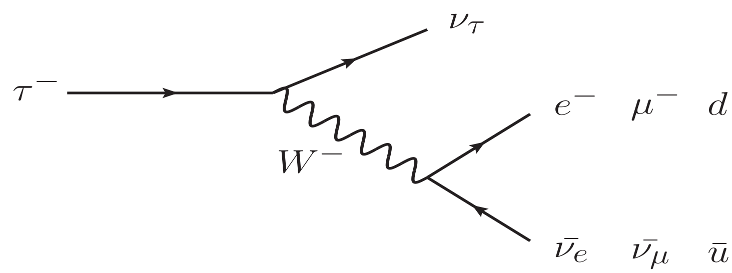

Figure 4.4**:** Feynman diagram of the possible decay modes of the τ^- lepton.

The decay rate to leptons or hadrons is known as branching ratio (BR) of the channel. The branching ratios of the tau decay can be summarized as follows: The branching ratio to hadrons $BR(\tau \to q\bar{q})$ is around 64%, and to leptons $BR(\tau \to \nu_\tau \ell \nu_\ell)$ is 36%. Because lepton universality, the BR to muons and electron is roughly the same ($\approx 17.5\%$). In fact, the source of the difference between $BR(\tau \to \nu_\tau e \nu_e)$ and $BR(\tau \to \nu_\tau \mu \nu_\mu)$ comes from the mass difference between the electron and the muon, which is $m_\mu \approx 200 \times m_e$. On the other hand, the tau lepton has a short life time ($t_{mean} = 290 \pm 0.53 \times 10^{-15}\ s$), which leads to a decay length of $ct_{mean} \approx 87\ \mu m$ [8]. This intrinsic feature of the tau lepton does not allow its reconstruction directly, because of this particle does not reach the first detector layers. Table [4.2] summarizes the main properties of the τ lepton [51].

Table 4.2**:** Possible decay channels of the τ lepton with their corresponding branching fractions.

Leptonic decay channels	
$\tau^\pm \to e^\pm \nu_e \nu_\tau$	17.8%
$\tau^\pm \to \mu^\pm \nu_\mu \nu_\tau$	17.4%

Hadronic decay channels	
$\tau^\pm \to h^\pm \nu_\tau$	11.5%
$\tau^\pm \to h^\pm \pi^0 \nu_\tau$	26.0%
$\tau^\pm \to h^\pm \pi^0 \pi^0 \nu_\tau$	10.8%
$\tau^\pm \to h^\pm h^\pm h^\mp \nu_\tau$	9.8%
$\tau^\pm \to h^\pm h^\pm h^\mp \pi^0 \nu_\tau$	4.8%

In general, τ decays can be misidentified with events that come from other processes such as electrons and muons from the Z^0 decay or similar signatures associated with QCD Multi-jets production. Therefore, the τ_h decay, which has the highest BR is the most accessible channel at experimental level. In order to measure a hadronic tau candidate (τ_h) as accurate as possible, reconstruction and identification algorithms are needed.

4.3.1 Tau reconstruction

The CMS experiment has developed reconstruction algorithms to isolate a hadronic tau candidate (τ_h). This software is known as Hadron Plus Strip (HPS) algorithm [70]. The HPS algorithm uses the particle flow algorithm to identify and reconstruct the physics objects in each sub-detector. In general, the HPS has four categories: electrons, muons, neutral, and charged hadrons. The dominant contribution of the hadronic decays is to three $\pi^{\pm}$ and two π^0, which are reconstructed by the HPS. The HPS focuses on photons and electrons that deposit their energy in the ECAL detector and the bending tracks of electrons and positrons. This algorithm clusters photons in an object called *strip*, then, it looks for electromagnetic candidates ($e^{\pm}$) within a mathematical cone given by $\Delta\eta \leq 0.05$ and $\Delta\phi \leq 0.20$. In addition, the deposition of energy in the ECAL must be consistent with the π^0 reconstruction. This deposited energy has a threshold of $E_{min} \geq 1\ GeV/c$. Finally, by combining the previous information with the information that comes from charge hadrons, the τ_h candidate can be reconstructed in its different decay modes [70]. Table [4.3] describes the different modes of the HPS algorithm.

Table 4.3: Different reconstruction modes generated by the HPS algorithm.

Mode		Topology
Single hadron	$h^-\nu_\tau$, $h^-\pi^0\nu_\tau$	$p_T(\pi^0) \approx 0$
One hadron + 1 strip	$h^-\nu_\tau$	γ's and π^0 collinear
One hadron + 2 strips	$h^-\nu_\tau$	γ's and π^0 well separated
One hadron + 3 strips	$h^-h^+h^-\nu_\tau$	outcoming hadrons from same vertex

For instance, Figure [4.5] shows schematically the hadronic tau decay ($\tau \rightarrow \pi^-\pi^0\nu_\tau$), which corresponds to the 54.5% of the whole spectrum of the tau hadronic decays. Similar to the reconstruction of b-jets, the HPS algorithm has different working points for isolation of the τ_h candidate. These requirements have the same labels: Very Loose, Loose, Medium, Tight, and Very Tight. For taus, these working points are calibrated using QCD Multi-jets events, which have a non-negligible probability to misidentified as τ_h candidates. In CMS, this misidentification rate is 1%, 2%, and 4% for Loose, Medium, and Tight working points respectively [70].

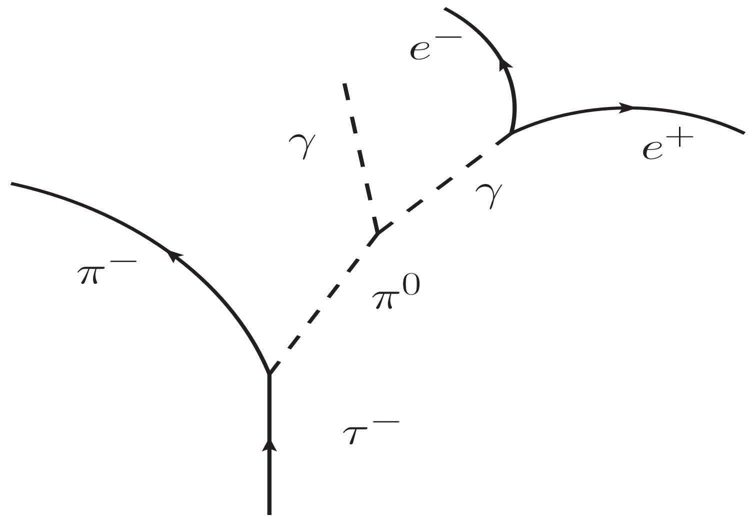

Figure 4.5: Single τ_h decay ($\tau^- \to \pi^- \nu_\tau$ or $\tau^- \to \pi^- \pi^0 \nu_\tau$). The strip is reconstructed by using the combined information that comes from the tracker and the ECAL. By adding the information of the charged hadron and the topology of the object, different decay channels are identified.

In CMS, the τ_h isolation working points have been measured on data in channels such as τ lepton decaying to hadrons and ν_τ at $\sqrt{s} = 13$ TeV. Figure [4.6] shows the isolation working points of the τ_h candidate, which is measured in $Z/\gamma^* \to \tau\tau$ events [71].

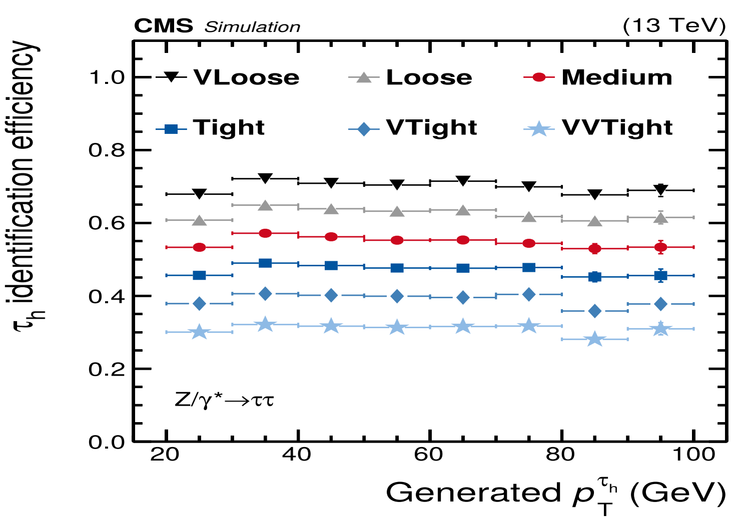

Figure 4.6: Efficiency of the τ_h candidate identification, which is estimated using simulated $Z/\gamma^* \to \tau\tau$ events. This efficiency is a function of the reconstructed $p_T(\tau_h)$ of the generated τ in MC.

Section 4.4

Muon reconstruction

In CMS, muons have been broadly studied. The reconstruction and identification efficiencies achieve 95% in the total pseudorapidity coverage for low p_{T} muons. In addition, the misidentification rate of muons as hadrons is around 1% [72]. The muon candidate reconstruction has two main steps. In the first step, the muon candidate is reconstructed using the information that comes from either the tracker or the muon detectors. The muon candidate is actually a *local physics object* defined in each sub-detector separately. In the second stage, the information of the tracker is added to the information of muon chambers to obtain a *global physics object*. The algorithm to obtain a global muon is based upon the Kalman-filter method [73]. This method provides a reconstruction efficiency of 99% within the acceptance of detectors. Since low p_{T} muons do not reach the muon chambers, this method works for $p_{\mathrm{T}}(\mu) \geq 5$ GeV.

Section 4.5

Electron reconstruction

In CMS, the reconstruction of electrons requires both the information of the deposited energy in the ECAL sub-detector and the reconstructed tracks in the tracker. The ECAL collects the energy of electron candidates using mainly the highest point of energy in crystals of the ECAL detector. The crystal with the highest energy is taken as a seed to search for electromagnetic activity in a mathematical cone defined in (η, ϕ) space. Additionally, the tracker matches all trajectories compatible with the energy deposition in the ECAL detector.

The efficiency of the electron reconstruction has been studied in Z^0 and J/ψ decays to electron-positron pairs. In general, the uncertainty is below 0.3% for a kinematic region of $5 \leq p_{\mathrm{T}}(e) \leq 100$ GeV. In addition, the threshold of the energy for the seed crystal is around $E_{T,seed}^{min} = 1$ GeV and the coverage of the algorithm is 5×1 cristals near the seed [74].

Section 4.6

The missing transverse energy ($p_{\mathbf{T}}^{miss}$)

In a particle accelerator, collisions occur along the beam axis. For that reason, the transverse momentum of bunches of protons is zero. This kinematic constraint is given by:

$$\sum_i \vec{p_\mathrm{T}}^i = 0, \tag{4.2}$$

This vectorial term must remain invariant after hard scattering processes. Nevertheless, after the pp collisions, there are particles that emerge that do not interact with the detector such as neutrinos or hypothetical neutral particles ($\tilde{\chi}_1^0$'s), which naturally create an imbalance of the transverse momentum. We can measure this imbalance using the conservation of the momentum in the transverse plane.

$$\begin{aligned} \sum_i \vec{p_\mathrm{T}}^i &= \sum_j \vec{p_\mathrm{T}}^j(visible) + \sum_k \vec{p_\mathrm{T}}^k(invisible) = 0 \\ &\sum_k \vec{p_\mathrm{T}}^k(invisible) = -\sum_j \vec{p_\mathrm{T}}^j(visible), \end{aligned} \tag{4.3}$$

where all the particles detected are referred to as *visible*, and *invisible* represents all particles not reconstructed by the detector. The missing transverse momentum ($\vec{p_\mathrm{T}}^{miss}$) is defined as:

$$\vec{p_\mathrm{T}}^{miss} = -\sum_j \vec{p_\mathrm{T}}^j(visible). \tag{4.4}$$

The magnitude of the missing transverse momentum is known as the missing transverse energy ($|\vec{p_\mathrm{T}}^{miss}|$). In CMS, the scale and resolution of the $\vec{p_\mathrm{T}}^{miss}$ depend strongly on the bunch crossing, the multi-scattering per bunch (pileup), and the algorithms that are used. There are three main algorithms to reconstruct the p_T^{miss}: PF$\vec{p_\mathrm{T}}^{miss}$, Calo$\vec{p_\mathrm{T}}^{miss}$, and TC$\vec{p_\mathrm{T}}^{miss}$. The PF$\vec{p_\mathrm{T}}^{miss}$ algorithm is fully based on the PF routine, which takes the information in each sub-detector to generate the missing transverse vector through Equation (4.4). The Calo$\vec{p_\mathrm{T}}^{miss}$ algorithm uses the information in the ECAL and HCAL detectors as well as the coordinates (η, ϕ), and p_T to generate the missing transverse vector. The TC$\vec{p_\mathrm{T}}^{miss}$ algorithm uses the information of the ECAL and HCAL detector as well as reconstructed tracks in the tracker to increase the efficiency of the $\vec{p_\mathrm{T}}^{miss}$. This efficiency depends on several factors such as energy fluctuations in the ECAL and HCAL and multi-scattering, in fact, the most important contribution to the systematic uncertainty is the pileup re-weighting that can achieve up to 95% of the total systematic uncertainties [75].

Section 4.7

Pileup re-weighting

At the LHC, the number of collisions per bunch crossing depends mainly on time for bunch crossing and the number of protons per bunch. For Run-II, the time scale of the bunch crossing is 25 ns, which generates an average of 25 collisions per crossing. The CMS detector can handle this amount of information. Nonetheless, the real conditions of the accelerator can generate more than 25 collisions. The effect of extra collision during a bunch crossing is known as pileup [76]. The pileup depends mainly on the instantaneous luminosity ($\mathcal{L}$), inelastic cross-sections (σ_i), and the time for bunch crossing ($t_{bx} = 25\ ns$). We can model the pileup effect taking the average number of collisions proportional to these variables.

$$\mu = \mathcal{L} \times \sigma_i \times t_{bx} \tag{4.5}$$

The probability of obtaining n pp collisions given a mean value μ follows a Poisson distribution [77].

$$P(n, \mu) = \frac{\mu^n}{n!} e^{-\mu} \tag{4.6}$$

Figure [4.7] shows the pileup measured by the CMS experiment during 2016 and 2017 at $\sqrt{s} = 13$ TeV [78]. Note that, the mean values are 27 and 37 respectively. Since there are extra vertices in pp collisions, the pileup has an important role in the reconstruction of jets.

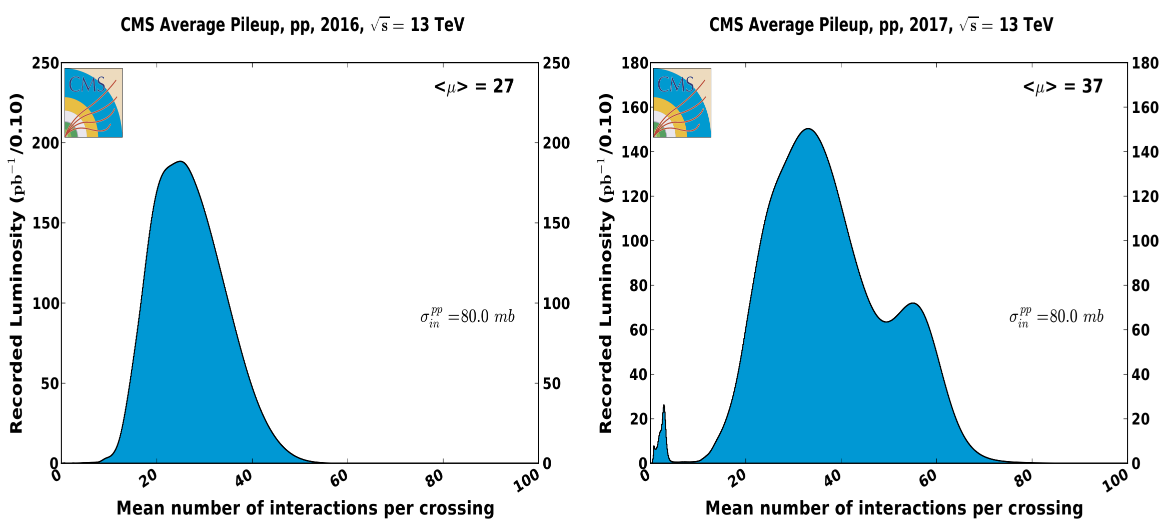

Figure 4.7: Pileup summaries the multiple scattering during the bunch crossing. These distributions are the pileup during 2016 (left) and 2017 (right) at $\sqrt{s} = 13$ TeV.

Since it is quite difficult to simulate the real bunch crossing in simulations, the MC must incorporate the pileup effects as accurate as possible. One option is to calculate the ratio between the pileup measured on data (N^{Data}) and the number of vertices (i) generated in the MC simulation (N_i^{MC}).

$$w_i^{pileup} = \frac{N_i^{Data}}{N_i^{MC}}. \tag{4.7}$$

In Equation (4.7), w_i^{pileup} represents a weight to correct the pileup in the MC simulations event by event. Pileup distributions for both, data and MC simulation must be normalized to unity.

Section 4.8

Definition of experimental variables

4.8.1 Cross section and luminosity

In particle physics, a cross-section (σ) represents the *probability of production* of a specific process, which is a function of the energy of center of mass $\sqrt{s}$. This quantity is related to the level of the interaction between the beam and the target, or between two beams. The fundamental unit used to measure the luminosity is the barn ($1b = 10^{-28}m^2$).

The luminosity is a parameter related to the accelerator and its performance; it can be defined as instantaneous or integrated luminosity. Instantaneous luminosity is defined as *the number of particles detected per unit of surface and unit of time.* To define luminosity in a particle collider, such as the LHC, we need to consider two beams, A and B, interacting in opposite directions. In the case of the LHC, each beam is composed of groups of protons (bunches) that have N_A and N_B particles. Each particle in beam A can scatter with any particle in beam B; then we might have N_B collisions per each particle in a bunch A. Since there are N_A protons in a bunch A we will have $N_A \times N_B$ possible interactions between two bunches. Therefore, the luminosity must be proportional to this quantity. Another important factor in the estimation of the luminosity is the frequency of collision of bunches. If the frequency of collision of protons increases, this is directly translated into a higher luminosity. Finally, other parameters such as the effective interaction area between two bunches $4\pi(\sigma_A \times \sigma_B)$ [79] and the angle of the collision between bunches, $F \leq 1$, are also important to determine an adequate expression for the luminosity in a particle collider [78]:

$$\mathcal{L} \sim \frac{N_A \times N_B \times f \times F}{4\pi(\sigma_A \times \sigma_B)}. \tag{4.8}$$

For example, some parameters for the calculation of the luminosity at the LHC are [8]:

$N_A \times N_B = (1.15 \times 10^{11})^2$, $f = 4 \times 10^7\ s^{-1}$, the bunch cross-section $S_{eff} = 4\pi(1.6 \times 10^{-5}) \times (1.6 \times 10^{-5})\ cm^2$ and $F \sim 0.96$. With these values, the luminosity is $\mathcal{L} \sim 10^{34}\ cm^{-2}s^{-1}$. On the other hand, the integrated luminosity is defined as the integral of $\mathcal{L}$ in a defined period of time.

$$L = \int \mathcal{L} dt \tag{4.9}$$

In particular, Figure [4.8] shows the integrated luminosity for 2016 and 2017, where the amount of data available for analyses is 36.1 and 41.3 fb^{-1} respectively [78]. Finally, the expected number of events associated with a production mechanism (N_i, Equation (4.10)) is related to its cross-section and the stored integrated luminosity. In general, N_i depends on the reconstruction efficiencies (ϵ_j) of the different objects that are implicated in the study.

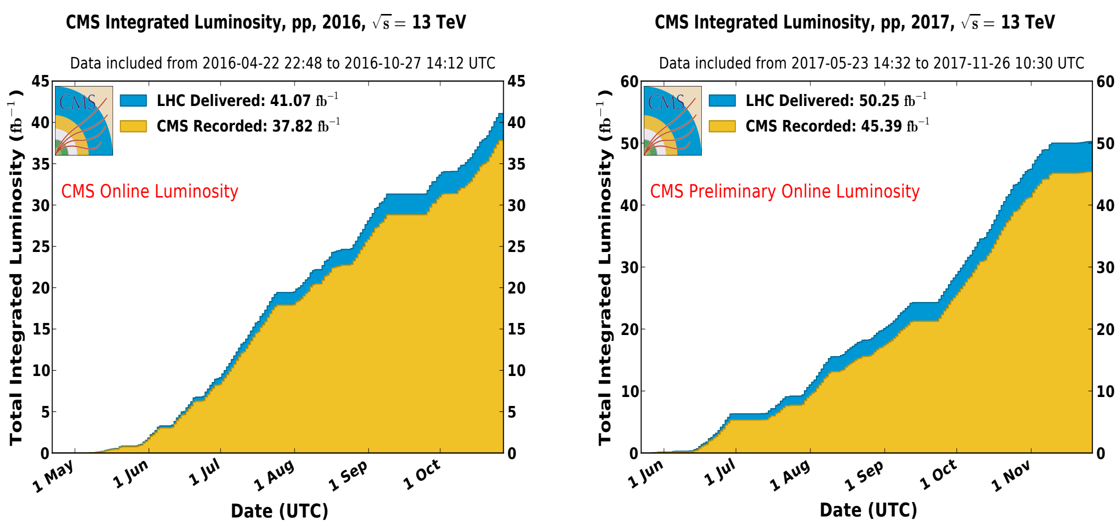

Figure 4.8**:** Integrated luminosity recorded by the CMS experiment during 2016 (left) and 2017 (right).

$$N_i = \sigma_i \times L \times \prod_{j}^{Phys-Obj} \epsilon_j \tag{4.10}$$

One of the most important parts of experimental analysis is the background estimation, which is described in Chapter 7. The estimation of each background in the search region (SR) is mainly related to the efficiency terms in Equation (4.10). For example, by including a τ_h candidate in the final state, the reconstruction efficiency must be estimated in a dedicated control region (CR) for such purpose.

4.8.2 Transverse mass

Consider the decay of a particle of mass M into two particles (called decay-products) such as: $W \to \ell\nu$, which is described by the Feynman diagram in Figure [4.9]. We can calculate the invariant mass associated with the W boson using the four-momentum of decay product.

$$\begin{aligned} P_i^\mu &= P_W^\alpha, & P_\mu P^\mu = M_W^2 \\ P_f^\nu &= P_\ell^\beta + P_{\bar{\nu}}^\gamma & P_\nu P^\nu = (E_\ell + E_{\bar{\nu}})^2 - (\vec{p}_\ell + \vec{p}_{\bar{\nu}})^2 \end{aligned} \tag{4.11}$$

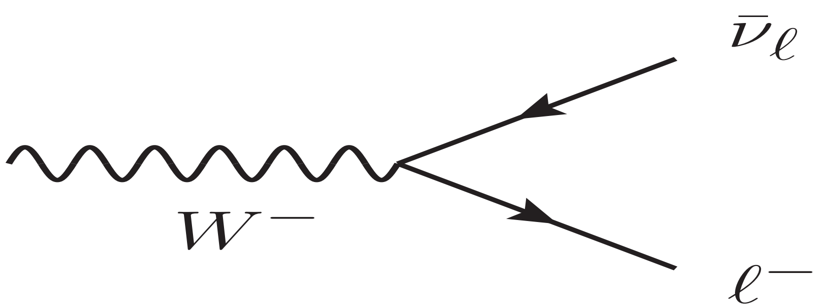

Figure 4.9**:** Description of the W boson decay to lepton ($\ell = e, \mu, \tau$) plus neutrino ($\nu = \nu_e, \nu_\mu, \nu_\tau$).

The conservation of the four-momentum leads to:

$$\begin{aligned} m_W^2 &= E_\ell^2 + E_{\bar{\nu}}^2 + 2E_\ell E_{\bar{\nu}} - |\vec{p}_\ell|^2 - |\vec{p}_{\bar{\nu}}|^2 - 2|\vec{p}_\ell||\vec{p}_{\bar{\nu}}| \cos\Delta\phi_{\ell,\bar{\nu}} \\ m_W^2 &= m_\ell^2 + m_{\bar{\nu}}^2 + 2[E_\ell E_{\bar{\nu}} - |\vec{p}_\ell||\vec{p}_{\bar{\nu}}| \cos\Delta\phi_{\ell,\bar{\nu}}]. \end{aligned} \tag{4.12}$$

Using the known relation between momentum and energy ($m_i^2 = E_i^2 - |\vec{p}_i|^2$), where $i = \ell, \bar{\nu}$. Equation (4.12) becomes [80, 81]:

$$m_W^2 = m_\ell^2 + m_{\bar{\nu}}^2 + (m_{\rm T})^2, \tag{4.13}$$

The *transverse mass* ($m_{\rm T}$) in the high energy limit $E_i \approx |\vec{p}_i|$, where $i = \ell, \bar{\nu}$ is defined as:

$$m_{\rm T}(\ell, p_{\rm T}^{miss}) = \sqrt{2p_{\rm T}(\ell)|\vec{p_{\rm T}}^{miss}|(1 - \cos\Delta\phi_{\ell,p_{\rm T}^{miss}})}, \tag{4.14}$$

where neutrino is taken as $p_{\rm T}^{miss}$. The $m_{\rm T}$ is an important distribution of the experimental analysis reported in this dissertation.

4.8.3 Dijet mass

In some experimental analyses the invariant mass of a system of two jets is interesting, such as SUSY searches through Vector Boson Fusion (VBF) production [82], in which the topology of the event leads to a set of two jets with a high pseudorapidity gap ($|\Delta\eta_{ij}| > 3.0$). In those scenarios, the invariant mass of the two jets system has the following approximation:

$$\begin{aligned} m^2_{j_1,j_2} &= (E_{j_1} + E_{j_2})^2 - (p_{j_1} + p_{j_2})^2 \\ &= E_1^2 + E_2^2 + 2E_1E_2 - (p_1^2 + p_2^2 + 2\mathbf{p}_1 \cdot \mathbf{p}_2) \\ &= m_1^2 + m_2^2 + 2(E^1E^2 - \mathbf{p}_1 \cdot \mathbf{p}_2) \end{aligned} \tag{4.15}$$

To calculate the dot product between the three-momentums, we use the CMS coordinate system, in which the three-momentum is parametrized as: $\vec{p} = (p_{\mathrm{T}}, \eta, \phi)$, where $p^2 - p_{\mathrm{T}}^2 = p_z^2$, and $p = p_{\mathrm{T}} \cosh(\eta)$. Figure [4.10] describes the geometry of the three-momentum.

$$\begin{aligned} \vec{p} &= [p_x, p_y, p_z] \\ &= [p_{\mathrm{T}} \cos(\phi), p_{\mathrm{T}} \sin(\phi), p_{\mathrm{T}} \sinh(\eta)] \end{aligned} \tag{4.16}$$

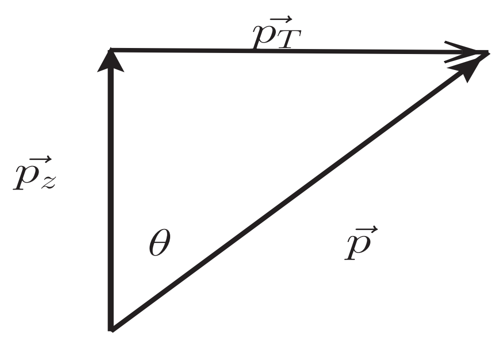

Figure 4.10: Geometry of the three-momentum using the CMS coordinate system.

η is related to the θ coordinate as follows:

$$\begin{aligned} \eta &= -ln(\tan\theta/2) \\ \cosh\eta &= \frac{e^{-ln(\tan\theta/2)} + e^{ln(\tan\theta/2)}}{2} \\ &= \frac{1 + \tan^2\theta/2}{2\tan\theta/2} \\ &= \frac{\sec^2\theta/2}{2\tan\theta/2} = 1/\operatorname{sen}\theta \end{aligned} \tag{4.17}$$

By using the hyperbolic functions, the invariant mass is therefore:

$$\begin{aligned} m^2_{j_1,j_2} &= 2(E^1E^2 - \mathbf{p}_1 \cdot \mathbf{p}_2) \\ &= 2(E^1E^2 - (p^1_{\mathrm{T}}p^2_{\mathrm{T}}\cos(\phi_1)\cos(\phi_2) + p^1_{\mathrm{T}}p^2_{\mathrm{T}}\sin(\phi_1)\sin(\phi_2) + p^1_{\mathrm{T}}p^2_{\mathrm{T}}\sinh(\eta_1)\sinh(\eta_2))) \\ &= 2(E^1E^2 - p^1_{\mathrm{T}}p^2_{\mathrm{T}}(\cos(\phi_1 - \phi_2) + \sinh(\eta_1)\sinh(\eta_2)) \end{aligned} \tag{4.18}$$

In general, the transverse component of energy is $E = \frac{E_{\mathrm{T}}}{\sin(\theta)} = E_{\mathrm{T}}\cosh(\eta)$. Hence:

$$m^2_{j_1,j_2} = 2(E^1_{\mathrm{T}}E^2_{\mathrm{T}}\cosh(\eta_1)\cosh(\eta_2) - p^1_{\mathrm{T}}p^2_{\mathrm{T}}(\cos(\phi_1 - \phi_2) + \sinh(\eta_1)\sinh(\eta_2))) \tag{4.19}$$

The *invariant mass* (m_{j_1,j_2}) in the high energy limit $E_{\mathrm{T}} \approx p_{\mathrm{T}}$ is:

$$m^2_{j_1,j_2} = 2p^1_{\mathrm{T}}p^2_{\mathrm{T}}(\cosh(\eta_1 - \eta_2) - \cos(\phi_1 - \phi_2)). \tag{4.20}$$

For VBF searches, since $0 < \cos(\phi_1 - \phi_2) < 1$ the invariant mass becomes:

$$m_{j_1,j_2} \approx \sqrt{2p^1_{\mathrm{T}}p^2_{\mathrm{T}}(\cosh(\eta_1 - \eta_2))} \tag{4.21}$$

CHAPTER 5

State of art of SUSY searches

The large plethora of experimental searches conducted until now have certainly contributed to exclude several SUSY scenarios and values of the phase space through the last 30 years. Some relevant studies are listed below:

- Search with large missing transverse energy at CERN in 1987 [83].
  - Experiment: UA1 (e^+e^- collisions).
  - Energy: $\sqrt{s} = 630$ GeV, data: 715 nb^{-1}.
  - $m(\tilde{q}) < 45$ GeV,
  - $m(\tilde{g}) < 53$ GeV excluded.
- Search for squark and gluino production at CERN in 1989 [84].
  - Experiment: UA2 (e^+e^- collisions).
  - Energy: $\sqrt{s} = 630$ GeV, data: 7.4 pb^{-1}.
  - $m(\tilde{q}) < 74$ GeV,
  - $m(\tilde{g}) < 79$ GeV excluded.
- Limits on masses of SUSY particles at Tevatron in 1990 [85].
  - Experiment: CDF ($p\bar{p}$ collisions).
  - Energy: $\sqrt{s} = 1.8$ TeV, data: 7.4 pb^{-1}.
  - $m(\tilde{g}) < 73$ GeV excluded.
- Limits on masses of SUSY particles at LEP between 1995-2000 [86].
  - Experiment: LEP (DELPHI, ALEPH, OPAL, L3) (e^+e^- collisions).
  - Energy: $\sqrt{s} = [130, 208]$ GeV, data: 2×10^3 pb^{-1}.
  - $m(\tilde{\chi}_1^{\pm}) < 103.5$ GeV,
  - $m(\tilde{\chi}_1^{\pm}) < 70$ GeV,
  - $m(\tilde{\mu}) < 100$ GeV excluded.

- Limits on masses of SUSY particles at Tevatron in 2012 [87].
  - Experiment: CDF and D0 ($p\bar{p}$ collisions).
  - Energy: $\sqrt{s} = 1.8$ TeV, data: 5.2 fb^{-1}.
  - $m(\tilde{b}) > 247$ GeV for massless scalar neutrino,
  - $m(\tilde{\chi}^0) > 100$ GeV for $160 < m(\tilde{b}) < 200$ GeV excluded.
- Limits on masses of SUSY particles at LHC in 2012 [88].
  - Experiment: CMS (pp collisions).
  - Energy: $\sqrt{s} = 8$ TeV, data: 18.9 fb^{-1}.
  - $m(\tilde{t}) < 755$ GeV for $\tilde{\chi}_1^0$ mass up to 200 GeV excluded.
- SUSY searches for electroweak production of charginos, and neutralinos at LHC in 2014 [89].
  - Experiment: CMS (pp collisions).
  - Energy: $\sqrt{s} = 8$ TeV, data: 19.5 fb^{-1}.
  - $m(\tilde{\chi}_1^{\pm})$, $m(\tilde{\chi}_1^0)$ up to 720 GeV and sleptons up to 260 GeV are excluded.

Section 5.1

Current SUSY searches at the LHC

SUSY motivates experimental searches, which can be divided into two sectors: color and electroweak searches. The color sector, describes the possible SUSY production of gluinos and squarks through the strong interaction [90]. The LHC provides a suitable environment dominated by high hadronic production, which is adequate to study the color sector. On the other hand, the electroweak production of electrowikinos or sleptons is significantly smaller than those produced by strong processes [89]. Since the production of the electrowikinos or sleptons has a cross-section that is smaller than strong processes, the sensitivity of those channels could be limited at the LHC. Nevertheless, backgrounds that come from SM events are generally smaller in searches targeting electroweak SUSY production. Thus, electroweak searches are competitive and complementary to color searches at the LHC. In addition, no research carried out by CMS and ATLAS collaborations has been successful so far. A large part of the SUSY phase space has been excluded at the LHC, including a variety of final states with leptons, photons and jets. The latest results (2018) of CMS and ATLAS collaborations are described in the following sub-sections:

5.1.1 Results in the color sector

Figure [5.1] shows the upper limits of the gluino mass, which decays into top quarks and the LSP. This limit was performed by the CMS experiment in 2018 [91]. Gluino masses are excluded up to 1825 GeV. On the other hand, Figure [5.2] shows the upper limits on the gluino mass performed by the ATLAS collaboration in 2018 [92]. Masses are excluded up to 2000 GeV for low values of the mass of the LSP. In other scenarios, the LSP masses are excluded up to 1000 GeV for gluino masses of ≈ 1400 GeV.

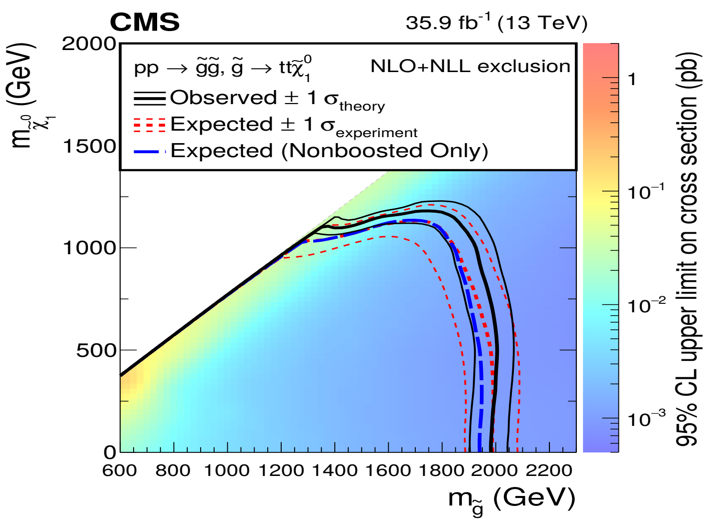

Figure 5.1: Upper limits on the gluino mass performed by the CMS experiment in 2018.

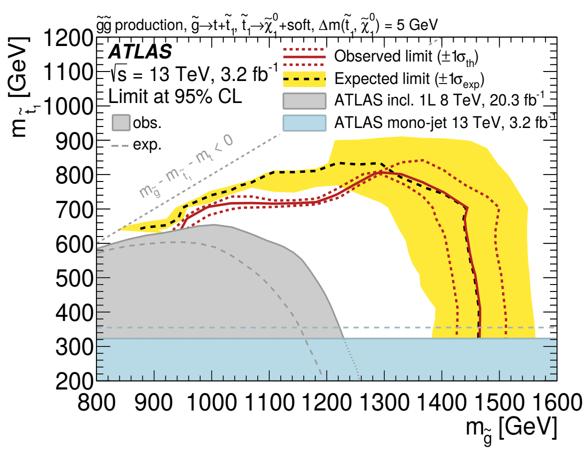

Figure 5.2: Upper limits on the gluino mass performed by the ATLAS experiment in 2018.

5.1.2 Results in the electroweak sector

Figure [5.3] shows upper limits on the $\tilde{\chi}_1^{\pm} - \tilde{\chi}_1^0$ pair production, which was performed by the CMS experiment in 2018 [93]. Chargino masses are excluded up to 710 GeV for $\tilde{\chi}_1^{\pm} - \tilde{\chi}_1^0$ production, and chargino masses are excluded up to 630 GeV for chargino pair production. Figure [5.4] shows upper limits of $\tilde{\chi}_1^{\pm} - \tilde{\chi}_1^0$ pair production carried out by the ATLAS experiment in 2018 [94]. Chargino masses are excluded up to 760 GeV in scenarios where the $\tilde{\chi}_1^{\pm}$ is produced with an associated $\tilde{\chi}_1^0$, and chargino masses are excluded up to 630 GeV in $\tilde{\chi}_1^{\pm}$ pair production scenarios.

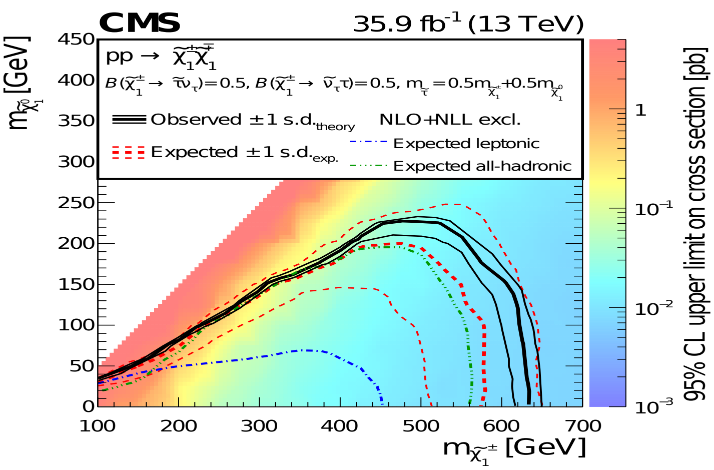

Figure 5.3: Upper limits on the $\tilde{\chi}_1^{\pm} - \tilde{\chi}_1^0$ production including sleptons in the final state performed by the CMS experiment in 2018.

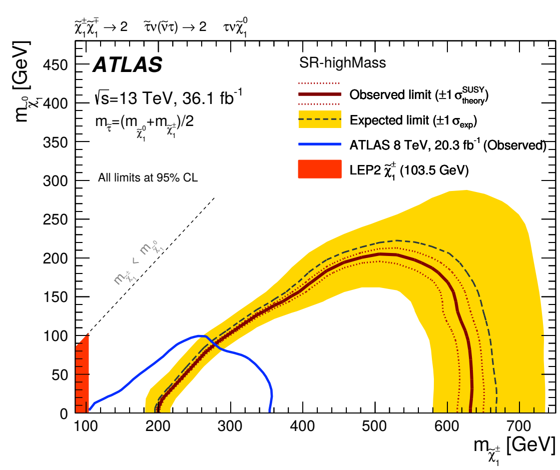

Figure 5.4: Upper limits on the $\tilde{\chi}_1^{\pm}$ pair production performed by the ATLAS experiment in 2018.

As a summary, Figure [5.5] shows the timeline in years for the relevant variables associated with different SUSY searches as well as the experiment where they were performed.

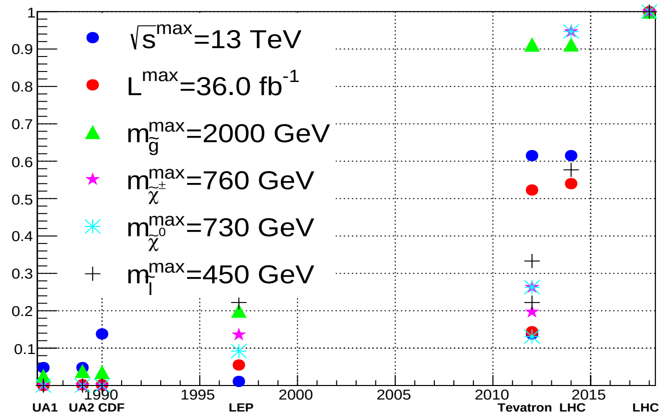

Figure 5.5: Timeline for the relevant SUSY searches, for different experiments. The normalization factor is based on the latest value achieved for each quantity. The fastest growing is the exclusion of the gluino mass.

In order to compare the rate of change of these quantities, a normalization factor consistent with 1 for the maximum values was applied. For instance, the higher excluded mass of the gaugino (<2000 GeV) would be one (1.0) for 2018 on the plot. Thereby, the value excluded by UA1 would be 53/2000 $\approx$ 0.026. By consulting the plot, our ability to exclude values in the phase space depends on the energy of the collision and the amount of data collected (exponentially). For 2018, the CMS experiment has collected around $\approx 10^6$ more data than in the UA1 experiment. Similarly, the highest rate of exclusion in that period is the gluino mass $m(\tilde{g})$, where three orders of magnitude have been excluded in 30 years.

Section 5.2

Compressed mass spectra scenarios

The relic dark matter density ($\Omega_{DM}h^2$) is the remanent amount of DM today. The relic density is related to production mechanisms given by the specific model in particle physics. There are thermal [95,96] and non-thermal [97,98] [99] models which could explain the observed relic DM density. In addition, the relic abundance depends on the couplings and the mass of particles as well [100]. By including some hypotheses, we can predict the relic abundance in some interesting scenarios such as non-thermal production of DM axions, which have physical properties defined by the Pieccei-Quien symmetry breaking [97], or Weakly Interacting

Massive Particles (WIMP) produced in thermal equilibrium. In fact, the thermal production mechanisms have an interesting description in SUSY models as well as a deep relation with the relic abundance [101, 102]. We focus on the second scenario, which has additional motivation for this research. In thermal DM models with SUSY, the DM abundance is strongly connected with scenarios where the mass gap between the LSP and the specific sfermion is small. By consulting the experimental exclusion plots, Figures [5.3], and [5.4], the very compressed mass region has been excluded yet due to low sensitivity in that phase space. Briefly, we show the connection between the DM candidate and the observed relic abundance, which currently has the value [100]:

$$\Omega_{DM} h^2 = 0.1186 \pm 0.002. \tag{5.1}$$

In thermal equilibrium, the number density is described by the Boltzmann equation [100]. First of all, consider the annihilation process of N supersymmetric particles $\chi_i (i = 1, ..., N)$ with mass m_i. These processes are carried out under the R-parity conservation assumption. On the other hand, the annihilation of the SM particles that results in the production of SUSY particles is possible as well. Then, the associated Boltzmann equation is:

$$\frac{dn_{\chi_i}}{dt} = -3Hn_{\chi_i} - \sum_{j=1}^{N} n_i n_j < \sigma_{ij} v_{ij} > (\chi_i \chi_j \to X^{SM}) + n_X^2 < \sigma_{ij} v_{ij} > (X^{SM} \to \chi_i \chi_j), \tag{5.2}$$

where H is the Hubble constant ($H_0 = 73 \pm 3$ km s^{-1} Mpc^{-1}), σ_{ij} is referred to the annihilation cross-section, and v_{ij} is the relative velocity. The first term on the right side of Equation (5.2), represents the change on the density number due to the expansion of the universe. The other terms are associated to the annihilation and creation of supersymmetric particles. Equation (5.3) with $n = \sum_i^N$ becomes:

$$\frac{dn}{dt} = -3Hn + - < \sigma v > (n^2 - (n^{eq})^2) \tag{5.3}$$

where n^{eq} follows the Maxwell-Boltzman distribution [102]:

$$n^{eq} = g \left(\frac{mT}{2\pi} \right)^{3/2} e^{-m/T} \tag{5.4}$$

In fact, when the temperature of the universe drops the number density and the velocity of particles drops as well. This scenario is known as Cold Dark Matter (CDM), which is described by non-relativistic thermal equilibrium. Following the timeline in the evolution of the universe, there is a point called *freeze-out* where the abundance remains constant, after this point the system is non-thermal equilibrium. After the freeze-out the relic abundance can be expressed as [100]:

$$\Omega_\chi h^2 = \frac{h^2 m_\chi s_0 Y_0}{\rho_{crit}}, \qquad \rho_{crit} = \frac{3H^2}{8\pi G}, \tag{5.5}$$

which is strongly depending on the mass of the supersymmetric dark matter candidate. In Equation (5.5), s_0 represents the the entropy of the universe today, and Y_0 comes from the integration of the Boltzmann equation (Y=n/s). In addition, if the typical annihilation cross-section falls in the electroweak scale, it could be reached by the LHC. This is a great opportunity to explore possible SUSY production scenarios, where the LSP is compatible with cosmological constraints. However, taking into account only the $\tilde{\chi}_1^0 - \tilde{\tau}$ annihilation processes the predicted relic abundance does not agree with that predicted by cosmology. In order to solve this issue, coannihilation terms are included [100], which involves mixing of different particles (e.g, $\tilde{\tau}\tilde{\chi}_1^0 \to X^{SM}$). Figure [5.6] taken from [95], shows the $\tilde{\chi}_1^0 - \tilde{\tau}$ mass difference as function of $\tilde{\chi}_1^{\pm}$ masses which give a relic DM density consistent with the predicted cosmological value. Note that, in order to get a consistent relic density the $\tilde{\chi}_1^0 - \tilde{\tau}$ mass difference has to be small, which is challenging to prove experimentally.

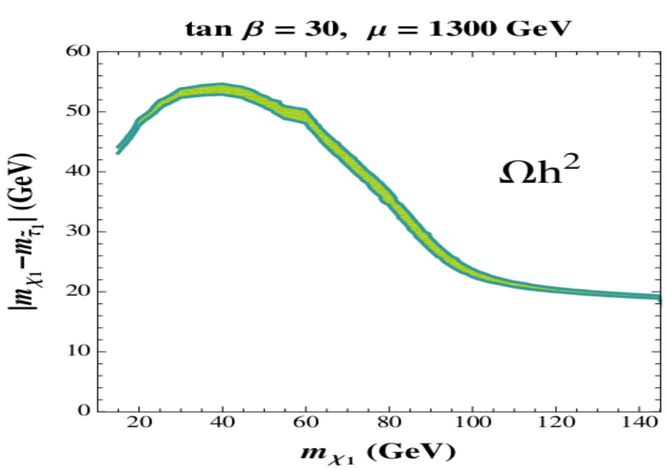

Figure 5.6: Difference between the LSP ($\tilde{\chi}_1^0$) and the $\tilde{\tau}$ as a function of the neutralino mass. To predict a relic abundance that is consistent with the observed value, the $\Delta m(\tilde{\chi}_1^0, \tilde{\tau})$ must be small. This kinematic constraint is known as compressed mass spectra scenarios.

In Chapter 6, we present the feasibility study at phenomenological level, which includes a hard jet tagged as Initial State Radiation (ISR), a large p_{T}^{miss}, and a soft τ_h in the final state. Since the interesting connection between particle physics and cosmology, we explore compressed mass spectra scenarios given by $\Delta m(\tilde{\chi}_1^0, \tilde{\tau}) = 50$ GeV.

CHAPTER 6

Probing the stau-neutralino coannihilation region with a soft tau lepton and an ISR jet

Section 6.1

Motivation for the $\tilde{\tau} - \tilde{\chi}_1^0$ coannihilation region

According to experimental results from the Planck collaboration [103, 104], the measured relic dark matter density in the universe is $\Omega_{DM} h^2 = 0.1186 \pm 0.002$, as shown in Equation (5.1), obtained under the hypothesis of ΛCDM universe. To obtain a consistent result from the theoretical perspective, using SUSY, some models include the so called $\tilde{\tau} - \tilde{\chi}_1^0$ coannihilation (CA) mechanism [95, 105, 106]. In models considering CA, the mass difference (gap) between the $\tilde{\tau}$ and the $\tilde{\chi}_1^0$ must be small (50 GeV at most). Experimentally, the region that satisfies the CA requirement is referred to as compressed mass spectra. At the LHC, the production of $\tilde{\tau}$ can occur directly or through cascade decays from charginos $\tilde{\chi}_i^{\pm}$ with $i = 1, 2$, and neutralinos $\tilde{\chi}_j^0$, with $j = 1, 2, 3, 4$. Table [6.1] summarizes the possible production mechanisms of scalar τ candidates, assuming Drell-Yan processes.

To explore the CA region with τ leptons at the LHC, a new experimental technique was proposed through a phenomenological study [107]. The logic behind the experimental technique was based upon the following experimental facts. Because CA requires a $\Delta m(\tilde{\tau}, \tilde{\chi}_1^0) < 50$ GeV, the momentum of the τ leptons in the detector is expected to be small, which implies that these particles might be lost during the reconstruction process in the detector. In addition, the associated $\tilde{\chi}_1^0$ particles can be produced in opposite directions which will not allow the detection of sizable p_{T}^{miss}. Finally, hadronic decays of τ leptons account for 64% of possible final states. Considering these experimental constrains the study proposed an experimental search at the LHC with final states with exactly one low momentum hadronic τ candidate, one central jet from initial state radiation (ISR) with high transverse momentum, and large p_{T}^{miss}. The presence of the ISR jet creates a recoil effect that allows to generate a kinematic boost to the event topology by creating a natural difference in the direction of the associated $\tilde{\chi}_1^0$'s in the event. This allows the indirect detection of $\tilde{\chi}_1^0$'s in the event through large measured values of p_{T}^{miss}. Figure [6.2] shows a sketch of the effect of the ISR jet in the event topology.

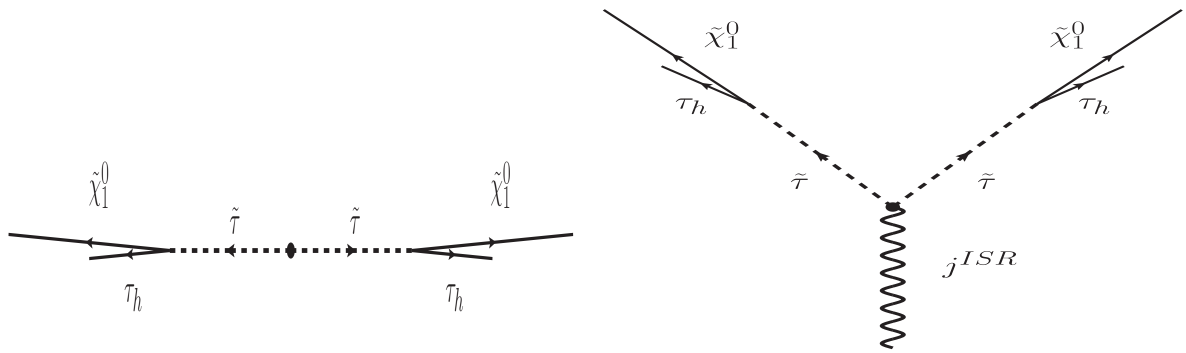

Figure 6.1: Electroweak SUSY production of $\tilde{\tau}$ without ISR jet (left), and including the ISR jet a p_{T}^{miss} due to the neutralinos is generated.

Since the outcoming particles from each $\tilde{\tau}$ decay are collimated in the original boost direction (Figure [6.1] left) they will have on average opposite directions (back-to-back). Therefore the presence of $\tilde{\chi}_1^0$ candidates will not be detected as p_{T}^{miss}. Nevertheless, when an ISR jet is required in the event topology the ISR boost changes the back-to-back direction of the associated $\tilde{\tau}$ products allowing the indirect detection of neutralinos as large p_{T}^{miss} (Figure [6.1] right). Mathematically, if we estimate the conservation of momentum we expect:

$$\begin{aligned} \vec{p_{\mathrm{T}}}^{i} &= \vec{p_{\mathrm{T}}}^{f} \\ 0 &= \vec{p_{\mathrm{T}}}(\tau^{+}) + \vec{p_{\mathrm{T}}}(\tau^{-}) + \vec{p_{\mathrm{T}}}(\tilde{\chi}_1^0) + \vec{p_{\mathrm{T}}}(\tilde{\chi}_1^0) \end{aligned} \tag{6.1}$$

As mentioned before, if we include an ISR jet in the compressed region ($\vec{p_{\mathrm{T}}}(\tilde{\chi}_1^0) >> \vec{p_{\mathrm{T}}}(\tau)$) we get:

$$\begin{aligned} \vec{p_{\mathrm{T}}}(\mathrm{j}^{ISR}) &= \vec{p_{\mathrm{T}}}(\tau^{+}) + \vec{p_{\mathrm{T}}}(\tau^{-}) + \vec{p_{\mathrm{T}}}(\tilde{\chi}_1^0) + \vec{p_{\mathrm{T}}}(\tilde{\chi}_1^0) \\ \vec{p_{\mathrm{T}}}(\mathrm{j}^{ISR}) &= \vec{p_{\mathrm{T}}}(\tilde{\chi}_1^0) + \vec{p_{\mathrm{T}}}(\tilde{\chi}_1^0)'. \end{aligned} \tag{6.2}$$

Evidently, this kinematic behavior could lead us to explore the hidden SUSY sector in a possible experimental scenario. To achieve that purpose, we characterize the simulations of the hypothetical signal as well as the non-reducible background of this study.

Section 6.2

Signal and main background processes

In general, $\tilde{\tau}$'s could be produced directly from interaction between two SM particles or indirectly from cascade decays of charginos $\tilde{\chi}_i^{\pm}$, with $i = 1, 2$, and neutralinos $\tilde{\chi}_i^0$, with $j = 1, 2, 3, 4$. These decay channels are summarized in Table [6.1].

Table 6.1: Different decay channels for hypothetical $\tilde{\tau}$ inclusive production.

Channel	Time arrow $\rightarrow$		Fraction of σ_{T}
Direct	$\tilde{\tau}^{\pm}\tilde{\tau}^{\mp}j$	$\tau^{\pm}\tau^{\pm}\tilde{\chi}_1^0\tilde{\chi}_1^0 j$	$\sim 2\%$
Indirect	$\tilde{\chi}_2^0\tilde{\chi}_2^0 j \rightarrow \tilde{\tau}^{\pm}\tau^{\pm}\tilde{\tau}^{\mp}\tau^{\mp}j$	$\tau^{\pm}\tau^{\mp}\tau^{\pm}\tau^{\mp}\tilde{\chi}_1^0\tilde{\chi}_1^0 j$	$\vdots$
	$\tilde{\chi}_1^{+}\tilde{\chi}_1^{-} j \rightarrow \tilde{\tau}^{+}\tilde{\tau}^{-}\nu\nu j$	$\tau^{\pm}\tau^{\pm}\tilde{\chi}_1^0\tilde{\chi}_1^0\nu\nu j$	$\sim 33\%$
	$\tilde{\chi}_1^{\pm}\tilde{\chi}_2^0 j \rightarrow \tilde{\tau}^{\pm}\tilde{\tau}^{\mp}\tilde{\tau}^{\pm}\nu j$	$\tau^{\pm}\tau^{\mp}\tau^{\pm}\tilde{\chi}_1^0\tilde{\chi}_1^0\nu j$	$\sim 64.4\%$

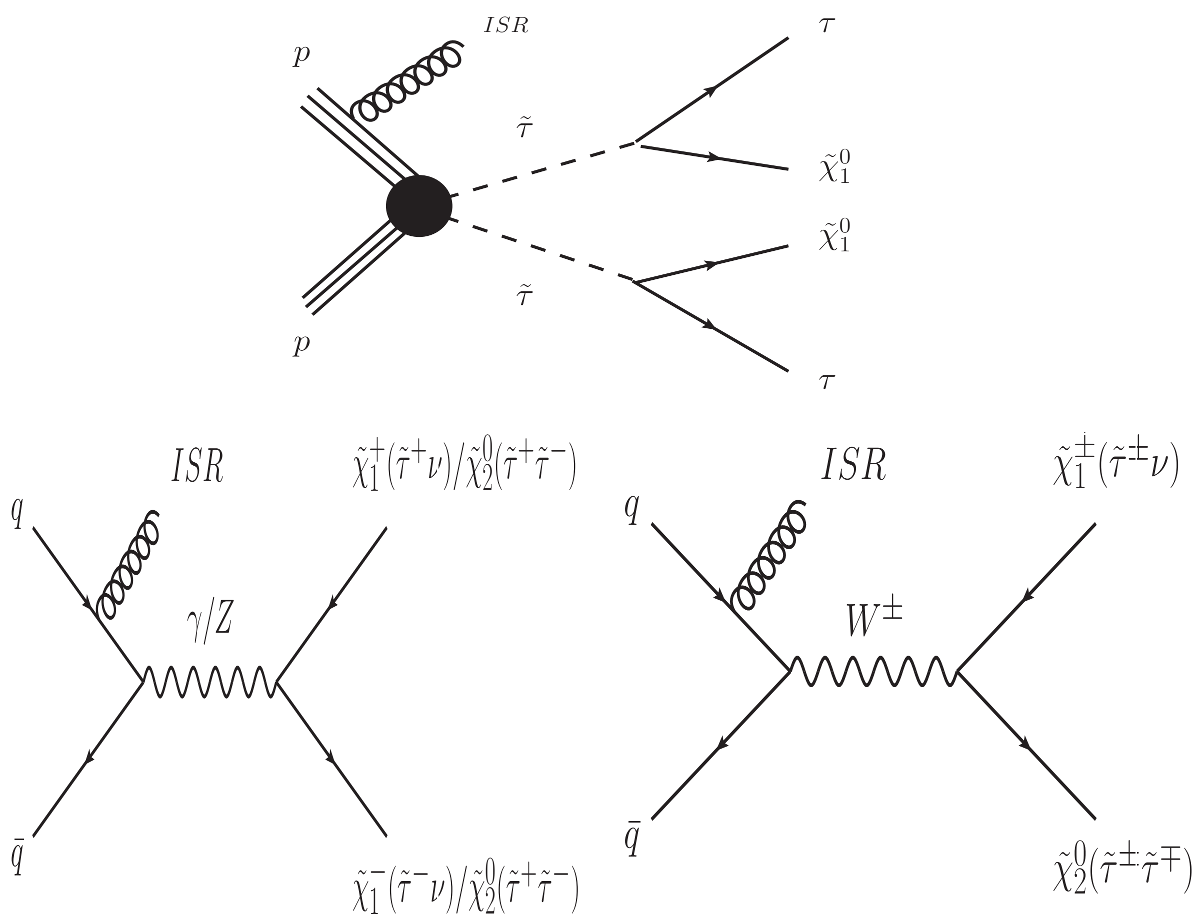

Figure 6.2: Direct $\tilde{\tau}$ channel decay plus ISR jet (top). Chargino/neutralino pairs production mediated by γ/Z^0 bosons plus ISR jet (bottom:left), and $\tilde{\chi}_1^{\pm}\tilde{\chi}_2^0$ production mediated by $W^{\pm}$ boson plus ISR jet (bottom:right).

Figure [6.2] shows Feynman diagrams for the hypothetical production of signal events mediated by γ/Z^0 (left) and $W^{\pm}$ (right) bosons. The jet drawn in the diagram corresponds to an emission before the hard scattering (ISR). As explained before, the LHC collides protons at a center of mass energy of $\sqrt{s} = 13$ TeV. An ISR jet is identified as a spontaneous radioactive emission of a gluon or quark, which comes from the partons associated with the accelerated protons before the hard collisions between bunches occur.

The production of signal and SM background processes was generated using the accepted high energy packages (`Mad-Graph v2.2.3`, `Pythia v6.146`, `Delphes v3.3.2`) described in appendix B. For each process, the physical parameter connected with production probability is the cross-section, which is explained in Chapter 4. The corresponding cross-section can be found using the simulation packages such as: `Mad-Graph` and `Pythia`. `Mad-Graph` software emulates the production of a hard process between partons, whereas `Pythia` handles the fragmentation process between quarks and gluons, which are related to the strong interaction. Both outputs are different between each other, one of the reason is that `Pythia` generates additional jets in order to reproduce the real hadronic environment, These jets must be matched with the jets produced in `Mad-Graph`. To generate physical results between these two packages an algorithm referred to as MLM is implemented (appendix B) [108]. This algorithm computes an efficiency corresponding to the matching process, which is needed to obtain the correct values of the cross-sections. Basically, this algorithm minimizes the distance between partons at `Mad-Graph` level and optimizes the minimum clustering energy required by `Pythia`. On the other hand, leptons are required to have at least $p_{\mathrm{T}}(\ell) > 10$ GeV and $|\eta(\ell)| < 2.5$, whereas, jets within $p_{\mathrm{T}}(\mathrm{j}) > 20$ GeV in the total pseudorapidity coverage are selected.

Signal samples are produced in the scenario where the R-parity is conserved. Additionally, we have direct and indirect $\tilde{\tau}$ pairs production, in the indirect case, there are cascades of $\tilde{\chi}^{\pm}$ and $\tilde{\chi}^0_2$. Since the composition of these states is still unknown, we have the following benchmark: first, $\tilde{\chi}^{\pm}$ and $\tilde{\chi}^0_2$ are wino-like, whereas, $\tilde{\chi}^0_1$ is mostly bino. Second, the mass gap between $\tilde{\tau}$ and $\tilde{\chi}^0_1$ is less than 50 GeV, which is motivated by the coannihilation region. Finally, $m(\tilde{\tau}) = 0.5m(\tilde{\chi}^{\pm}_1) + 0.5m(\tilde{\chi}^0_1)$ [107]. The syntax in `Mad-Graph` for signal production is given by:

```
import model mssm
define l+ = e+ mu+ ta+
define l- = e- mu- ta-
generate p p > ta2+ ta2- j , (ta2+ > ta+  n1), (ta2- > ta- n1)   QCD=1   @1
```

The cross-sections corresponding to the signal are summarized in Table [6.2].

On the other hand, all processes with a similar signature to the signal events are known as *Background* of the SM. The understanding of the backgrounds in an experimental study

Table 6.2: Signal cross sections (σ_s).

Signal Point	SUSY masses [GeV]	σ [pb]
1	$m(\tilde{\chi}_1^{\pm}) = 100$, $m(\tilde{\tau}) = 75$, $m(\tilde{\chi}_1^0) = 50$	10.80 ± 0.01
2	$m(\tilde{\chi}_1^{\pm}) = 100$, $m(\tilde{\tau}) = 80$, $m(\tilde{\chi}_1^0) = 60$	10.76 ± 0.01
3	$m(\tilde{\chi}_1^{\pm}) = 100$, $m(\tilde{\tau}) = 85$, $m(\tilde{\chi}_1^0) = 70$	10.73 ± 0.01
4	$m(\tilde{\chi}_1^{\pm}) = 100$, $m(\tilde{\tau}) = 90$, $m(\tilde{\chi}_1^0) = 80$	10.71 ± 0.01
5	$m(\tilde{\chi}_1^{\pm}) = 100$, $m(\tilde{\tau}) = 95$, $m(\tilde{\chi}_1^0) = 90$	10.70 ± 0.01
6	$m(\tilde{\chi}_1^{\pm}) = 200$, $m(\tilde{\tau}) = 175$, $m(\tilde{\chi}_1^0) = 150$	1.331 ± 0.001
7	$m(\tilde{\chi}_1^{\pm}) = 200$, $m(\tilde{\tau}) = 180$, $m(\tilde{\chi}_1^0) = 160$	1.330 ± 0.001
8	$m(\tilde{\chi}_1^{\pm}) = 200$, $m(\tilde{\tau}) = 185$, $m(\tilde{\chi}_1^0) = 170$	1.328 ± 0.001
9	$m(\tilde{\chi}_1^{\pm}) = 200$, $m(\tilde{\tau}) = 190$, $m(\tilde{\chi}_1^0) = 180$	1.327 ± 0.001
10	$m(\tilde{\chi}_1^{\pm}) = 300$, $m(\tilde{\tau}) = 275$, $m(\tilde{\chi}_1^0) = 250$	0.4443 ± 0.0001
11	$m(\tilde{\chi}_1^{\pm}) = 300$, $m(\tilde{\tau}) = 280$, $m(\tilde{\chi}_1^0) = 260$	0.4436 ± 0.0001
12	$m(\tilde{\chi}_1^{\pm}) = 300$, $m(\tilde{\tau}) = 285$, $m(\tilde{\chi}_1^0) = 270$	0.4431 ± 0.0001
13	$m(\tilde{\chi}_1^{\pm}) = 300$, $m(\tilde{\tau}) = 290$, $m(\tilde{\chi}_1^0) = 280$	0.4425 ± 0.0001

is fundamental. The most important sources of background in this study are $W + jets$ and $Z + jets$.

6.2.1 $W + jets$ background

This background is characterized by the production of a W boson, which can decay into a lepton and a neutrino or into a quark-anti-quark pair, plus associated ISR or FSR jets. The W boson can decay [8] 64% of the time into a quark anti-quark pair ($W \to qq'$). In this case, we have jets and p_{T}^{miss}. The p_{T}^{miss} in hadronic decays of W bosons results from detector or reconstruction effects and not from undetected particles. Leptonic decays constitute the 34% of the W branching fraction: $W^+ \to \ell^+\nu_\ell$ and $W^- \to \ell^-\bar{\nu}_\ell$ with $\ell = e^-, \mu^-, \tau^-$. The p_{T}^{miss} in this case is related with the undetected neutrinos (ν_ℓ). A Feynman diagram representing the production of a $W + jets$ process, with a subsequent leptonic decay, is presented in the Figure [6.3].

The syntax in `Mad-Graph` for the $W + jets$ production is given by:

```
import model sm
define w = w+ w-
generate p p > w         @0
add process p p > w j    @1
add process p p > w j j  @2
```

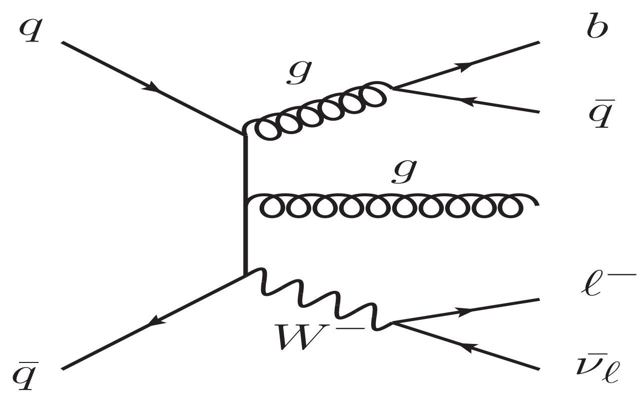

Figure 6.3**:** Feynman diagram associated with $W + jets$ production.

6.2.2 $Z + jets$ background

Drell-yan is a SM process due for the annihilation of quarks in a high energy collisions, creating a virtual photon (γ) or a Z boson. The dominant branching fractions of the Z boson are: 10% decay to leptons ($Z \to \ell^+\ell^-$ with $\ell = e^-, \mu^-, \tau^-$), 20% to neutrinos ($Z \to \nu_\ell\bar{\nu}_\ell$), and the remaining 70% decays to a quark-anti-quark pair ($Z \to q\bar{q}$) [8]. Figure [6.4], shows the corresponding Feynman diagram for the production and decay of a Z boson (γ) into a pair of oppositely charged leptons.

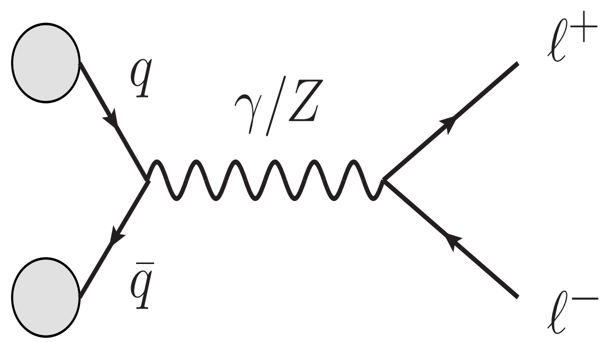

Figure 6.4**:** Feynman diagram associated with $Z + jets$ production.

The syntax in `Mad-Graph` for the $Z + jets$ production is given by:

```
import model sm
define pr = p b b~
define l+ = e+ mu+ ta+
define l- = e- mu- ta-
```

```
generate pr pr > l+ l- /h @0
add process pr pr > l+ l- j /h @1
add process pr pr > l+ l- j j /h @2
```

Note that, the contribution of the Higgs boson ($/h$) is removed. Finally, Table [6.3] summaries the cross-section associated with each background of the SM.

Table 6.3: Background cross sections (σ_B).

Process	σ [pb]
$\gamma^*/Z(\rightarrow 2\ell/2\nu)$ + jets	2240 ± 5
$W(\rightarrow \ell\nu)$ + jets	31800 ± 62

Section 6.3

Event selection criteria

The event selection criteria used in the phenomenological analysis was aimed to reduce the background component at the lowest possible level while keeping a high signal rate. Additionally, experimental constraints related to the available trigger system, as explained in Section 3.3, the minimum p_{T} thresholds for leptons and jets, and the detector acceptances at ATLAS and CMS were also taken into consideration. Table [6.4] summarizes the final event selection criteria used in the study.

Table 6.4: Selection criteria for a hadronic τ_h and an ISR jet. Where the ISR is the highest-p_{T} jet in the event.

Criteria	Value
$N(\mathrm{j}^{lead})$ & $N(\mathrm{j}^{others})$	$== 1$ & ≥ 0
$p_{\mathrm{T}}(\mathrm{j}^{lead})$ & $p_{\mathrm{T}}(\mathrm{j}^{others})$	≥ 100 & ≥ 30 GeV
$\lvert\eta(\mathrm{j}^{lead\&others})\rvert$	≤ 2.5
$N(\tau_h)$	$== 1$
$p_{\mathrm{T}}(\tau_h)$	$> 15\& < 35$ GeV
$\lvert\eta(\tau_h)\rvert$	≤ 2.3
$N(e^-/\mu^-)$ & $N(b-jets)$	$== 0$
$\Delta R(\tau_h, \mathrm{j})$	> 0.4 (Overlap removal)
p_{T}^{miss}	> 230 GeV

The Signal Region (SR) is defined by the set of selections found in Table [6.4]. The threshold used in each criterion was obtained by using a figure of merit known as statistical significance ($\mathcal{S}$), given by [109]:

$$\mathcal{S} = \frac{N_S}{\sqrt{N_S + N_B}}, \tag{6.3}$$

The optimization was performed using as benchmark scenario the sixth signal point in Table [6.2]. To begin with, jets were constrained to the central region of the detector, $|\eta(\mathrm{j})| < 2.5$, because the ISR jet is expected to boost the p_{T}^{miss}. The $p_{\mathrm{T}}(\mathrm{j}^{lead})$ threshold was chosen upon experimental trigger constrains, determined using published articles from ATLAS and CMS, and also through optimization. The selection of the highest p_{T}-central jet as the ISR jet has a generator-level matching efficiency of 95% [107]. Events were also required to have exactly one τ_h with $15 < p_{\mathrm{T}}(\tau_h) < 35$ GeV and $|\eta(\tau_h)| < 2.3$. The τ_h candidate and the jet must not overlap; this is accomplished by using an $\eta - \phi$ requirement defined as $\Delta R(\tau_h, \mathrm{j}) = \sqrt{\Delta\phi^2 + \Delta\eta^2} > 0.4$. To reduce the contribution of background events from processes with real (prompt) light leptons (muons and electrons), such as $W + jets$, $Z + jets$, and $t\bar{t}$, the analysis vetoed events with well reconstructed electrons and muons with $p_{\mathrm{T}}(e^-/\mu^-) > 10$ GeV and $|\eta(e^-/\mu^-)| < 2.5$. To further reduce the contribution from $t\bar{t}$, events with jets with $p_{\mathrm{T}}(b - jets) > 30$ GeV and $|\eta(b - jets)| < 2.5$ tagged as b-jets were not allowed. Figure [6.5] shows the p_{T} distribution normalized to unity for the leading jet (left) and the τ_h (right) for two different signal points and the main backgrounds. These distributions help to motivate the p_{T} thresholds used in the analysis.

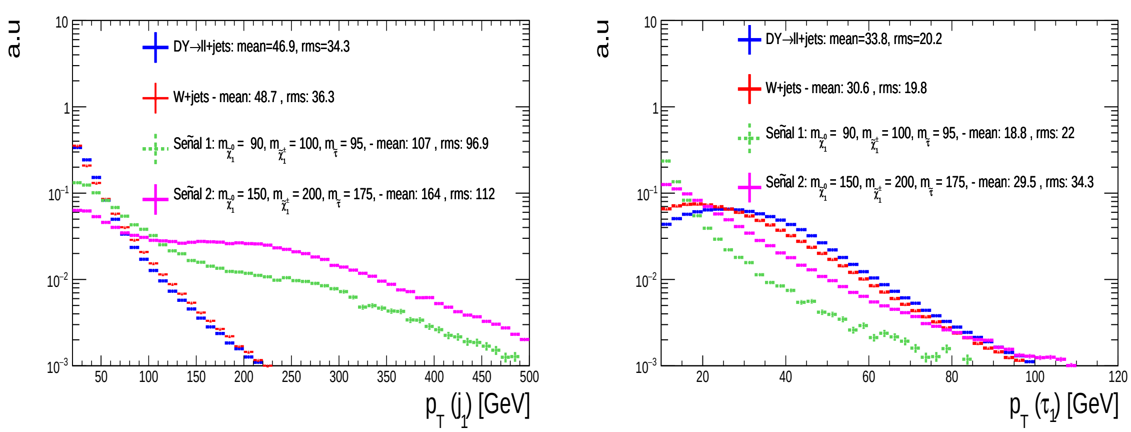

Figure 6.5: ISR jet and τ_h p_{T} distributions normalized to unity for two signal benchmark points and the main background processes.

Requiring high values of p_{T}^{miss} reduces the QCD background contribution to a negligible level. Figure [6.6] shows the p_{T}^{miss} distribution normalized to unity for the signal and background. The p_{T}^{miss} distribution for signal has a significantly broader spectrum when compared to the background due to the presence of neutralinos ($\tilde{\chi}_1^0$). The best value of the signal significance was measured to be $p_{\mathrm{T}}^{miss} > 230$ GeV.

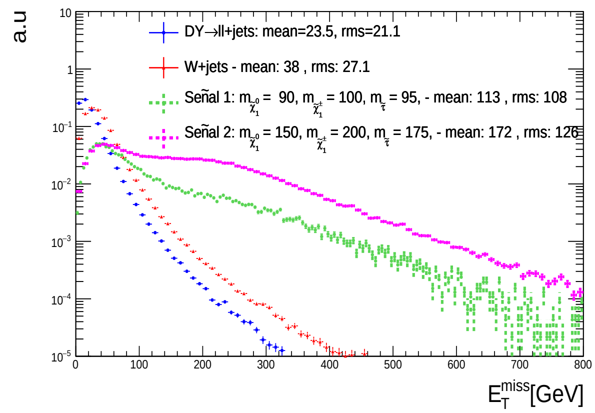

Figure 6.6**:** p_{T}^{miss} distribution normalized to unity for two signal benchmark points and the main background processes.

Since the ISR creates a recoil effect in the event topology, the p_{T}^{miss}, j^{lead}, and τ_h are then naturally correlated. Therefore, the best signal significance was obtained by scanning the p_{T}^{miss} versus $p_{\mathrm{T}}(\tau_h)$ space. Figure [6.7] shows the yields of this optimization, where the best values are found between $15 < p_{\mathrm{T}}(\tau_h) < 35$ GeV for $p_{\mathrm{T}}^{miss} > 230$ GeV.

Other sets of variables were explored, such as angular correlations between τ_h and jets, angular correlations between jets and the p_{T}^{miss}, the scalar sum of the p_{T} of jets (H_{T}) and the ratio between p_{T}^{miss} and p_{T}(j^{lead}). Nevertheless, neither of these observables showed a significant improvement in the final result.

Section 6.4

Analysis and results

The transverse mass (m_{T}) distribution between the τ_h and the p_{T}^{miss} was used as the main observable to study the sensitivity of the analysis. The m_{T} was found as the observable that gives the best signal-background separation. Equation (4.14) shows the m_{T} definition mathematically. Figure [6.8] shows the final expected yields for signal and background, after applying all of the event selection criteria described in Section 6.3. The expected yields were calculated assuming an integrated luminosity of 30 fb^{-1} at the LHC. The low m_{T} region is mainly dominated by the background, whereas in the tail of the distribution the signal stands above the background.

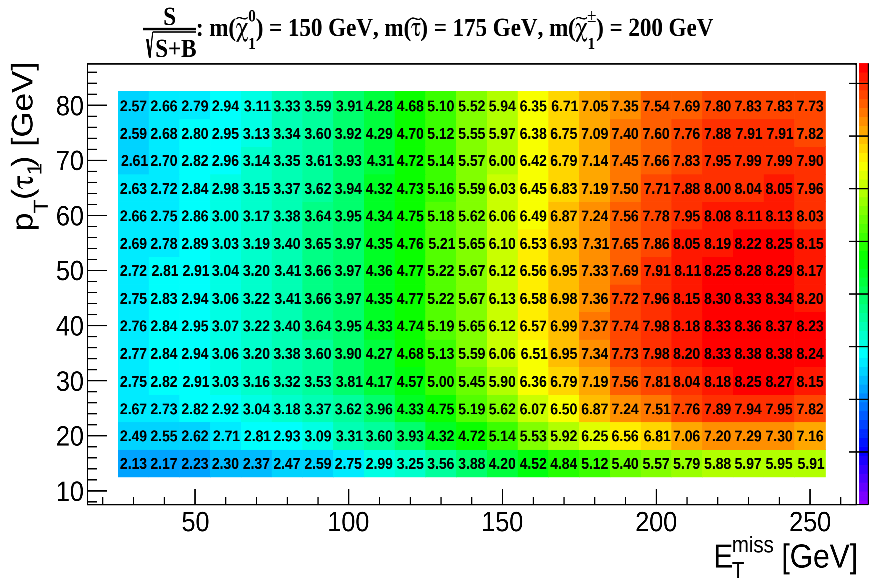

Figure 6.7: $p_{\mathrm{T}}(\tau_h)$ vs p_{T}^{miss} optimization process, setting $p_{\mathrm{T}}^{lead}(\mathrm{j}) > 100$ GeV, $p_{\mathrm{T}}(\tau_h) > 15$ GeV, and extra leptons and b-jet vetoed.

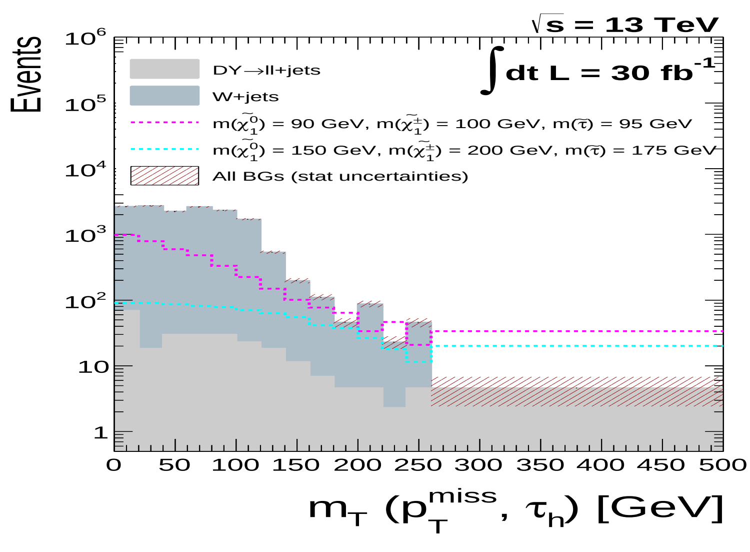

Figure 6.8: $m_{\mathrm{T}}(\tau_h, p_{\mathrm{T}}^{miss})$ distribution for the main backgrounds and two chosen signal points. This distribution is presented after all selections.

Using the $m_{\mathrm{T}}(\tau_h, p_{\mathrm{T}}^{miss})$ distribution, the sensitivity of the analysis was estimated following a test statistic approach based on a profile likelihood ratio. The p-value is calculated as the probability under a background-only hypothesis to obtain a value of the test statistic as large as that obtained with a signal plus background hypothesis. The significance, z, is then determined as the value at which the integral of a Gaussian between z and infinity results in a value equal to the local p-value [107]. The likelihood ratio is calculated using the number of expected signal events, s_i, the estimated background b_i, and the observed data d_i [110]:

$$X = \prod_{i=1}^{n} X_i, \tag{6.4}$$

with

$$X_i = \frac{e^{-(s_i+b_i)}(s_i+b_i)^{d^i}}{d_i!} \Bigg/ \frac{e^{-b_i}b_i^{d_i}}{d_i!} \tag{6.5}$$

The confidence level to have a signal plus background hypothesis is:

$$CL_{s+b} = P_{s+b}(X < Xobs) = \sum_{X(d_i^{'}) \leq X(d_i)} \prod_{i=1}^{n} \frac{e^{-(s_i+b_i)}(s_i+b_i)^{d_i^{'}}}{d_i^{'}!} \tag{6.6}$$

Where $X(d_i$ is the statistical test in each bin i, and the sum runs over the final value $X(d_i^{'})$. The complete expression requires the background only-hypothesis as well.

$$CL_b = P_b(X \leq X_{obs}), \tag{6.7}$$

Finally, the frequentist confidence level CL_s can be estimated as:

$$CL_s = CL_{s+b}/CL_b. \tag{6.8}$$

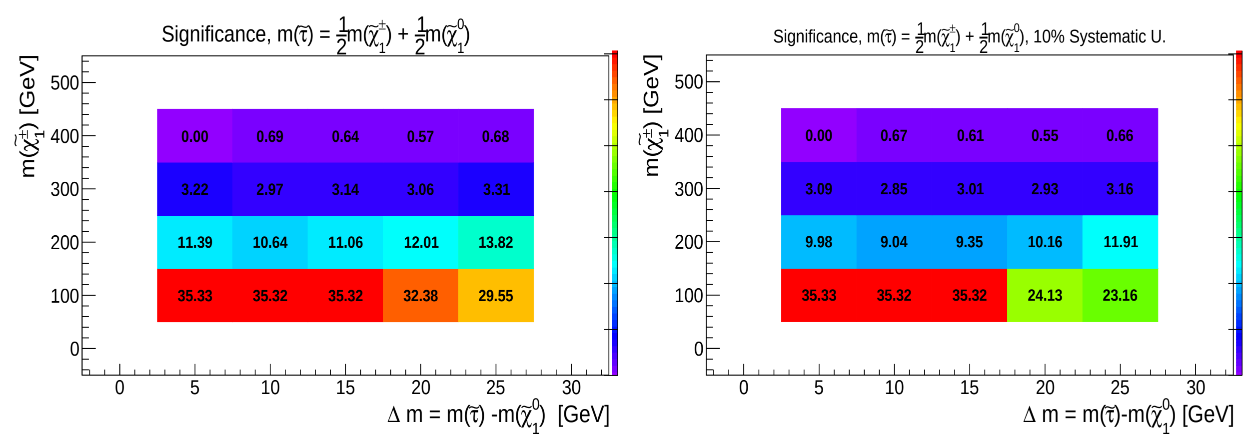

Figure 6.9**:** Signal significance using the shape based statistical analysis of the m_{T} distribution. No systematic effects (left) and including systematic effects (right).

The proposed methodology provides 5σ and 3σ significance for $\tilde{\chi}_1^{\pm}$ masses up to approximately 250 and 300 GeV respectively, in the compressed scenario $m(\tilde{\tau}) - m(\tilde{\chi}_1^0) < 25$ GeV. The results presented in Figure [6.9] were estimated considering a 10% flat systematic uncertainty and without systematic uncertainties in order to determine the effect on the results. The main sources of systematic uncertainty are 6% of τ_h identification, 5% for ISR modelling, and 1% for trigger effects [107]. As a conclusion, this study proposed a new experimental technique to study the very compressed mass spectra region with taus, $m(\tilde{\tau}) - m(\tilde{\chi}_1^0) < 25$ GeV, and showed potential to study experimentally $\tilde{\chi}_1^{\pm}$ masses up to 300 GeV. It is important to mention that the compressed region with taus has been quite difficult to study experimentally. In the next Chapter, we present the complete experimental study based on a data sample of $L = 77.2\ fb^{-1}$ of pp collisions, collected by the CMS experiment during the 2016 and 2017 runs.

CHAPTER 7

Experimental analysis

The experimental search considered final states with exactly one τ_h candidate, one high p_{T} central jet, and large p_{T}^{miss}. This final state allows to explore the SUSY compressed mass sector with τ leptons, where experimental sensitivity is very limited. The analysis was conducted using 77.2 fb^{-1} of proton-proton data at $\sqrt{s} = 13$ TeV, collected in 2016 and 2017 by the CMS detector at the CERN LHC. The data is found to be in agreement with the SM background expectation. Therefore, upper limits are set at 95% confidence level (CL) on the production cross-section as a function of $\tilde{\chi}_1^{\pm}$ and $\tilde{\tau}$ masses.

The details of the experimental analysis are presented in the sections that follow.

Section 7.1
Strategy

As shown in Table [6.1], the hypothetical production of $\tilde{\tau}$ particles through electroweak processes can occur directly or trough electroweakinos $(\tilde{\chi}_1^{\pm}, \tilde{\chi}_2^0)$. Final states include two or more τ leptons, p_{T}^{miss} from associated $\tilde{\chi}_1^0$'s and neutrinos, and an ISR jet. Nevertheless, as explained in Chapter 6, τ_h candidates from the signal, in compressed mass spectrum scenarios, can be lost in reconstruction due to their low p_{T}. Therefore, the experimental analysis selected events with exactly one τ_h candidate, large p_{T}^{miss}, and a high p_{T} ISR jet, which coincides with the methodology proposed by the phenomenological study. In addition, the selection of exactly one τ_h candidate allowed to reduce background events from $Z(\rightarrow \tau_h\tau_h)$, diboson (WW, ZZ, WZ), and processes from light-flavor interactions referred to as Quantum-Chromodynamics (QCD Multi-jets). Figure [7.1] shows the τ_h multiplicity $(N(\tau_h))$ for signal events with $\Delta m(\tilde{\chi}_1^{\pm}, \tilde{\chi}_1^0) =$ 50 GeV. Note the fraction of events with more than one τ_h is very small, which validates the criterion chosen at [107].

In the experimental analysis, the m_{T} distribution was also found as the best observable to search for the presence of signal events in data. The final event selection criteria used in the experimental analysis are summarized in Table [7.1]. The thresholds selected for the different variables will be explained in Section 7.4. Note the selection criteria used for the

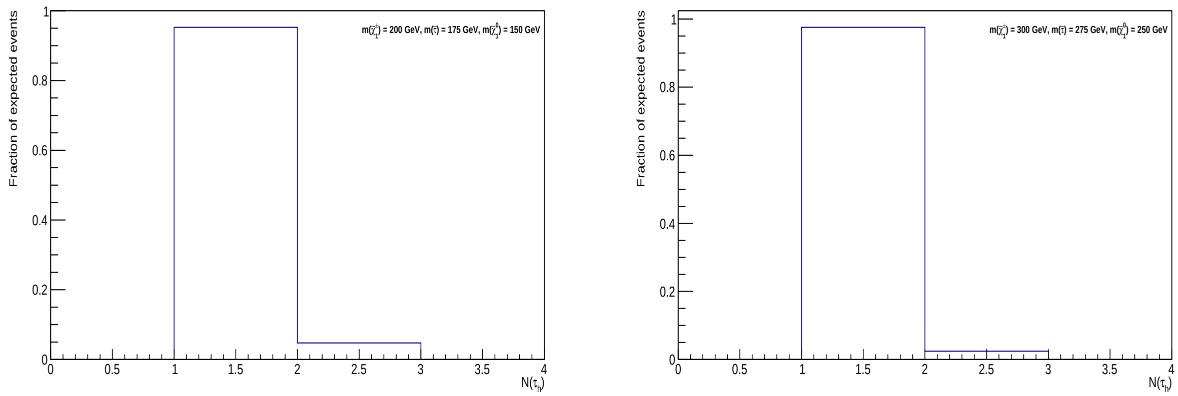

Figure 7.1: τ_h multiplicity for two representative signal points $m(\tilde{\chi}_1^0) = [150, 250]$ GeV in the compressed region, which includes the processes $\tilde{\chi}_1^{\pm}\tilde{\chi}_2^0$, $\tilde{\chi}_1^{\pm}\tilde{\chi}_1^{\pm}$, $\tilde{\chi}_1^{\pm}\tilde{\chi}_1^{\mp}$, $\tilde{\chi}_2^0\tilde{\chi}_2^0$, where $\tilde{\chi}_1^{\pm}\tilde{\chi}_2^0$ is the largest contribution.

experimental analysis is quite similar to that used in the phenomenological search. The main difference between the two studies comes from the inclusion of a $\Delta\phi(\mathrm{j}^{lead}, p_{\mathrm{T}}^{miss})$ requirement in the experimental analysis, used to reject QCD Multi-jets events [111].

Table 7.1: Event selection criteria of the SR.

Criteria	Value
Basic	Remove cosmics & MET Filters
$N(\mathrm{j}^{lead})$ & $N(\mathrm{j}^{others})$	$== 1$ & ≥ 0
$p_{\mathrm{T}}(\mathrm{j}^{lead})$ & $p_{\mathrm{T}}(\mathrm{j}^{others})$	≥ 100 & ≥ 30 GeV
$\lvert\eta(\mathrm{j}^{lead\&others})\rvert$	≤ 2.5
$Isolation(\mathrm{j}^{lead\&others})$	Loose & Tight in 2017
$N(\tau_h)$	$== 1$
$p_{\mathrm{T}}(\tau_h)$	$> 20 \& < 40$ GeV
$\lvert\eta(\tau_h)\rvert$	≤ 2.3
Isolation(τ_h)	Tight
Hps	Old Decay Mode Finding 1 prong
$N(e^-/\mu^-)$ & $N(b-jets)$	$== 0$
$Isolation(b-jets)$	Medium WP
QCD rejection cut	$\Delta\phi(\mathrm{j}^{lead}, p_{\mathrm{T}}^{miss}) > 0.7$
p_{T}^{miss}	> 230 GeV
	PFMet with HF and type-I corrections, MET-v2 in 2017

The final estimation of the main backgrounds in the signal region is based on methods that use data and simulation. Background events with a small contribution, roughly less than 3%, are estimated only using Monte Carlo predictions. The main backgrounds in the SR are:

$Z + jets$, $W + jets$, $t\bar{t}$ and QCD Multi-jets, while diboson and single-top correspond to small contributions. The different methods used to estimate the main backgrounds are based on the so-called control regions (CR). A CR is characterized by a dominant contribution of events from a background of interest. A CR can be obtained by changing one or more conditions in the selection criteria for the signal. The changes aimed to significantly enhance the contribution of a given background. For example, if criterion X is good to reject over 90% of background B_i is likely that by inverting X one can obtain a region where B_i is the dominant contribution. A CR can be used for different purposes, such as measuring the agreement between data and simulation to derive factors to correct the normalization and shapes, and to assign systematic uncertainties in the signal region.

After the detailed study of the expected contribution of each background in the signal region, the $m_{\mathrm{T}}(\tau_h, p_{\mathrm{T}}^{miss})$ distribution is used to search for any possible enhancement of data events above the prediction of known SM processes. If no significant deviation is found between the observed data and the expected SM background, upper limits on the signal production cross-section are set as a function of transverse mass (Equation (7.1)) at 95% CL. Systematic and statistical uncertainties are included in the limit calculation as nuisance parameters.

$$m_{\mathrm{T}}(\tau_h, p_{\mathrm{T}}^{miss}) = \sqrt{2p_{\mathrm{T}}(\tau_h)|\vec{p_{\mathrm{T}}}^{miss}|(1 - \cos\Delta\phi_{\tau_h, p_{\mathrm{T}}^{miss}})} \tag{7.1}$$

Section 7.2

Data and MonteCarlo samples

The data used in this research come from proton-proton collisions to the center of mass energy $\sqrt{s}$ = 13 TeV carried out during 2016 and 2017. Figure [4.7] shows the integrated luminosity of $L = 37.82\ fb^{-1}$ and $L = 45.39\ fb^{-1}$ for 2016 and 2017. Nevertheless, the available data is $L = 35.9$ and $41.3\ fb^{-1}$ respectively, which are validated by the Data Quality Monitor (DQM) at CMS. All storage information is certified by the JSON files:

- `Cert_271036-284044_13TeV_03Feb2017ReReco_Collisions16_JSON.txt`
- `Cert_294927-306462_13TeV_EOY2017ReReco_Collisions17_JSON.txt`

7.2.1 Data samples

The main source of data for this analysis is the MET and SingleMuon samples. The MET sample selects data with a p_{T}^{miss} requirement maintaining unbiased the selections over leptons. The SingleMuon sample is used to performed trigger efficiency studies and τ kinematics emulation through muons. Table [7.2] shows the certified datasets.

Table 7.2: Certified dataset used in this experimental analysis.

Physics Sample	Official CMS Datasets
Run 2016B Met Run2016B-03Feb2017	/Met/Run2016B-03Feb2017-v3/MINIAOD
Run 2016C Met Run2016C-03Feb2017	/Met/Run2016C-03Feb2017-v1/MINIAOD
Run 2016D Met Run2016D-03Feb2017	/Met/Run2016D-03Feb2017-v1/MINIAOD
Run 2016E Met Run2016E-03Feb2017	/Met/Run2016E-03Feb2017-v1/MINIAOD
Run 2016F Met Run2016F-03Feb2017	/Met/Run2016F-03Feb2017-v1/MINIAOD
Run 2016G Met Run2016G-03Feb2017	/Met/Run2016G-03Feb2017-v1/MINIAOD
Run 2016Hv2 Met Run2016H-03Feb2017	/Met/Run2016H-03Feb2017_ver2-v1/MINIAOD
Run 2016Hv3 Met Run2016H-03Feb2017	/Met/Run2016H-03Feb2017_ver3-v1/MINIAOD
Run 2016B SingleMu Run2016B-03Feb2017	/SingleMuon/Run2016B-03Feb2017_ver2-v2/MINIAOD
Run 2016C SingleMu Run2016C-03Feb2017	/SingleMuon/Run2016C-03Feb2017-v1/MINIAOD
Run 2016D SingleMu Run2016D-03Feb2017	/SingleMuon/Run2016D-03Feb2017-v1/MINIAOD
Run 2016E SingleMu Run2016E-03Feb2017	/SingleMuon/Run2016E-03Feb2017-v1/MINIAOD
Run 2016F SingleMu Run2016F-03Feb2017	/SingleMuon/Run2016F-03Feb2017-v1/MINIAOD
Run 2016G SingleMu Run2016G-03Feb2017	/SingleMuon/Run2016G-03Feb2017-v1/MINIAOD
Run 2016Hv2 SingleMu Run2016H-03Feb2017	/SingleMuon/Run2016H-03Feb2017_ver2-v1/MINIAOD
Run 2016Hv3 SingleMu Run2016H-03Feb2017	/SingleMuon/Run2016H-03Feb2017_ver3-v1/MINIAOD

7.2.2 MonteCarlo samples

Table 7.3: Simulated samples used in this experimental analysis.

Process	Samples	MC Generator	Cross-section [pb]
$Z(\to \ell\ell)$	m > 50 GeV	NLO_MG5	5765.4000
Mass-Binned	$200 < m < 400$ GeV	NLO_MG5	7.9077
	$400 < m < 500$ GeV	NLO_MG5	0.4263
	$500 < m < 700$ GeV	NLO_MG5	0.2390
	$700 < m < 800$ GeV	NLO_MG5	0.0341
	$800 < m < 1000$ GeV	NLO_MG5	0.0288
	$1000 < m < 1500$ GeV	NLO_MG5	0.0150
	$1500 < m < 2000$ GeV	NLO_MG5	0.0018
	$2000 < m < 3000$ GeV	NLO_MG5	0.0004
$W + jets$			
HT-Binned	$0 < HT < 70$ GeV	LO_MG5	61523.508
	$70 < HT < 100$ GeV	LO_MG5	1600.976
	$100 < HT < 200$ GeV	LO_MG5	1632.534
	$200 < HT < 400$ GeV	LO_MG5	436.597
	$400 < HT < 600$ GeV	LO_MG5	59.366
	$600 < HT < 800$ GeV	LO_MG5	14.626
	$800 < HT < 1200$ GeV	LO_MG5	6.677
	$1200 < HT < 2500$ GeV	LO_MG5	1.613
	$2500 < HT < \infty$ GeV	LO_MG5	0.039
$t\bar{t}$		POWHEG	831.76
Di-Boson	WW	Pythia8	63.21
	WZ	Pythia8	22.82
	ZZ	Pythia8	10.32
Single-top	t-channel-top-4f	POWHEG	136.02
	t-channel-antitop-4f	POWHEG	80.95
	tW-top-5f	POWHEG	35.6
	tW-antitop-5f	POWHEG	35.6
QCD Multi-jets			
HT-Binned	$50 < HT < 100$ GeV	NLO_MG5	246700000.0
	$100 < HT < 200$ GeV	NLO_MG5	28080000.0
	$200 < HT < 300$ GeV	NLO_MG5	1712000.0
	$300 < HT < 500$ GeV	NLO_MG5	347500.0
	$500 < HT < 700$ GeV	NLO_MG5	32100.0
	$700 < HT < 1000$ GeV	NLO_MG5	6823.0
	$1000 < HT < 1500$ GeV	NLO_MG5	1208.0
	$1500 < HT < 2000$ GeV	NLO_MG5	120.0
	$2000 < HT < \infty$ GeV	NLO_MG5	25.3

The simulated samples correspond with the official Monte-Carlo (MC) production generated using specialized software such as: `Mad-Graph`, `Pythia8`, `POWHEG` among others in 2016 (miniAOD) and 2017 (nanoAOD). These packages simulate high energy process to leading order (LO in appendix B), additionally, more accurate calculations to the cross-section require higher orders known as: next-to-leading order (NLO) and next-next-to-leading order (NNLO) approximation. Table [7.3] presents the MC samples that are used in this analysis, which have the level of accuracy required.

The simulated samples require extra-corrections. Since the pile-up distribution is different in the MC and data, the MC is re-weighted following the process explained in Section 4.7. In addition, the trigger effect must be studied in both MC and data in order to maximize the efficiency of the trigger selection in this study. We discuss the election of the trigger and its efficiency for this research in the next section.

Section 7.3

Trigger selection

Data events were filtered using triggers based on p_{T}^{miss}:

- `HLT_PFMETNoMu120_PFMHTNoMu120_IDTight`: 2016 and 2017

The behavior of the trigger was studied in a dedicated CR dominated (enriched) with $W(\rightarrow\ \mu\nu)$+jets events. Table [7.4] presents the event selection criteria used to obtain the $W(\rightarrow\ \mu\nu)$+jets CR. Data events were filtered using a single muon trigger, see Table [7.4]. The $p_{\mathrm{T}}(\mu)$ threshold is set to be over the plateau of the trigger efficiency turn on curve (`HLT_IsoMu24_v`). The $p_{\mathrm{T}}^{miss} > 50$ GeV selection was used to suppress events from QCD Multi-jet processes. The $N(b-jets) = 0$ selection reduces significantly the contribution from $t\bar{t}$ and single-top events. The jet p_{T} criterion was reduced to 30 GeV to study the trigger efficiency as a function of p_{T}(j) motivated by its strong correlation with p_{T}^{miss}. In addition, since the trigger strongly depends on p_{T}^{miss}, the efficiency as a function of this variable was also studied.

Table 7.4: Event selection criteria for trigger efficiency studies.

Criteria	Value
Single muon selections	
Trigger(μ)	`HLT_IsoMu24_v` & `IsoMu27` in 2017
$N(\mu)$	≥ 1
$p_{\mathrm{T}}(\mu)$	≥ 30 GeV
$\lvert\eta(\mu)\rvert$	< 2.1
$Isolation(\mu)$	Tight
N(j)	≥ 1
p_{T}(j)	≥ 30
$\lvert\eta(\mathrm{j})\rvert$	≤ 2.5
$Isolation$(j)	Loose & Tight in 2017
$N(b-jets)$	0
$Isolation(b-jets)$	Medium WP
p_{T}^{miss}	> 50 GeV
Trigger(p_{T}^{miss})	`HLT_PFMETNoMu120_PFMHTNoMu120_IDTight`

The trigger efficiency was calculated using the tag and probe method [112]. The denominator, referred to as tag events, is defined as the events that pass the selection criteria outlined in Table [7.4], except the Trigger(p_{T}^{miss}) requirement. The numerator, probe events, are defined as those passing all the selections in Table [7.4]. The efficiency is measured as the ration of between probe and tag events:

$$\epsilon_{Trigger(p_{\mathrm{T}}^{miss})} = \frac{N(\mu + Trigger(p_{\mathrm{T}}^{miss}))^{W(\to\mu\nu)+jets}}{N(\mu)^{W(\to\mu\nu)+jets}} \tag{7.2}$$

The trigger efficiency was studied in two scenarios. The first scenario corresponds to the methodology explained above. In the second scenario, the muon is treated as ν, which means that the $p_{\mathrm{T}}(\mu)$ is vectorially added to the p_{T}^{miss}. This is done in order to study the trigger performance with different p_{T}^{miss} conditions. Note that the $W^{-}(\to \tau\bar{\nu}) \to \tau_h \nu\bar{\nu}$ case, which has a similar topology as our final state, lays between these two scenarios.

7.3.1 Scenario 1: μ is not treated as a neutrino (ν)

The firing of the trigger is studied for several samples. Figure [7.2] left shows the trigger efficiency as function of p_{T}^{miss} for $W(\to \mu\nu) + jets$ simulated events and data. The expected contribution of other non-$W(\to \mu\nu) + jets$ processes is subtracted from data using simulation. Figure [7.2] right shows the trigger efficiency as a function of p_{T}^{miss} for all the expected events from simulation and the observed data. Note that the data-simulation agreement improves as p_{T}^{miss} increases; there is agreement around the plateau of the trigger turn-on curve and beyond.

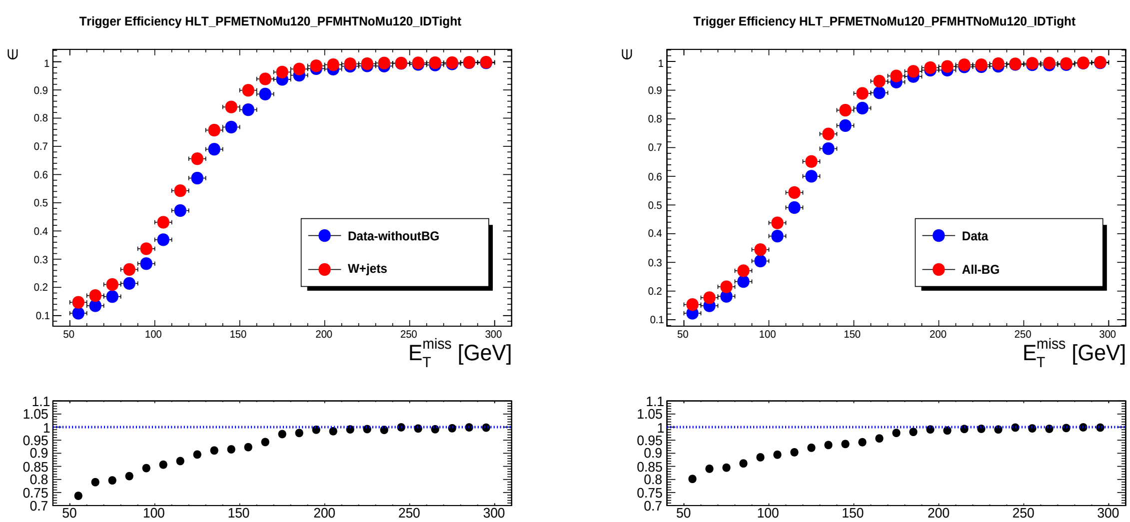

Figure 7.2: Trigger efficiency in case one (μ is not treated as ν) for expected $W(\to \mu\nu)$+jets events in data. $N^{Data-non\,W(\to\mu\nu)+jets}$ (blue points left), and nominal $W(\to \mu\nu)$+jets sample (red points left). All data sample N^{data} (blue points right), and all background MC samples (red points right).

Figure [7.3] left shows the comparison between data and data minus non-$W(\rightarrow \mu\nu) + jets$ events. From this comparison it is clear the contribution from non-$W(\rightarrow \mu\nu) + jets$ events is small and mainly distributed across low p_{T}^{miss} values (below 150 GeV). Figure [7.3] right shows the region between 200 and 300 GeV, where it can be seen that the efficiency reaches over 98% for $p_{\mathrm{T}}^{miss} > 210$ GeV.

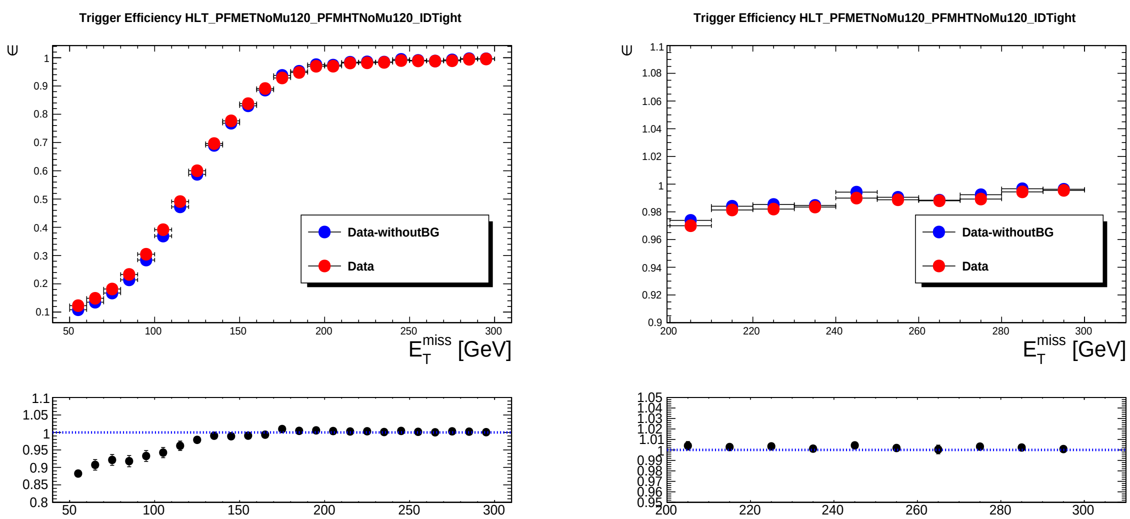

Figure 7.3**:** Trigger efficiency in case one (μ is not treated as ν) for expected $W(\rightarrow \mu\nu)$+jets events in data. $N^{Data-non\,W(\rightarrow\mu\nu)+jets}$ (blue points left), and all data sample (red points left). A zoom above 200 GeV is performed for viewing the trigger behavior on the plateau of the turn on curve (right).

7.3.2 Scenario 2: μ is treated as a neutrino (ν)

In this case, the p_{T} of the selected muon is vectorially added to the p_{T}^{miss}. This allows to emulate a situation with a larger p_{T}^{miss} spectrum. The firing of the trigger is studied for several samples. Figure [7.4] left shows the trigger efficiency as function of p_{T}^{miss} for $W(\rightarrow \mu\nu) + jets$ simulated events and data. The expected contribution of other non-$W(\rightarrow \mu\nu) + jets$ processes is subtracted from data using simulation. Figure [7.4] right shows the trigger efficiency as a function of p_{T}^{miss} for all the expected events from simulation and the observed data. Note that the data-simulation agreement improves as p_{T}^{miss} increases; there is agreement around the plateau of the trigger turn-on curve and beyond.

Figure [7.5] left shows the comparison between data and data minus non-$W(\rightarrow \mu\nu) + jets$ events. From this comparison it is clear the contribution from non-$W(\rightarrow \mu\nu) + jets$ events is small and mainly distributed across low p_{T}^{miss} values (below 150 GeV). Figure [7.5] right shows the region between 200 and 300 GeV, where it can be seen that the efficiency reaches over 96% for $p_{\mathrm{T}}^{miss} > 210$ GeV. Since the final state is expected to have a large p_{T}^{miss} spectrum, the trigger efficiency is measured using this second scenario, where the muon is treated as a ν.

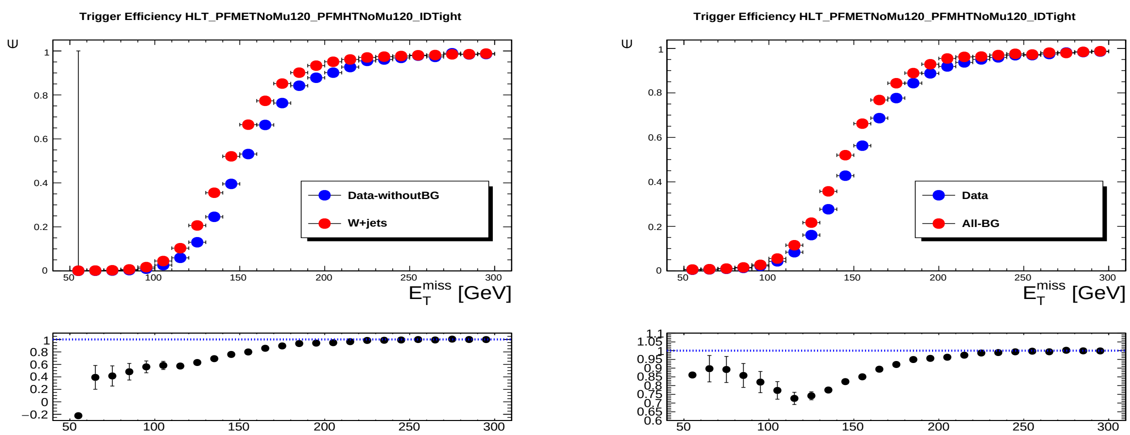

Figure 7.4: Trigger efficiency in case two (μ is treated as ν) for expected $W(\rightarrow \mu\nu)$+jets events in data. $N^{Data-non\,W(\rightarrow\mu\nu)+jets}$ (blue points left), and nominal $W(\rightarrow \mu\nu)$+jets sample (red points left). All data sample N^{data} (blue points right), and all background MC samples (red points right).

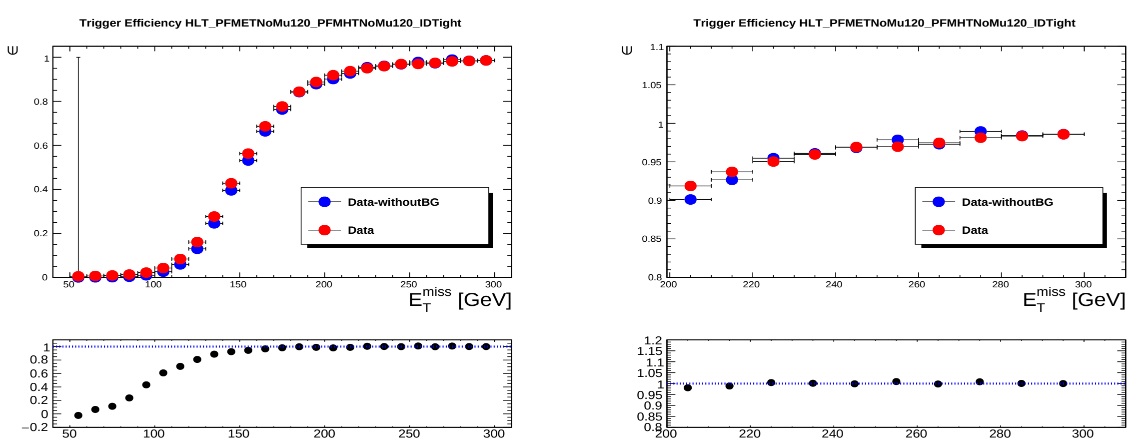

Figure 7.5: Trigger efficiency in case two (μ is treated as ν) for expected $W(\rightarrow \mu\nu)$+jets events in data. $N^{Data-non\,W(\rightarrow\mu\nu)+jets}$ (blue points left), and all data sample (red points left). A zoom above 200 GeV is performed for viewing the trigger behavior on the plateau of the turn on curve (right).

7.3.3 $p_{\mathbf{T}}^{miss}$ and $p_{\mathbf{T}}$(j) trigger correlation

As mentioned before, the ISR kinematic boost generates a correlation between the j^{ISR} and p_{T}^{miss}. Additionally, since the trigger depends on the p_{T}^{miss} a two dimensional (2D) correlation plot between the p_{T}(j^{ISR}) and the p_{T}^{miss} is appropriate to understand the performance of the trigger. Figure [7.6] shows the trigger efficiency as a function of the correlation between p_{T}(j^{lead}) and p_{T}^{miss}. Note that, efficiency values over 96% are obtained for the minimum threshold of p_{T}(j^{ISR}) > 100 GeV and p_{T}^{miss} > 230 GeV. It is worth mentioning that these values match the ones previously obtained in the phenomenological analysis through optimization for best signal significance.

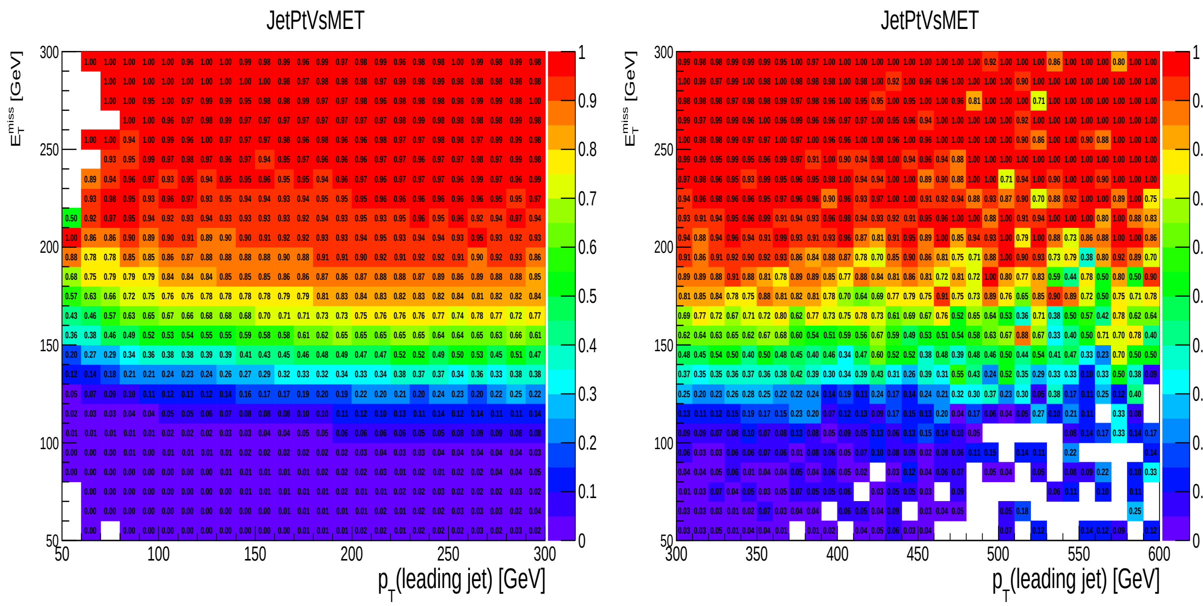

Figure 7.6: Trigger correlation between p_{T}(j^{lead}) and the p_{T}^{miss}, The efficiency is entirely based on data in the kinematic p_{T}-regions given by: p_{T}(j^{lead}) = $[50, 300]$ GeV (left), and p_{T}(j^{lead}) = $[300, 600]$ GeV (right).

Section 7.4

Optimization studies

The optimization of the SR was performed using both: trigger efficiency constraints obtained in the previous section ($p_{\mathrm{T}}(\mathrm{j}^{lead}) > 100$ GeV and $p_{\mathrm{T}}^{miss} > 230$ GeV) and the figure of merit described by Equation (6.3).

$$\mathcal{S} = \frac{N_S}{\sqrt{N_S + N_B}}, \tag{7.3}$$

Table [7.5] presents the preliminary event selection criteria for the optimization studies.

Table 7.5: Event selection criteria for optimization studies.

Criteria	Value
Trigger(p_{T}^{miss})	`HLT_PFMETNoMu120_PFMHTNoMu120_IDTight`
$N(\mathrm{j}^{lead})$ & $N(\mathrm{j}^{others})$	$== 1$ & ≥ 0
$p_{\mathrm{T}}(\mathrm{j}^{lead})$ & $p_{\mathrm{T}}(\mathrm{j}^{others})$	≥ 100 & ≥ 30 GeV
$\lvert\eta(\mathrm{j}^{lead\&others})\rvert$	≤ 2.5
$Isolation(\mathrm{j}^{lead\&others})$	Loose & Tight in 2017
$N(\tau_h)$	$== 1$
$p_{\mathrm{T}}(\tau_h)$	> 20 GeV
$\lvert\eta(\tau_h)\rvert$	≤ 2.3
Isolation(τ_h)	Tight
Hps	Old Decay Mode Finding 1 prong
$N(e^-/\mu^-)$ & $N(b-jets)$	$== 0$
p_{T}^{miss}	> 230 GeV
$Isolation(b-jets)$	Medium WP
Overlaps removal	$\Delta R > 0.3$

The $p_{\mathrm{T}}(\tau_h)$ was optimized using two approaches. In the first one, the $p_{\mathrm{T}}(\tau_h)$ is set as a minimum threshold ($p_{\mathrm{T}}(\tau_h) > p_{\mathrm{T}}^i$ GeV), where p_{T}^i starts at 20 GeV and it is varied in steps of 10 GeV. Figure [7.7] shows the minimum $p_{\mathrm{T}}(\tau_h)$ optimization yield for three different signal points, where the LSP masses are set to $[270, 360, 450]$ GeV. Note that the maximum value of significance is $\mathcal{S}_{max} = 0.485$ for the $m(\tilde{\chi}_1^0) = 270$ GeV signal point.

In the second approach, the $p_{\mathrm{T}}(\tau_h)$ is considered as a maximum threshold ($20 < p_{\mathrm{T}}(\tau_h) < p_{\mathrm{T}}^i$ GeV), where p_{T}^i starts in 30 GeV and it is varied in steps of 10 GeV. Figure [7.8] shows the maximum $p_{\mathrm{T}}(\tau_h)$ optimization yield for three different signal points, where the LSP masses are set to $[270, 360, 450]$ GeV. Note that the maximum value of significance is $\mathcal{S}_{max} = 1.770$ for the $m(\tilde{\chi}_1^0) = 270$ GeV signal point. Following the results, the final criterion is set to

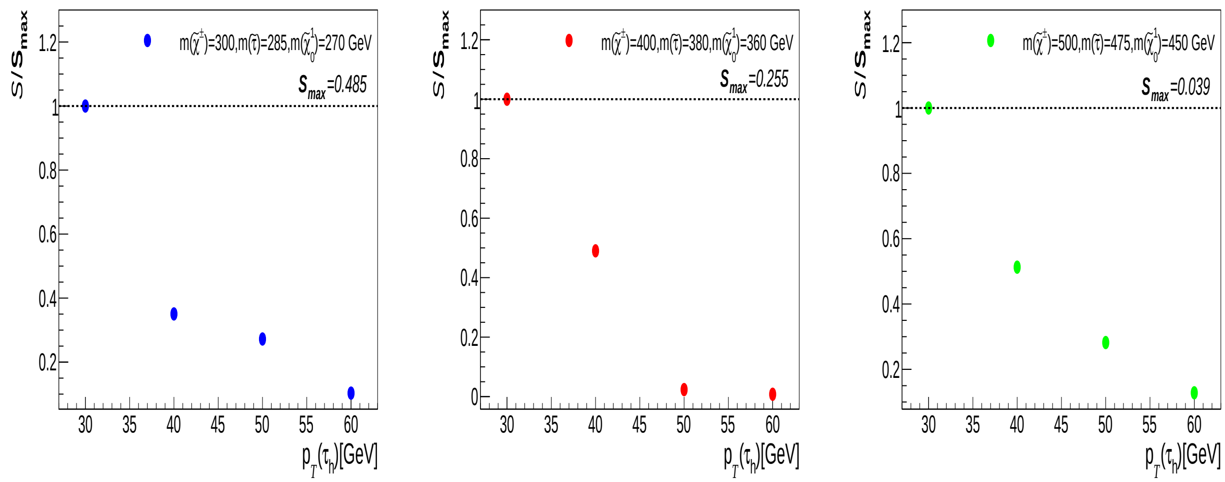

Figure 7.7: Optimization of the $p_{\mathrm{T}}(\tau_h)$ criteria, using signal points for LSP masses of $[270, 360, 450]$ GeV. The tested values are $p_{\mathrm{T}}(\tau_h) > p_{\mathrm{T}}^i$, with $p_{\mathrm{T}}^i = [30, 40, 50, 60]$ GeV.

$20 < p_{\mathrm{T}}(\tau_h) < 40$ GeV. The selected thresholds are close with respect to the values obtained in the phenomenological study. In addition, since a profile binned likelihood is performed to search for signal, using the $m_{\mathrm{T}}(\tau_h, p_{\mathrm{T}}^{miss})$ distribution, the $p_{\mathrm{T}}(\tau)$ and the p_{T}^{miss} variables are indirectly optimized.

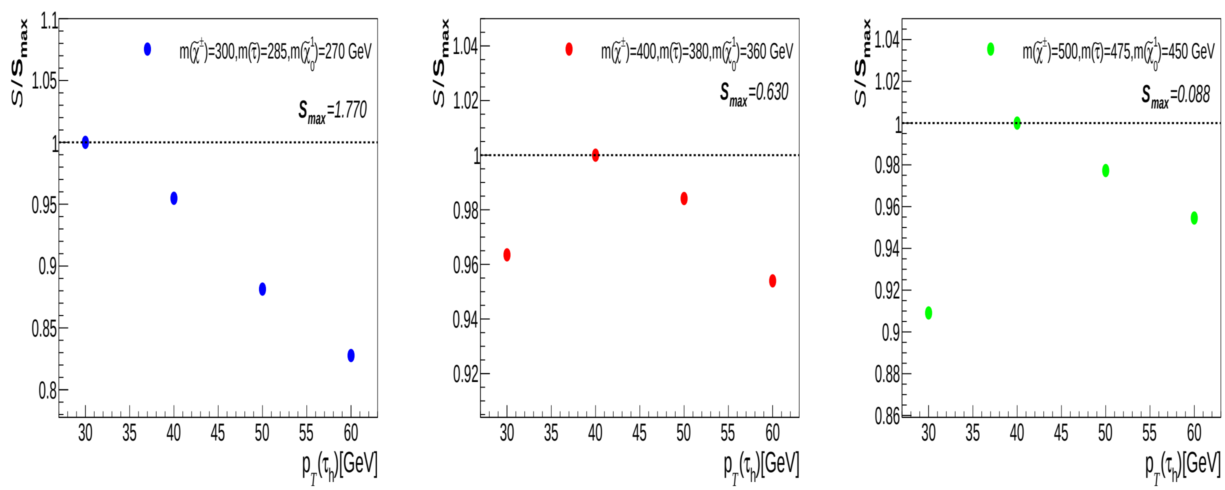

Figure 7.8: Optimization of the $p_{\mathrm{T}}(\tau_h)$ criteria, using signal points for LSP masses of $[270, 360, 450]$ GeV. The tested values are $20 \leq p_{\mathrm{T}}(\tau_h) \leq p_{\mathrm{T}}^i$, with $p_{\mathrm{T}}^i = [30, 40, 50, 60, 70]$ GeV.

Events were required to have exactly τ_h candidates with exactly 1 prong (Hps algorithm 4.3.1) to minimize the presence of misidentified jets as hadronic taus. This selection allows to reduce significantly the contribution of QCD Multi-jets events which is especially dominant in the high mass tail of the $m_{\mathrm{T}}(\tau_h, p_{\mathrm{T}}^{miss})$ distribution.

As explained before, the $p_{\mathrm{T}}(\mathrm{j}^{lead})$ was initially studied using the 2D correlation trigger efficiency [7.6]. In addition, the optimal threshold for the $p_{\mathrm{T}}(\mathrm{j}^{lead})$ was also studied using the best signal significance by setting $p_{\mathrm{T}}(\mathrm{j}^{lead})$ as a minimum threshold ($p_{\mathrm{T}}(\mathrm{j}^{lead}) > p_{\mathrm{T}}^{i}$ GeV), where p_{T}^{i} starts in 100 GeV based on trigger constrains, and it was varied in steps of 10 GeV. Figure [7.9] shows the $p_{\mathrm{T}}(\mathrm{j}^{lead})$ optimization yield for three different signal points, where the LSP masses are set to $[270, 360, 450]$ GeV. Note that, the maximum value of significance is $\mathcal{S}_{max} = 1.197$ for the $m(\tilde{\chi}_1^0) = 270$ GeV signal point. Values above 100 GeV do not generate relevant changes in the significance, which motivates the minimum threshold selection obtained from the trigger efficiency studies. The final selection is $p_{\mathrm{T}}(\mathrm{j}^{lead}) > 100$ GeV.

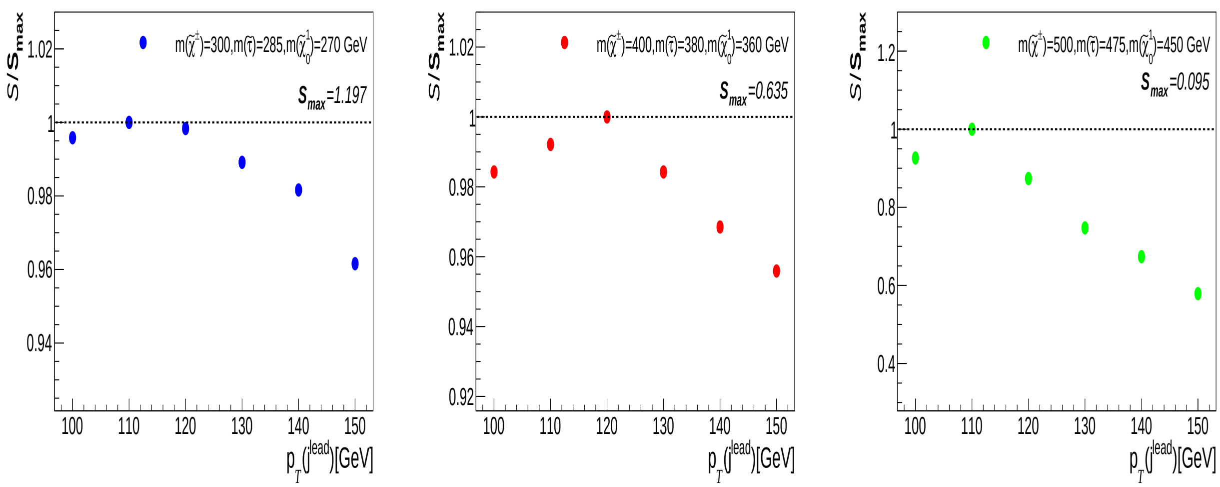

Figure 7.9: Optimization of the $p_{\mathrm{T}}(\mathrm{j}^{lead})$ criteria, using signal points for LSP masses of $[270, 360, 450]$ GeV. The tested values are $p_{\mathrm{T}}(\mathrm{j}^{lead}) > p_{\mathrm{T}}^{i}$, with $p_{\mathrm{T}}^{i} = [100, 110, 120, 130, 140, 150]$ GeV.

Section 7.5

Background estimation

For this analysis, various factors are to be considered to obtain the expected background contribution in the SR. Among these factors are the modelling of ISR jets in simulation, the τ_h and b-jets identification efficiencies, and the modelling of p_{T}^{miss}. Additionally, the QCD-Multijets contribution requires a fully data-driven approach due to the lack of statistics in the MC, which causes mismodelling of this background in the tails of the $m_{\mathrm{T}}(\tau_h, p_{\mathrm{T}}^{miss})$ distribution. In the subsections that follow, the background estimation methodology is explained.

7.5.1 Boost ISR weights

To understand the ISR jet modelling in simulation, a sample enriched with $Z(\rightarrow \mu\mu)$+jets events is used. Note that this CR is expected to have no real p_{T}^{miss} contribution. In this way, any effect related to data-simulation differences in the p_{T}^{miss} efficiency ($\epsilon_{p_{\mathrm{T}}^{miss}}$) is decoupled. The excellent reconstruction of muons at CMS, which have a significantly lower misidentification rate (fake rate) with respect to τ_h candidates, allows to have a high purity of $Z(\rightarrow \mu\mu)$+jets events. Moreover, the lepton universality can be used to obtain the expected kinematic of ISR plus taus $Z(\rightarrow \tau\tau)$+ ISR jet. The number of events is defined as:

$$N_{Z\rightarrow\mu\mu} = \sigma_Z \cdot L_{int} \cdot \epsilon_\mu^2 \cdot \epsilon_{ISR} \cdot \epsilon_{others}, \tag{7.4}$$

where σ_Z is the production cross-section, L_{int} is the integrated luminosity, ϵ_μ is the muon reconstruction efficiency, ϵ_{ISR} is the efficiency of the ISR modelling, and ϵ_{others} is the efficiency of other sources of this CR. Figure [7.10] shows the Feynman diagram that describes this CR.

To obtain this CR, a muon pair ($\mu\mu$) with invariant mass compatible with Z-mass peak ($80 < m(\mu\mu) < 100$ GeV) is required. Selected muons must be within of the central pseudorapidity coverage ($\eta(\mu) < 2.1$) and have a $p_{\mathrm{T}}(\mu)$ above the plateau of the trigger turn-on curve (≥ 30 GeV). Jets were selected with the same selection criteria used in the SR. Table [7.6] summarizes the event selection criteria for this CR.

The presence of the ISR jet creates a natural boost in the event topology and consequently the Z boson is not produced at rest. Therefore, the Z boson is produced with non-null transverse momentum, which can be measured by calculating vectorially the transverse momentum of the di-muon pair.

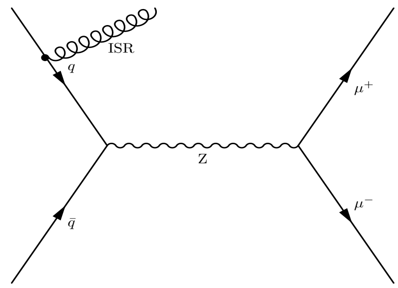

Figure 7.10: Feynman diagram associated with the $Z(\rightarrow \mu\mu)$+ISR jet production.

Table 7.6: Event selection criteria for Z-boost ISR weights.

Criteria	Value
Trigger(μ)	`HLT_IsoMu24_v` & `IsoMu27` in 2017
$N(\mu)$	$== 2$
$p_{\mathrm{T}}(\mu)$	≥ 30 GeV
$\lvert\eta(\mu)\rvert$	≤ 2.1
$Q_{\mu^1} \times Q_{\mu^2}$	-1[OS]
$m(\mu_1\mu_2)$	$> 80 \& < 100$ GeV
$Isolation(\mu)$	Tight
$N(\mathrm{j}^{lead})$ & $N(\mathrm{j}^{others})$	$== 1$ & ≥ 0
$p_{\mathrm{T}}(\mathrm{j}^{lead})$ & $p_{\mathrm{T}}(\mathrm{j}^{others})$	≥ 100 & ≥ 30 GeV
$\lvert\eta(\mathrm{j}^{lead\&others})\rvert$	≤ 2.4
$Isolation(\mathrm{j}^{lead\&others})$	Loose & Tight in 2017

Figure [7.11] shows the transverse momentum of the di-muon pair (Z-boost) and the H_{T} distribution, defined as the scalar sum of the p_{T} of all jets. These plots expose the disagreement between data and MC due to the kinematic boost caused by the ISR jet. There are two convoluted effects to be considered, the ISR kinematic boost and the jet energy resolution. In order to study the first effect, we use the jet recoil ($\vec{u}$) defined as:

$$\vec{u} = -\left(\vec{p_{\mathrm{T}}}^{miss} + \vec{Z}_{\mathrm{T}}\right), \tag{7.5}$$

where $\vec{p_{\mathrm{T}}}^{miss}$ is the vectorial missing transverse momentum and $\vec{Z}_{\mathrm{T}}$ is the transverse momentum of the Z boson, obtained using the momentum vector sum of the two selected muons. Note that by construction $\vec{u}$ is not parallel to $\vec{Z}_{\mathrm{T}}$. Therefore, to study the ISR jet recoil effect over $\vec{Z}_{\mathrm{T}}$ the projection of $\vec{u}$ along $\vec{Z}_{\mathrm{T}}$ is obtained ($\vec{r}_T$):

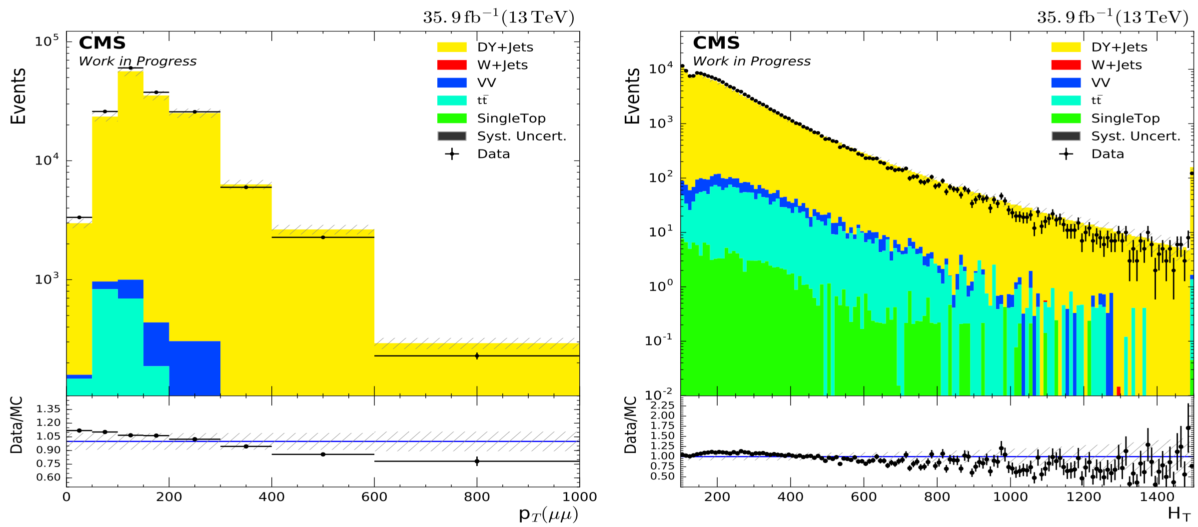

Figure 7.11: Z-Boost [GeV] (left) and H_{T} [GeV] (right) distributions for $Z(\to \mu\mu)$+ISR (2016).

$$r_T = \frac{\vec{Z}_{\mathrm{T}} \cdot \vec{u}}{|\vec{Z}_{\mathrm{T}}|}, \tag{7.6}$$

Figure [7.12] shows the parallel recoil of the ISR jet. Note there are differences in the data to simulation agreement. Therefore, correction factors must be applied.

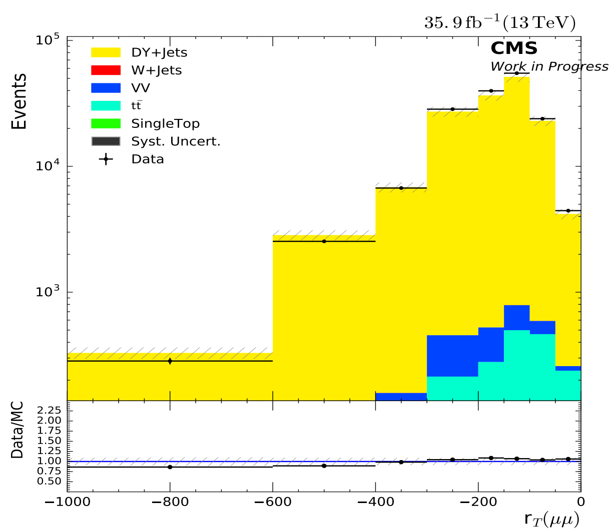

Figure 7.12: Jet Recoil Parallel to Z-Boost [GeV] (2016). Since the recoil is anti-parallel to the Z boson, r_T has negative domain.

In order to obtain the correction factors for $|\vec{Z}_{\mathrm{T}}|$, a weight for each bin is extracted directly from the data/MC ratio plot in Figure [7.13], left. Figure [7.13] right shows the $|\vec{Z}_{\mathrm{T}}|$ distribution after the applying the weights. Figure [7.14] shows the $\vec{Z}_{\mathrm{T}}$ distribution with 2017 data.

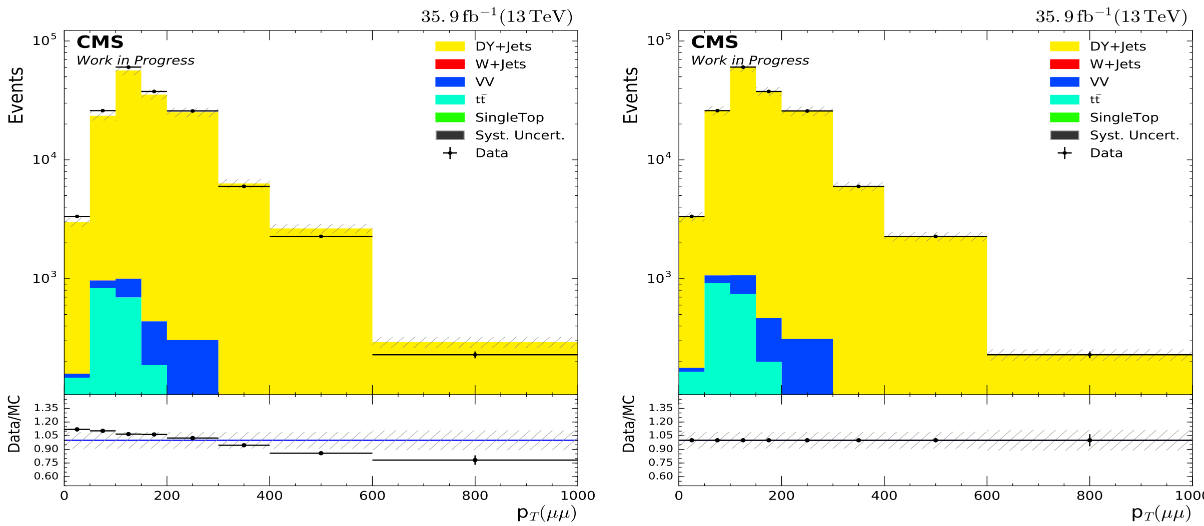

Figure 7.13**:** Z-Boost [GeV] distribution without boost weights (left) and after applying weights (right) for events in the $Z(\rightarrow \mu\mu)$ + ISR jet control region (2016).

Table [7.7] shows the ISR weights obtained directly from these distributions, the errors are purely statistical. There is an agreement between the weights for 2016 and 2017 data. The correction for the ISR modelling falls between 6-11%, which is consistent with other studies performed by the SUSY group [111].

Table 7.7**:** Event weights by Z-Boost for 2016 and 2017 datasets.

Jet recoil bin [GeV]	2016	2017
1: 0-50	1.12 ± 0.03	1.09 ± 0.02
2: 50-100	1.10 ± 0.01	1.11 ± 0.01
3: 100-150	1.07 ± 0.01	1.08 ± 0.01
4: 150-200	1.06 ± 0.01	1.07 ± 0.01
5: 200-300	1.02 ± 0.01	1.02 ± 0.01
6: 300-400	0.95 ± 0.02	0.94 ± 0.01
7: 400-600	0.86 ± 0.03	0.84 ± 0.02
8: 600-1000	0.78 ± 0.11	0.79 ± 0.05

Figure [7.15] presents the validation of the ISR weights in the parallel recoil r_T distribution for both 2016 and 2017 datasets. There is an agreement between data and MC, which falls in a resolution $\sim 5\%$ consistent with the resolution scale at CMS. Therefore, no further correction

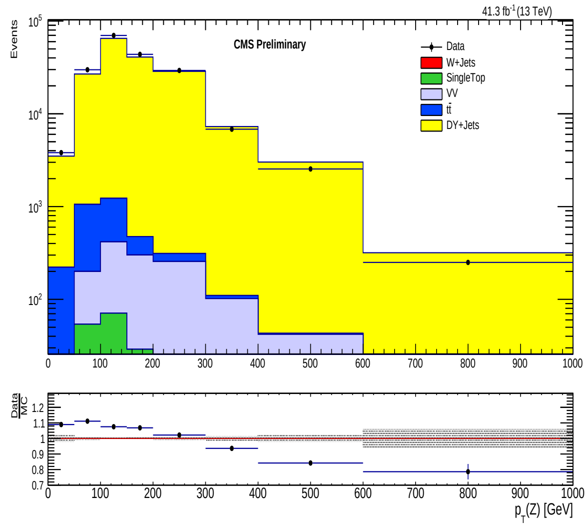

Figure 7.14**:** Z-Boost [GeV] distribution without boost weights for events in the $Z(\to \mu\mu)+$ ISR jet control region (2017).

in ISR modelling is needed.

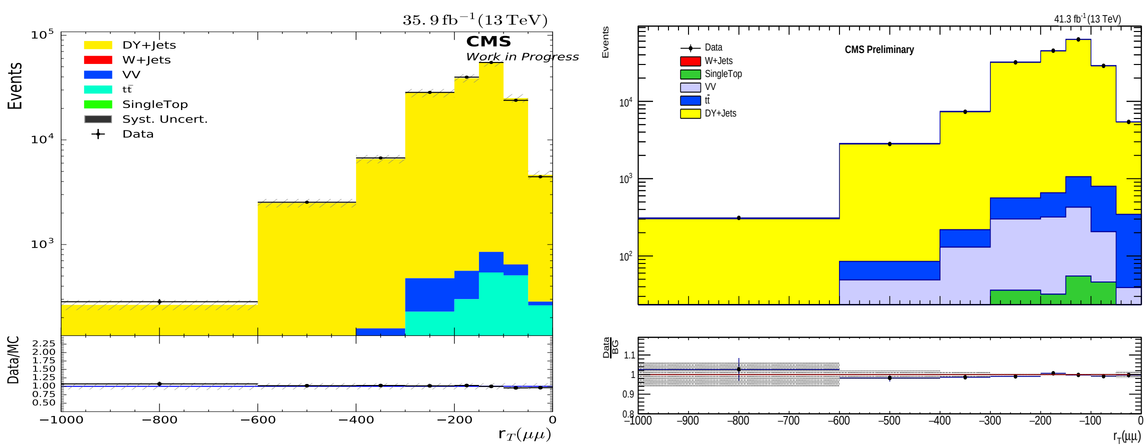

Figure 7.15**:** Parallel recoil r_T [GeV] after applying ISR boost weights for 2016 (left) and 2017 (right).

As a conclusion, the ISR weights generate an improvement in the ISR modelling in MC, which is consistent with the scale resolution of jets at CMS. The validation test showed a good correction for the ISR jet in this analysis. A closure test in another orthogonal CR is presented in the following section.

7.5.2 Validation of ISR weights using $W(\rightarrow \mu\nu)$+jets events

In order to validate the ISR weights obtained from the enriched $Z(\rightarrow \mu\mu)+$ ISR jet region, a new CR enriched with $W(\rightarrow \mu\nu)+$ ISR jet events was used. Figure [7.16] shows the Feynman diagram associated with this CR.

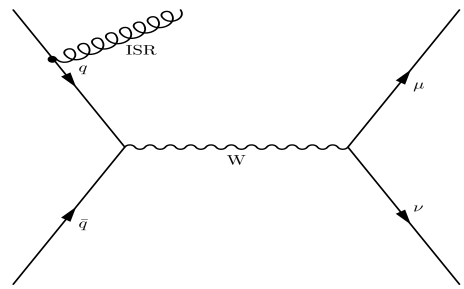

Figure 7.16: Feynman diagram associated with the $W(\rightarrow \mu\nu)+$ ISR jet production.

Table 7.8: Event selection criteria for ISR weights validation.

Criteria	Value
Trigger(μ)	`HLT_IsoMu24_v` & `IsoMu27` in 2017
$N(\mu)$	$== 1$
$p_{\mathrm{T}}(\mu)$	≥ 30 GeV
$\lvert\eta(\mu)\rvert$	≤ 2.1
$Isolation(\mu)$	Tight
$N(\mathrm{j}^{lead})$ & $N(\mathrm{j}^{others})$	$== 1$ & ≥ 0
$p_{\mathrm{T}}(\mathrm{j}^{lead})$ & $p_{\mathrm{T}}(\mathrm{j}^{others})$	≥ 100 & ≥ 30 GeV
$\lvert\eta(\mathrm{j}^{lead\&others})\rvert$	≤ 2.4
$Isolation(\mathrm{j}^{lead\&others})$	Loose & Tight in 2017
p_{T}^{miss}	≥ 230 GeV
$m_{\mathrm{T}}(\mu, p_{\mathrm{T}}^{miss})$	$60 >$ & < 100 GeV
QCD rejection cut	$\Delta\phi(\mathrm{j}^{lead}, p_{\mathrm{T}}^{miss}) > 0.7$

The event selection criteria selects events with exactly one muon with $|\eta(\mu)| < 2.1$ and $p_{\mathrm{T}}(\mu) > 30$ GeV. Since there is real p_{T}^{miss}, associated with the neutrino from the W decay, the same p_{T}^{miss} and jet requirements as in the SR were used. In addition, to increase purity, a transverse mass cut close to the Jacobian $(m(W))$ peak was applied $(60 < m_{\mathrm{T}}(\mu, p_{\mathrm{T}}^{miss}) < 100$ GeV). Finally, the $\Delta\phi(\mathrm{j}^{lead}, p_{\mathrm{T}}^{miss}) > 0.7$ criterion was also used. Table [7.8] summarizes the event selection criteria used to obtain the $W(\rightarrow \mu\nu)$+jets CR, which is studied for the 2016 and 2017 datasets.

As in the previous CR ($Z(\rightarrow \mu\mu)$+jets), the W is produced with non-null transverse momentum. Therefore, the ISR weights are applied to this boson to correct the boosting effect in simulation. Figure [7.17] shows the $p_{\mathrm{T}}(\mu)$ and p_{T}^{miss} distributions for the 2016 dataset. After applying the ISR weights the data to simulation ratio has an improvement of around $\sim 7\%$ in both distributions. In addition, the modelling of the shape improves, naturally reducing the associated systematic uncertainty of the $W + jets$ background in the SR.

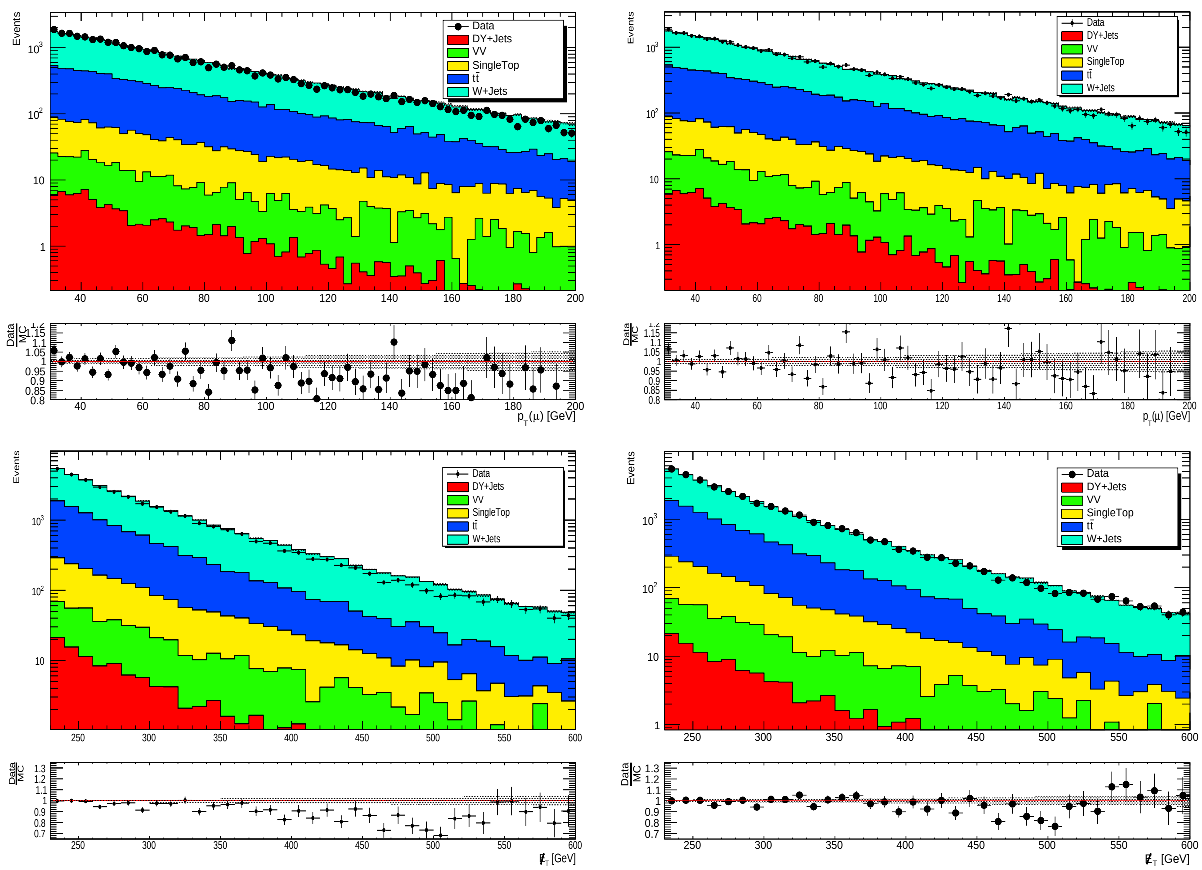

Figure 7.17**:** Top Row: Muon p_{T} without boost weights (left) and with weights (right); Bottom Row: p_{T}^{miss} without boost weights (left) and with weights (right) (2016).

Figure [7.18] shows the weights closure test for 2017 data. Data to simulation agreement is observed. This closure test study gives the confidence to use simulation. By using the ISR weights, the p_{T}^{miss} modelling has an improvement, which is evident in the tails of the distribution. After this correction, the prediction of $W + jets$ in the SR is studied.

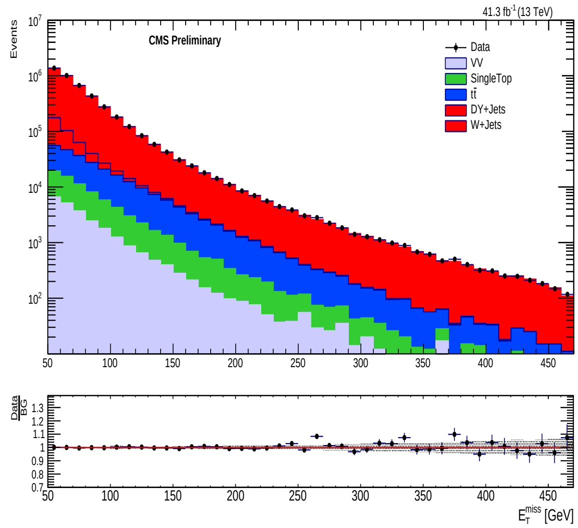

Figure 7.18: p_{T}^{miss} distribution after applying Z-boost weights for 2017 dataset.

Table [7.9] presents the yields of each background for this CR in the 2016 dataset.

Table 7.9: Data and background yields in $W(\rightarrow \mu\nu)+$ ISR jet CR for 2016.

Process	Yield
Data	34344
$W + jets$	23702.10 ± 84.32
$Z + jets$	107.11 ± 3.19
Diboson	383.78 ± 11.53
$t\bar{t}$	9062.12 ± 59.48
Single Top	1452.41 ± 15.39
$\sum_{BG}$	34707.52 ± 105.01
$SF(Data/BG)$	0.98 ± 0.01

Since the scale factor obtained from the yields in Table [7.9] is consistent with unity, the prediction of the $W + jets$ background in the SR was obtained directly from simulation after applying the ISR weights and this scale factor.

$$SF(Data/BG)^{W+jets} = 0.98 \pm 0.01. \tag{7.7}$$

7.5.3 τ_h kinematics emulation using muons

To validate the m_{T} shape and expected yields obtained for $W + jets$ from simulation an emulation of the τ_h kinematics was performed using a CR with muons. The method is described in the following items:

- Estimate the fraction of τ momentum taken by the visible products (τ_h). This fraction is defined as $R(p_{\mathrm{T}}^{\tau_{gen}}) = p_{\mathrm{T}}^{\tau_h,RECO}/p_{\mathrm{T}}^{\tau_{gen}}$, where $p_{\mathrm{T}}^{\tau_{gen}}$ is the momentum of the τ at generation level before it decays, and $p_{\mathrm{T}}^{\tau_h,RECO}$ is the reconstructed transverse momentum of the τ_h candidate. The minimum reconstructed value of p_{T} is 15 GeV, which is matched with the corresponding τ_{gen} using a matching requirement given by $\Delta R(\tau_{gen}, \tau_{\mathrm{h},RECO}) < 0.4$. The fraction of momentum is calculated for several values of $p_{\mathrm{T}}^{\tau_{gen}}$. Figure [7.19] shows the fraction of momentum carried by the τ_h candidate.

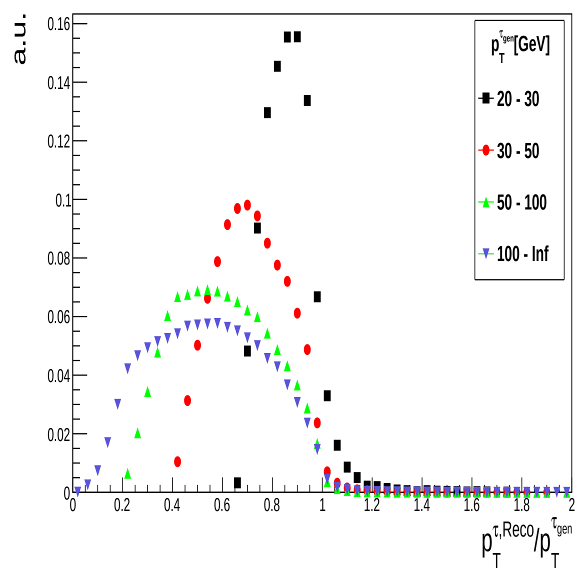

Figure 7.19**:** Fraction of momentum carried out by the hadronic tau (τ_h).

- Calculate the matching efficiency, which means how often does a $\tau_{\mathrm{h},RECO}$ candidate is matches to *true* a gen-level τ. The expression is given by:

$$\epsilon_{Matching} = \frac{N(p_{\mathrm{T}}(\tau_h^{RECO}(matched)))}{N(p_{\mathrm{T}}(\tau_{gen}))} \tag{7.8}$$

- Calculate the reconstruction identification efficiency associated with the reconstruction algorithms. The expression is given by:

$$\epsilon_{ID} = \frac{N(p_{\mathrm{T}}(\tau_h^{RECO}(matched + ID)))}{N(p_{\mathrm{T}}(\tau_h^{RECO}))} \tag{7.9}$$

- Emulate the reconstructed τ_h kinematics using muons (i.e, muons are treated as τ_{gen} particle before decay).
- Recalculate the p_{T}^{miss} vectorially by adding the four-momentum of the emulated τ_h, since the ν_τ contribution cannot be measured.

The lepton universality and the small momentum scale uncertainty for muons ($\sigma(p_{\mathrm{T}}^{\mu}) < 2\%$) allows to describe muons as gen-level taus $p_{\mathrm{T}}^{\mu} \approx p_{\mathrm{T}}^{\tau_{gen}}$. Therefore, the emulated τ is given by:

$$p_{\mathrm{T}}(\tau_h)_{Emulated} = p_{\mathrm{T}}^{\mu} \cdot R(p_{\mathrm{T}}^{\tau_{gen}}) \cdot \epsilon_{Matching} \cdot \epsilon_{ID}. \tag{7.10}$$

Figure [7.20] shows the emulated $m_{\mathrm{T}}(\tau_h, p_{\mathrm{T}}^{miss})$ distributions, using the nominal $W + jets$ MC sample (left) and emulating the τ_h lepton using muon events from data (right). The CR is built throughout the selection that satisfied the SR, but requiring $40 < p_{\mathrm{T}}(\tau_h) < 60$ GeV to avoid any overlap with the SR. Agreement is observed across $m_{\mathrm{T}}(\tau_h, p_{\mathrm{T}}^{miss})$ spectrum. The data/simulation ratio agreement gives further confidence in the simulation. This method is only used to validate the $W + jets$ simulation.

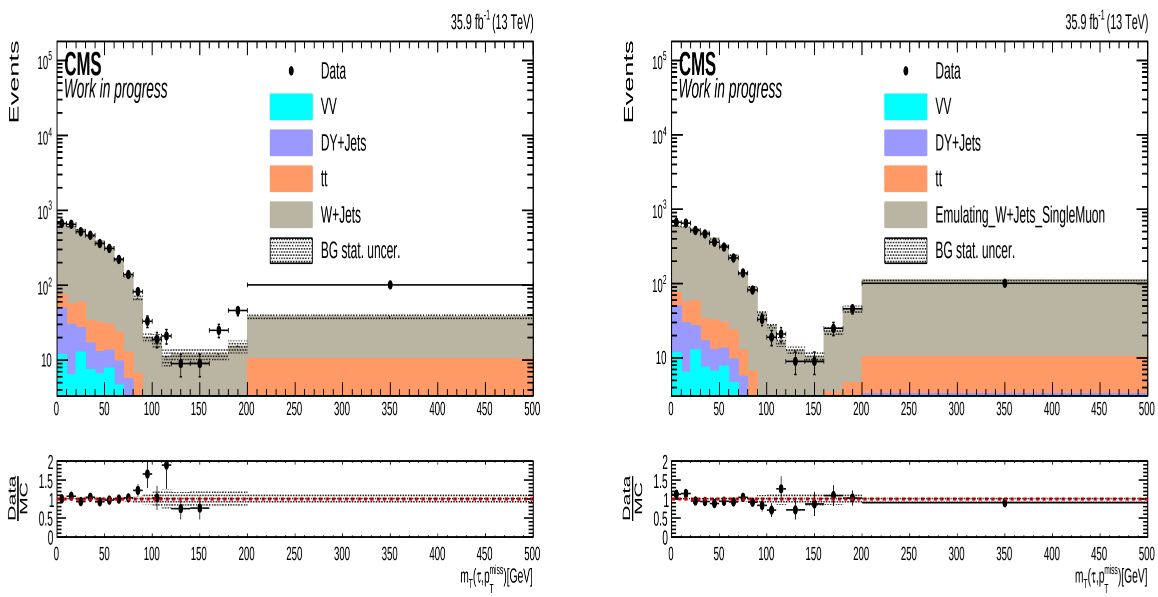

Figure 7.20: CR (sideband of the SR) that uses the nominal $W + jets$ MC sample (left), and emulating the τ_h kinematics using the Single Muon sample.

7.5.4 τ_h ID efficiency studies

Since the final state has a τ_h candidate it is natural to study the modelling of the reconstruction and identification efficiencies. To perform the study an enriched sample with $Z(\rightarrow \tau_h\tau_h)$+ISR jet events was used. Events are required to have two τ_h candidates reconstructed with pseudorapidity coverage of $|\eta(\tau_h)| \leq 2.1$. The p_{T} of the τ_h's is set above 60 GeV to be on the plateau of the turn-on curve of the di-tau trigger (Trigger($\tau_h\tau_h$)). In addition, the di-tau invariant mass is required to be on-shell around the Z boson mass, $50 < m_{\tau_h^1,\tau_h^2} < 100$ GeV, to reduce the contribution of QCD Multi-jets events. The jet selection is the same as in the SR, which avoids the low resolution of jets in the outer pseudorapidity coverage ($|\eta(j)| > 2.5$). In order to reduce the fake identification rate of τ_h candidates as jets a $\Delta R(\tau_h, j) \geq 0.3$ selection is applied. Furthermore, to increase the purity of this CR, the anti-muon (`againstMuonTight3`) and anti-electron (`againstElectronMVALooseMVA6`) discriminators are applied to reduce the light-lepton identification fake rate. It is important to note that the ISR weights corrections were applied to the simulation. Table [7.10] shows the event selection criteria used to obtain the $Z(\rightarrow \tau_h\tau_h)$+ISR jet CR.

Table 7.10: Event Selection Criteria for $Z(\rightarrow \tau_h\tau_h)$+ISR jet CR.

Criteria	Value
Trigger($\tau_h\tau_h$)	`HLT_DoubleMediumIsoPFTau35_Trk1_eta2p1`
$N(\tau_h)$	≥ 2
$p_{\mathrm{T}}(\tau_h)$	≥ 60 GeV
$\|\eta(\tau_h)\|$	≤ 2.1 GeV
$Q_{\tau_h^1} \times Q_{\tau_h^2}$	-1[OS]
$m_{\tau_h^1,\tau_h^2}$	$> 50 \& < 100$ GeV
$N(\mathrm{j}^{lead})$ & $N(\mathrm{j}^{others})$	$== 1$ & ≥ 0
$p_{\mathrm{T}}(\mathrm{j}^{lead})$ & $p_{\mathrm{T}}(\mathrm{j}^{others})$	≥ 100 & ≥ 30 GeV
$\|\eta(\mathrm{j}^{lead\&others})\|$	≤ 2.4
$Isolation(\mathrm{j}^{lead\&others})$	Loose & Tight in 2017
$N(b-jets)$	$== 0$
$Isolation(b-jets)$	Medium WP

Figure [7.21] shows the Feynman diagram associated with the CR $Z(\rightarrow \tau_h\tau_h)$ + ISR jet.

The expected number of events depend on the Z boson cross section (σ_Z), the integrated luminosity (L_{int}), the τ_h ID efficiency, the ISR efficiency (calculated in Section 7.5.1), and other possible effects. Equation (7.11) presents all factors that contribute to the expected number of events in the $Z(\rightarrow \tau_h\tau_h)$ + ISR jet CR.

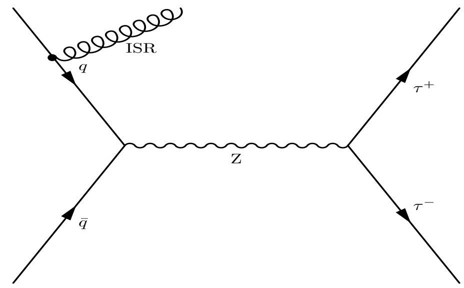

Figure 7.21: Feynman diagram associated with the $Z(\rightarrow \tau\tau)$+ISR jet production.

$$N_{Z\rightarrow\tau_h\tau_h} = \sigma_Z \cdot L_{int} \cdot \epsilon^2_{\tau_h} \cdot \epsilon_{ISR} \cdot \epsilon_{other} \quad (7.11)$$

Figure [7.22] shows $p_{\mathrm{T}}(j^{lead})$ and $p_{\mathrm{T}}(\tau_h^1)$ distributions of the $Z(\rightarrow \tau_h\tau_h)$+ISR jet CR. Note there is agreement between data and simulation cross the $p_{\mathrm{T}}(\tau_h)$ distribution.

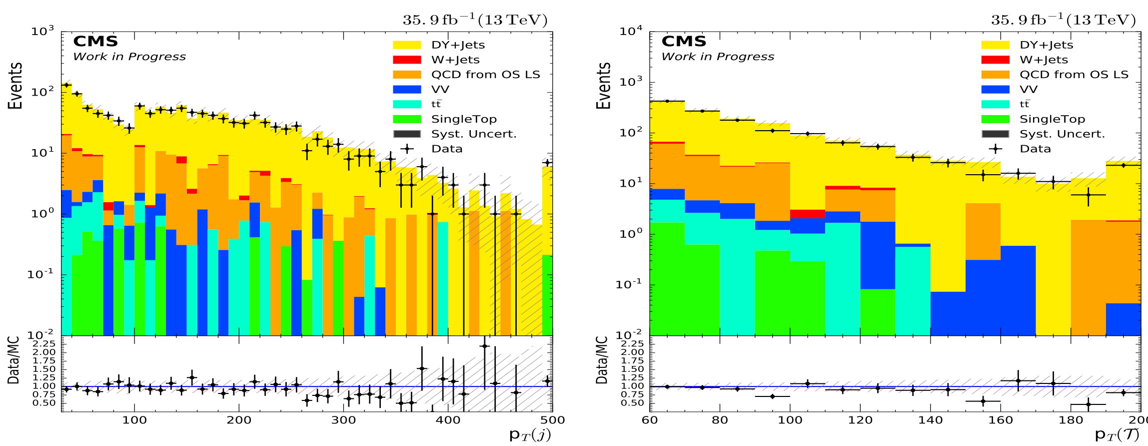

Figure 7.22: $p_{\mathrm{T}}(j^{lead})$ (left) and $p_{\mathrm{T}}(\tau_h^1)$ (right) distribution for 2016 dataset.

Figure [7.23] shows $m(\tau_h^1, \tau_h^2)$ and p_{T}^{miss} distributions. Since the topology of the final state requires exactly two taus, the QCD Multi-jets background can contribute with two jets that are misidentified as τ_h's. The electric charge of this two jets system could have either the same or opposite sign, which allows to compute a transfer factor to estimate the QCD Multi-jets contribution in this CR. Figure [7.24] shows the ABCD diagram to compute the QCD Multi-jets contribution in the $Z(\rightarrow \tau_h\tau_h)$ + ISR jet CR.

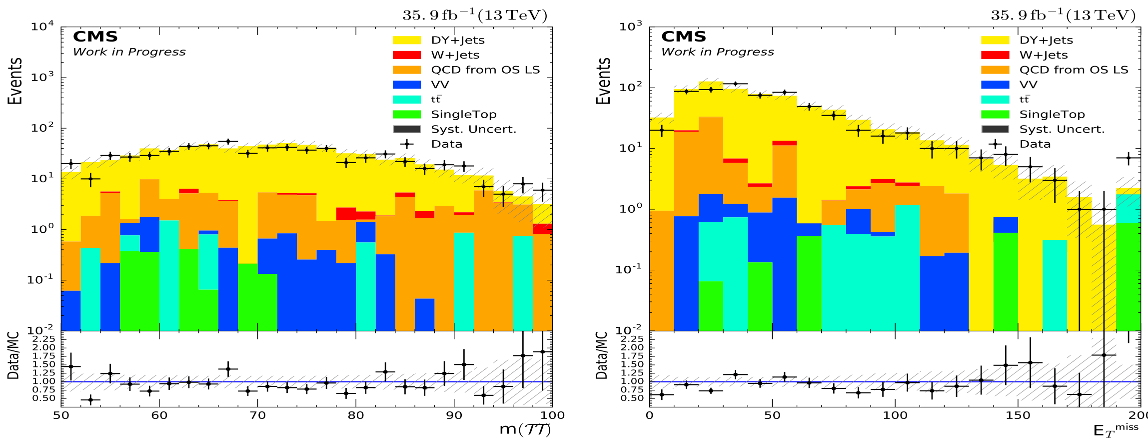

Figure 7.23**:** $m(\tau_h^1, \tau_h^2)$ (left) and p_{T}^{miss} (right) distribution for 2016 dataset.

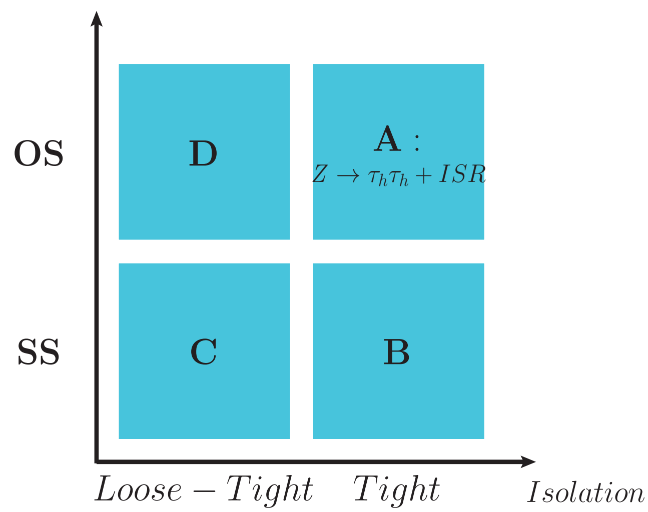

Figure 7.24**:** Definition of control regions (CR)'s for estimating the QCD-Multijets contribution in the $Z(\to \tau_h\tau_h)$ + ISR jet.

To calculate the QCD Multi-jets background in this CR (region **A**), the criterion $Q_{\tau_h^1} \times Q_{\tau_h^2}$ is switched to select events with the same-sign electric charge and all other requirements are maintained (region **B**). We will refer to this as the $CRB^{QCD}_{Z\to\tau_h\tau_h+ISR}$. The purity of the $CRB^{QCD}_{Z\to\tau_h\tau_h+ISR}$ is calculated to be $> 95\%$. The contribution of other backgrounds in CRB are subtracted from data ($W + jets$, $Z + jets$, $t\bar{t}$). The Final QCD-Multijet contribution in the $Z(\to \tau_h\tau_h)$ + ISR jet CR is calculated by taking data events in $CRB^{QCD}_{Z\to\tau_h\tau_h+ISR}$ and scale them by a factor of 1.22 ± 0.12 (1.20 ± 0.15) in 2016 (2017) datasets using Equation [7.12].

$$N_{CRA}^{data-driven} = N_{CRB}^{Data-NonQCD} \times TF_{SS}^{OS}, \tag{7.12}$$

This quantity corresponds to the charge asymmetry between QCD-Multijet events with opposite and same electric charge [113]. The transfer factor (TF) is obtained by requiring two τ_h candidates that pass `Loose` isolation requirement but fail the `Tight` requirement in the opposite-sign (**D**) region, and in the same-sign (**C**) region using Equation (7.13).

$$TF_{SS}^{OS}(data - driven) = \frac{N_{CRD}^{OS}}{N_{CRC}^{SS}} = \frac{N_{Z\to\tau_h\tau_h+ISR}^{OS}(data - driven)}{N_{Z\to\tau_h\tau_h+ISR}^{SS}(data - driven)}. \tag{7.13}$$

Table 7.11: Background and data yields in the $Z(\to\tau\tau)+$ ISR control region for 2016 and 2017 datasets.

Process	2016	2017
Data	665	801
$W + jets$	6.86 ± 1.55	8.8 ± 2.0
$Z + jets$	623.93 ± 12.57	728.1 ± 14.7
Diboson	6.32 ± 1.33	6.8 ± 1.5
$t\bar{t}$	5.24 ± 1.42	9.0 ± 2.4
QCD	69.92 ± 10.96	84.0 ± 13.2
Single Top	1.56 ± 0.53	3.2 ± 1.1
$\sum_{BG}$	713.8 ± 16.7	839.9 ± 20.1
$SF(Data/BG)$	0.92 ± 0.05	0.95 ± 0.04

The contribution of $Z + jets$ is scaled by 0.95×0.95 for 2016 data and 0.83×0.83 for 2017 data (these factors correspond to the POG recommended 5% and 17% corrections per real τ_h leg respectively). Table [7.11] shows the background and data yield for 2016 and 2017 datasets. The data-simulation ratio measured from $Z(\to\tau\tau)+$ ISR control region is 0.92 ± 0.05 and 0.95 ± 0.04, which are consistent with each other. Moreover, Figure [7.25] presents the $m_{\mathrm{T}}(\tau_h, p_{\mathrm{T}}^{miss})$ distribution for the 2016 and 2017 datasets, which shows agreement in the modelling of $Z + jets$ events. Therefore, after applying the correction factors derived so far, the expected $Z + jets$ background in the SR was taken directly from simulations.

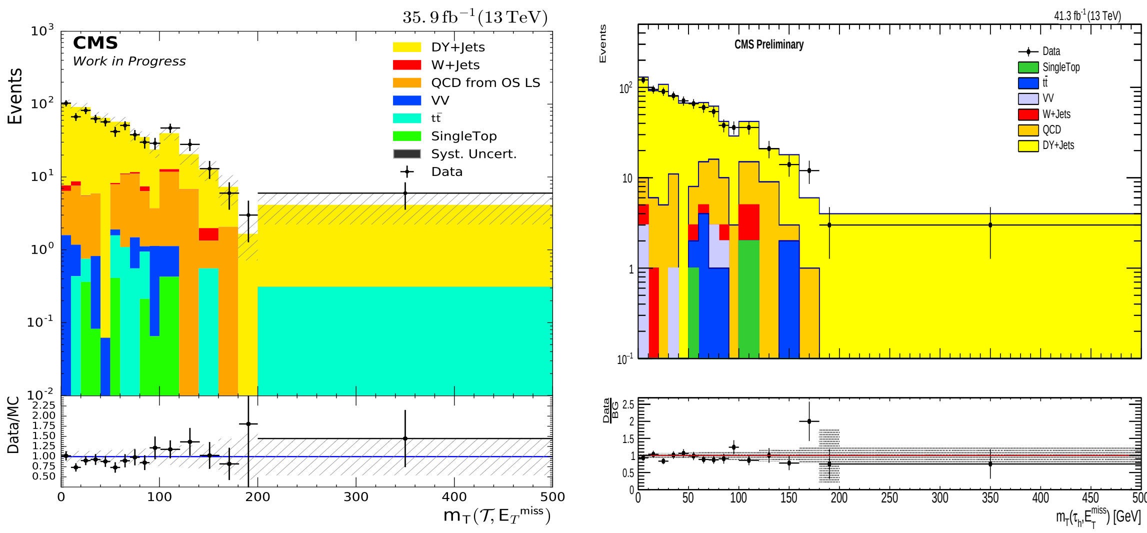

Figure 7.25: $m_{\mathrm{T}}(\tau_h, p_{\mathrm{T}}^{miss})$ distribution in the $Z(\to \tau\tau)$+ISR control region for 2016 (left) and 2017 (right) datasets.

7.5.5 $t\bar{t}$ background estimation

The estimation of the $t\bar{t}$ contribution was performed using a semi-data driven approach. For such purpose, four CR's, which are characterized by a different b-jet multiplicity and τ_h isolation requirements were studied. Figure [7.26] shows the Feynman diagram associated with the $t\bar{t}$+ISR jet production.

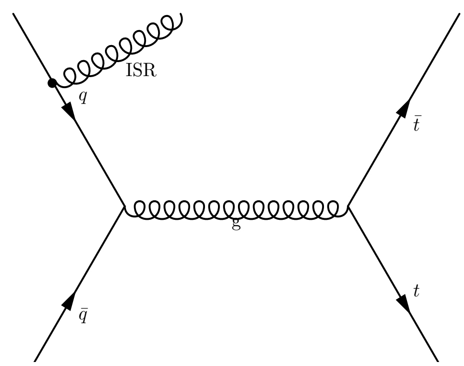

Figure 7.26: Feynman diagram associated with the $t\bar{t}$+ISR jet production.

By construction different, each CR has a different background composition and purity. The definition of each CR is presented in Table [7.12]. All the other event selection criteria are the same as in the SR.

Table 7.12: Event selection difference between the SR and different $t\bar{t}$+ISR jet CR's.

Region	$N(b-jets)$	τ ID isolation	N(Signaltracks)
SR	0	Tight	1
CR1	1	Tight	1or2or3
CR2	2	Tight	1or2or3
CR1	1	VTight	1
CR2	2	VTight	1

As mentioned before, the b-jets are vetoed in the SR and the τ_h isolation requirement is set to as `Tight`. Four CR's are built by including one or two b-jets in the final state, which naturally enhances the fraction of $t\bar{t}$ events. Also, by loosening the τ_h isolation requirement the number of QCD Multi-jets events increases. Table [7.13] presents the event selection criteria for $t\bar{t}$+jet ISR control region. The first CR requires one b-jet in the final selection, which has high purity in $t\bar{t}$ events. Nevertheless, the QCD Multi-jets contamination is non-negligible. Figure [7.27] shows $p_{\mathrm{T}}(\tau_h)$ and $m_{\mathrm{T}}(\tau_h, p_{\mathrm{T}}^{miss})$ distribution for this CR. Note the disagreement between data and MC at high-m_{T}.

Table 7.13: Event selection criteria for $t\bar{t}$+ISR jet CR's.

Criteria	Value
Trigger(p_{T}^{miss})	`HLT_PFMETNoMu120_PFMHTNoMu120_IDTight`
$N(\mathrm{j}^{lead})$ & $N(\mathrm{j}^{others})$	$== 1$ & ≥ 0
$p_{\mathrm{T}}(\mathrm{j}^{lead})$ & $p_{\mathrm{T}}(\mathrm{j}^{others})$	≥ 100 & ≥ 30 GeV
$\lvert\eta(\mathrm{j}^{lead\&others})\rvert$	≤ 2.5
$Isolation(\mathrm{j}^{lead\&others})$	Loose & Tight in 2017
$N(\tau_h)$	$== 1$
$p_{\mathrm{T}}(\tau_h)$	> 20 & < 40 GeV
$\lvert\eta(\tau_h)\rvert$	≤ 2.3
Isolation(τ_h)	Tight or VTight
Hps	Old Decay Mode Finding: 1or2or3 prongs
$N(b-jets)$	$==$ 1 or 2
QCD rejection cut	$\Delta\phi(\mathrm{j}^{lead}, p_{\mathrm{T}}^{miss}) > 0.7$
p_{T}^{miss}	> 230 GeV

The second CR requires events with exactly two b-jets in the final state, which reduces the QCD Multi-jets contribution in the full m_{T} spectrum. This CR has a better data-to-MC agreement across the full m_{T} spectrum, with respect to the first CR.

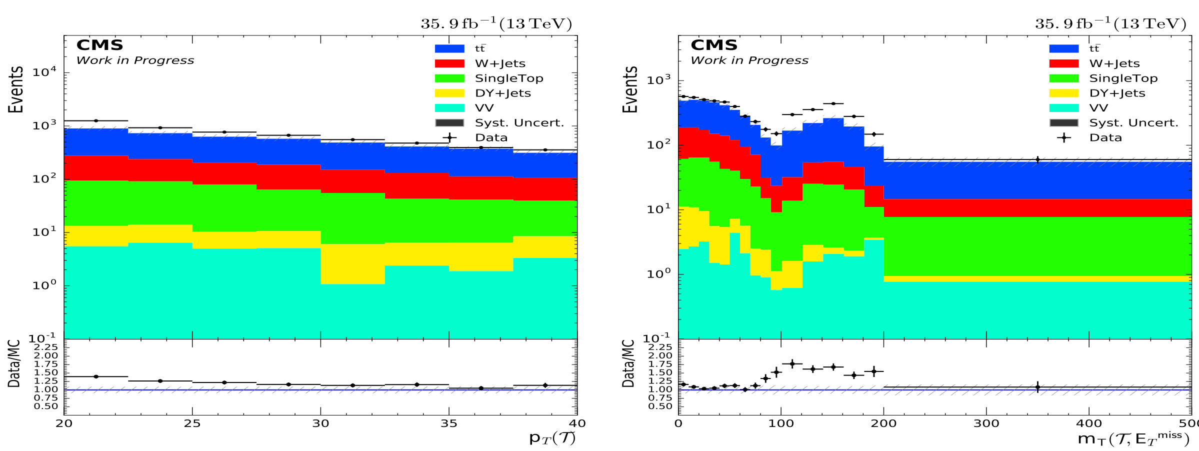

Figure 7.27: $p_{\mathrm{T}}(\tau_h)$ (left) and $m_{\mathrm{T}}(\tau_h, p_{\mathrm{T}}^{miss})$ (right) for events with exactly 1 b-jet and `Tight` ID for τ_h (2016).

Figure [7.28] shows different distributions associated with the CR1 and the CR2.

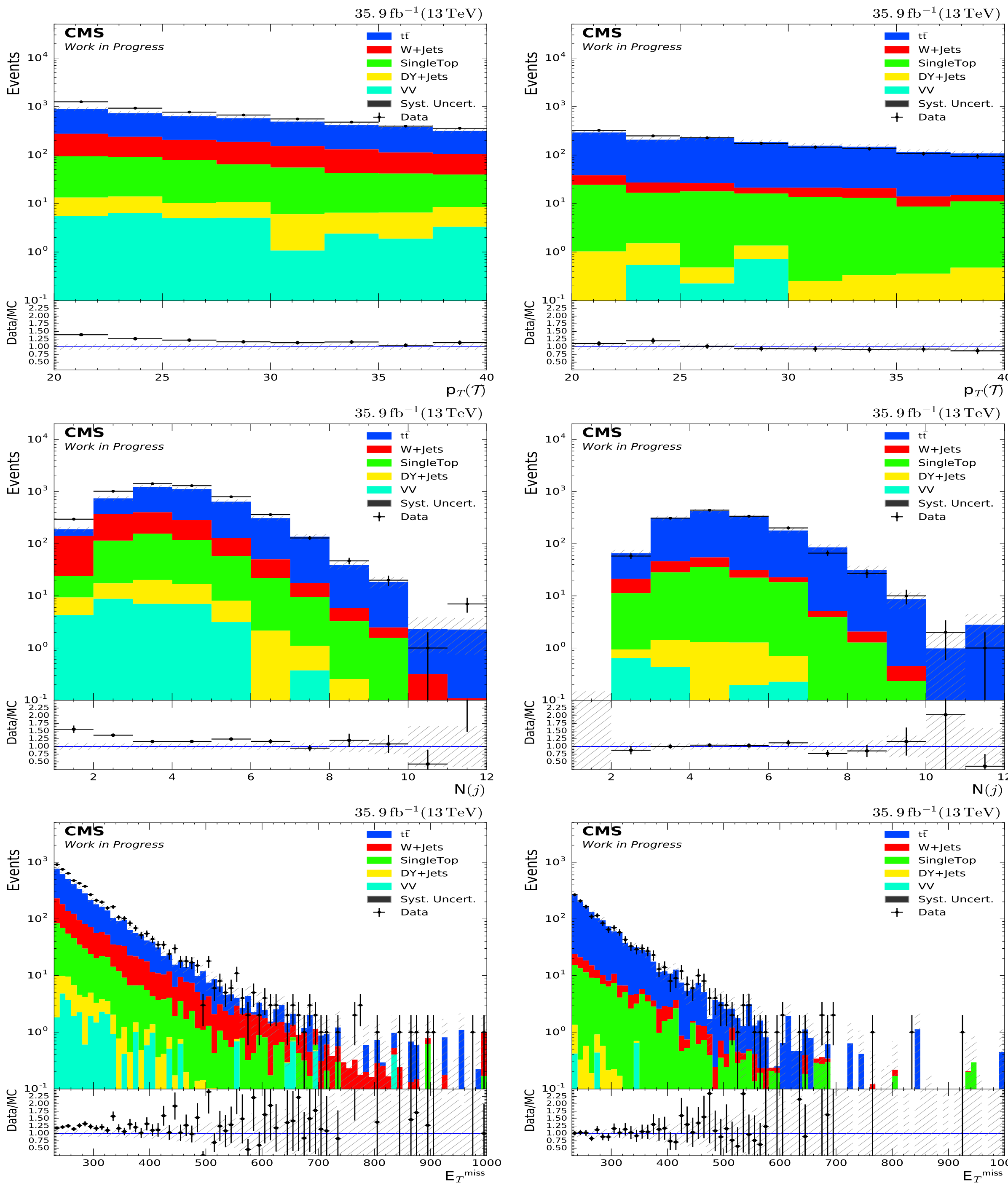

Figure 7.28: Top Row: $p_{\mathrm{T}}(\tau_h)$ with exactly 1 b-jet (left) and for 2 b-jets (right); Middle Row: Jet multiplicity with exactly 1 b-jet (left) and for 2 b-jets (right); Bottom Row: p_{T}^{miss} with exactly 1 b-jet (left) and for 2 b-jets (right) for events with `Tight` τ_h ID (2016).

Note that the data-to-MC agreement is better in all distributions in CR2. Nevertheless, to further reduce the contribution of fake-τ_h candidates CR3 and CR4 were studied. These two regions have tighter τ_h criteria, `VTight` (see Table 7.12). This selection reduces the fake rate by $\sim 50\%$. Additionally, one signal track is selected, which further reduces the fake-τ_h rate (2 signal tracks for fakes is expected). Figure [7.30] shows some relevant distributions for the CR3 and CR4. These results give a good understanding and confidence of the $t\bar{t}$ contribution in the SR. Since the m_{T}-shape is well modelled by MC yields, the contribution of this background was taken directly from the simulation. In addition, a suitable scale factor was calculated from CR4, since it had the highest purity, using the m_{T} distribution (Figure [7.29]). Table [7.14] shows all data and MC yield for the 2016 and 2017 datasets. Note there is an agreement between scale factors for 2016 and 2017 data. Finally, the deviation from unity in the data/MC ratio was fit to a degree one polynomial, and it was used to assign systematic uncertainty in the m_{T} shape in the SR (Section 7.6).

Table 7.14: Background and data yields in the CR4 for $t\bar{t}$+ISR jet events. 2016 and 2017 datasets.

Process	2016	2017
Data	783	915
$W + jets$	38.72 ± 3.32	41.0 ± 4.5
$Z + jets$	2.73 ± 0.47	1.9 ± 0.4
Diboson	0.64 ± 0.53	0.7 ± 0.7
$t\bar{t}$	705.53 ± 18.89	805.8 ± 21.7
Single Top	80.54 ± 4.35	112.1 ± 5.0
$\sum_{BG}$	828.2 ± 82.8	961.5 ± 22.7
$SF(Data/BG)$	0.94 ± 0.05	0.95 ± 0.04

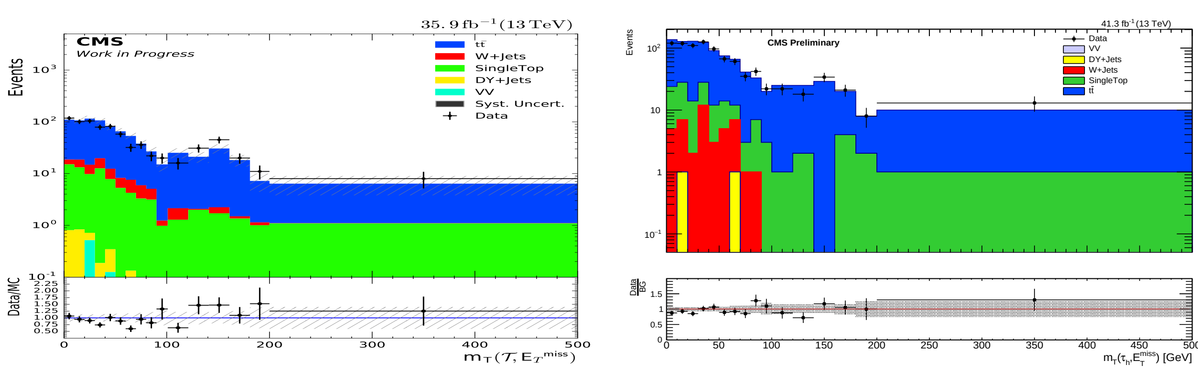

Figure 7.29: $m_{\mathrm{T}}(\tau_h, p_{\mathrm{T}}^{miss})$ distribution for the $t\bar{t}$+ISR jet in CR4. 2016 (left) and 2017 (right) datasets.

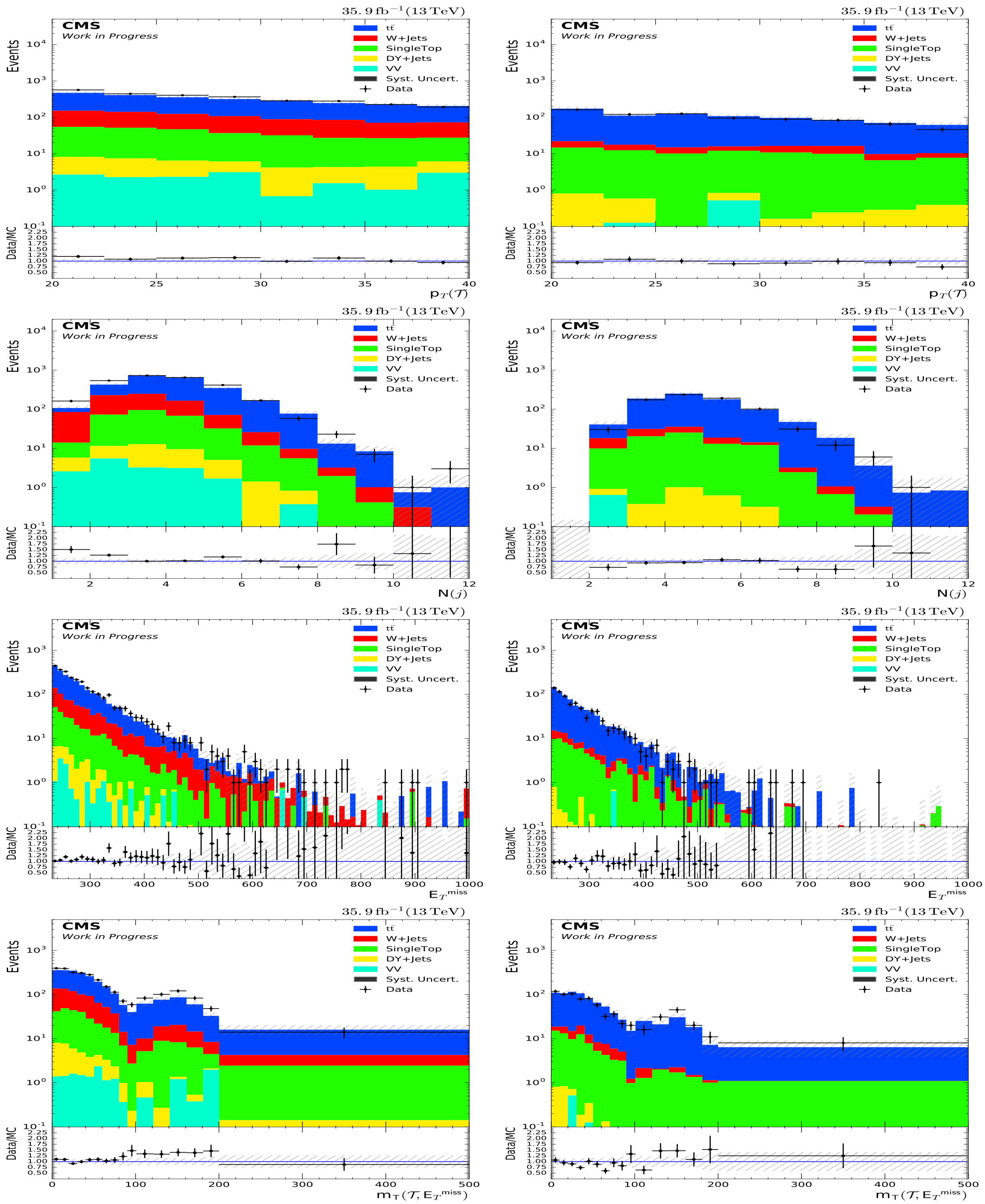

Figure 7.30: Top Row: $p_{\mathrm{T}}(\tau_h)$ with exactly 1 b-jet (left) and for 2 b-jets (right); Second Row: Jet multiplicity with exactly 1 b-jet (left) and for 2 b-jets (right); Third Row: p_{T}^{miss} with exactly 1 b-jet (left) and for 2 b-jets (right); Bottom Row: m_{T} with exactly 1 b-jet (left) and for 2 b-jets (right) for events with `VTight` ID for τ_h (2016).

7.5.6 QCD Multi-jets background estimation

To obtain the contribution of QCD Multi-jets events in the SR a semi data-driven approach was implemented, using the classic ABCD method. Three CR's enriched with QCD Multi-jets events are obtained using side-bands of the τ_h isolation requirement, and by inverting the $|\Delta\phi(\mathrm{j}^{lead}, p_{\mathrm{T}}^{miss})|$ criterion. Figure [7.31] shows a sketch of the different CR's. Events in **CRA** correspond to the nominal SR, while events in **CRB** pass the same selections as in the SR but fail the `Tight` τ_h isolation criterion and pass the `Loose` point (`Loose-Tight`). In the case of **CRE** (**F**) it has the same selections as **CRB** (**A**) but in addition the $|\Delta\phi(\mathrm{j}^{lead}, p_{\mathrm{T}}^{miss})|$ requirement is inverted. The estimation methodology consists of using data events from **CRB** to predict the shape of the m_{T} distribution for QCD Multi-jets events in the SR. There are of course several concerns that one might have: Is it possible to obtain the correct shape in the SR using events from **CRB**? How the normalization of QCD Multi-jets events can be obtained in the SR? To answer the first question, we used **CRE** and **CRF** to validate that the shape of the m_{T} distribution is not biased or strongly correlated with τ_h isolation. To address the second question, we had to find a way to measure transfer factor(s) to extrapolate from **CRB** and **CRA** to account for the difference in τ_h isolation selection. This was accomplished by using two additional CR's enriched with $Z(\rightarrow \mu\mu)$+jets and $W(\rightarrow \mu\nu)$+jets events, as shown in Figure [7.32]. Note that, **CRC** corresponds to non-isolated τ_h events (`Loose-Tight`) and **CRD** contains events passing the nominal `Tight` τ_h isolation requirement.

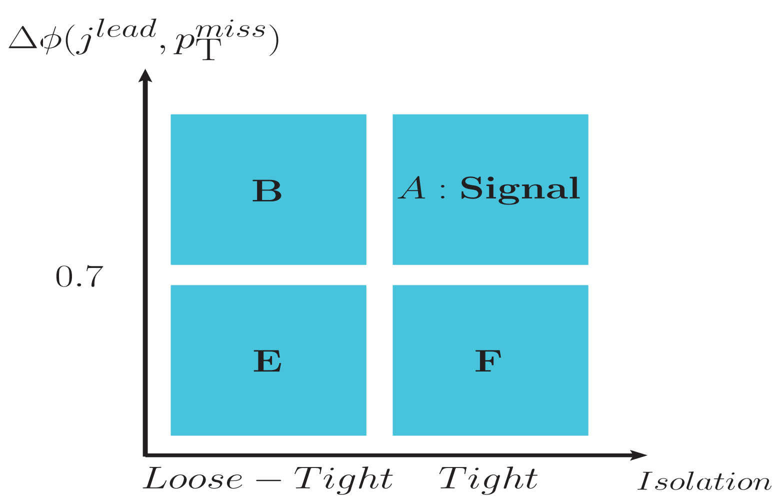

Figure 7.31: Definition of control regions CR's to estimate the QCD Multi-jets contribution in the SR.

The transfer factors are calculated as a function of $p_{\mathrm{T}}(\tau_h)$ and are obtained by dividing the number of events that pass the `Tight` requirement between the number of events that pass the

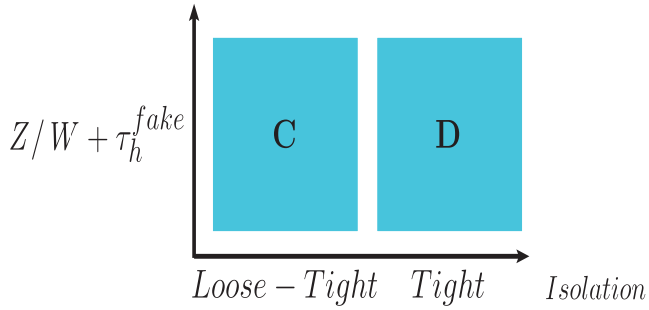

Figure 7.32: Definition of control regions (CR)'s to measure the $Ratio^{Tight}_{Loose-nonTight}$ in $Z(\rightarrow \mu\mu)+\tau_h^{fake}$ and $W(\rightarrow \mu\nu)+\tau_h^{fake}$.

`Loose-Tight` isolation requirement, which is commonly referred to as *tight to loose ratio*:

$$Ratio^{Tight}_{Loose-nonTight} = \frac{N^{Tight}_{CRD}}{N^{Loose-nonTight}_{CRC}} \tag{7.14}$$

Since $Z(\rightarrow \mu\mu)$ events are simple to select and have very low backgrounds (high purity) when an additional τ_h candidate is requested, $Z(\rightarrow \mu\mu)+\tau_h$, it is quite likely that such candidate is a jet that has been wrongly identified as a τ_h particle (fake). These events are denoted as $Z(\rightarrow \mu\mu)+\tau_h^{fake}$. Therefore, since QCD Multi-jets events are composed by jets passing τ_h identification criteria, one can then use CR's **CRC** and **CRD** to derive the $p_{\mathrm{T}}(\tau_h)$-dependent transfer factors and use these factors to extrapolate from **CRB** to the SR.

The estimation of the expected number of QCD Multi-jets events in the SR is performed using Equation (7.15), where $N^{data-nonQCD}_{CRB}$ corresponds to the number of events in data that fall in CRB after subtracting the contribution of other non-QCD Multi-jets backgrounds using simulation, and $Ratio^{Tight}_{Loose-nonTight}$ are the $p_{\mathrm{T}}(\tau_h)$ dependent transfer factors obtained from CR's **CRC** and **CRD**. The Feynman diagrams associated with these CR's are shown in Figure [7.33].

$$N^{data-driven}_{SR} = N^{data-nonQCD}_{CRB} \times Ratio^{Tight}_{Loose-nonTight}(p_{\mathrm{T}}(\tau_h)). \tag{7.15}$$

The event selection criteria that defines the CR's previously described are summarized in Table [7.15]. The $Z(\rightarrow \mu\mu)+\tau_h^{fake}$ CR requires a well-identified muon pair, with opposite electric charge, dimuon invariant mass that falls within the $Z-$peak, and a τ_h candidate (fake) passing the same identification selections as in the SR. The second CR, $W(\rightarrow \mu\nu)+\tau_h^{fake}$ requires one muon and a τ_h candidate (fake). In both CR's, there is spurious p_{T}^{miss} associated with the mismeasurement of jets in $Z(\rightarrow \mu\mu)+\tau_h^{fake}$ and real p_{T}^{miss} from the production of

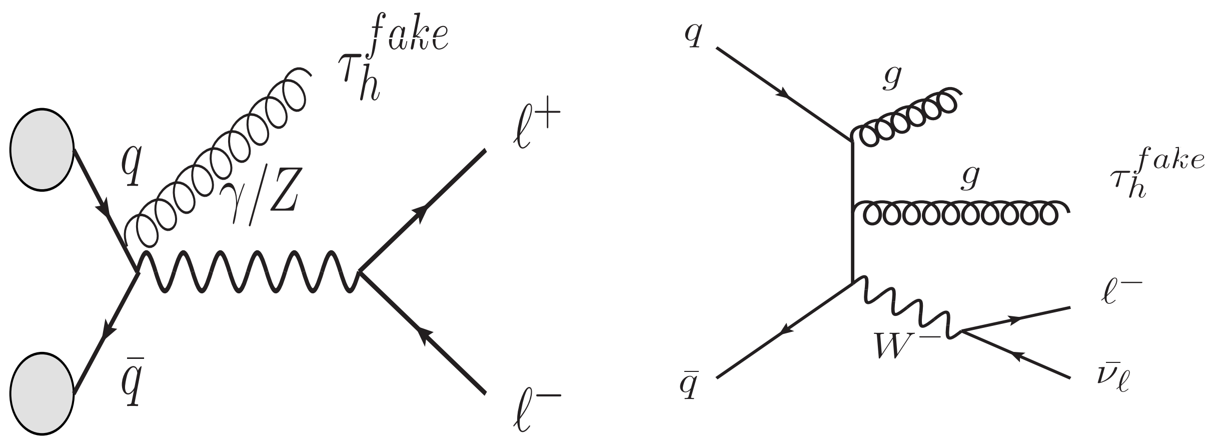

Figure 7.33: Feynman diagrams associated with $Z(\rightarrow \mu\mu) + \tau_h^{fake}$ and $W(\rightarrow \mu\nu) + \tau_h^{fake}$ CR's to estimate QCD Multi-jets via fully data-driven approach.

a muon-neutrino in the $W(\rightarrow \mu\nu) + \tau_h^{fake}$ CR. After subtracting the contribution of other backgrounds in data using simulation in each CR, the $Ratio^{Tight}_{Loose-nonTight}$ is calculated using Equation (7.16). For the $Z(\rightarrow \mu\mu) + \tau_h^{fake}$ CR, the number of events is calculated as $(data - nonZ + jets)$ and for the $W(\rightarrow \mu\nu) + \tau_h^{fake}$ CR the number of events is estimated as $(data - non W + jets)$.

Table 7.15: Event selection criteria for $Z(\rightarrow \mu\mu) + \tau_h^{fake}$ and $W(\rightarrow \mu\nu) + \tau_h^{fake}$.

Criteria	$Z(\rightarrow \mu\mu) + \tau_h^{fake}$	$W(\rightarrow \mu\nu) + \tau_h^{fake}$
Trigger	`HLT_IsoMu24_`	`HLT_IsoMu24_`
$N(\mu)$	2	1 & Veto on other μ
$p_{\mathrm{T}}(\mu)$	≥ 30 GeV	≥ 30 & ≥ 10 GeV
$\lvert\eta(\mu)\rvert$	≤ 2.1	≤ 2.1
$p_{\mathrm{T}}(\tau_h)$	$> 20 \& < 40$ GeV	$> 20 \& < 40$ GeV
$\lvert\eta(\tau_h)\rvert$	≤ 2.1	≤ 2.1
$Q(\mu_1) \times Q(\mu_2)$	-1	-
$N(e^-) \& N(b - jets)$	-	$== 0$
$p_{\mathrm{T}}(e^-)$	-	≥ 10 GeV
$p_{\mathrm{T}}(b - jets)$	-	≥ 30 GeV
p_{T}^{miss}	≥ 30 GeV	≥ 30 GeV
$m(\mu_1, \mu_2)$	$> 70 \& < 110$ GeV	-
$m_{\mathrm{T}}(\mu, p_{\mathrm{T}}^{miss})$	-	$> 50 \& < 120$ GeV

$$Ratio^{Tight}_{Loose-nonTight}(data - driven) = \frac{N^{Tight}_{CRD}}{N^{Loose-nonTight}_{CRC}} = \frac{N^{Tight}_{Z/W+jets}(data - driven)}{N^{Loose-nonTight}_{Z/W+jets}(data - driven)} \quad (7.16)$$

Figure [7.34] shows the $p_{\mathrm{T}}(\tau_h)$ distributions for events passing `Tight` isolation (left) and for events passing the `Loose` but failing `Tight` isolation requirement (right) in the $Z(\rightarrow \mu\mu) + \tau_h^{fake}$ region. After subtracting other backgrounds from data, the $Ratio^{Tight}_{Loose-nonTight}$ is calculated in each bin of the $p_{\mathrm{T}}(\tau_h)$. Figure [7.35] shows the behavior of this ratio for the 2016 (left) and 2017 (right) datasets. The errors deployed in Figure [7.35] are only statistical. Table [7.16] presents the different $Ratio^{Tight}_{Loose-nonTight}$ in bins of $p_{\mathrm{T}}(\tau_h)$ and their associated statistical uncertainties for the 2016 and 2017 datasets, measured in the $Z(\rightarrow \mu\mu) + \tau_h^{fake}$ CR. Note that the weights are consistent for 2016 and 2017 data. In order to reduce systematic uncertainties in the QCD Multi-jets background prediction, these values are fitted with a polynomial of degree one, which is also shown in Figure [7.35].

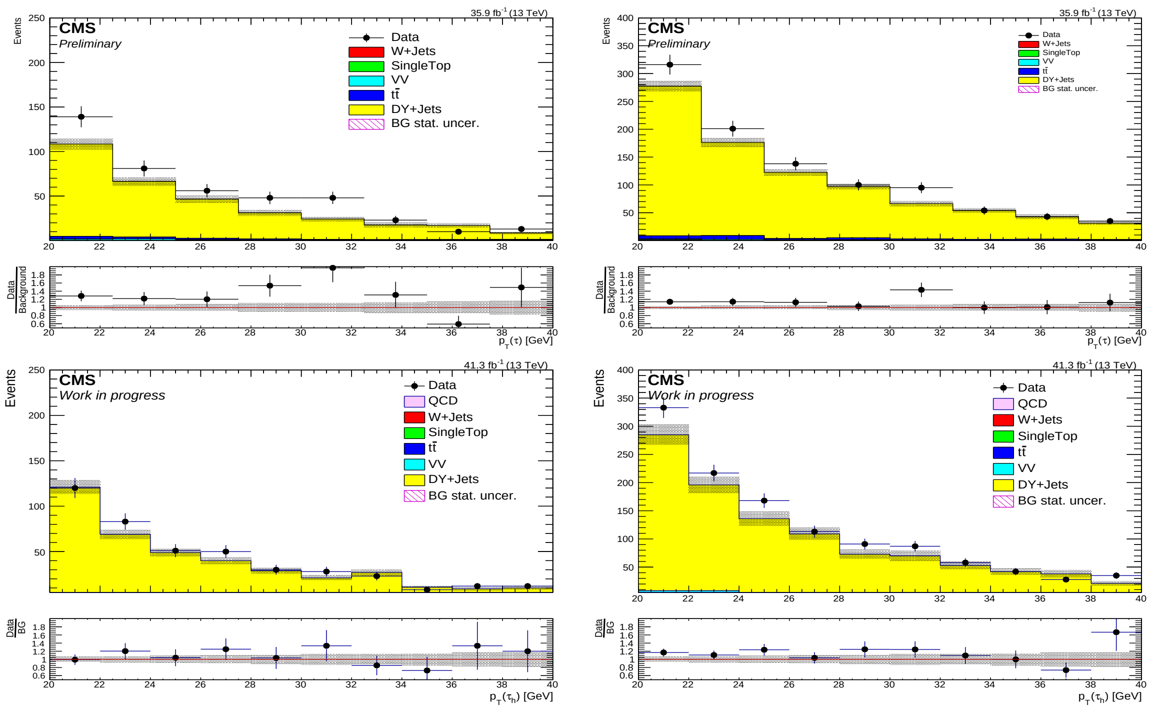

Figure 7.34: Top (Bottom) row: $Z(\rightarrow \mu\mu)+\tau_h^{fake}$ region, `Tight` (left) and `Loose-Tight` isolation requirement for 2016 and (2017) data and simulation.

The selection criteria used to obtain the $W(\rightarrow \mu\nu) + \tau_h^{fake}$ CR is outlined in Table [7.15] as well. For this CR, Figure [7.36] shows the $p_{\mathrm{T}}(\tau_h)$ distributions for events passing `Tight` isolation (left) and for events passing `Loose` but failing `Tight` (right). After subtracting other backgrounds from data, the $Ratio^{Tight}_{Loose-nonTight}$ is calculated as function of $p_{\mathrm{T}}(\tau_h)$, as done in the $Z(\rightarrow \mu\mu) + \tau_h^{fake}$ CR. Figure [7.37] shows the behavior of this ratio for the 2016 (left) and 2017 (right) datasets. The errors deployed in Figure [7.37] are only statistical. Table [7.17] presents the different $Ratio^{Tight}_{Loose-nonTight}$ in bins of $p_{\mathrm{T}}(\tau_h)$ and their associated statistical uncertainties

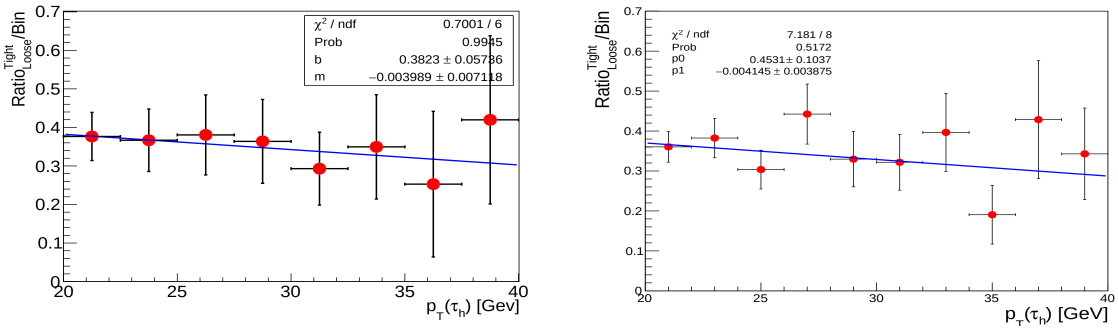

Figure 7.35: $p_{\mathrm{T}}(\tau_h)$ dependence of the $Ratio^{Tight}_{Loose-nonTight}$ in the $Z(\rightarrow \mu\mu) + \tau_h^{fake}$ region for 2016 and (2017) datasets, left (right).

Table 7.16: Region $Z(\rightarrow \mu\mu) + \tau_h^{fake}$: $Ratio^{Tight}_{Loose-nonTight}$ values in each bin of $p_{\mathrm{T}}(\tau_h)$ for 2016 and 2017 datasets.

2016		2017	
$p_{\mathrm{T}}(\tau_h)$ [GeV]	$Ratio^{Tight}_{Loose-nonTight}$	$p_{\mathrm{T}}(\tau_h)$ [GeV]	$Ratio^{Tight}_{Loose-nonTight}$
$[20, 22.5]$	0.37 ± 0.06	$[20, 22]$	0.36 ± 0.04
$[22.5, 25]$	0.36 ± 0.08	$[22, 24]$	0.38 ± 0.05
$[25, 27.5]$	0.38 ± 0.10	$[24, 26]$	0.30 ± 0.05
$[27.5, 30]$	0.36 ± 0.10	$[26, 28]$	0.44 ± 0.08
$[30, 32.5]$	0.29 ± 0.09	$[28, 30]$	0.33 ± 0.07
$[32.5, 35]$	0.34 ± 0.13	$[30, 32]$	0.32 ± 0.07
$[35, 37.5]$	0.25 ± 0.19	$[32, 34]$	0.40 ± 0.10
$[37.5, 40]$	0.42 ± 0.22	$[34, 36]$	0.19 ± 0.07
-	-	$[36, 38]$	0.43 ± 0.15
-	-	$[38, 40]$	0.34 ± 0.11

for the 2016 and 2017 datasets. Note that the weights are consistent for 2016 and 2017 data. As in the previous CR these values are fitted with a polynomial of degree one.

The weights obtained from $Z(\rightarrow \mu\mu) + \tau_h^{fake}$ region are used in the final QCD Multi-jets prediction since this CR has a better purity than the $W(\rightarrow \mu\nu) + \tau_h^{fake}$ CR. The weights obtained in the $W(\rightarrow \mu\nu) + \tau_h^{fake}$ CR were used to perform a closure test and assign systematic uncertainty on the QCD Multi-jets prediction in the SR. As mentioned before, to obtain the QCD Multi-jets contribution in the SR we take the shape of the $m_{\mathrm{T}}(\tau_h, p_{\mathrm{T}}^{miss})$ distribution from the CRB, and we re-weight the shape using the measured $Ratio^{Tight}_{Loose-nonTight}$. This methodology is considered a data-driven approach. Because the $p_{\mathrm{T}}(\tau_h)$ is correlated with the $m_{\mathrm{T}}(\tau_h, p_{\mathrm{T}}^{miss})$ distribution, we created a 2D histogram to re-weight the $m_{\mathrm{T}}(\tau_h, p_{\mathrm{T}}^{miss})$ distribution in the non-isolated region to obtain this distribution in the SR. To address the question: Can we

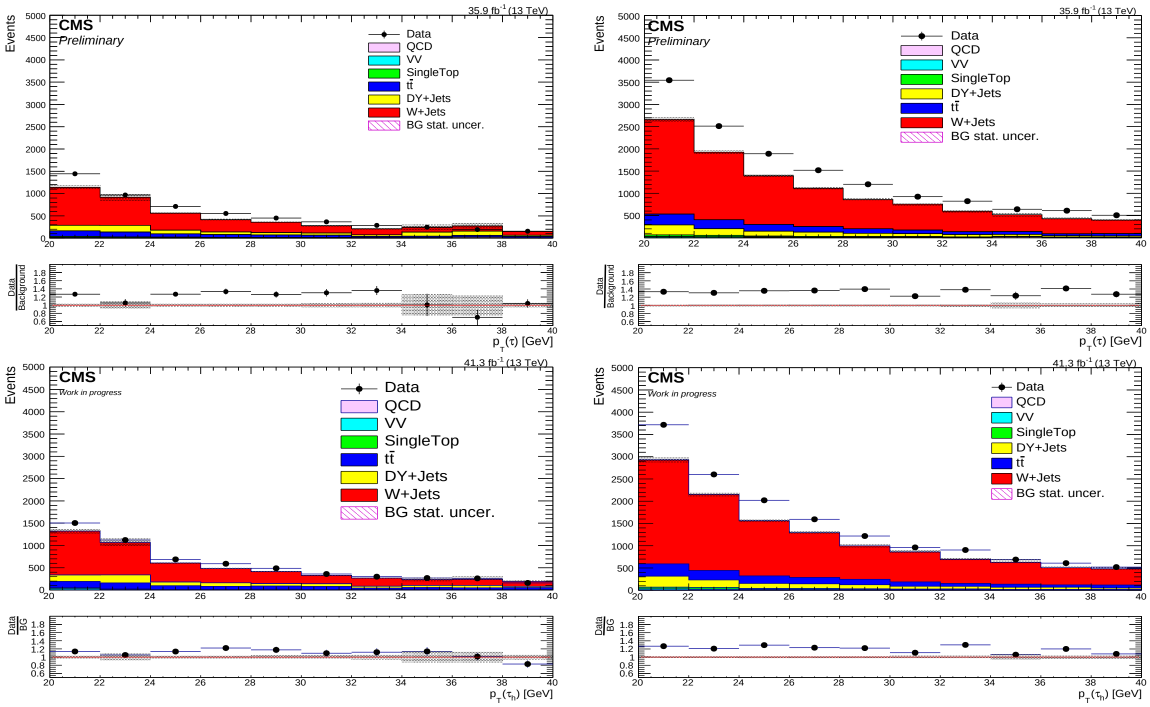

Figure 7.36: Top (Bottom) row: $W(\to \mu\nu) + \tau_h^{fake}$ region, `Tight` (left) and `Loose-Tight` isolation requirement for 2016 and (2017) data and simulation.

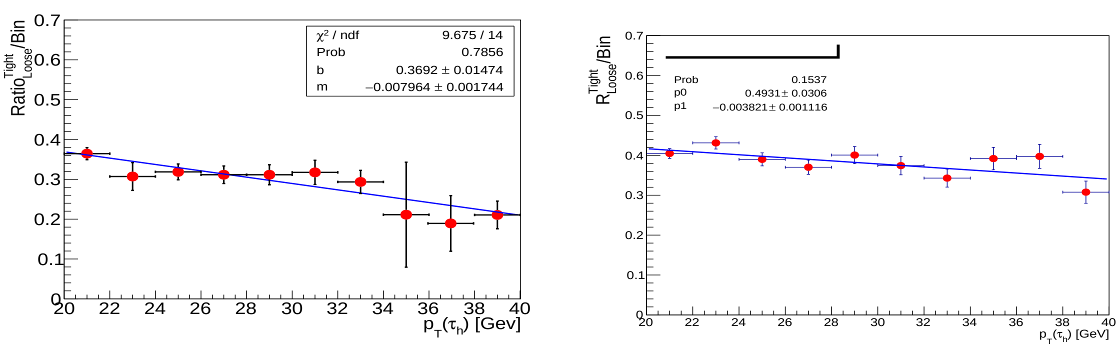

Figure 7.37: $p_T(\tau_h)$ dependence of $Ratio^{Tight}_{Loose-nonTight}$ in the $W(\to \mu\nu) + \tau_h^{fake}$ region for 2016 and (2017) datasets, left (right).

obtain the correct shape in the SR? We performed a closure test in data by using the enriched QCD Multi-jets regions (CRE and CRF) described in Figure [7.31]. In such case, we predict the QCD Multi-jets contribution in the CRF (isolated) by re-weighting the 2D histogram obtained from CRE (non-isolated), after subtracting the non-QCD contributions from MC.

Figure [7.38] (left) presents the 2D template to estimate QCD Multi-jets events in the isolated region (CRF), which has been re-binned to the optimized SR binning of the

Table 7.17: Region $W(\rightarrow \mu\nu) + \tau_h^{fake}$: $Ratio^{Tight}_{Loose-nonTight}$ values in each bin of $p_{\mathrm{T}}(\tau_h)$ for 2016 and 2017 datasets.

2016		2017	
$p_{\mathrm{T}}(\tau_h)$ [GeV]	$Ratio^{Tight}_{Loose-nonTight}$	$p_{\mathrm{T}}(\tau_h)$ [GeV]	$Ratio^{Tight}_{Loose-nonTight}$
$[20, 22]$	0.36 ± 0.01	$[20, 22]$	0.40 ± 0.01
$[22, 24]$	0.30 ± 0.03	$[22, 24]$	0.43 ± 0.02
$[24, 26]$	0.31 ± 0.01	$[24, 26]$	0.39 ± 0.02
$[26, 28]$	0.31 ± 0.02	$[26, 28]$	0.37 ± 0.02
$[28, 30]$	0.31 ± 0.02	$[28, 30]$	0.40 ± 0.02
$[30, 32]$	0.31 ± 0.03	$[30, 32]$	0.37 ± 0.02
$[32, 34]$	0.29 ± 0.02	$[32, 34]$	0.34 ± 0.02
$[34, 36]$	0.21 ± 0.13	$[34, 36]$	0.39 ± 0.03
$[36, 38]$	0.20 ± 0.06	$[36, 38]$	0.40 ± 0.03
$[38, 40]$	0.21 ± 0.03	$[38, 40]$	0.31 ± 0.03

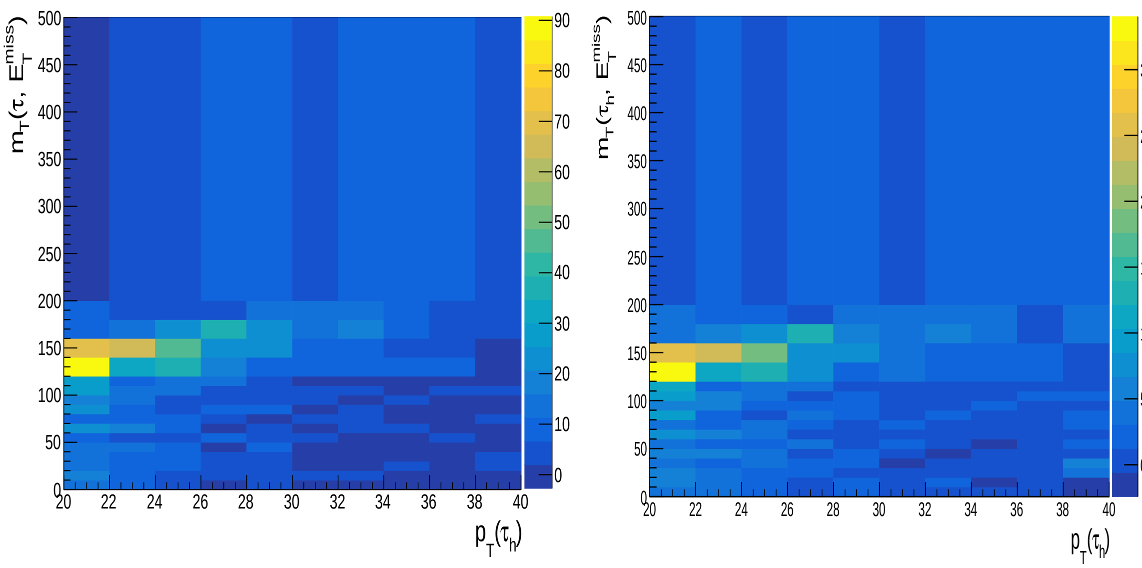

Figure 7.38: 2D histogram represents the response template to predict QCD Multi-jets events. CRE (left) and after applying weights CRF (right), which are a function of $m_{\mathrm{T}}(\tau_h, p_{\mathrm{T}}^{miss})$ and $p_{\mathrm{T}}(\tau_h)$. The expected histogram in CRF is obtained using the $Ratio^{Tight}_{Loose-nonTight}$ yields in the region $W(\rightarrow \mu\nu) + \tau_h^{fake}$.

$m_{\mathrm{T}}(\tau_h, p_{\mathrm{T}}^{miss})$. Figure [7.38] (right) is the re-weighted histogram using the $Ratio^{Tight}_{Loose-nonTight}$, which would be the QCD Multi-jets contribution in region CRF. Using this response template, Figure [7.39] shows the prediction of QCD Multi-jets events in the CRF using the $Ratio^{Tight}_{Loose-nonTight}$ obtained through the fully data-driven method from $Z(\rightarrow \mu\mu) + \tau_h^{fake}$ (left) and $W(\to \mu\nu) + \tau_h^{fake}$ (right). This closure test is performed for both 2016 (first row) and 2017 (second row) datasets and MC. Note there is agreement between data and the background prediction, which supports the QCD Multi-jets prediction in the SR using this approach.

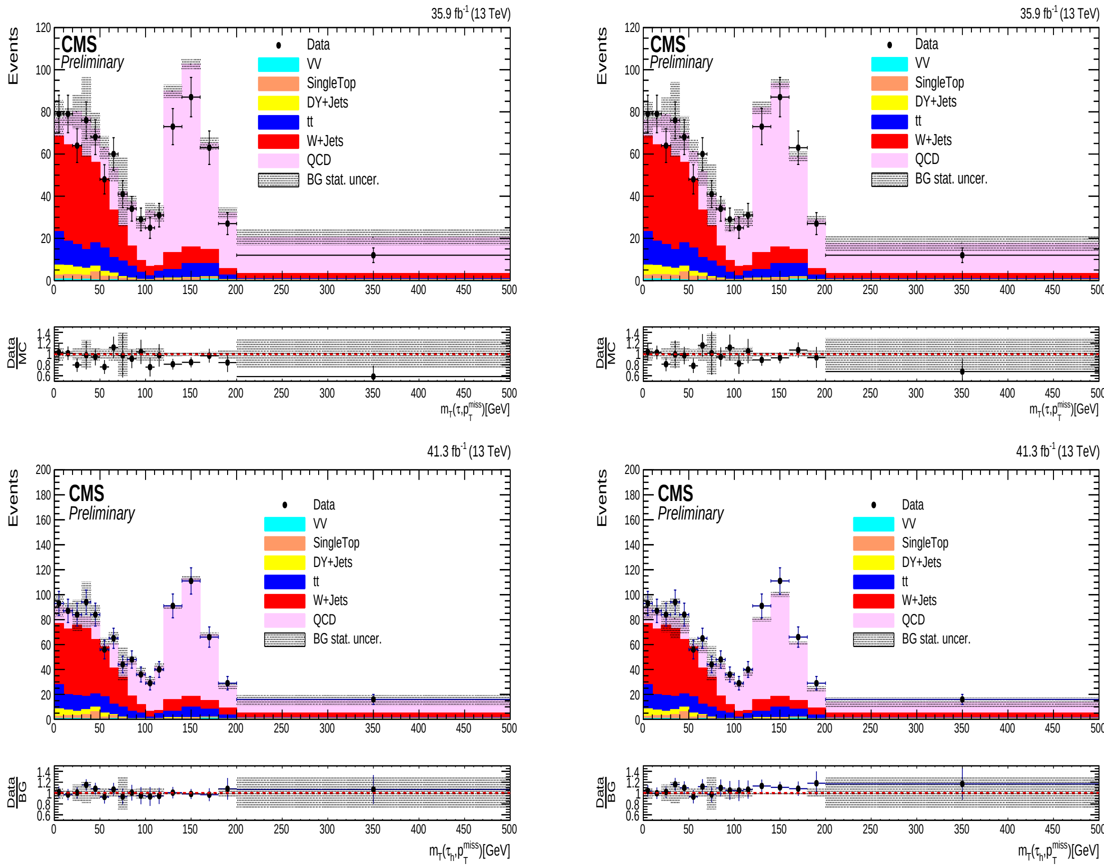

Figure 7.39: Final yield of QCD Multi-jets events in CRF. The 2D histogram is re-weighted for Z weights (left) and W weights (right) for 2016 (above) and 2017 (below) datasets.

The final closure test is predicting the QCD Multi-jets contribution using only MC information as described this method. We use the 2D histogram obtained from QCD MC in CRE, and we predict the yield of QCD Multi-jets background in CRF by re-weighting the histogram with the $Ratio^{Tight}_{Loose-nonTight}$. Figure [7.40] presents the yield that is consistent within the statistical uncertainties for 2016 (left) and 2017 (right). The agreement between data and the predicted background information gives further confidence to estimate the QCD Multi-jets component in the SR using the fully data-driven approach.

Finally, the 2D histogram correlation between $p_{\mathrm{T}}(\tau_h)$ and $m_{\mathrm{T}}(\tau_h, p_{\mathrm{T}}^{miss})$ and the $Ratio^{Tight}_{Loose-nonTight}$ obtained from fully data-driven methods establish a robust method of

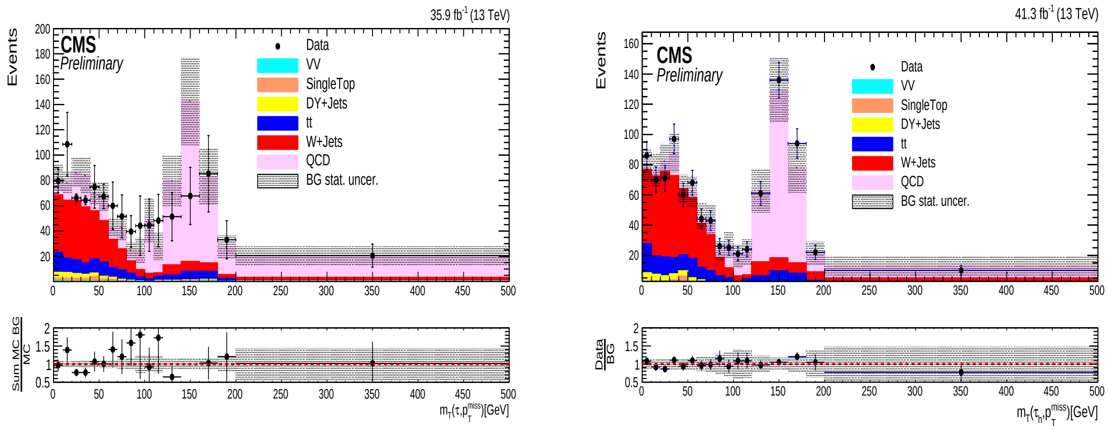

Figure 7.40**:** QCD Multi-jets prediction in CRF using the shape extracted from MC in CRE for 2016 (left) and 2017 (right) datasets.

estimation. The shape of $m_{\mathrm{T}}(\tau_h, p_{\mathrm{T}}^{miss})$ distribution is taken from CRB (as is described in Figure [7.31]), which is SR-like but the τ_h isolation cut is inverted. Table [7.18] summarizes the expected yield of this background in the SR for 2016 and 2017 datasets.

Table 7.18**:** Summary of the expected yields for QCD Multi-jets background in the SR.

Weights/Region	2016	2017
	$N_{SR}^{data-driven}$	$N_{SR}^{data-driven}$
$Z(\rightarrow \mu\mu) + \tau_h^{fake}$	1530.4 ± 18.6	1480.0 ± 16.8
$W(\rightarrow \mu\nu) + \tau_h^{fake}$	1359.9 ± 13.4	1508.0 ± 14.9

Section 7.6

Systematic uncertainties

Different sources of systematic uncertainty were considered in the analysis. Systematic uncertainties associated with the Parton distribution function (PDF) set used in the simulation, the uncertainty associated with the estimation of the luminosity collected by the CMS detector, uncertainties associated with the identification of the objects used in the analysis (leptons, jets, p_{T}^{miss}), among others, were included.

The uncertainties considered in the analysis are described in the subsections that follow.

7.6.1 PDFs

The systematic effect due to the PDF is obtained by comparing the default `CTEQ6.6L` used in signal with respect to the `MSTW2008nnlo` and `NNPDF20` [114] sets. The maximal deviation from the central value in the default PDF, in the expected number of events, is used as a systematic uncertainty. The maximum value found was 6.0%.

7.6.2 Initial state radiation (ISR)

In Section 7.5.1, the weights and their statistical uncertainties to correct the ISR modelling are shown. The uncertainties are a function of the $p_{\mathrm{T}}(Z)$. This statistical component varies from 1-3% at low values of $p_{\mathrm{T}}(Z)$ up to $\approx 14\%$ for high values of $p_{\mathrm{T}}(Z)$ as is shown in Table [7.19].

Table 7.19: Relative statistical uncertainties for the Z-Boost.

Z-Boost Bin [GeV]	Weight Uncertainty
1: 0-50	2.23%
2: 50-100	1.21%
3: 100-150	1.09%
4: 150-200	1.18%
5: 200-300	1.29%
6: 300-400	1.95%
7: 400-600	3.23%
8: 600-1000	14.45%

To study the possible variations of shape and normalization of the $m_{\mathrm{T}}(\tau_h, p_{\mathrm{T}}^{miss})$ distribution, we vary the values of these weights up and down by 1σ, where σ is the statistical uncertainty presented in Table [7.19]. For the main backgrounds, $Z + jets$ and $W + jets$, the effect on the shape is studied in the SR. Figure [7.41] shows the systematic effect associated with the weight statistical uncertainties in the SR for $Z + jets$ (left) and $W + jets$ (right). The red line corresponds with the central value of the weights and the blue (green) line is the variation of the weights up (down) by 1σ. This systematic uncertainty is known as shape-based uncertainty, which is as much as 15% for high values. In addition, a normalization uncertainty of 1% is applied to $Z + jets$, $W + jets$, and signal yields in the final limit.

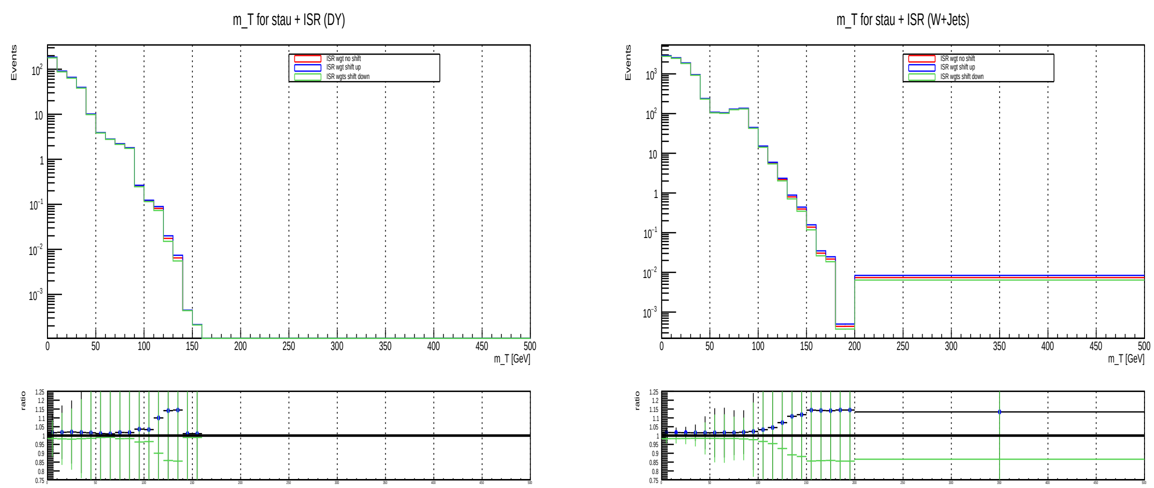

Figure 7.41: Comparison of the $m_{\mathrm{T}}(\tau_h, p_{\mathrm{T}}^{miss})$ distributions by changing the value of the ISR-weight by $\pm\sigma$ for the $Z + jets$ (left) and $W + jets$ (right) simulations.

7.6.3 Luminosity (L_{int})

A 2.5% uncertainty on the measured luminosity, which is reported by the LHC-luminosity report [115] was considered.

7.6.4 Trigger and object identification

To extract a systematic uncertainty associated with the Trigger, we performed a fit on the trigger turn-on curve. The value that was obtained was 3%.

On the other hand, a 6% uncertainty on the τ_h identification efficiency was included, following the POG recommendation. Finally, systematic uncertainties for the muons and electrons identification up to $\approx 2\%$ were included.

7.6.5 B-Tagging efficiency

We considered the mismeasured rate of b-jets by the b-tagging POG [116], which is around $\approx$ 10%. The systematic uncertainty on the requirement of 0 jets misidentified as b-jets is driven by propagating the $\approx$ 10% using the following Equation (it is the signal efficiency for requiring 0 jets miss-tagged as b-jets):

$$\epsilon^{\mathrm{NBtag}<1} = 1 - \sum_{n=1} P(n) \cdot \sum_{m=1}^{n} C(n,m) \cdot f^m \cdot (1-f)^{n-m} \tag{7.17}$$

where $P(n)$ is the probability to obtain n additional jets (which are non-tau and non-lepton) in the event, $C(n,m)$ is the combinatorial of n *choose* m, and f the mistagging rate. The probability to obtain at least one additional jet in the event is $\approx$ 10%. Hence, the probability to obtain at least one jet has the systematic effect of $\approx$ 1%. In addition, the b-tagging and mistagging rates are correlated for backgrounds with similar composition, which have no real b-jets such as $Z + jets$ and $W + jets$ but are uncorrelated for backgrounds with a different composition such as $Z + jets$ and $t\bar{t}$. These b-jets uncertainties follow the POG recommendations.

7.6.6 Tau energy scale

The tau POG recommendation on the energy scale is 5% for the signal acceptance. The four-momentum must be scaled by a factor $k = 1.05$ or 0.95 ($p_{smeared} = k \cdot p_{original}$) and all variables are recalculated using this new four-momentum. Hence, the shape variations of the $m_{\mathrm{T}}(\tau_h, p_{\mathrm{T}}^{miss})$ are taken into account in the final limit calculation [117].

7.6.7 Electron energy scale

We considered an effect on the signal acceptance efficiency of a 1% (2.5%) on the electron energy scale in the barrel (endcap) region. The systematic uncertainty is less than 1% [118].

7.6.8 Muon momentum scale

The effect of signal acceptance is around 1% for the muon momentum scale uncertainty. The systematic uncertainty is less than 1% [119].

7.6.9 Jet energy scale

An effect of 2$-$5% on the jet energy scale uncertainty on the signal acceptance, which is recommended by the JetMet POG, was considered. For the maximum value (5%) the four-momentum must be scaled by $k = 1.05$ or 0.95 ($p_{smeared} = k \cdot p_{original}$) and all variables are recalculated using this new four-momentum. Hence, the shape variations of the $m_{\mathrm{T}}(\tau_h, p_{\mathrm{T}}^{miss})$ are taken into account in the final limit calculation [120].

7.6.10 p_{T}^{miss} scale

The uncertainty associated to the p_{T}^{miss} is driven by light leptons energy/momentum scale (LES), tau energy scale (TES), jet energy scale (JES), and unclustered energy (UCE) [121], described above. A 10% uncertainty on the UCE creates at most a 0.5% fluctuation in the signal acceptance.

7.6.11 Additional shape systematics

In the CR's, shape-based uncertainties based on the deviation to the unity of the data/MC ratio were assigned. By fitting the data/MC ratio with a polynomial of degree 1, the data-MC agreement on the $m_{\mathrm{T}}(\tau_h, p_{\mathrm{T}}^{miss})$ shape was parametrized. Figure [7.42] shows the data/MC ratio as a function of $m_{\mathrm{T}}(\tau_h, p_{\mathrm{T}}^{miss})$ in the $Z \to \tau_h\tau_h$ and $t\bar{t}$ CR's and their the fitting respectively, which results in a systematic effect of up to $\approx 20\%$.

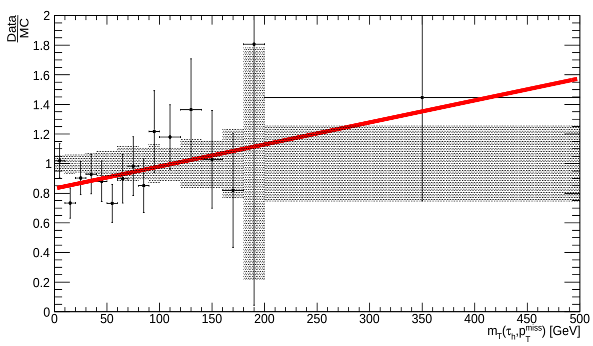

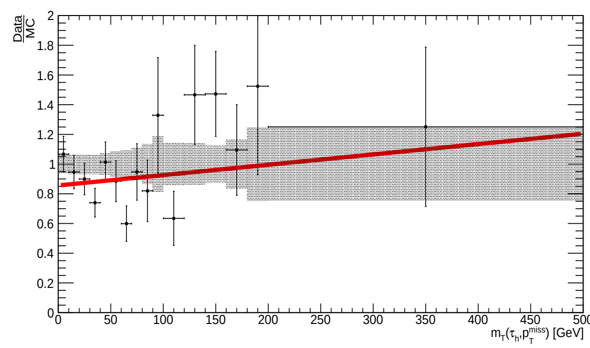

Figure 7.42**:** data/MC ratio as a function of $m_{\mathrm{T}}(\tau_h, p_{\mathrm{T}}^{miss})$ in the $Z \to \tau\tau$ and $t\bar{t}$ control region. The deviation from the flat perfect result is treated as a systematic uncertainty.

7.6.12 Non-QCD background closure/normalization

Since the background estimation uses scale factors to correct the simulation yields, which are obtained from the different CR's, the deviation of the data-MC ratio from unity is assigned as the systematic uncertainty of such scale factors.

7.6.13 QCD background closure/normalization

We used the $Ratio^{Tight}_{Loose-nonTight}$ to obtain the normalization factor driven by $Z(\rightarrow \mu\mu)+\tau_h^{fake}$ events for the QCD Multijets background in the signal region. Since the weights were also measured using $W(\rightarrow \mu\nu) + \tau_h^{fake}$ events, a systematic uncertainty on the difference of the result with respect to the nominal $Z + jets$ weights were used. Table [7.20] shows the relative difference between weights in both regions, which is propagated bin-by-bin in the $m_{\mathrm{T}}(\tau_h, p_{\mathrm{T}}^{miss})$ distribution. This effect is a shape-based systematic uncertainty.

Table 7.20: Values of the $Ratio^{Tight}_{Loose-nonTight}$ for each bin of $p_{\mathrm{T}}(\tau_h)$ in $W(\rightarrow \mu\nu) + \tau_h^{fake}$ and $Z(\rightarrow \mu\mu) + \tau_h^{fake}$ regions.

	$Ratio^{Tight}_{Loose-nonTight}$		
$p_{\mathrm{T}}(\tau_h)$ [GeV]	$W(\rightarrow \mu\nu) + \tau_h^{fake}$	$Z(\rightarrow \mu\mu) + \tau_h^{fake}$	R. Difference
$[20, 22]$	0.361 ± 0.039	0.378 ± 0.268	4.5%
$[22, 24]$	0.345 ± 0.033	0.371 ± 0.227	7.0%
$[24, 26]$	0.329 ± 0.028	0.363 ± 0.191	9.3%
$[26, 28]$	0.313 ± 0.024	0.355 ± 0.163	11.8%
$[28, 30]$	0.298 ± 0.022	0.347 ± 0.146	14.1%
$[30, 32]$	0.282 ± 0.022	0.339 ± 0.146	16.8%
$[32, 34]$	0.266 ± 0.024	0.332 ± 0.163	19.8%
$[34, 36]$	0.250 ± 0.028	0.324 ± 0.191	22.8%
$[36, 38]$	0.234 ± 0.033	0.316 ± 0.227	25.9%
$[38, 40]$	0.218 ± 0.039	0.308 ± 0.268	29.2%

7.6.14 Summary of systematic uncertainties

Table [7.21] summarizes all systematic uncertainties for this analysis.

Table 7.21: Systematic uncertainties of this analysis. All values are given in percentage and s is referred to as shape variations.

Source	$W + jets$	$Z + jets$	$t\bar{t}$	VV	QCD-Multijets	Signal
Luminosity	2.5	2.5	2.5	2.5	2.5	2.5
ID(μ)	< 1	< 1	< 1	< 1	< 1	1
ID(e)	< 1	< 1	< 1	< 1	< 1	1
ID(τ_h)	6	8	9	9	–	9
ID($b - jets$)	2	2	7	2	2	2
Trigger	3	3	3	3	3	3
JES	s	s	s	s	–	s
TES	s	s	s	s	–	s
MMS	< 1	< 1	< 1	< 1	–	< 1
EES	< 1	< 1	< 1	< 1	–	< 1
Pileup	5	5	5	5	–	5
Pdf	4.8	4.8	4.2	3.5	–	6.0
bin-by-bin stat	s	s	s	s	–	s
Closure+Norm	2	8	6	–	23	–
j^{ISR}	s	s	–	–	–	s
Prefiring	–	–	–	–	–	s
Gen. Scale	1	1	3.5	–	–	2
Fast Sim.	–	–	–	–	–	s
$Ratio^{Tight}_{Loose-nonTight}$	–	–	–	–	s	–

Section 7.7

Results and discussion

Before presenting the final results, we summarize the different steps of the analysis as follows.

- The trigger efficiency was studied as a function of the p_{T} of the leading jet in the event and as a function of p_{T}^{miss}. The optimal values to be on the plateau of the efficiency turn-on curve are $p_{\mathrm{T}}^{miss} > 230$ GeV and $p_{\mathrm{T}}(j^{lead}) > 100$ GeV. These values prove to be consistent with the values found in the phenomenological study.

- After applying the p_{T}^{miss} and $p_{\mathrm{T}}(j^{lead})$ thresholds, motivated by the constraints related with the behavior of the trigger efficiency, the $p_{\mathrm{T}}(\tau_h)$ value was obtained through maximizing the signal significance using the $N_S/\sqrt{N_S + N_B}$ figure of merit. A $20 < p_{\mathrm{T}}(\tau_h) < 40$ GeV selection was applied, which is consistent with the phenomenological approach: $15 < p_{\mathrm{T}}(\tau_h) < 35$ GeV. The difference lies in the experimental threshold for the τ_h reconstruction at CMS, which is $p_{\mathrm{T}}(\tau_h)_{min} = 20$ GeV.

- The data-simulation agreement for the different backgrounds was studied in dedicated CR's. For some backgrounds, correction factors were derived in order to scale properly the prediction from the simulation in the SR, while the prediction of QCD Multi-jets events was conducted following a data-driven approach. The summary of the main steps to estimate the background is presented below.

  1. The modelling of the ISR-jet in the simulation was studied. This led to obtain a set of weights to correct the expected kinematics associated Z production, which is boosted due to the presence of the ISR-jet, as well as to establish a scale factor to correct the p_{T}^{miss} modelling. The weights were obtained using a $Z + jets$ CR. A closure test was performed using simulation. Systematic uncertainties on the normalization and shapes were obtained using a complementary $W + jets$ CR to derive the weights.
  2. To verify the simulation of $W + jets$ events an emulation technique of the τ_h kinematics using muons was developed. The emulation showed good agreement between the observed data and the background expectation in both, shape and normalization. This emulation is based on muon data set in some SR side-band, where the selection criteria is SR-like but the $p_{\mathrm{T}}(\tau_h)$ is set to $(40 \leq p_{\mathrm{T}}(\tau_h) \leq 60)$ GeV. This shape analysis is only used for closure purposes.
  3. To estimate the ID efficiency of the τ_h candidate, an enriched CR with $Z \to \tau_h\tau_h$ events were studied. This CR led to estimate a scale factor to correct the $Z + jets$

background contribution in the SR. Furthermore, this measurement of the scale factor required to include the POG recommendation per τ leg 0.95/(0.83) for 2016/(2017).

4. The $t\bar{t}$ background contribution in the SR was studied using a set of CR's. These CR's had different isolation criteria and a number of identified b-jets. The $t\bar{t}$ contribution in the SR was obtained by scaling the MC simulation by a factor of 0.94 ± 0.05 for the 2016 dataset.

5. Since QCD Multi-jets events are not properly modelled in simulation, the contribution of this background in the SR requires a fully data-driven approach. By measuring the so-called Tight-Loose ratios in dedicated $Z \to \mu\mu\tau_h^{fake}$ and $W \to \mu\nu\tau_h^{fake}$ CR's, the QCD Multi-jets events are calculated extrapolating the events in the non-isolated region using the $p_{\mathrm{T}}(\tau_h)$ dependent ratios. Additionally, a closure test based upon the regions where $\Delta\phi(j^{lead}, p_{\mathrm{T}}^{miss}) < 0.7$ was performed. This closure test validated the methodology to estimate the QCD Multi-jets events in this analysis.

- All possible sources of systematic uncertainties were studied, which were propagated in the final upper limit accordingly.

We present the results in the compressed mass spectra scenario where $\Delta m(\tilde{\chi}_1^{\pm}, \tilde{\chi}_1^0) = 50$ GeV. The inclusive channel was studied where $Br(\tilde{\chi}_2^0 \to \tilde{\tau}\tau \to \tau\tau\tilde{\chi}_1^0) = Br(\tilde{\chi}_1^{\pm} \to \nu\tilde{\tau} \to \nu\tau\tilde{\chi}_1^0) = 100\%$.

Figure [7.43] shows the final $m_{\mathrm{T}}(\tau_h, p_{\mathrm{T}}^{miss})$ distribution in the SR. The dominant backgrounds are $W + jets$ and $Z + jets$, in this plot the signal is multiplied by a factor of 10. The background prediction is in agreement with the observed data, ruling out the possibility of physics beyond the standard model. The result is interpreted under the MSSM, assuming R-parity conservation. The analysis focused on the production of $\tilde{\tau}$ particles through electroweak processes, considering direct pair-production with an associated ISR jet and through cascade of $\tilde{\chi}_1^{\pm}$ and $\tilde{\chi}_2^0$, as described in Table [6.1]. Furthermore, the composition of $\tilde{\chi}_1^{\pm}$ and $\tilde{\chi}_2^0$ was considered wino-like (they belong to same gauge multiplet), assuming mass degeneracy between the $\tilde{\chi}_2^0$ and the $\tilde{\chi}_1^{\pm}$ ($m(\tilde{\chi}_2^0) = m(\tilde{\chi}_1^{\pm})$. Finally, the $m(\tilde{\tau})$) was parametrized as:

$$m(\tilde{\tau}) = m(\tilde{\chi}_1^0) + K(m(\tilde{\chi}_1^{\pm}) - m(\tilde{\chi}_1^0)), \tag{7.18}$$

where K determines the $m(\tilde{\tau})$ composition, which is set to $K = 0.5$, in a democratic scenario where the mixing is 50%/50%.

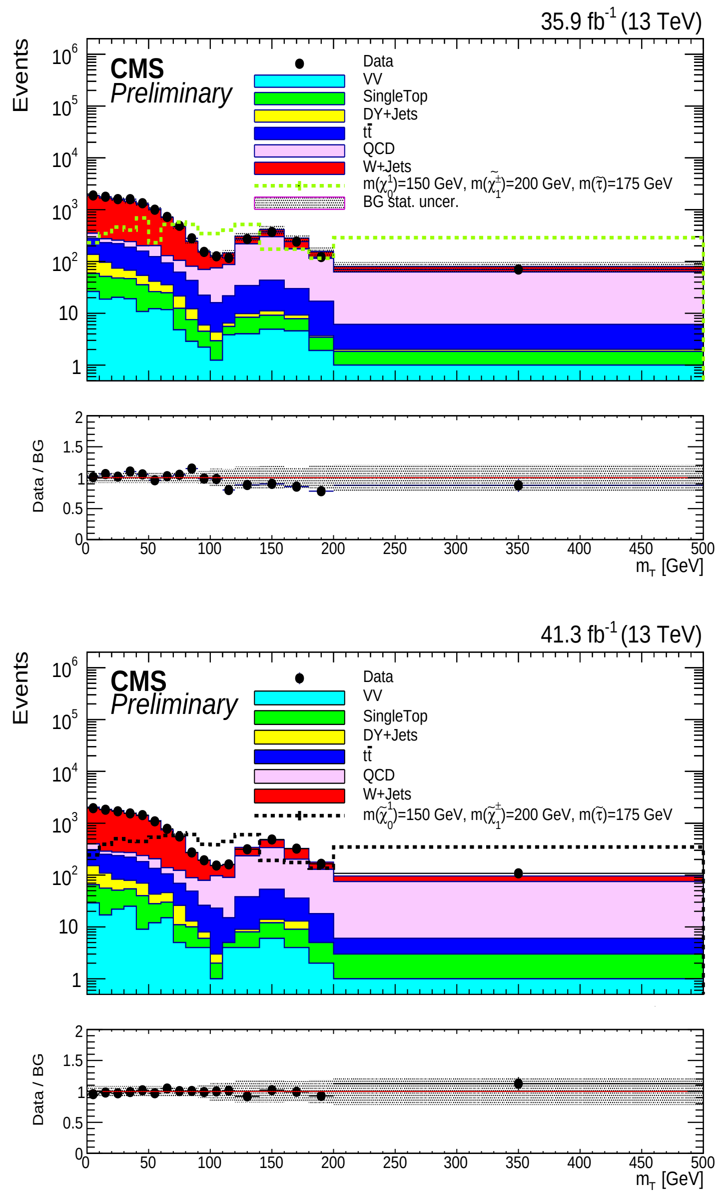

Figure 7.43: $m_{\mathrm{T}}(\tau_h, p_{\mathrm{T}}^{miss})$ distributions in the SR (unblinded) for 2016 (left) and 2017 (right) datasets. Note that, there is not evidence of new physics in the all $m_{\mathrm{T}}(\tau_h, p_{\mathrm{T}}^{miss})$ spectrum.

Figure [7.44] shows the observed and expected upper limit at 95% confidence level on the cross-section, for the observed data, the expected background and the theoretical prediction. The upper limit was calculated following a profile-binned likelihood approach, using the transverse mass distribution between the τ_h and the p_{T}^{miss}, with the full CL_s estimator. The Higgs limit tool, which is the recommended software at CMS collaboration for that purpose [122], was used to estimate the limits. The limit tool works using the yields of data, background, and signal. In addition, all systematic and statistical uncertainties were included as nuisance parameters. To construct the binned likelihood, input data cards with the corresponding yields per bin were used. Correlations among systematic effects were taken into consideration, using a correlation matrix built in each data card, following the recommended format in the Higgs Limit tool guidelines. One card per bin per mass signal point was produced. The cards for a given signal point were combined using a script provided by the Higgs tool.

In Figure [7.44], the solid black line corresponds to the observed upper limit, the dashed-black-line represents the expected limit using the background-only hypothesis, and the blue line is the theoretical prediction. The green and yellow bands represent the one and two sigma deviation from the expected limit, respectively. The upper limit is referred to the value of the chargino mass ($m(\tilde{\chi}_1^{\pm})$) where the observed limit crosses the theoretical prediction. For this experimental analysis $\tilde{\chi}_2^0/\tilde{\chi}_1^{\pm}$ masses are excluded up to 290 GeV for the compressed scenario defined by $\Delta m(\tilde{\chi}_1^{\pm}, \tilde{\tau}) = 25$ GeV.

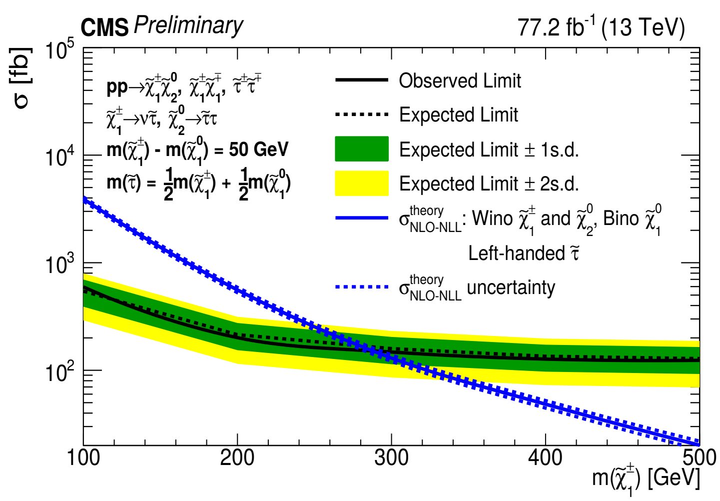

Figure 7.44: Expected and observed upper limit for the cross section at 95% of confidence level as a function of $m(\tilde{\chi}_2^0) = m(\tilde{\chi}_1^{\pm})$. The color bands represent one and two standard deviations for the background-only hypothesis.

Figure [7.45] shows the observed upper limit cross section at 95% of confidence level, for the direct $\tilde{\tau}$ pair production as a function of $m(\tilde{\tau})$ and $\Delta m(\tilde{\tau}, \tilde{\chi}_1^0)$. The bottom plot presents the upper limit as a function of the $m(\tilde{\tau})$, in the particular case where the $\Delta m(\tilde{\tau}, \tilde{\chi}_1^0)$ is set to 50 GeV. These results are better than other $\tilde{\tau}$ searches. $\tilde{\chi}_1^{\pm}/\tilde{\chi}_2^0$ masses are excluded up to 230 GeV [123] at CMS, and $\tilde{\chi}_2^0$ masses are excluded up to 150 GeV [124] at ATLAS, for compressed mass spectra searches.

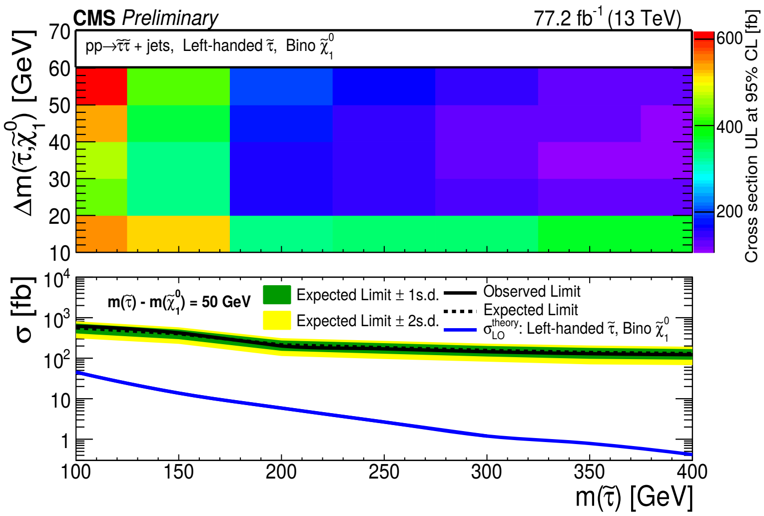

Figure 7.45**:** Expected and observed upper limit for the cross section at 95% of confidence level as a function of $\Delta m(\tilde{\tau}, \tilde{\chi}_1^0)$ and $m(\tilde{\tau})$. The bottom canvas represents the upper limit for the direct $\tilde{\tau}$ production cross section at 95% of confidence level. The compressed mass spectra scenario is set by the $\Delta m(\tilde{\tau}, \tilde{\chi}_1^0) = [10, ..., 50]$ GeV.

This search has exceeded the sensitivity from previous searches, including results reported by LEP experiment [125, 126].

Section 7.8

Contribution to the analysis at CMS

The specific contributions of the author of this thesis are summarized here:

- Performed all the studies related to the trigger performance, described in Section 7.3, using 2016 data and simulation.
- Studied the p_{T}^{miss} and $p_{\mathrm{T}}(j^{lead})$ trigger correlation in the trigger, described in Section 7.3.3, using 2016 data.
- Performed the optimization studies to establish the selections for the $p_{\mathrm{T}}(\tau_h)$, $p_{\mathrm{T}}(j^{ISR})$, and p_{T}^{miss} (at the end determined by the trigger), as shown in Section 7.4.
- Performed studies to determine the $m_{\mathrm{T}}(\tau_h, p_{\mathrm{T}}^{miss})$ as the main discriminating observable to search for the presence of signal events.
- Performed studies to implement the $\Delta\phi(jet^{lead}, p_{\mathrm{T}}^{miss})$ criterion to reject QCD, described in Section 7.5.6.

- Developed the technique and performed the study for the emulation of the kinematics of τ's using μ's to emulate $W \rightarrow \tau\nu$+jets background, as described in Section 7.5.3.

- Developed the technique, with the help of the co-conveners of the Exotica group, to estimate the QCD Multi-jets background with 2016 data, described in Section 7.5.6.

- Performed the shape systematic uncertainty estimation associated with the $Ratio^{Tight}_{Loose-nonTight}$ for each bin of $p_{\mathrm{T}}(\tau_h)$, described in Section 7.5.6.

It is important to mention that this work would not have been possible without the support and guidance from Professor Andrés Floréz from the University Los Andes, my thesis advisor, Professor Alfredo Gurrola from the Vanderbilt University, who is my Co-advisor, and Ph.D candidate Savanna Starko from the Vanderbilt University, who worked actively in this experimental analysis for both datasets. I would like to stress that my contributions are the ones detailed above for 2016 data. I also would like to deeply express my gratitude to each one of the scientists mentioned above, for the guidance and outpouring support provided during my Ph.D studies.

CHAPTER 8

Conclusions

In this research, we explored the compressed mass spectra scenarios using the data collected by the CMS detector during 2016 and 2017. The data corresponding to a total cumulative integrated luminosity of 77.2 fb^{-1}, for proton-proton collisions at a center of mass energy of $\sqrt{s} = 13$ TeV. The compressed mass spectra scenario is referred to a kinematic region where the mass gap between the $\tilde{\tau}$ and the $\tilde{\chi}_1^0$ must be small. This requirement was motivated for the direct connection between the cosmology and the thermal production of dark matter through SUSY models. In which, to obtain the observed value of the relic dark matter density $\Omega_{DM}h^2 = 0.1186 \pm 0.002$ using SUSY, the mass gap is set to $\Delta m(\tilde{\tau}, \tilde{\chi}_1^0) = 50$ GeV. At experimental level, nevertheless, this kinematic region has been difficult to prove in previous searches.

At phenomenological level, we explored the feasibility of this analysis by including an ISR-jet in the final state, which naturally generates a boosting to the event. In addition, selection criteria of high p_{T}^{miss} and low momentum for the τ_h candidate ($20 < p_{\mathrm{T}}(\tau_h) < 40$ GeV) showed an improvement of the relation the signal events and the expected background prediction for the compress spectra region. The $m_{\mathrm{T}}(\tau_h, p_{\mathrm{T}}^{miss})$ distribution was used to obtain the expected sensitivity. For the experimental study, no data excess was observed above the expected background prediction from the SM processes. The results were interpreted based upon the MSSM in the context of the R-parity conservation. Expected and observed limits were obtained at 95% confidence level using the fully CL_s estimator. $\tilde{\chi}_2^0/\tilde{\chi}_1^{\pm}$ masses are excluded up to 290 GeV, which exceed the previous limits for the compressed mass spectra region. Additionally, this exclusion limit allows to the theorist's other interpretations depending on the model. The ISR-jet technique is expected to be a tool to explore this kind of experimental searches for the future cumulative luminosity of the CMS detector (Run-III).

Ethic considerations are supported by the regular procedure to submit any experimental analysis inside the CMS collaboration. The JSON files showed in Chapter 7 validate the confidence of data for physics analyses. Besides, the collaboration has several steps to guarantee the quality of physics contribution. These steps are commonly known as: pre-approval, approval (unblinded SR), CWR, and final reading. This thesis presents an analysis that has been submitted through CMS filters to obtain the final contribution of this search.

References

[1] Griffiths, David, *Introduction to elementary particles*, John Wiley & Sons, 2008

[2] Yang, Chen Ning, *Elementary particles*, volume 2181, Princeton University Press, 2015

[3] Feltesse, Joël, "Introduction to deep inelastic scattering: past and present," *inspirehep*, 2012, inspirehep:1229668

[4] Abachi, So, Abbott, B, Abolins, M, Acharya, BS, Adam, I, Adams, DL, Adams, M, Ahn, S, Aihara, H, Alitti, J, *et al.*, "Observation of the top quark," *Physical Review Letters*, volume 74, no. 14, p. 2632, 1995, arxiv:9902013

[5] Brandelik, R, Braunschweig, W, Gather, K, Kadansky, V, Lübelsmeyer, K, Mättig, P, Martyn, H-U, Peise, G, Rimkus, J, Sander, HG, *et al.*, "Evidence for planar events in e+ e- annihilation at high energies," *Physics Letters B*, volume 86, no. 2, pp. 243–249, 1979, sciencedirect:037026937990830

[6] Rubbia, Carlo, "Experimental observation of the intermediate vector bosons W+, W-, and Z 0," *Reviews of Modern Physics*, volume 57, no. 3, p. 699, 1985, CERN:166082

[7] Chatrchyan, Serguei, Khachatryan, Vardan, Sirunyan, Albert M, Tumasyan, Armen, Adam, Wolfgang, Aguilo, Ernest, Bergauer, T, Dragicevic, M, Erö, J, Fabjan, C, *et al.*, "Observation of a new boson at a mass of 125 GeV with the CMS experiment at the LHC," *Physics Letters B*, volume 716, no. 1, pp. 30–61, 2012, sciencedirect:0370269312008581

[8] Beringer, J. *et al.*, *Particle Data Group*, Lawrence Berkeley National Laboratory, 2012, http://pdg.lbl.gov/

[9] Branco, Gustavo C, Lavoura, Luis, and Silva, Joao Paulo, *CP violation*, Oxford University Press & Sons, 1999

[10] Cronin, JW, "The discovery of CP violation," *The European Physical Journal H*, volume 36, no. 4, pp. 487–508, 2012, 10.1140/epjh/e2011-20057-4

[11] Kane, Gordon L, *Modern elementary particle physics*, Addison-Wesley, 1993

[12] Greiner, Walter and Maruhn, Joachim A, *Symmetries*, Springer, 1996

[13] Dummit, David Steven and Foote, Richard M, *Abstract algebra*, volume 3, Wiley Hoboken, 2004

[14] Juárez Wysozka, Sara Rebeca, "Conceptos básicos acerca del espín, helicidad, quiralidad y polarización de una partícula de Dirac," *Revista mexicana de fisica E*, volume 56, no. 2, pp. 197–206, 2010, ResearchGate:262659499

[15] Bernstein, Jeremy, "Spontaneous symmetry breaking, gauge theories, the Higgs mechanism and all that," *Reviews of Modern Physics*, volume 46, no. 1, p. 7, 1974, calstatela.edu

[16] Attebury, Garhan, Avdeeva, E, Bockelman, Brian, Bose, S, Claes, Daniel R, Dominguez, A, Eads, Michael, Keller, J, Kravchenko, Ilya, Lazo-Flores, J, *et al.*, "Observation of a new boson at a mass of 125 GeV with the CMS experiment at the LHC," *Physics Letters B*, 2012, arxiv:1207.7235v2

[17] Collaboration, Atlas *et al.*, "Observation of a new particle in the search for the Standard Model Higgs boson with the ATLAS detector at the LHC," *Physics Letters B*, 2012, arxiv:1207.7214

[18] Burgess, Cliff and Moore, Guy, *The standard model: A primer*, Cambridge University Press, 2006

[19] Fukuda, Y, Hayakawa, T, Ichihara, E, Inoue, K, Ishihara, K, Ishino, H, Itow, Y, Kajita, T, Kameda, J, Kasuga, S, *et al.*, "Evidence for oscillation of atmospheric neutrinos," *Physical Review Letters*, volume 81, no. 8, p. 1562, 1998, PRL 81.1562

[20] Davis Jr, Raymond, Harmer, Don S, and Hoffman, Kenneth C, "Search for neutrinos from the sun," *Physical Review Letters*, volume 20, no. 21, p. 1205, 1968, Osti:4811423

[21] Fukuda, S, Fukuda, Y, Ishitsuka, M, Itow, Y, Kajita, T, Kameda, J, Kaneyuki, K, Kobayashi, K, Koshio, Y, Miura, M, *et al.*, "Determination of solar neutrino oscillation parameters using 1496 days of Super-Kamiokande-I data," *Physics Letters B*, volume 539, no. 3, pp. 179–187, 2002, cern:0205075

[22] the royal swedish academy of sciences, "Neutrino oscillation," *the royal swedish academy of sciences*, 2015, Nobel prize 2015

[23] Barger, Vernon, Marfatia, Danny, and Whisnant, Kerry Lewis, *The physics of neutrinos*, Princeton University Press, 2012

[24] Martin, Stephen P, *A supersymmetry primer*, Fermilab Press, 1997, arxiv:9709356v5

[25] Komatsu, Eiichiro, Smith, KM, Dunkley, J, Bennett, CL, Gold, B, Hinshaw, G, Jarosik, N, Larson, D, Nolta, MR, Page, L, *et al.*, "SEVEN-YEAR WILKINSON MICROWAVE ANISOTROPY PROBE (WMAP WMAP is the result of a partnership between Princeton University and NASA's Goddard Space Flight Center. Scientific guidance is provided by the WMAP Science Team.) OBSERVATIONS: COSMOLOGICAL INTERPRETATION," *The Astrophysical Journal Supplement Series*, volume 192, no. 2, p. 18, 2011, arxiv:1001.4744

[26] Bergström, Lars, "Non-baryonic dark matter: observational evidence and detection methods," *Reports on Progress in Physics*, volume 63, no. 5, p. 793, 2000), arxiv:0002126

[27] Hicken, Malcolm, Wood-Vasey, W Michael, Blondin, Stephane, Challis, Peter, Jha, Saurabh, Kelly, Patrick L, Rest, Armin, and Kirshner, Robert P, "Improved dark energy constraints from 100 new CfA supernova type Ia light curves," *The Astrophysical Journal*, volume 700, no. 2, p. 1097, 2009, arxiv:0901.4804

[28] Aghanim, N, Akrami, Y, Ashdown, M, Aumont, J, Baccigalupi, C, Ballardini, M, Banday, AJ, Barreiro, RB, Bartolo, N, Basak, S, *et al.*, "Planck 2018 results. VI. Cosmological parameters," *arXiv preprint arXiv180706209*, 2018, arxiv:1807.06209

[29] Lüst, Dieter and Theisen, Stefan, "Lectures on string theory." *Lecture Notes in Physics, Berlin Springer Verlag*, volume 346, 1989

[30] Giudice, Gian F, Rattazzi, Riccardo, and Wells, James D, "Quantum gravity and extra dimensions at high-energy colliders," *Nuclear Physics B*, volume 544, no. 1, pp. 3–38, 1999, arxiv:9811291

[31] Sakurai, Jun John and Napolitano, Jim, *Modern quantum mechanics*, Addison-Wesley, 2011

[32] Murayama, Hitoshi, "Supersymmetry phenomenology," *arXiv*, 2000, arxiv:0002232

[33] Kac, Victor G, "Lie superalgebras," *Advances in mathematics*, volume 26, no. 1, pp. 8–96, 1977, Elsevier:81957395

[34] Kazakov, DI, "Beyond the standard model (in search of supersymmetry)," *arXiv preprint hep ph0012288*, 2000, arxiv:0012288

[35] Vempati, Sudhir K, "Introduction to MSSM," *arXiv*, 2012, arxiv:1201.0334

[36] Eidelman, Simon, Hayes, KG, Olive, KA ea, Aguilar-Benitez, M, Amsler, C, Asner, D, Babu, KS, Barnett, RM, Beringer, J, Burchat, PR, *et al.*, "Review of particle physics," *Physics letters B*, volume 592, no. 1-4, pp. 1–5, 2004, Elsevier:qt6tm958q0

[37] Haber, Howard E, "Introductory low-energy supersymmetry," *arXiv preprint hep ph9306207*, 1993, arxiv:9306207

[38] Wilczek, Frank, "Majorana returns," *Nature Physics*, volume 5, no. 9, pp. 614–618, 2009. phys:Majorana_return434

[39] Choi, SY, Kalinowski, J, Moortgat-Pick, G, and Zerwas, PM, "Analysis of the neutralino system in supersymmetric theories," *The European Physical Journal C Particles and Fields*, volume 22, no. 3, pp. 563–579, 2001, arxiv:0108117

[40] Fuks, Benjamin, Klasen, Michael, Schmiemann, Saskia, and Sunder, Marthijn, "Realistic simplified gaugino-higgsino models in the MSSM," *The European Physical Journal C*, volume 78, no. 3, p. 209, 2018, arxiv:1710.09941

[41] Kuroda, Masaaki, "Complete Lagrangian of MSSM," *arXiv preprint hep ph9902340*, 1999, arxiv:9902340

[42] Krippendorf, Sven, Quevedo, Fernando, and Schlotterer, Oliver, "Cambridge Lectures on Supersymmetry and Extra Dimensions," *arXiv preprint arXiv10111491*, 2010, arxiv:1011.1491

[43] Martin, Stephen P, "A supersymmetry primer," *Perspectives on supersymmetry II*, World Scientific, pp. 1–153, 2010, arxiv:9709356

[44] Laboratory, CERN, *CERN document server*, Cern, Access date September-2019, CERN:DocumentServer

[45] Breskin, Amos and Voss, Rüdiger, *The CERN large hadron collider: accelerator and experiments*, Cern Geneva, 2009

[46] Faq, CERN, "LHC, the guide," *URL*, p. 63, 2009, Faq:LHC

[47] Bruce, R, Bracco, C, De Maria, R, Giovannozzi, M, Mereghetti, A, Mirarchi, D, Redaelli, S, Quaranta, E, and Salvachua, B, "Reaching record-low β* at the CERN Large Hadron Collider using a novel scheme of collimator settings and optics," *Nuclear Instruments and Methods in Physics Research Section A Accelerators Spectrometers Detectors and Associated Equipment*, volume 848, pp. 19–30, 2017

[48] Collaboration, CMS, *Luminosity public results*, Cern, Access date March-2019, CMS:LumiPublicresults

[49] Laboratory, CERN, *CERN document server*, Cern, Access date September-2019, CERN:DocumentServer:CMS

[50] Jacson, JD, "Classical Electrodynamics 3rd eddition," , 1998

[51] Martin, Brian R and Shaw, Graham, *Particle physics*, John Wiley & Sons, 2017

[52] Klyukhin, VI, Amapane, Nicola, Andreev, V, Ball, Alan, Cure, B, Herve, A, Gaddi, A, Gerwig, H, Karimaki, V, Loveless, R, *et al.*, "The CMS magnetic field map performance," *IEEE Transactions on Applied Superconductivity*, volume 20, no. 3, pp. 152–155, 2010, arxi:1110.0607

[53] collaboration, CMS *et al.*, "Precise mapping of the magnetic field in the CMS barrel yoke using cosmic rays," *Journal of Instrumentation*, volume 5, no. 03, p. T03021, 2010, iop:T03021

[54] TDR, CMS, *CMS physics: technical design report V. 2 physics performance*, Cern Geneva1, 2006, CERN:942733

[55] collaboration, CMS *et al.*, "Description and performance of track and primary-vertex reconstruction with the CMS tracker," *Journal of Instrumentation*, volume 9, no. 10, p. P10009, 2014 iop:1748-0221

[56] collaboration, CMS *et al.*, "Performance and operation of the CMS electromagnetic calorimeter," *Journal of Instrumentation*, volume 5, no. 03, p. T03010, 2010, iop:1748-0221

[57] collaboration, CMS *et al.*, "Performance of the CMS hadron calorimeter with cosmic ray muons and LHC beam data," *Journal of Instrumentation*, volume 5, no. 03, p. T03012, 2010, iop:1748-0221

[58] collaboration, CMS *et al.*, "Performance of CMS muon reconstruction in pp collision events at $\sqrt{s} = 7$ TeV," *Journal of Instrumentation*, volume 7, no. 10, p. P10002, 2012, iop:1748-0221

[59] collaboration, CMS *et al.*, "The CMS trigger system," *arXiv preprint arXiv160902366*, 2016, arxiv:1609.02366

[60] Trigger, The CMS and Group, Data Acquisition, "The CMS high level trigger," *arXiv preprint hep ex0512077*, 2005, arxiv:0512077

[61] Bauer, G, Beccati, B, Behrens, U, Biery, K, Bouffet, O, Branson, J, Bukowiec, S, Cano, E, Cheung, H, Ciganek, M, *et al.*, "The data-acquisition system of the CMS experiment at the LHC," *Journal of Physics: Conference Series*, volume 331, IOP Publishing, 2011, iop:1742-6596

[62] collaboration, CMS, Collaboration, CMS, *et al.*, "Particle-flow event reconstruction in CMS and performance for jets, taus and MET," Technical report, CMS-PAS-PFT-09-001, 2009, inspirehep:925379

[63] Atkin, Ryan, "Review of jet reconstruction algorithms," *Journal of Physics: Conference Series*, volume 2008, IOP Publishing, 2015, iop:1742-6596

[64] Cacciari, Matteo, Salam, Gavin P, and Soyez, Gregory, "The anti-kt jet clustering algorithm," *Journal of High Energy Physics*, volume 2008, no. 045, p. 063, 2008, iop:1126-6708

[65] Dokshitzer, Yu L, Leder, GD, Moretti, S, and Webber, BR, "Better jet clustering algorithms," *Journal of High Energy Physics*, volume 1997, no. 08, p. 001, 1997, arxiv:9707323

[66] Cabrera, Andres Leonardo, *Search for a SUSY signature through Vector Boson Fusion with one muon, jets and missing trasverse energy at* $\sqrt{s} = 13$ *TeV in the CMS experiment*, Universidad de los Andes, PhD Thesis, 2018

[67] Schröder, Matthias, collaboration, CMS, *et al.*, "Performance of jets at CMS," *Journal of Physics: Conference Series*, volume 587, IOP Publishing, 2015, iop:1742-6596

[68] collaboration, CMS *et al.*, "Identification of b-quark jets with the CMS experiment," *Journal of Instrumentation*, volume 8, no. 04, p. P04013, 2013, iop:1748-0221

[69] collaboration, CMS *et al.*, "Identification of b quark jets at the CMS Experiment in the LHC Run 2," *Journal of Instrumentation*, 2016

[70] collaboration, CMS *et al.*, "Performance of τ-lepton reconstruction and identification in CMS," *Journal of Instrumentation*, volume 7, no. 01, p. P01001, 2012, iop:1748-0221

[71] Sirunyan, AM, Tumasyan, A, Adam, W, Ambrogi, F, Asilar, E, Bergauer, T, Brandstetter, J, Dragicevic, M, Erö, J, Del Valle, A Escalante, *et al.*, "Performance of reconstruction and identification of tau leptons decaying to hadrons and ν_τ in pp collisions at $\sqrt{s} = 13$ TeV," *Journal of Instrumentation*, volume 13, 2018, arxiv:1809.02816

[72] collaboration, CMS *et al.*, "Performance of CMS muon reconstruction in pp collision events at $\sqrt{s} = 7$ TeV," *Journal of Instrumentation*, volume 7, no. 10, p. P10002, 2012, iop:1748-0221

[73] Frühwirth, Rudolf, "Application of Kalman filtering to track and vertex fitting," *Nuclear Instruments and Methods in Physics Research Section A Accelerators Spectrometers*

Detectors and Associated Equipment, volume 262, no. 2-3, pp. 444–450, 1987, NuclearInstruments:1987

[74] collaboration, CMS *et al.*, "Performance of electron reconstruction and selection with the CMS detector in proton-proton collisions at sqrt (s)= 8 TeV," *arXiv preprint arXiv150202701*, 2015, arxiv:1502.02701

[75] collaboration, CMS *et al.*, "Missing transverse energy performance of the CMS detector," *Journal of Instrumentation*, volume 6, no. 09, p. P09001, 2011, iop:1748-0221

[76] Collaboration, CMS, *Luminosity public results*, Cern, Access date April-2019, CMS:LumiPublicresults

[77] Perloff, A, collaboration, CMS, *et al.*, "Pileup measurement and mitigation techniques in CMS," *Journal of Physics: Conference Series*, volume 404, IOP Publishing, 2012, iop:1742-6596

[78] Antchev, G, Aspell, P, Atanassov, I, Avati, V, Baechler, J, Berardi, V, Berretti, M, Bossini, E, Bozzo, M, Brogi, P, *et al.*, "Luminosity-independent measurements of total, elastic and inelastic cross-sections at," *EPL Europhysics Letters*, volume 101, 2013, iop:0295-5075

[79] Herr, Werner and Muratori, Bruno, "Concept of luminosity," *proceedings of CERN Accelerator School*, volume 361, 2003

[80] Gripaios, Ben, "Transverse observables and mass determination at hadron colliders," *Journal of High Energy Physics*, volume 2008, no. 02, p. 053, 2008, iopscience

[81] Cheng, Hsin-Chia and Han, Zhenyu, "Minimal kinematic constraints and MT2," *Journal of High Energy Physics*, volume 2008, no. 12, p. 063, 2008, arxiv:0810.5178

[82] Khachatryan, Vardan, Sirunyan, AM, Tumasyan, A, Adam, W, Asilar, E, Bergauer, T, Brandstetter, J, Brondolin, E, Dragicevic, M, Erö, J, *et al.*, "Search for Dark Matter and Supersymmetry with a Compressed Mass Spectrum in the Vector Boson Fusion Topology in Proton-Proton Collisions at s= 8 TeV," *Physical review letters*, volume 118, 2017, PhysRevLett.118.021802

[83] Albajar, C, Jorat, Ginette, Colas, P, Smith, D, Mohammadi, M, Bettini, A, Scott, W, Lacava, F, Haynes, W, Holthuizen, DJ, *et al.*, "Events with large missing transverse energy at the CERN collider; 3, mass limits on supersymmetric particles," *Phys Lett B*, volume 198, no. CERN-EP-87-148, pp. 261–270, 1987, CERN:198710041

[84] Alitti, J, Ansari, R, Ansorge, RE, Bagnaia, P, Bareyre, P, Blaylock, G, Bonamy, P, Bonesini, M, Borer, K, Buskulic, D, *et al.*, "A search for squark and gluino production at the CERN pp collider," *Physics Letters B*, volume 235, no. 3-4, pp. 363–372, 1990, CERN:198912391

[85] Abe, F, Amidei, D, Apollinari, G, Ascoli, G, Atac, Mahmut, Auchincloss, P, Baden, AR, Barbaro-Galtieri, Angela, E. Barnes, V, Bedeschi, Franco, Behrends, S, Belforte, S, Bellettini, G, Bellinger, J, Bensinger, J, Beretvas, A, Berge, P, Bertolucci, Sergio, Bhadra, S, and Freeman, J, "Limits on the masses of supersymmetric particles from 1.8-TeV pp-bar collisions." *Physical review letters*, volume 62, pp. 1825–1828, 05 1989

[86] Lipniacka, Anna, "Understanding SUSY limits from LEP," *arXiv preprint hep ph0210356*, 2002, arxiv:0210356

[87] Jaffré, Michel, "SUSY searches at the Tevatron," *EPJ Web of Conferences*, volume 28, EDP Sciences, 2012. epjconf_hcp2012_09006

[88] Khachatryan, Vardan, Sirunyan, AM, Tumasyan, Armen, Adam, W, Asilar, E, Bergauer, T, Brandstetter, J, Brondolin, E, Dragicevic, M, Erö, J, *et al.*, "Search for direct pair production of supersymmetric top quarks decaying to all-hadronic final states in pp collisions at $\sqrt{s} = 8$ TeV," *The European Physical Journal C*, volume 76, no. 8, p. 460, 2016. arxiv:1603.00765

[89] Khachatryan, Vardan, Sirunyan, AM, Tumasyan, A, Adam, W, Bergauer, T, Dragicevic, M, Erö, J, Fabjan, C, Friedl, M, Frühwirth, R, *et al.*, "Searches for electroweak production of charginos, neutralinos, and sleptons decaying to leptons and W, Z, and Higgs bosons in pp collisions at 8 TeV," *The European Physical Journal C*, volume 74, no. 9, p. 3036, 2014. s10052-014-3036-7

[90] Aad, Georges, Abbott, B, Abdallah, J, Khalek, S Abdel, Abdinov, O, Aben, R, Abi, B, Abolins, M, AbouZeid, OS, Abramowicz, H, *et al.*, "Search for supersymmetry at $\sqrt{s} = 8$ TeV in final states with jets and two same-sign leptons or three leptons with the ATLAS detector," *Journal of High Energy Physics*, volume 2014, no. 6, pp. 1–50, 2014, springer-atlas

[91] Collaboration, CMS *et al.*, "Inclusive search for supersymmetry in pp collisions at $\sqrt{s} = 13$ TeV using razor variables and boosted object identification in zero and one lepton final states," *arXiv preprint arXiv181206302*, 2018, arxiv:1712.08501

[92] Aaboud, Morad, Aad, G, Abbott, B, Abdallah, J, Abdinov, O, Abeloos, B, Aben, R, AbouZeid, OS, Abraham, NL, Abramowicz, H, *et al.*, "Search for top squarks in final

states with one isolated lepton, jets, and missing transverse momentum in s= 13 TeV p p collisions with the ATLAS detector," *Physical Review D*, volume 94, no. 5, p. 052009, 2016, PhysRevD.94.052009

[93] Sirunyan, Albert M, Tumasyan, Armen, Adam, Wolfgang, Ambrogi, Federico, Asilar, Ece, Bergauer, Thomas, Brandstetter, Johannes, Brondolin, Erica, Dragicevic, Marko, Erö, J, *et al.*, "Search for supersymmetry in events with a τ lepton pair and missing transverse momentum in proton-proton collisions at $\sqrt{s} = 13$ TeV," *Journal of High Energy Physics*, volume 2018, no. 11, p. 151, 2018. JHEP11(2018)151

[94] Aaboud, Morad, Aad, G, Abbott, B, Abdallah, J, Abdinov, O, Abeloos, B, Aben, R, AbouZeid, OS, Abraham, NL, Abramowicz, H, *et al.*, "Search for the direct production of charginos and neutralinos in final states with tau leptons in $\sqrt{s} = 13$ TeV pp collisions with the ATLAS detector," *European Physics C*, volume 78, no. 154, 2018. arxiv:1708.07875

[95] Carena, Marcela, Gori, Stefania, Shah, Nausheen R, Wagner, Carlos EM, and Wang, Lian-Tao, "Light stau phenomenology and the Higgs $\gamma\gamma$ rate," *Journal of High Energy Physics*, volume 2012, no. 7, p. 175, 2012, JHEP07(2012)175

[96] Cerdeno, David G, Munoz, Carlos, and Seto, Osamu, "Right-handed sneutrino as thermal dark matter," *Physical Review D*, volume 79, no. 2, p. 023510, 2009, arxiv:0807.3029

[97] Wreszinski, Walter F, "DARK ENERGY: CASIMIR EFFECT, GENERALIZED PERFECT HOMOGENEITY AND AXIONS," *arXiv preprint quant ph0603026*, 2007, arxiv:0603026v6

[98] Jeannerot, Rachel, Zhang, Xinmin, and Brandenberger, Robert, "Non-thermal production of neutralino cold dark matter from cosmic string decays," *Journal of High Energy Physics*, volume 1999, no. 12, p. 003, 2000, iop:1126-6708

[99] Chu, Xiaoyong, Mambrini, Yann, and Quevillon, Bryan, "Thermal and non-thermal production of dark matter via Z'-portal (s)," *Journal of Cosmology and Astroparticle Physics*, volume 2014, no. 01, p. 034, 2014, iop:1475-7516

[100] Drees, Manuel and Hajkarim, Fazlollah, "Neutralino dark matter in scenarios with early matter domination," *Journal of High Energy Physics*, volume 2018, no. 12, p. 42, 2018, JHEP12(2018)042

[101] Bertone, Gianfranco, Hooper, Dan, and Silk, Joseph, "Particle dark matter: Evidence, candidates and constraints," *Physics reports*, volume 405, no. 5-6, pp. 279–390, 2005, arxiv:0404175

[102] Edsjö, Joakim, Schelke, Mia, Ullio, Piero, and Gondolo, Paolo, "Accurate relic densities with neutralino, chargino and sfermion coannihilations in mSUGRA," *Journal of Cosmology and Astroparticle Physics*, volume 2003, no. 04, p. 001, 2003, arxiv:0301106

[103] Hinshaw, Gary, Larson, D, Komatsu, Eiichiro, Spergel, David N, Bennett, CLaa, Dunkley, J, Nolta, MR, Halpern, M, Hill, RS, Odegard, N, *et al.*, "Nine-year Wilkinson Microwave Anisotropy Probe (WMAP) observations: cosmological parameter results," *The Astrophysical Journal Supplement Series*, volume 208, no. 2, p. 19, 2013, arxiv:1212.5226

[104] Iminniyaz, Hoernisa, Salai, Burhan, and Lv, Guo-Liang, "Relic Density of Asymmetric Dark Matter in Modified Cosmological Scenarios," *Communications in Theoretical Physics*, volume 70, no. 5, p. 602, 2018, arxiv:1804.07256

[105] Belanger, G, Boudjema, F, Hugonie, C, Pukhov, A, and Semenov, A, "Relic density of dark matter in the next-to-minimal supersymmetric standard model," *Journal of Cosmology and Astroparticle Physics*, volume 2005, no. 09, p. 001, 2005, arxiv:0505142

[106] Allahverdi, Rouzbeh, Dutta, Bhaskar, and Gao, Yu, "keV photon emission from light nonthermal dark matter," *Physical Review D*, volume 89, no. 12, p. 127305, 2014, arxiv:1403.5717

[107] Flórez, Andrés, Bravo, Luis, Gurrola, Alfredo, Ávila, Carlos, Segura, Manuel, Sheldon, Paul, and Johns, Will, "Probing the stau-neutralino coannihilation region at the LHC with a soft tau lepton and a jet from initial state radiation," *Phys Rev D*, volume 94, p. 073007, Oct 2016, PhysRevD.94.073007

[108] Alwall, Johan, Artoisenet, Pierre, de Visscher, Simon, Duhr, Claude, Frederix, Rikkert, Herquet, Michel, and Mattelaer, Olivier, "New Developments in MadGraph/MadEvent," *AIP Conference Proceedings*, volume 1078, AIP, 2008, arxiv:0809.2410

[109] Alvarez, Joseph L, "Poisson-based detection limit and signal confidence intervals for few total counts," *Health physics*, volume 93, no. 2, pp. 120–126, 2007, Alvarez:2007

[110] Junk, Thomas, "Confidence level computation for combining searches with small statistics," *Nuclear Instruments and Methods in Physics Research Section A Accelerators Spectrometers Detectors and Associated Equipment*, volume 434, no. 2-3, pp. 435–443, 1999, arxiv:9902006

[111] Collaboration, CMS *et al.*, "Search for supersymmetry with a compressed mass spectrum in events with a soft τ lepton, a highly energetic jet, and large missing transverse

momentum in proton-proton collisions at $\sqrt{s} = 13$ TeV," *arXiv preprint arXiv191001185*, 2019, arxiv:1910.01185

[112] Beaudette, Florian, "The CMS particle flow algorithm," *arXiv preprint arXiv14018155*, 2014, arxiv:1401.8155

[113] Kom, Chun-Hay and Stirling, W James, "Charge asymmetry in W+ jets production at the LHC," *The European Physical Journal C*, volume 69, no. 1-2, pp. 67–73, 2010, arxiv:1004.3404

[114] Nadolsky, Pavel M, Lai, Hung-Liang, Cao, Qing-Hong, Huston, Joey, Pumplin, Jon, Stump, Daniel, Tung, Wu-Ki, and Yuan, C-P, "Implications of CTEQ global analysis for collider observables," *Physical Review D*, volume 78, no. 1, p. 013004, 2008, arxiv:0802.0007

[115] Zanetti, Marco, "Beams scan based absolute normalization of the CMS luminosity measurement," *CERN*, 2011, CERN:1357856

[116] collaboration, CMS *et al.*, "Performance of b-jet identification in CMS," *CMS Physics Analysis Summary CMS PAS BTV 11 001*, volume 60, 2011

[117] Pioppi, Michele, "Tau reconstruction and identification with particle-flow techniques using the CMS detector at LHC," *Nucl Phys B Proc Suppl*, volume 189, no. CMS-CR-2008-094, pp. 311–316, 2008, CERN:1358716

[118] collaboration, CMS *et al.*, "Performance of electron reconstruction and selection with the CMS detector in proton-proton collisions at $\sqrt{s} = 7$ TeV," *arXiv preprint arXiv150202701*, 2015, arxiv:1502.02701

[119] Collaboration, C, "Performance of muon identification in pp collisions at $\sqrt{s} = 7$ TeV," *CMS Physics Analysis Summary CMS PAS MUO 10 002 CERN Geneva*, 2010, CERN:MUON

[120] Heister, Arno, Konoplyanikov, Viktor, Tully, Christopher, Petrushanko, Sergey, Rohlf, James, Kodolova, Olga, and Ulyanov, A, "Measurement of Jets with the CMS Detector at the LHC," Technical report, CERN-CMS-NOTE-2006-036, 2006, CERN:933705

[121] collaboration, CMS *et al.*, "Missing transverse energy performance of the CMS detector," *Journal of Instrumentation*, volume 6, no. 09, p. P09001, 2011, iopscience:1748-0221

[122] Collaboration, CMS, *Higgs limit tool*, Cern, Access date June-2019, CMS:HiggLimitTool

[123] Sirunyan, Albert M, Tumasyan, Armen, Adam, Wolfgang, Ambrogi, Federico, Asilar, Ece, Bergauer, Thomas, Brandstetter, Johannes, Brondolin, Erica, Dragicevic, Marko, Erö, Janos, *et al.*, “Search for new physics in events with two soft oppositely charged leptons and missing transverse momentum in proton–proton collisions at $\sqrt{s} = 13$ TeV,” *Physics Letters B*, volume 782, pp. 440–467, 2018, Elsevier

[124] Aaboud, Morad, Aad, Georges, Abbott, Brad, Abdinov, Ovsat, Abeloos, Baptiste, Abidi, Syed Haider, AbouZeid, OS, Abraham, Nadine L, Abramowicz, Halina, Abreu, Henso, *et al.*, “Search for electroweak production of supersymmetric states in scenarios with compressed mass spectra at $\sqrt{s} = 13$ TeV with the ATLAS detector,” *Physical Review D*, volume 97, no. 5, p. 052010, 2018, PhysicalReviewD:97-052010

[125] Heister, A, Schael, S, Barate, R, Bruneliere, R, De Bonis, I, Decamp, D, Goy, C, Jezequel, S, Lees, J-P, Martin, F, *et al.*, “Search for scalar leptons in e+ e- collisions at centre-of-mass energies up to 209 GeV,” *Physics Letters B*, volume 526, no. 3-4, pp. 206–220, 2002, arxiv:0112011

[126] Abdallah, J, Collaboration, Delphi, *et al.*, “Searches for supersymmetric particles in e+ e-collisions up to 208 GeV and interpretation of the results within the MSSM,” *arXiv preprint hep ex0311019*, 2003, arxiv:0311019

[127] Andrea, Jeremy, Fuks, Benjamin, and Maltoni, Fabio, “Monotops at the LHC,” *Physical Review D*, volume 84, no. 7, p. 074025, 2011, arxiv:1106.6199

[128] Agram, Jean-Laurent, Andrea, Jeremy, Buttignol, Michael, Conte, Eric, and Fuks, Benjamin, “Monotop phenomenology at the large hadron collider,” *Physical Review D*, volume 89, no. 1, p. 014028, 2014, arxiv:1311.6478

[129] Allahverdi, Rouzbeh, Dalchenko, Mykhailo, Dutta, Bhaskar, Gao, Yu, and Kamon, Teruki, “Distinguishing standard model extensions using monotop chirality at the LHC,” *arXiv preprint arXiv150702271*, 2015, arxiv:1507.02271

[130] Alvarez, Ezequiel, Leskow, Estefania Coluccio, Drobnak, Jure, and Kamenik, Jernej F, “Leptonic monotops at the LHC,” *Physical Review D*, volume 89, no. 1, p. 014016, 2014, arxiv:1310.7600

[131] Boucheneb, Idir, Cacciapaglia, Giacomo, Deandrea, Aldo, and Fuks, Benjamin, “Revisiting monotop production at the LHC,” *Journal of High Energy Physics*, volume 2015, no. 1, pp. 1–24, 2015, JHEP01(2015)017

[132] Khachatryan, Vardan, Sirunyan, AM, Tumasyan, A, Adam, W, Bergauer, T, Dragicevic, M, Erö, J, Fabjan, C, Friedl, M, Frühwirth, R, *et al.*, “Search for Monotop Signatures

in Proton-Proton Collisions at s= 8 TeV," *Physical review letters*, volume 114, no. 10, p. 101801, 2015, PRL 114-2015

[133] Theveneaux-Pelzer, Timothée, "Search for monotop events using the ATLAS detector at the LHC," *arXiv preprint arXiv14123629*, 2014, arxiv:1412.3629

[134] Wang, Jian, "Search for the signal of monotop production at the early LHC," *QCD Higher-Order Effects and Search for New Physics*, Springer, pp. 107–129, 2016, arxiv:1109.5963

[135] Fuks, Benjamin, Richardson, Peter, and Wilcock, Alexandra, "Studying the sensitivity of monotop probes to compressed supersymmetric scenarios at the LHC," *The European Physical Journal C*, volume 75, no. 7, pp. 1–11, 2015, European Physical Journal C 75:308

[136] Alwall, Johan, Herquet, Michel, Maltoni, Fabio, Mattelaer, Olivier, and Stelzer, Tim, "MadGraph 5: going beyond," *Journal of High Energy Physics*, volume 2011, no. 6, p. 128, 2011, JHEP06%282011%29128

[137] Conte, Eric, Dumont, Béranger, Fuks, Benjamin, and Wymant, Chris, "Designing and recasting LHC analyses with MadAnalysis 5," *The European Physical Journal C*, volume 74, no. 10, p. 3103, 2014, s10052-014-3103-0

[138] Sjöstrand, Torbjörn, Mrenna, Stephen, and Skands, Peter, "A brief introduction to PYTHIA 8.1," *Computer Physics Communications*, volume 178, no. 11, pp. 852–867, 2008, arxiv:0710.3820

[139] De Favereau, J, Delaere, Christophe, Demin, Pavel, Giammanco, Andrea, Lemaitre, Vincent, Mertens, Alexandre, Selvaggi, Michele, Collaboration, Delphes 3, *et al.*, "DELPHES 3: a modular framework for fast simulation of a generic collider experiment," *Journal of High Energy Physics*, volume 2014, no. 2, p. 57, 2014, JHEP02(2014)057

[140] Leader, Elliot and Predazzi, Enrico, *An introduction to gauge theories and modern particle physics*, volume 1, Cambridge University Press, 1996

[141] Oleari, Carlo, "The powheg-box," *arXiv preprint arXiv10073893*, 2010, arxiv:1007.3893

[142] Boos, EE, Bunichev, VE, Dubinin, MN, Ilyin, VA, Savrin, VI, Collaboration, CompHEP, *et al.*, "CompHEP: developments and applications," *Journal of Physics: Conference Series*, IOP Publishing, 2017, iop:1742-6596

[143] Gleisberg, Tanju, Höche, Stefan, Krauss, F, Schönherr, M, Schumann, S, Siegert, F, and Winter, J, "Event generation with SHERPA 1.1," *Journal of High Energy Physics*, volume 2009, no. 02, p. 007, 2009, iop:1126-6708

[144] Agostinelli, Sea, Allison, John, Amako, K al, Apostolakis, John, Araujo, H, Arce, P, Asai, M, Axen, D, Banerjee, S, Barrand, G 2, *et al.*, "GEANT4—a simulation toolkit," *Nuclear instruments and methods in physics research section A Accelerators Spectrometers Detectors and Associated Equipment*, volume 506, no. 3, pp. 250–303, 2003, inspirehep:fermilab-pub-03-339.pdf

Appendices

APPENDIX A

Search for new physics at the LHC with a simplified dark matter model

Section A.1

Monotop models

This model has a particular signature, which is defined by a top quark in association with missing transverse energy p_{T}^{miss} [127, 128]. There are only two allowed processes (to tree-level) in the final state. In the first, the process occurs through baryon number-violation, and second, flavor-change neutral interaction, which has coupling with the third generation of the SM [128, 129]. The classification depends on the particle that is associated with the p_{T}^{miss}. In the first case, the top quark is produced through flavor-changing neutral interaction in association with a new invisible *bosonic* state, in the second one, the top is produced in association with a *fermion* state. Figure [A.1] describes both mechanisms.

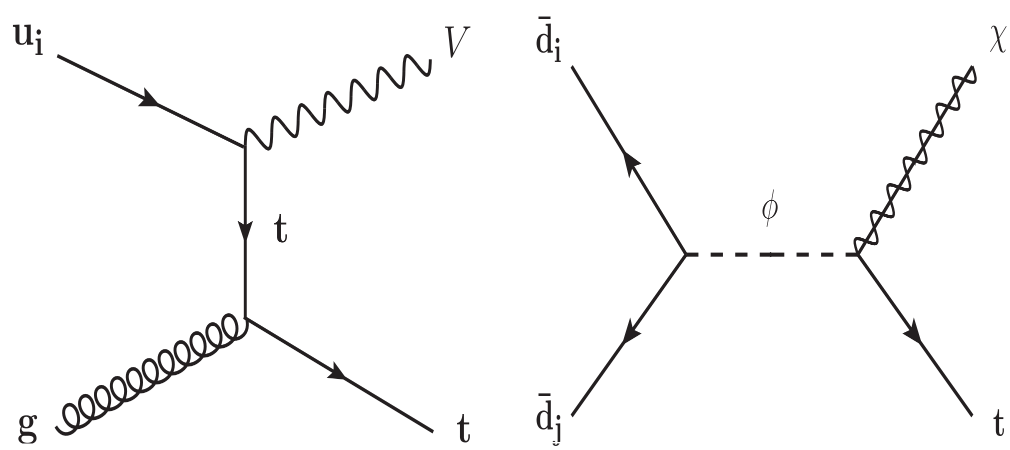

Figure A.1: Feynman diagram associated with the monotop production, which has two cases: up-type quark with a vector state V (left) and resonant production mediated by a colored scalar field S (right). The states (V, χ) correspond to p_{T}^{miss}.

These diagrams are generated by the Lagrangian that describes this theory [128,131], which contains higher-dimensional spin operators:

$$
\begin{aligned}
\mathcal{L} &= \mathcal{L}_{SM} \\
&+ \phi\overline{u}\big[a^0_{FC} + b^0_{FC}\gamma_5\big]u + V_\mu\overline{u}\big[a^1_{FC}\gamma^\mu + b^1_{FC}\gamma^\mu\gamma_5\big]u \\
&+ \epsilon^{ijk}\varphi_i\overline{d}^c_j\big[a^0_{SR} + b^q_{SR}\gamma_5\big]d_k + \varphi_i\overline{u}^i\big[a^{1/2}_{SR} + b^{1/2}_{SR}\gamma_5\big]\chi \\
&+ \epsilon^{ijk}\widetilde{\varphi}_i\overline{d}^c_j\big[\widetilde{a}^0_{SR} + \widetilde{b}^q_{SR}\gamma_5\big]u_k + \widetilde{\varphi}_i\overline{d}^i\big[\widetilde{a}^{1/2}_{SR} + \widetilde{b}^{1/2}_{SR}\gamma_5\big]\chi \\
&+ \epsilon^{ijk}X_{\mu,i}\overline{d}^c_j\big[a^q_{VR}\gamma^\mu + b^q_{VR}\gamma^\mu\gamma_5\big]d_k \\
&+ X_{\mu,i}\overline{u}^i\big[a^{1/2}_{VR}\gamma^\mu + b^{1/2}_{VR}\gamma^\mu\gamma_5\big]\chi + h.c.,
\end{aligned}
\tag{A.1}
$$

In Equation (A.1), the superscripts c mean charge conjugation, i, j, k are color indices. the matrices in the flavor space $a^{\{0,1\}}_{FC}$ and $b^{\{0,1\}}_{FC}$ contain quark interactions with the bosonic particles ϕ and V. On the other hand, $a^{1/2}_{\{S,V\}R}$ and $b^{1/2}_{\{S,V\}R}$ are interactions between up-type quark, the invisible fermion χ, and the new colored states φ and X. The couple with the down-type quark is given by $a^q_{\{S,V\}R}$ and $b^q_{\{S,V\}R}$.

Some research has explored scenarios where all axial coupling vanished [128], hence:

$$
b = 0 \tag{A.2}
$$

This condition sets all parameters.

$$
\begin{aligned}
(a^0_{FC})_{13} &= (a^0_{FC})_{31} = (a^1_{FC})_{13} = (a^1_{FC})_{31} = a, \\
(a^q_{SR})_{12} &= -(a^q_{SR})_{21} = (a^{1/2}_{SR})_3 = (a^q_{VR})_{11} = (a^{1/2}_{VR})_3 = a.
\end{aligned}
\tag{A.3}
$$

Other couplings become zero. This election defines two mechanisms of production already mentioned, in the first one, a single scalar and the second a vector is added to the SM. `Mad-Graph` calculates the cross-section of the Monotop processes. Figure [A.2] shows the relation between the masses of φ, χ and the coupling parameter, the cross-section expected of a few *pb* at the LHC accelerator (8 TeV) with moderate values of $a \approx 0.1$, and the masses of 1 TeV and 1.3 TeV respectively. In scenarios where $b \neq 0$, there are different helicity states (left, right-handed and mixing). The specific work is to estimate the associated SM backgrounds of these hypothetical processes to determine whether experimental sensitivity at 13 TeV to measure the *helicity states* of this new physics [129]. For leptonic channel, the helicity is defined by $p_{\mathrm{T}}(b)/(p_{\mathrm{T}}(b) + p_{\mathrm{T}}(\ell))$, and $E(b)/E(t)$ in the hadronic case. Currently, there are searches at experimental level by CMS [132] and ATLAS [133], which connects the phenomenological study with experimental studies.

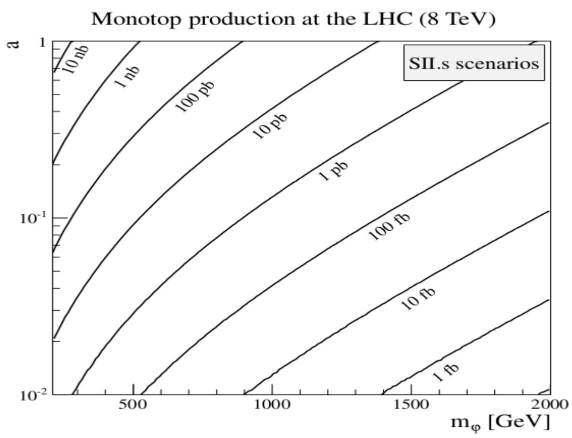

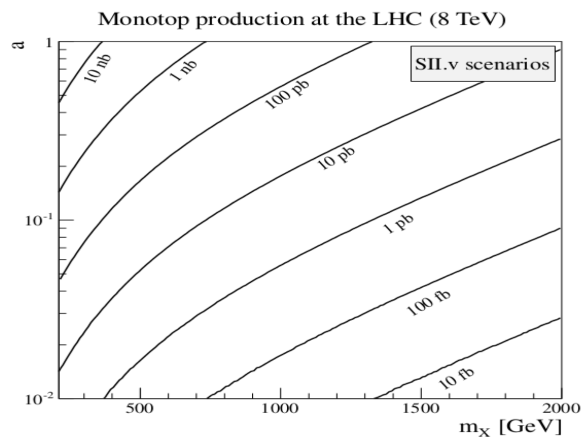

Figure A.2: Total cross-section of the monotop production at $\sqrt{s} = 8$ TeV at LHC. The scalar resonance m_φ (left) and the vector resonance m_χ (right).

A.1.1 Main background processes

The hypothetical signal processes are mixing with background processes that come from SM. These processes simulate the same final set by signal events. In this case, backgrounds are identified through the top decay.

$$\begin{aligned} pp &\rightarrow t + p_{\mathrm{T}}^{miss} \rightarrow bW + p_{\mathrm{T}}^{miss} \rightarrow bjj + p_{\mathrm{T}}^{miss} \\ pp &\rightarrow t + p_{\mathrm{T}}^{miss} \rightarrow bW + p_{\mathrm{T}}^{miss} \rightarrow b\ell + p_{\mathrm{T}}^{miss}, \end{aligned} \tag{A.4}$$

where j and b denote light and b-jets respectively, ℓ charged lepton, and p_{T}^{miss}. Not only $W + jets$ and $Z + jets$ are backgrounds, but also $t\bar{t}$ and Single top are considered [127, 128].

A.1.2 Semi-leptonic and di-leptonic $t\bar{t}$ processes

$t\bar{t}$ is an SM process due to the annihilation of the partons in the scattering process, an energetic gluon is created. Afterwards, that gluon decays into $t\bar{t}$ pair, these particles decay into $W^{\pm}$ boson and one b-jet the 91% of times. The W decays 64% into a quark anti-quark pair, $W \rightarrow q\bar{q}$ (hadronic decay) and the 34% into lepton plus neutrino, $W^+ \rightarrow \ell^+\nu_\ell$ and $W^- \rightarrow \ell^-\bar{\nu}_\ell$ (leptonic decay). In Figure [A.3] are presented both cases when one of the W decay hadronically and the other leptonically, the total contribution is called Semi-leptonic $t\bar{t}$ (left). Likewise, when both W decay leptonically the final states are called Di-leptonic $t\bar{t}$ (right).

The syntax in `Mad-Graph` for the production of $t\bar{t}$:

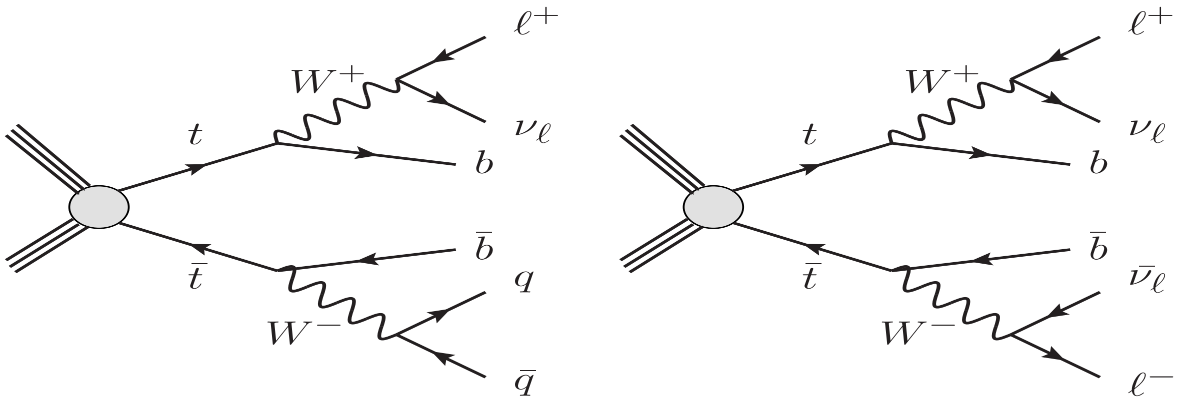

Figure A.3: Semi-leptonic (left) and di-leptonic (right) $t\bar{t}$ plus jets processes.

```
\\Semi-leptonic tt
import model sm
generate p p > t t~, (t > w+ b, w+ > j j), (t~ > w- b~, w- > l- vl~)       @0
add process p p > t t~, (t > w+ b, w+ > l+ vl), (t~ > w- b~, w- > j j)     @0
add process p p > t t~ j, (t > w+ b, w+ > j j), (t~ > w- b~, w- > l- vl~)  @1
add process p p > t t~ j, (t > w+ b, w+ > l+ vl), (t~ > w- b~, w- > j j)   @1

\\Di-leptonic tt
import model sm
generate p p > t t~, (t > w+ b, w+ > l+ vl), (t~ > w- b~, w- > l- vl~)      @0
add process p p > t t~ j, (t > w+ b, w+ > l+ vl), (t~ > w- b~, w- > l- vl~) @1
```

A.1.3 Single-top process

The Single-top is an SM process characterized by the annihilation of the partons in the scattering process, this involves the production of time-like W, which then decays into a top and bottom quarks. The top quark decays into $W^{\pm}$ boson and one b-jet the 91% of times. Then we have two b jets in the final states and the W decays 64% into a quark anti-quark pair, $W \to q\bar{q}$ (hadronic decay) and the 34% into lepton plus neutrino, $W^+ \to \ell^+\nu_\ell$ and $W^- \to \ell^-\bar{\nu}_\ell$ (leptonic decay). Figure [A.4] shows the s-channel of this process.

The syntax in `Mad-Graph` for the production of Single-top:

```
import model sm
```

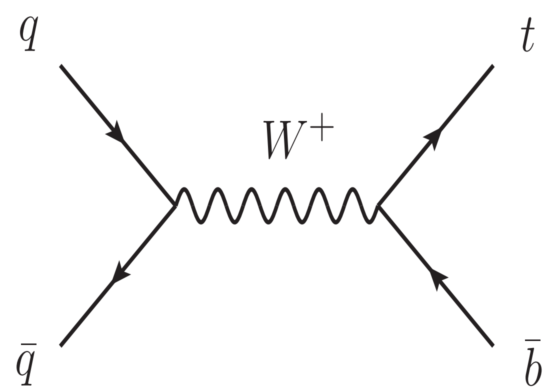

Figure A.4: Single-top production in s-channel.

```
define pr= b b~ p
generate pr pr > t j $$ w+ , (t > w+ b)
add process pr pr > t~ j $$ w- , (t~ > w- b~)
add process pr pr > t b~ j $$ w+ , (t > w+ b)
add process pr pr > t~ b j $$ w- , (t~ > w- b~)
add process pr pr > t w- , (t > w+ b)
add process pr pr > t~ w+ , (t~ > w- b~)
add process p p > w+ > t b~, (t > w+ b)
add process p p > w- > t~ b, (t~ > w- b~)
```

In summary, Table [A.1] presents the simulated cross-sections for theses SM backgrounds. There are other backgrounds; for instance see [129]. Nevertheless, the cross-sections are quite small, and these will not be taken into account.

Table A.1: Main cross sections of $t\bar{t}$ and Single-top backgrounds.

Process	σ [pb] `Mad-Graph`	σ [pb] `Pythia`	Matching efficiency
$t\bar{t}(\rightarrow$ 4jets 1ℓ $1\nu)$+ jets	290.8	151.9	52%
$t\bar{t}(\rightarrow$ 2jets 2ℓ $2\nu)$+ jets	66.5	25.5	38%
Single top + jets	465.8	429.3	92%

Monotop signatures offer two different and complementary channels: leptonic and hadronic monotop channels.

Section A.2

Leptonic monotop

There are two sources of p_{T}^{miss} in the leptonic decay, the neutrino and the new invisible state. The analysis carried out by CMS collaboration at energy of the center of mass $\sqrt{s} = 8$ TeV [132] has the following event selection criteria: There is one isolated b-jet in the central region of the detector ($|\eta(b)| \leq 2.5$), the $p_{\mathrm{T}}(b) > 70$ GeV, and a veto over light jets is applied. Events are required to have exactly one lepton (either e or μ), which defines two channels, electron and muon channel. The isolated lepton must fall in the central pseudo-rapidity coverage ($|\eta(\ell)| \leq 2.5$), the $p_{\mathrm{T}}(\ell) > 30$ GeV, and the overlap removal is applied. Finally, $p_{\mathrm{T}}^{miss} > 100$ GeV. In this study, we proposed a new selection in the m_{T} distribution to increase the experimental sensitivity of the signal. Table [A.2] summaries the event selection criteria for the leptonic channel.

Table A.2: Event selection criteria for the leptonic channel.

Criteria	CMS Selections
$N(b-jets)$	$= 1$
$p_{\mathrm{T}}(b)$	> 70 GeV
$\|\eta(b)\|$	< 2.5
$N(\mathrm{j})$	$= 0$
$p_{\mathrm{T}}(\mathrm{j})$	> 30 GeV
$\|\eta(\mathrm{j})\|$	< 2.5
$N(\ell)$ $(\ell = \mu - OR - e\ )$	$= 1$
$p_{\mathrm{T}}(\ell)$	> 30 GeV
$\|\eta(\ell)\|$	< 2.1
$N(other - \ell)$	$= 0$
$p_{\mathrm{T}}(W)$	> 50 GeV
$\|\Delta\phi(\ell, b - jet)\|$	< 1.7
Overlaps removal	$\Delta R > 0.3$
p_{T}^{miss}	> 100 GeV
$m_{\mathrm{T}}(\ell, p_{\mathrm{T}}^{miss})$	> 400 GeV

The $m_{\mathrm{T}}(\ell, p_{\mathrm{T}}^{miss})$ selection is based on the shape of the distribution. The Monotop production is characterized by high values of transverse mass. Figure [A.5] presents the transverse mass for the electron channel. The distribution has small values for the background component, which allows to select events above $m_{\mathrm{T}}(\ell, p_{\mathrm{T}}^{miss}) > 400$ GeV.

To discriminate the signal yield from the background events, we implement a distribution associated with the top kinematics. If we redefine the momentum of the lepton as: $p_{\mathrm{T}}(\ell') \rightarrow$

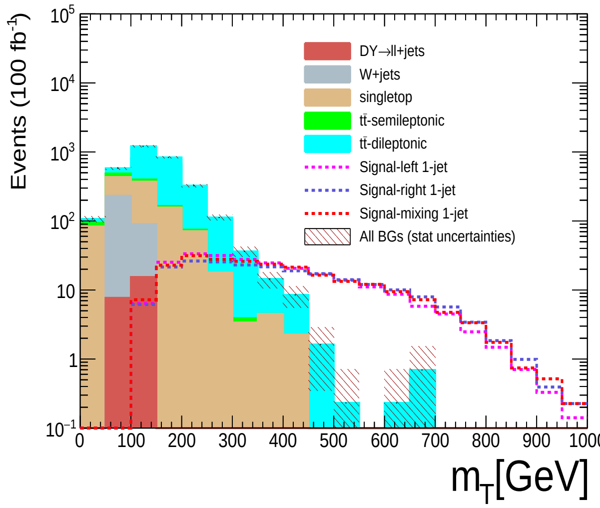

Figure A.5**:** $m_{\mathrm{T}}(\ell, p_{\mathrm{T}}^{miss})$ distribution of the electron channel, the criterion of $m_{\mathrm{T}}(\ell, p_{\mathrm{T}}^{miss}) > 400$ GeV is applied.

$p_{\mathrm{T}}(\ell + b - jet)$, the transverse mass will be associated with the top particle ($m_{\mathrm{T}}(t, p_{\mathrm{T}}^{miss})$). This distribution is a better likelihood variable, which is presented for both, electron and muon channels in Figure [A.6].

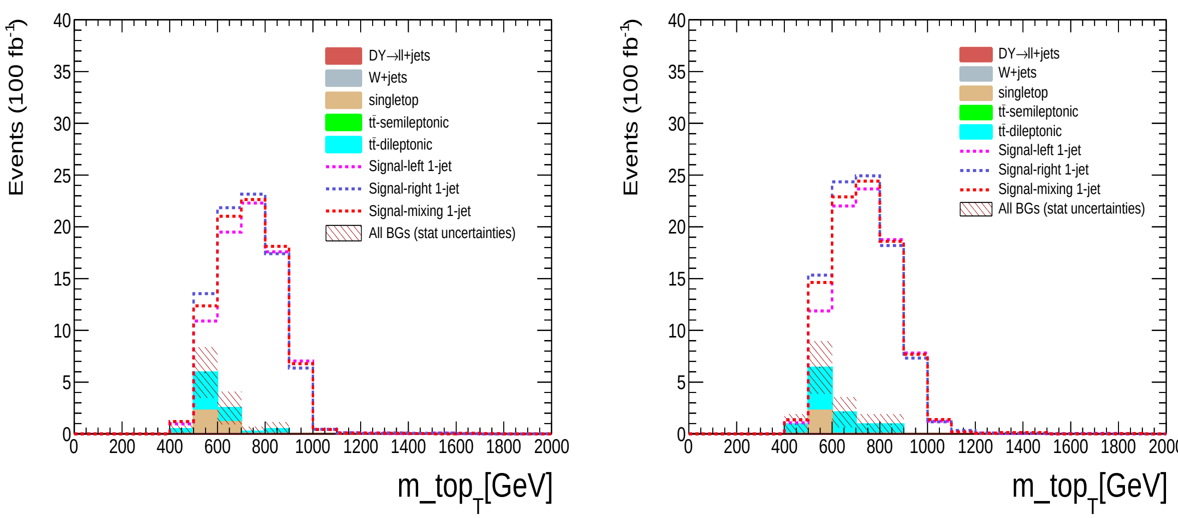

Figure A.6**:** $m_{\mathrm{T}}(t, p_{\mathrm{T}}^{miss})$ distribution for both, electron (left) and muon (right) channels. This distribution shows a clear distinction between signal and background events.

Finally, helicity states for the top quark in the leptonic channel is given by [132]:

$$H(\ell, b) = \frac{p_{\mathrm{T}}(b)}{p_{\mathrm{T}}(b) + p_{\mathrm{T}}(\ell)}, \tag{A.5}$$

Figure [A.7] shows the observable associated with the helicity for both channels to the expected luminosity of 100 fb^{-1}. In our model, we have three chirality states: left-handed, right-handed and non-polarized. This result has a great perspective to measure the helicity of new particles at experimental level, in which, the chiral nature of new particles in scenarios beyond the standard model (BSM) can be established.

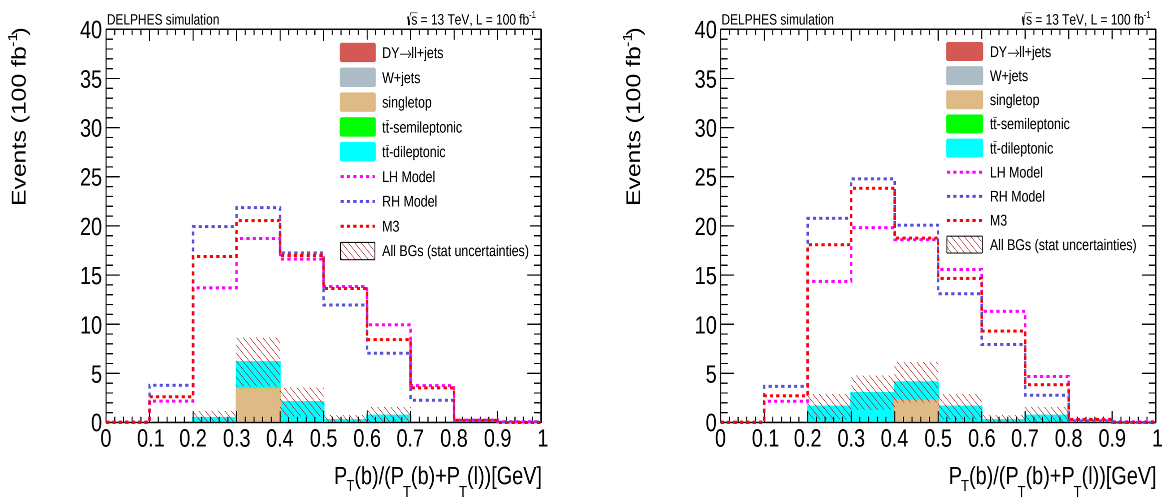

Figure A.7**:** The helicity distribution for both, electron (left) and muon (right) channels.

Section A.3

Hadronic monotop

In the hadron decay, we need exactly one jet from the fragmentation of $b - quark$ and two o three-light jets for reconstructing the top quark. The analysis carried out by the CMS collaboration at center of mass energy of $\sqrt{s} = 8$ TeV [132] has the following event selection criteria: There is one isolated b-jet in the central region of the detector ($|\eta(b)| \leq 2.5$), the $p_{\mathrm{T}}(b) > 70$ GeV. A set of light jets are selected to obtain the kinematics associated with the top quark and the $p_{\mathrm{T}}(\mathrm{j}) > 30$ GeV. In addition, jets must be located in the central region of the detector ($|\eta(\mathrm{j})| < 2.5$). A veto over all leptons is applied in the final selection. Finally, $p_{\mathrm{T}}^{miss} > 350$ GeV is applied. Table [A.3] summaries the event selection criteria of the hadronic channel.

Table A.3: Event selection criteria for the hadronic channel.

Criteria	CMS Selections
$N(b)$	$= 1$
$p_{\mathrm{T}}(b)$	> 70 GeV
$\lvert\eta(b)\rvert$	< 2.5
$N(\mathrm{j})$	$= 2$
$p_{\mathrm{T}}(\mathrm{j})$	> 30 GeV
$\lvert\eta(\mathrm{j})\rvert$	< 2.5
$N(\ell)$	$= 0$
p_{T}^{miss}	> 350 GeV
$m(j, j, b)$	< 450 GeV

In this case, we can apply an extra selection to discriminate more background events. The invariant mass the three jets system is a good variable due to the single-top events have a long tail toward high mass value. Therefore, a cut below $m(\mathrm{j}, \mathrm{j}, b) < 450$ GeV could suppress those events. Figure [A.8] shows the invariant mass distribution after the last selection.

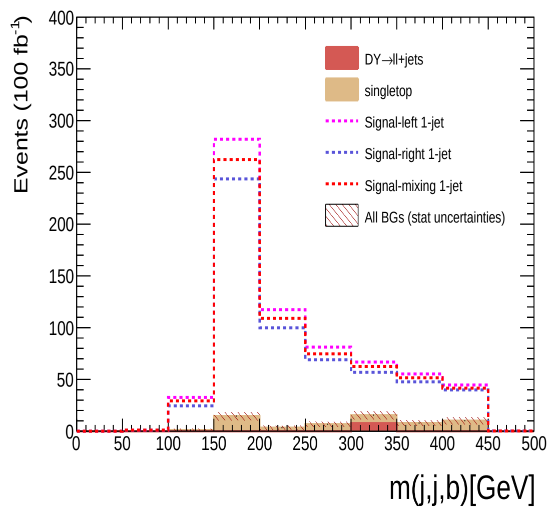

Figure A.8: Invariant mass distribution of the three jets system, the distribution is consistent with the top mass resonance.

Finally, helicity states for the top quark in the hadronic channel is given by [132]:

$$H(b, t) = \frac{E(b)}{E(t)}, \tag{A.6}$$

The top energy $E(t)$ is the sum of the energies of the all reconstructed jets. Figure [A.9] shows the helicity distribution for the hadronic channel to the expected luminosity of 100 fb^{-1}.

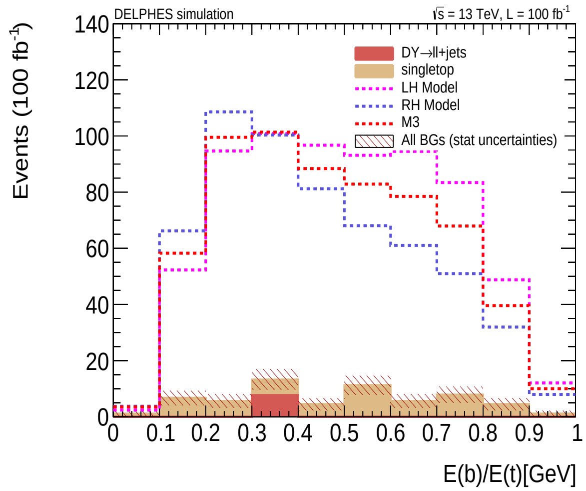

Figure A.9**:** The helicity distribution of the hadronic channel after all selections.

Possibly, measuring the helicity of new particles in the hadronic case leads to establish the chiral nature of new particles in scenarios beyond the standard model (BSM).

APPENDIX B

Simulation packages in high energy physics

Simulations of high energy processes associated with the SM, which is commonly the experimental background and hypothetical signals in extended models such as: SUSY, Extra-dimensions, or GUT address the phenomenological and experimental research. In general, simulations consist of three steps: hard scattering among partons, fragmentation and hadronization, and detector responses. The hard scattering is generated using specialized software, which computes the cross-sections of each specific process. Strong interactions among quarks generate fragmentation and hadronization processes, which are usually non-perturbative, and outcoming particles have interactions with the detector, which must be emulated as well. The detector generates kinematic changes, smearing effect in the four-vectors. Furthermore, the reconstruction and identification driven some information losses. The most common simulation software in high energy physics is: `Mad-Graph` [136, 137], `Pythia` [138], and `Delphes` [139]. Table [B.1] shows the current versions of these packages.

Table B.1: Simulation packages used in high energy physics.

Package	Version
`Mad-Graph`	2.2.3
`Pythia`	8.205
`Delphes`	3.3.2

Section B.1

Mad-Graph

`Mad-Graph` is a simulation package that emulates hard scattering processes in a particle accelerator. This program is based upon physical parameters, which can be set by the user. In addition, the simulation works in an approximation known as *asymptotical free*, which was confirmed by James Bjorken in 1968 [140]. This program computes cross-sections (σ) of physical processes and the kinematic information of all particles involved in collisions. In order to calculate the cross-section, *Parton Distribution Functions* (PDF)'s $f = f(x, Q^2)$ play an important role. These PDF's depend on the fraction of momentum carried by the parton

x_i and the scale of energy Q^2. Equation (B.1), shows the standard formula to obtain the cross-section.

$$
\begin{aligned}
d\sigma_{ij\to lm} &= \left(\int_0^1\int_0^1 f_i(x_i,Q^2)f_j(x_j,Q^2)dx_idx_j\right)\times\frac{d^3p_l}{(2\pi^2)2E_l}\frac{d^3p_m}{(2\pi^2)2E_m} \\
&\times\ \delta^4(p_i+p_j-p_l-p_m)\times|\mathcal{M}_{ij\to lm}|^2
\end{aligned}
\tag{B.1}
$$

`Mad-Graph` can simulate a large variety of processes in the SM such as: production of vector bosons ($W^{\pm}, Z^0$), quark anti-quark pairs ($q\bar{q}$), double production of vector bosons ($W^{\pm}W^{\mp}$, Z^0Z^0, $W^{\pm}Z^0$), among others. In addition, `Mad-Graph` can also simulate processes beyond SM such as: SUSY, Extra-dimensions (Z', W'), and Monotop models.

Section B.2

Pythia

`Pythia` is an event generator used in cases where the asymptotic freedom approximation is not valid anymore. Processes such as the fragmentation and hadronization require a non-perturbative treatment, and even fitting using real data. This program mainly reproduces these non-perturbative processes and emulates initial and final state radiation states as well. `Pythia` code flow is divided in three steps [138]:

- The generation of hard processes such as $gg \to h^0 \to Z^0Z^0$ are produced using perturbation theory, which only covers partially the parton interaction.
- After hard processes simulation, `Pythia` includes jets that come from ISR and FSR, as well as, multiple parton-parton interactions, and form-factor of the colliding beams. These effects contribute to get a realistic partonic structure as accurate as possible in a non-perturbative regime.
- Finally, the chain of fragmentation generates decays from partons into stable and unstable particles. This step is completely non-pertubative and requires parametrization of real data.

B.2.1 Matching algorithm MLM

Since `Pythia` generates extra-jets to emulate ISR and FSR states. Merging the information that comes from `Mad-Graph` and `Pythia` is needed. Technically, this matching process is controlled by two parameters within the simulation. These parameters are known as *xqcut* and *qcut*. *xqcut* is defined as the minimum distance among partons in `Mad-Graph` and *xqcut* is referred to an energy threshold of jet clustering in `Pythia`. Basically, the concern is the overcounting of objects in each event. The optimization of these parameters is performed by studying a distribution known as *Differential jet Rate* (DJR), which shows the transition among events that have 0,1 or 2 jets. The smoothness of the distribution in the points where the transition occurs determines the optimal values *xqcut* and *qcut*. Table [B.2] shows some optimal points of SM background production.

Table B.2**:** Optimal values of the DJR distribution to generate SM backgrounds.

Process	$xqcut$	$qcut$
$W + jets$	15	30
$Z + jets$	15	35
Semi-leptonic $t\bar{t}$	30	70
Di-leptonic $t\bar{t}$	30	70

Figure [B.1] shows the DJR distribution for $Z + jets$ and $W + jets$ cases, Note that, the transitions points 0 to 1 Jet and 1 to 2 jets are smooth.

Section B.3

Delphes

After the hadronization process, `Delphes` simulates the interaction between particles and detectors (i,e. the CMS detector). This process pretends to emulate all detection condition such as: reconstruction efficiencies, resolution and acceptance of the detector and systematic uncertainties. The simulation incorporates as many effects as possible like the tracking system embedded in a magnetic field, electromagnetic and hadron calorimeters and muon identification systems. Charged particles are reconstructed as tracks in the tracking volume, long-lived particles that reach the calorimeters deposit their energy depending on the interaction. The ECAL reconstructs electrons and photons, The HCAL reconstructs neutral and charged hadrons, and finally, the muon system detects muons. The position is defined by the geometry of the specific detector, for instance, $(p_{\mathrm{T}}, \eta, \phi, E)$ in a cylindrical detector is convenient. Some aspects of the reconstruction step are:

- Photons and leptons are reconstructed using a threshold in their transverse momentum $p_{\mathrm{T}}(\gamma, \ell) > 10$ GeV. Furthermore, they can be a candidate in the jet collection. The electron energy is smeared according to the resolution of the calorimeter.

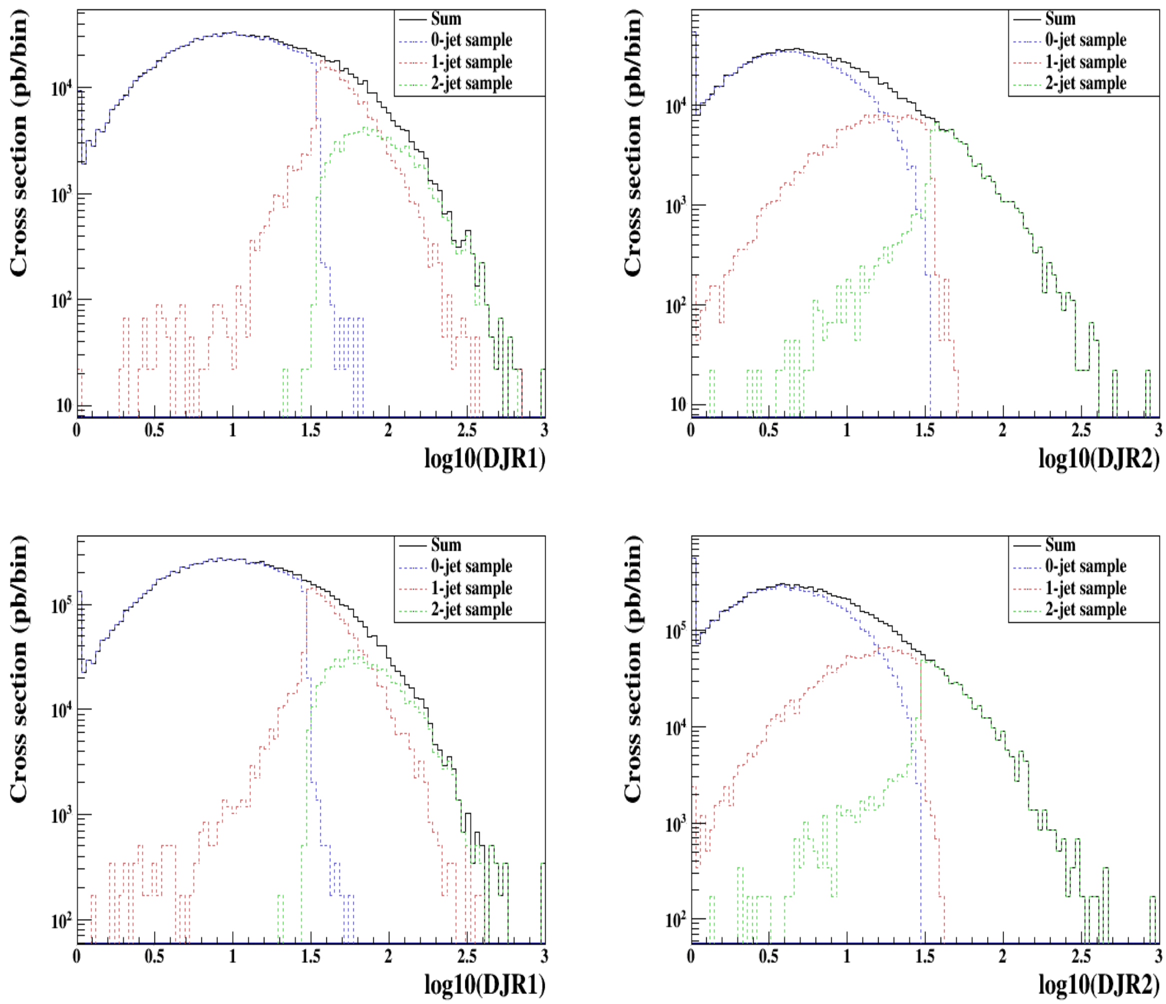

Figure B.1**:** Differential jet rate distribution for $Z + jets$ (above) and $W + jets$ (below). The transitions of 0 to 1 jet (left) and 1 to 2 jets (right). The optimal values are obtained when the distributions are smoothness during the transition.

- The isolation of charged leptons requires a minimum distance in the $\eta - \phi$ plane given by $\Delta R > 0.5$ and a minimum threshold of $p_{\mathrm{T}}(\ell^{\pm}) > 2$ GeV.

- The muon identification depends on the minimum threshold of $p_{\mathrm{T}}(\mu) \geq 3$ GeV within the pseudo-rapidity coverage $|\eta(\mu)| < 2.4$. In addition, Gaussian smearing to the muon resolution is applied.

- The jet reconstruction can be performed through six different reconstruction algorithms. The most used is the *anti-kt* algorithm, which has minimum distance of $\Delta R = 0.7$ and momentum threshold is $p_{\mathrm{T}}(j) > 20$ GeV in the whole pseudo-rapidity coverage $|\eta(j)| < 5.0$.

- In Delphes, the tau collection is a sub-class that belongs to the jet class. The visible τ_h corresponds with hadronic decay of the τ lepton, which occurs roughly 64% of times. Figure [B.2] shows the spectrum of τ decays. In general, the τ_h candidate has a particular signature in the calorimeter, which is narrower than jets that come from other sources [139].

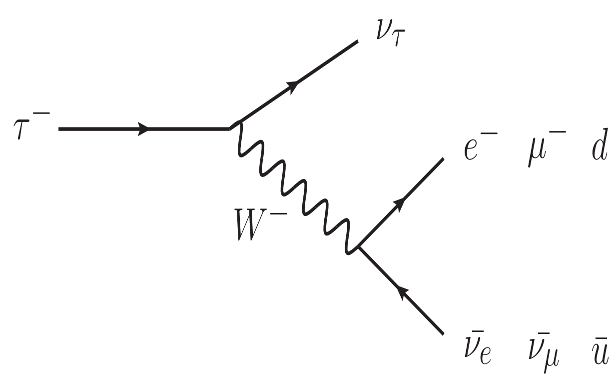

Figure B.2: Feynman diagram of the τ lepton decay, the hadronic decay $\tau \to \bar{u}d$ corresponds to 64%, which is reconstructed as a jet (τ_h) in the detectors.

Finally, there are other packages such as: POWHEG [141], Comhep [142], and Sherpa [143], which are commonly used by CMS and ATLAS collaborations. On the other hand, simulating the detector response is usually done with Geant4 as well [144].